Understanding Powder Feedstock-Part Performance Relationships in Additive Manufacturing

by

Arash Soltani Tehrani

A dissertation submitted to the Graduate Faculty of
Auburn University
in partial fulfillment of the
requirements for the Degree of
Doctor of Philosophy

Auburn, Alabama
August 6, 2022

Keywords: Additive Manufacturing; Fatigue; Powder Characterization; Powder Bed Fusion; Directed Energy Deposition; Machine Learning

Approved by

Nima Shamsaei, Chair, Philpott-WestPoint Stevens Distinguished Professor, Department of Mechanical Engineering
Shuai Shao, Associate Professor, Department of Mechanical Engineering
Robert L. Jackson, Professor, Department of Mechanical Engineering
Hans-Werner van Wyk, Associate Professor, Department of Mathematics and Statistics
Mahdi Habibnejad-Korayem, Adjunct Assistant Professor, Department of Mechanical and Mechatronics Engineering, University of Waterloo
Daniel Silva, Assistant Professor, Department of Industrial and Systems Engineering

Abstract

In this dissertation, the relationships between the powder feedstock and the mechanical performance of additively manufactured (AM) parts were investigated. In this regard, different aspects of powder feedstock were considered. First, the effects of the particle size distribution (PSD) and shape on tensile and fatigue performance of AM Ti-6Al-4V parts via a laser powder bed fusion (L-PBF) were investigated. Two plasma atomized Grade 23 Ti-6Al-4V powder batches were used with PSDs of 15-45 μm (fine) and 15-53 μm (coarse) with highly spherical particles. Both batches showed comparable powder flowability due to very spherical powder particles. The fine powder, however, showed some improvement in packing state due to the narrower PSD resulting in fewer empty spaces between the powder particles. The powder characteristics resulted in negligible changes in tensile strength, which were attributed to the similar microstructures in the specimens manufactured from both powders.

The tensile ductility, however, improved by using the coarse powder ascribed to the smaller defects in coarse powder specimens. Although the overall number of defects was considerably lower in fine powder specimens, some large defects were noted in the case of fine powder specimens, which was explained by more spattering during fabrication with this powder caused by higher O content. Such large defects were found detrimental to both tensile ductility and fatigue performance. In addition, no variation was observed along with the powder delivery system, related to the excellent flowabilities of both powders. Second, the plasma atomized Ti-6Al-4V powder changes throughout L-PBF fabrication and with continuous reuse were traced. It was found that continuously reusing the powder can improve the powder packing state and flowability.

However, the O content also increased with powder reuse. Although reusing the powder up to 3 times improved fatigue performance, further reuse up to 7 times resulted in adverse effects compared with the unused powder.

The lower fatigue performance and tensile ductility of specimens manufactured using 7-times reused powder were correlated with the higher O content in 7-times reused powder batch, which resulted in more spattering during the fabrication and formation of large defects. This hypothesis was justified by observing larger and more frequent defects downstream of the argon flow, which is commonly used as the shielding gas during AM fabrication. The specimens in the downstream region also had slightly higher tensile strength owing to the higher O content, lower fatigue performance, and higher critical energy release rate. This study was repeated with gas atomized 17-4 precipitation hardening (PH) stainless steel (SS) with a nominal PSD of 15-45 μm to investigate the build location dependency with a powder consisting of also less spherical particles and track the changes with continuous powder reuse.

It was realized that the powder behavior, including flowability and packing state, did not change the tensile strength and the microstructure of the L-PBF 17-4 PH SS specimens even though they improved with continuous reuse. Fatigue performance in the high-cycle-fatigue (HCF) regime, however, significantly improved with powder reuse, ascribed to the smaller gas-entrapped pores in the specimens manufactured using 14-times reused powder. It was also noted that when the powder does not contain highly spherical powder particles, the lower powder flowability may jeopardize the powder bed layer uniformity and result in some variation along with the powder delivery system. For instance, more frequent and larger lack-of-fusion defects, which are detrimental to fatigue performance, were observed in the specimens placed west of the build plate (i.e., farther away from the feedstock bin).

Owing to the powder flowability improvement by continuously reusing the powder, this location dependency across the build plate decreased. Observing such variations across the build plate signified the importance of developing standardized powder atomization and reuse practices to ensure consistent build quality. The build-to-build variability due to the effects of powder reuse was also investigated in different AM technologies, including laser powder directed energy deposition (LP-DED) using NASA HR-1 superalloy with a nominal PSD of 45-105 μm. Multiple sets of thin walls were deposited using the unused NASA HR-1 powder as well as 1- to 5-times reused powder. The powder flowability did not change with continuously reusing the powder. The chemical composition also remained constant throughout all depositions. The PSD, however, coarsened with repetitive powder reuse resulting in fine particle reduction and mean particle size enlargement.

Investigating the powder particle shape did not reveal any changes with reuse. Therefore, it was assumed that highly spherical powder particles resulted in comparable flowability in all powder batches, although fine particles (typically known for lower flowability) decreased with powder reuse. The tensile strength and ductility were also investigated. No change in tensile strength was noticed due to the similar microstructures and O content in the LP-DED NASA HR-1 specimens. All deposited specimens had relative densities larger than 99.997%, and the maximum defect size in all specimens was almost comparable, which was correlated with the similar flowability of all powders. On the other hand, the similar defect content also resulted in identical tensile ductilities and fatigue performance. Moreover, the effects of specimen orientation with respect to the building direction (i.e., perpendicular or parallel) was investigated to better correlate the specimen property in the laboratory to part performance.

The tensile strength did not change with the orientation owing to the similar microstructures, defect content, and O concentration. The ductility, however, was somewhat lower in parallel specimens due to the more critical effects of surface undulations when subjected to tensile loading. The lower ductility of parallel specimens also showed slightly lower resistance to fatigue failures in the low-cycle-fatigue (LCF) regime. In this regime, the majority of fatigue life is spent in crack growth, and more ductile materials are typically favored. Therefore, the lower fatigue performance could be correlated with the lower ductility of parallel specimens. In the HCF regime, however, negligible changes with a greater scatter in data were observed owing to the dominant effects of micro-notches on the surface resulting from the layer-by-layer deposition process. Lastly, a single powder quality metric was identified to correlate several powder characteristics.

Such quality metrics and similar ones could contribute to faster adoption of AM technologies by indicating the effects of powder on the final part performance without the need for the experiment. The proposed powder quality metric could satisfactorily predict the powder behavior and correlate with observed mechanical properties in this dissertation. In addition, an image processing method was used to obtain the powder PSD and shape information (e.g., sphericity) from the 3D reconstructed images via X-ray computed tomography (CT). Subsequently, a machine learning algorithm was implemented via a feed-forward artificial neural network (ANN) multi-layer perceptron. Due to cost-effectiveness, developing statistical tools such as machine learning algorithms is essential for the faster adoption of AM technologies. The proposed ANN model was trained using the PSD and sphericity as well as the powder rheological characteristics. It was observed that the ANN model could effectively predict the powder quality score with a low mean absolute percentage error (MAPE), indicating the model's robustness.

Acknowledgments

I would like to sincerely thank my Ph.D. advisor, Dr. Nima Shamsaei, for his endless patience and encouragement throughout this journey. This dissertation could not have been completed without his support, knowledge, and guidance during our meetings, emails, and article revisions. In addition, I would like to thank Dr. Shuai Shao, Dr. Robert L. Jackson, and Dr. Hans-Werner van Wyk for serving on my Ph.D. committee. The support and feedback from them are greatly acknowledged. I also would like to offer my gratitude to Dr. Mahdi Habibnejad-Korayem from the University of Waterloo and Advanced Powder and Coating (AP&C), a General Electrics (GE) Additive Company, for his time and advice and for serving on my Ph.D. committee. I would like to also express my gratitude to Dr. Daniel Silva for serving on my Ph.D. committee as the University Reader, for his support toward the completion of this dissertation, and to Dr. Jeffrey Suhling and Dr. Hareesh Tippur, the Mechanical Engineering Department Chair and Associate Chair for Graduate Studies, for all their administrative support during the past five years.

I also would like to appreciate the funding support from the Auburn University, National Institute of Standards and Technology (NIST) under Award Nos. 70NANB18H220 and 70NANB19H170, Federal Aviation Administration (FAA) under Award No. FAA-12-C-AM-AU-003, National Aeronautics and Space Administration (NASA) under Award No. 80MSFC19C0010, National Science Foundation (NSF) under Award No. 1919818, and Delta Airlines. Last but not least, I would like to thank my wife, parents, family, and colleagues at the National Center for Additive Manufacturing Excellence (NCAME) for their unlimited support and encouragement in completing my Ph.D. program. Indeed, completing this dissertation would not

be feasible without their help. I would like to dedicate this dissertation to my wife, Sogol, my father, Farhang, and my sister, Shabnam.

Table of Contents

List of Tables

List of Figures

Abbreviations

A	*Surface area*
AE	*Aeration energy*
AM	*Additive manufacturing/additively manufactured*
ANN	*Artificial neural network*
AOR	*Angle of repose*
B	*Batch*
BCC	*Body-centered cubic*
BFE	*Basic flowability energy*
BDtap	*Tapped density*
CBD	*Conditioned bulk density*
CE	*Circular equivalent*
CPS	*Compressibility*
$D_{f,10}$	*10^{th} percentile particle Feret diameter*
$D_{f,50}$	*50^{th} percentile particle Feret diameter*
$D_{f,90}$	*90^{th} percentile particle Feret diameter*
DIC	*Digital image correlation*
E-PBF	*Electron powder bed fusion*
EB-PBF	*Electron beam powder bed fusion*
EBSD	*Electron backscatter diffraction*
ECCI	*Electron channeling contrast imaging*
EDS	*Energy-dispersive X-ray spectroscopy*
FCC	*Face-centered cubic*
FE	*Finite element*
FRI	*Flow rate index*
HCF	*High-cycle fatigue*
HA	*Heat-affected*
HE	*Hydrogen embrittlement*
HR	*Hausner ratio*
ICP	*Inductively coupled plasma*
L-PBF	*Laser powder bed fusion*
LB-PBF	*Laser beam powder bed fusion*
LCF	*Low-cycle fatigue*
LoF	*Lack of fusion*
MAPE	*Mean absolute percentage error*
MLP	*Multi-layer perceptron*
MCF	*Mid-cycle fatigue*
PBF	*Powder bed fusion*
PD	*Pressure drop*
PH	*Precipitation hardening*
PSD	*Particle size distribution*
S_{avg}	*Average sphericity*

S_{std}	*Standard deviation of sphericity*
SEM	*Scanning electron microscope/microscopy*
SE	*Specific energy*
SS	*Stainless steel*
Ti64	*Ti-6Al-4V*
UTS	*Ultimate tensile strength*
V	*Volume*
YS	*Yield strength*
XCT	*X-ray computed tomography*

Nomenclature

A_0	*Initial cross-sectional area of the gage*
A_f	*Fracture cross-sectional area of the gage*
$2N_f$	*Number of reversals to failure*
E'	*Cyclic modulus of elasticity of the stable cycle*
ε_f	*True fracture strain*
R_σ	*Ratio of minimum to maximum stress*
R_ε	*Ratio of minimum to maximum strain*
R_a	*Arithmetical mean height of the profiled line*
ρ_{10}	*Radii of the deepest valleys of the profiled line*
S_a	*Arithmetical mean height of the profiled surface*
S_t	*Maximum distance between the peaks and valleys*
S_{zISO}	*10-point height roughness*
ε_a	*Strain amplitude*
σ_a	*Stress amplitude*
σ_m	*Mean stress*
$\sigma'_{f,10^3}$	*Fatigue strength at 10^3 cycles*
σ_e	*Endurance limit*
K	*Strength coefficient*
K_{IC}	*Fracture toughness*
K_t	*Stress concentration factor*
K_f	*Fatigue notch factor*
J	*Energy release rate*
J_{IC}	*Critical energy release rate*
x	*Input vector*
y	*Output vector*
w	*Weight coefficient vector*
γ	*Grain size*
q	*Notch sensitivity factor*
n	*Strain hardening exponent (Chapter 5)/ Input feature (Chapter 6)*
Coarse/Fine powders	*The PSD of coarse and fine powder batches were 15-53 μm and 15-45 μm, respectively.*
East/West specimens	*East specimens were closer to the powder feedstock while the West ones were further away*
Gas-entrapped pore	*An AM process-induced volumetric defect formed due to entrapment of shielding gas.*
Lack-of-fusion defect	*An AM process-induced volumetric defect formed due to insufficient overlap between molten tracks or between layers.*
Void	*A tensile loading induced cavity within the material which can grow and coalesce with the neighboring voids to induce fracture.*

1. Introduction

Metal additive manufacturing (AM) is a sequential, layer-by-layer process of joining metallic materials until a three-dimensional part is manufactured [1]. This technology has received a booming interest due to its compatibility with several alloys, potentially decreasing the manufacturing lead time at a reduced cost, and lowering the weight of structural components [2,3]. Most AM processes start with a material feedstock (whether in the form of powder or wire) and a source of energy (i.e., laser, electron, or electrical arc) to join the layers. In laser-based AM technologies, numerous process parameters are involved during the process, including the laser power, laser speed (also known as scanning speed), hatching distance, and layer thickness. The combination of each process parameter set can result in a unique thermal history experienced in additively manufactured (AM) parts [4,5]. The resulting thermal history can influence the micro-/defect-structure and mechanical properties, often distinct from traditionally manufactured materials such as wrought and cast. Therefore, investigating such relationships between feedstock, process, structure, property, and ultimately part performance is essential in adopting AM technologies with industrywide applications (see Fig. 1).

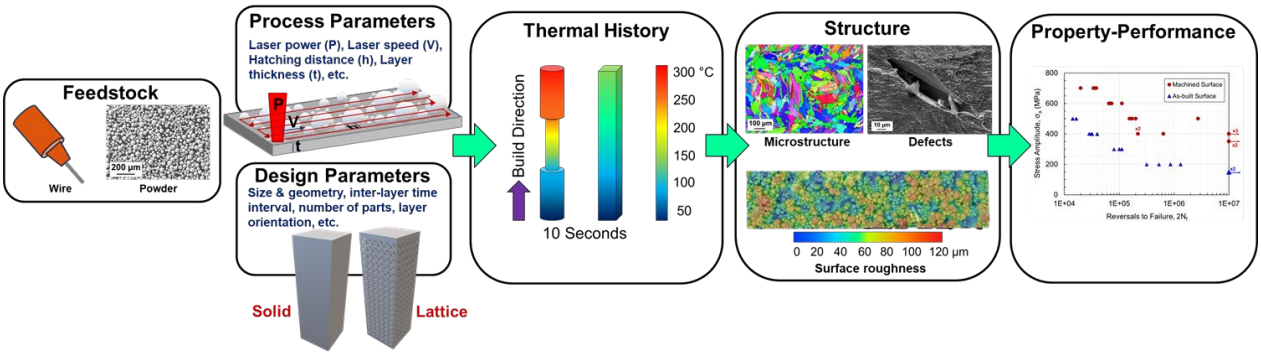

Fig. 1 The feedstock-process-structure-property-performance relationships in laser-based AM.

With the lack of knowledge of the whole system, it might be more efficient to investigate each aspect separately, e.g., the effects of thermal history or structure on AM part performance. The current study investigates the effects of feedstock (in powder form) and some design aspects (e.g.,

location of the parts on the build plate) on the micro-/defect-structure and mechanical properties of AM parts [1,6]. In general, understanding the powder feedstock behavior is not straightforward since the powder behavior is not easily measurable, and there are often different evaluation metrics. For instance, some studies have reported powder flowability and packing state as the most relevant metrics to AM technologies [7,8]. In addition, powder behavior is influenced by its characteristics. Some of these characteristics are morphological aspects (i.e., particle size and shape and surface texture), chemistry (i.e., bulk or surface chemistry), and microstructural features (i.e., crystalline structure and internal defects in the particles) [9].

Some studies attempted to understand how each characteristic can influence powder behavior [10]. For instance, it has been reported that finer particles can generally hinder the flowability of the powder due to their higher surface-to-volume ratios, and consequently, higher interparticle frictions [11]. Deleterious non-spherical particles can disrupt the powder flow, whereas the highly spherical ones can move more uniformly [12]. Large particles are also said to have a non-desirable packing as they may leave empty spaces between them [7], while they typically provide a smooth flow. The presence of different chemical elements due to powder atomization techniques (e.g., gas, water, or plasma atomization, and plasma rotating electrode process (PREP)) or fabrication process (e.g., under argon, nitrogen, or vacuum) can also considerably influence the powder packing and flow behaviors. For instance, powders with lower moisture content are favored as they generally provide a superior flow and packing state [10]. Moreover, interstitial elements (e.g., O or N) can result in different mechanical properties. For example, the higher O content in Ti-6Al-4V (Ti64) powder may yield parts that are less ductile and possess a higher strength [13].

Lastly, the microstructural features of the powder can contribute to further variations in part performance. For instance, whether the powder has been exposed to a high-temperature

environment or cyclic reheating can affect the powder microstructure and therefore, the final part performance. The presence of internal pores within the particles can also deteriorate the mechanical properties of AM parts by interrupting the smooth flow of the powder, poor packing state, and entrapment of gas bubbles within the solidified part [10]. However, the effect of powder on part performance is not unanimous among different research studies, and contrary results have sometimes been reported. For instance, some studies have shown coarser particles can result in higher ductility and fatigue resistance [14], while a reverse effect has been reported in some other studies [15], demonstrating superior tensile properties for the AM parts manufactured using fine powder.

In addition to size, other powder characteristics such as particle shape can considerably influence the part performance by dictating the powder packing and flow behaviors. It has been shown that irregular particles typically have insufficient flowabilities and poor packing state [10]. Therefore, parts with lower densities and deteriorated mechanical performance can be expected. The irregular shape of particles can also facilitate a higher O and moisture pickup during handling or fabrication, which have both been reported to degrade the powder packing state and flowability [10]. Consequently, a greater location dependency may arise with low flowability due to a nonuniform powder layer deposition on the build plate. Therefore, further investigations are needed to interpret particle size distribution (PSD) and shape effects on mechanical properties under static and dynamic loading conditions.

While different powders can have distinct characteristics, even the same powder that is continuously reused/recycled for AM fabrications can change and influence the volumetric defect content and surface texture, ultimately yielding different mechanical properties [7,14]. For instance, a higher tensile strength was reported when the AM parts were manufactured from reused

powder, attributed to the narrower PSD and higher O content [13]. Some studies also investigated the effects of reuse on fatigue behavior. For instance, Popov et al. [15] showed a lower fatigue performance for the parts manufactured from reused powder in an electron powder bed fusion (E-PBF/EB-PBF) system, which was ascribed to the increased O in the reused powder.

In addition, there is no understanding of whether the changes in mechanical properties due to power reuse are similar with different materials and AM technologies. For instance, a lower fatigue performance was reported for E-PBF Ti64 with reuse [14,15], while some slight improvement in fatigue performance of 17-4 precipitation hardened (PH) and 316L stainless steel (SS) parts manufactured using reused powder in a laser powder bed fusion (L-PBF/LB-PBF) AM machine was indicated in [16]. In other AM technologies, such as laser powder directed energy deposition (LP-DED), the powder is blown on the substrate instead of spreading a layer of powder. Therefore, powder characteristics such as flowability may be irrelevant to this technology. Hence it is still crucial to generate more understanding about the effect of powder characteristics on the performance of parts fabricated by different materials and AM technologies. Thus, the overall goal of this research is to investigate relationships between the powder feedstock and the AM part performance.

1.1. Project Goal and Objectives

The overall goal of this research is to investigate the influence of powder feedstock on AM part performance by determining the most influential powder characteristics in L-PBF and LP-DED processes affecting the mechanical properties. This research aims to achieve its goal by targeting several objectives. The **first objective** (**Chapter 2**) is to understand how PSD and particle shape affect the part performance. In this regard, we hypothesize that a powder batch with a narrower PSD and spherical particles yields superior tensile and fatigue performance, leaving fewer defects in the manufactured parts (Hypothesis 1a). In addition, the high particle sphericity

and the resulting high powder flowability increase the mechanical properties consistency across the build plate (Hypothesis 1b). The **second objective** (**Chapter 3**) is to investigate how powder characteristics, including PSD and particle shape, alter with the powder reuse practice and how these changes affect the AM part performance. It is hypothesized that if the PSD of Ti64 powder becomes narrower with powder reuse while the particle shape and O content remain the same, a higher fatigue resistance is expected (Hypothesis 2a). Moreover, powder reuse does not affect the consistency of parts' mechanical properties with respect to their location on the build plate (Hypothesis 2b).

The **third objective** (**Chapter 4**) is to determine whether the changes in powder characteristics with powder reuse are the same in all material systems. Thus, we theorize that an improved fatigue performance is also expected for other materials (e.g., 17-4 PH SS), provided the PSD becomes narrower (Hypothesis 3a). Furthermore, a powder batch with less particle sphericity gives rise to mechanical properties inconsistency across the build plate (Hypothesis 3b). Moreover, the **fourth objective** (**Chapter 5**) is to investigate which powder characteristics are crucial in LP-DED technology, where no powder bed is involved, and the powder is blown instead. Therefore, we speculate that powder flowability does not affect the mechanical properties of AM parts in LP-DED and other powder characteristics need to be considered (Hypothesis 4a). Additionally, excising the parts in different orientations to the build layer from deposited materials influences the mechanical properties (Hypothesis 4b). Lastly, the **fifth objective** (**Chapter 6**) is to explain the mechanical properties of laser-based AM parts merely with the powder quality. Therefore, it is proposed that most powder characteristics are correlated (Hypothesis 5a). In addition, statistical tools such as machine learning are applicable to assess the powder quality and interpret mechanical properties (Hypothesis 5b).

1.2. Background and Past Work Related to the Current Research

Powders can be atomized through different methods, including water, gas, plasma, and plasma rotating [12]. Using different atomization techniques can result in distinct powder PSDs and morphologies. For instance, water atomization, although less expensive, will commonly result in more irregularly-shaped particles compared with other approaches. Kassym et al. [17] compared water and gas atomized powders. Higher particle shape irregularity and O concentration were observed in the water atomized batch. Therefore, higher interparticle frictions, and consequently, a hindered flow and poor spreadability were noted [10]. Another important powder characteristic is PSD. Depending on the technique and sieving method, different PSDs can be achieved when powders are atomized. The PSD, which determines the relative amount of particles with different sizes, can be Gaussian (i.e., normal) or multimodal [10].

The multimodal PSDs, including bimodal, are more complex, and there is not enough knowledge about their effects on part quality. Therefore, one task of this dissertation is to interpret such PSDs and investigate their effects on mechanical properties. In the case of normal distributions, some attempts are available in the literature to understand the correlation of PSD variations with powder flow and packing behavior, and ultimately the part performance. For instance, Jian et al. [18] experimented with two AlSi10Mg powders with mean particle sizes of 20 μm and 50 μm. They observed a higher tensile ductility and, to some extent, higher fatigue performance at higher stress levels when the 50 μm powder was used. However, the difference was less significant in lower stress levels (i.e., high-cycle-fatigue (HCF) regimes). Although this study showed variations when different PSDs were used, no explanation for such behavior was reported concerning the effects of powder characteristics. The changes in mechanical properties were delineated merely by the defect content, which was higher for the powder with a smaller mean particle size.

Habibnejad et al. [19] also investigated Ti64 powders of various sizes. It was reported that larger mean particle sizes and narrower PSDs could result in less interparticle friction and better flowability [10]. However, finer particles may be favored in terms of packing as they can fill out empty spaces between particles. Different approaches have been proposed to identify flowability and packing state competing effects. For instance, Brika et al. [20] reported a figure of merit number, which accounted for powder rheological properties with equal weights. It was shown that this number could efficiently determine the powder's suitability for the PBF technologies. However, one deficiency of this approach was considering equal weights for powder rheological characteristics with various potential effects. This approach may not be the most accurate since different characteristics such as density and cohesivity may have different effects. As a result, Habibnejad et al. [19] modified the equation by considering different weights for the powder's bulk, rheological, and dynamic properties so that the number could better represent the powder's suitability.

In addition, powder characteristics may change during AM fabrication and with powder reuse/recycling due to complex laser-powder interactions [21]. Powder reuse usually refers to continuously reusing the powder until it is insufficient for the subsequent fabrications, or its properties do not meet specific criteria. Powder recycling, however, refers to the “top-up” practice in which unused (i.e., virgin) powder is mixed with the used one with different ratios [12]. Regardless of the approach, i.e., with or without rejuvenation, the powder characteristics may change in each cycle. There is still debate on how such variations in powder characteristics can manifest in the mechanical properties. For instance, Cordova et al. [22] investigated the reuse of Inconel 718 (IN718), Ti64, AlSi10Mg, and Scalmalloy and reported a general increasing trend in

PSD, particle elongation and satellites (i.e., very fine particles adhering to the surface of other particles [7]), and flowability with powder reuse in an L-PBF system.

This trend, however, may not always be true. Rather it most likely depends on many process conditions, such as the sieving system, gas flow, number of hours that the powder was exposed, powder atomization technique, and the initial PSD. For example, negligible changes in PSD and mechanical properties were reported in [23] when IN718 was reused for 10 cycles in an L-PBF system. In addition, the O content was the only factor that increased gradually throughout the reuse cycles. However, in [24], tensile and fatigue strength decreased slightly with reusing AlSi10Mg powder 8 times in an L-PBF system. In another powder reuse study, Alamos et al. [24] reported comparable powder characteristics, part densities, and tensile properties for the Ti64 specimens manufactured using 8-times reused Ti64 powder in an L-PBF system to that of the unused powder. However, a slight increase in O content was reported with powder reuse.

Harkin et al. [25] showed that reusing the Ti64 extra low interstitials (ELI) for 9 cycles in an L-PBF system did not alter its PSD. However, some improvement in powder flowability was reported after reuse. Carrion et al. [7] observed a higher fatigue performance for the L-PBF Ti64 specimens manufactured using heavily reused powder in the HCF regime (i.e., longer than 10^5 cycles). This observation was attributed to the more uniform powder bed resulting from the resued powder due to its narrower PSD. In contrast, Popov et al. [15] observed an inferior fatigue performance and a higher level of scatter in data, mainly in the HCF regime for the parts manufactured using the reused Ti64 powder in an E-PBF system. The lower fatigue performance was ascribed to the powder exposure to humidity and O content, resulting in lower flowability and more defects in the manufactured parts. However, when the parts underwent hot isostatic pressing

(HIP), reused powder specimens showed almost comparable fatigue performance to the unused powder.

Similar results were also reported by Soundarapandiyan et al. [14] when they compared two sets of specimens manufactured from unused and 10-times reused powders in an E-PBF system. As expected, negligible changes in microstructure were reported, which was the reason for almost comparable ultimate tensile and yield strength, impact energy, and hardness. Some improvements in the powder flowability, as well as sphericity, were also reported. Although the reused batch had a superior packing state and flowability, a reduction in fatigue life was seen in the HCF regime. This observation was ascribed to the removal of fine particles and the presence of high aspect ratio particles that can pass through the sieve filtration, resulting in an inferior reused powder packing state and ultimately lack-of-fusion defects in the manufactured parts.

The effects of powder reuse on the mechanical properties of AM parts with other materials have not been fully understood either. For instance, the reuse of gas atomized IN718 in an L-PBF system up to 10 times was studied in [26], in which an increase in PSD and O content and reduced flowability were reported. In addition, the powder feedstock quality decreased with subsequent reuse due to the accumulation of spattered particles. However, no correlation with mechanical properties was made. A similar PSD coarsening effect, along with improved flowability, was reported in [27]. In this study, no change in tensile properties was noticed with powder reuse up to 14 times. However, no results were provided regarding the fatigue performance.

Reusing the powder in other technologies such as LP-DED has also gained considerable attention. In this technology, higher build resolutions can be achieved with the compensation of a significantly larger amount of unused powder after each deposition, making powder reuse inevitable. Some research studies have been conducted to understand the effects of reused powder

in LP-DED [28–30]. For instance, Terrassa et al. [28] investigated the effects of reusing 316L SS in an LP-DED system. Negligible changes in powder characteristics and part performance were reported. The ultimate tensile and yield strength increased slightly, which was attributed to the marginal increase of O concentration in the powder. As evident from the mentioned studies, there are still many ambiguities regarding the effects of powder characteristics on the mechanical properties of AM parts. Therefore, more investigations are needed to explain the potential changes in mechanical properties due to powder characteristics and their change by reusing the powder.

1.3. Broader Impact

The results of this study can help AM users strategically select the powder with specific characteristics for AM fabrication. It potentially enables the AM practitioners to custom tailor the part performance, including surface roughness, microstructure, defects, as well as tensile and fatigue properties, by altering the powder characteristics such as PSD and particle shape. This study will also investigate the importance of each powder characteristic and contribute to the knowledge regarding powder flow and packing behavior, which is indeed insufficient in the current literature. The increased knowledge about the powder can ultimately increase the AM production efficiency. Moreover, this dissertation aims to locate the sources of variability in AM technologies that result from the powder feedstock. Suggestions will be provided for AM users to alleviate such sources of variability. This dissertation will also provide knowledge about powder reuse, which can ultimately benefit by significantly reducing the cost, which can further promote the broader adoption of AM technologies. Lastly, this dissertation will generate material data, including fatigue and tensile properties specifically for Ti64, 17-4 PH SS, and NASA HR-1, which will be publicly available for the AM community to use.

2. Ti-6Al-4V Powder Characteristics in Laser Powder Bed Fusion: The Effect on Tensile and Fatigue Behavior [31]

2.1. Introduction

Additive manufacturing (AM) has gained significant attention from industrial sectors and governmental agencies by providing manufacturers with more design freedom and the ability to fabricate complex geometries and reduce material waste. This booming interest to generate functional parts for load-bearing applications has also introduced some challenges toward mass production with AM technologies, which necessitates a more thorough understanding of the feedstock-part performance relationships [1,32]. One of the most critical facets is the state of the material feedstock − whether in the form of wire or powder, feedstock characteristics (i.e., morphology, chemistry, and microstructure [9]) can affect the mechanical performance of additively manufactured (AM) parts. In the case of laser or electron powder bed fusion (L-PBF or E-PBF) AM, where the powder is used as the feedstock, the particle size and morphology can play a critical role on the mechanical performance of the fabricated parts.

Morphological characteristics can be mainly divided into particle shape and size distribution, which have been reported to influence the surface roughness, volumetric defect content, and mechanical behavior—as well as their location dependency—of AM parts [10,33]. It has been well established that using a powder batch with highly spherical particles can improve powder flowability, spreadability, and packing state as a result of less interparticle friction [10]. However, when it comes to particle size and particle size distribution (PSD), choosing the appropriate range can be challenging. On one hand, the presence of fine particles in coarse ones can theoretically lead to a more densely packed powder bed. On the other hand, excess amount of fine particles—due to the higher surface area and more interparticle friction—can result in increased oxygen

pickup as well as particle interlocking (i.e., agglomeration) which can reduce powder's overall flowability and spreadability and lead to poor powder bed packing [11,20].

The differences in the powder bed packing state may influence the tensile, fatigue, and fracture properties since they can generate different surface roughness, volumetric defect contents, and microstructure in the fabricated parts. In terms of surface roughness, although it is generally acknowledged that the as-built rough surface compromises the tensile ductility and fatigue properties of AM specimens compared to machined and polished surfaces, how the surface roughness is affected by powder characteristics and rheological properties is not clear. While coarser particle size has been shown to lead to higher values in certain roughness parameters [9,10], such as the R_a (arithmetical mean deviation of a surface line profile), how well these popular parameters correlate with the mechanical properties, especially fatigue, is still debated. Therefore, it can be stated that the effect of powder characteristics on the mechanical properties of AM specimens with as-built surfaces is not well understood (***Knowledge Gap #1***).

In terms of volumetric defect content, coarser/larger particles that are relatively uniform in size have better flowability and are typically associated with lower defect contents in parts, even though the theoretical powder bed packing density is relatively low [34]. On the other hand, the hindered powder flow due to a large number of fine particles can give rise to inconsistent deposition of powder, empty pockets due to agglomerates, and higher defect content with strong location dependency [33]. The volumetric defects (e.g., gas-entrapped pores) generally do not affect the yield strength (YS) of materials, but they may be detrimental to their ductility and the ultimate tensile strength (UTS) since they are effective nucleation sites for tension-induced voids [35].

For instance, Jian et al. [18] observed lower defect content in parts fabricated by a coarser AlSi10Mg powder batch in L-PBF, which yielded a much higher ductility (almost twice) and a moderately increased UTS, but essentially the same YS compared with finer powder-produced ones. This observation was echoed by the results provided by Riener et al. [36] for L-PBF AlSi10Mg. Similarly, Brika et al. [20] have shown that specimens manufactured from a coarser Ti-6Al-4V (Ti64) powder batch via L-PBF had a higher part density (lower defect content), true fracture strain (ε_f), and UTS as compared to their counterparts fabricated from the finer powder batch [20]. However, although existing studies have investigated the effect of fine and coarse particles, the effect of wider/narrower PSD span has not been addressed (***Knowledge Gap #2***).

In terms of microstructure, the inter-particle contact may be inefficient in a poorly packed powder bed which may be associated with slightly lower thermal conductivity [7], slightly lower cooling rate, coarser microstructure, and thus slightly lower YS. This is supported by the E-PBF data reported by Nandwana et al. [37], where a coarser α-lath thickness was noticed in the typical α+β basketweave microstructure in the finer powder specimens. A lower UTS by about 6% for the specimens fabricated from the fine Ti64 powder batch was also reported. Although YS was not reported in this study, the same trend should hold since the strain hardening rate of Ti64 is very low [32,38].

While tensile properties of AM parts are affected by powder characteristics via both defect content and microstructure, the fatigue properties are primarily dictated by both surface and volumetric defects [3,39], more so in the high cycle fatigue (HCF) regime. In the machined surface condition, the effect of volumetric defect becomes apparent. For instance, Soltani-Tehrani et al. [33] reported that reusing the 17-4 PH stainless steel (SS) powder in an L-PBF system can result in smaller defects by changing the PSD, and consequently an enhanced HCF performance. Similar

influence of PSD and powder rheological properties on defect characteristics and fatigue performance in the resulting materials were echoed by other studies such as in [18,37]. However, the correlation of fatigue properties with powder characteristics, including their rheological properties, is still lacking (***Knowledge Gap #3***). Interestingly, the validity of the "coarser powder-better properties" trend noted above is not always true. For instance, Jian et al. [18] witnessed a higher fatigue resistance for the L-PBF AlSi10Mg specimens fabricated from the coarser batch (average particle size of 50 μm), while Nandwana et al. [37] reported that being inferior for the coarser Ti64 batch (median size of 90 μm, 10^{th} percentile size of 71.4 μm) in E-PBF AM. It is expected that excessively large particles are inefficient to absorb the incident energy which could lead to poor melting and defect formation [36,40].

Lastly, in the PBF technologies, the powder is distributed from the reservoir on one side of the powder bed to the other; thus, the packing state of powder may be location-dependent [33,41]. This location dependency has been primarily associated with powder flowability and spreadability [33]. To uncover such a correlation between the powder and location, Jacob et al. [41] investigated the spreadability of Inconel 718 and 17-4 PH SS with different PSDs. It was observed that the segregation of powder particles (i.e., the separation of the powder size constituents [42]) can result in the non-uniform deposition of powder in different locations. This behavior was explained by the "front stress-free turning powder wedge" phenomenon, which states that finer particles typically move to the bottom of the powder bulk, and consequently, are deposited closer to the dispenser, while coarser ones might deposit near the overflow bin (i.e., collector) [41,43]. The location-dependent powder bed packing state may produce defect content and mechanical properties of the resulting parts that are also location-specific [33]. However, this location dependency has hitherto been underexplored (***Knowledge Gap #4***)

To address the four knowledge gaps defined, this work evaluates the effect of powder characteristics on powder rheological behavior as well as on the microstructure, surface roughness volumetric defect content, and mechanical properties—and their location dependency—of L-PBF Ti64 parts. Ti64 is the most widely used titanium alloy in PBF technologies due to its high strength, low weight, biocompatibility, and corrosion resistance which has made it a suitable raw material for aviation, space, biomedical, and chemical applications [44]. Two batches of Ti64 powder with different PSD ranges (i.e., 15-53 μm and 15-45 μm) were utilized for fabrication, whose morphological and rheological characteristics were thoroughly characterized and used to correlate with the variations observed in tensile and fatigue properties of the fabricated parts. To investigate the location dependency of microstructural, defect, and mechanical properties, parts were placed across different locations on the build plate in the powder distribution direction and tracked during fabrication. This article is arranged as the following: Section 2 Methodology, Section 3 Experimental Results, and Section 4 Discussion on Experimental Results. Finally, conclusions are drawn in Section 5 based on the results and discussion.

2.2. Methodology

In this study, two powder batches of Advanced Powders and Coating (AP&C) plasma atomized spherical Ti64 Grade 23 with two different PSDs of 15-53 μm and 15-45 μm were used for fabrication. Hereon, the two powder batches are referred to respectively as “coarse” and “fine” throughout the manuscript. The chemical composition following the ASTM F3001 [45] and measured based on ASTM E1409, E1447, E1941, and E2371 [46–49], as well as D_{10}, D_{50}, D_{90} sizes obtained by laser diffraction according to ASTM B822 [50] for both batches are reported in Table 1. The D_x value signifies the x^{th} percentile particle size, i.e., x% of the particles are smaller than D_x μm [10]. The span value is defined as the $(D_{90}-D_{10})/D_{50}$ [20]. Both batches were sieved using an 80-μm filter before loading the feedstock bin to ensure there are no exceedingly large

particles or agglomerates in the batch. The same layout (shown in Fig. 2(a) and Fig. 2(b)) was designed and used for fabrication from both powder batches via EOS M290, an L-PBF AM machine, using the process parameters listed in Table 2. In this table, the energy density level associated with the infill parameters was also calculated which was the ratio of laser power to hatching distance, scanning speed, and layer thickness [51].

Table 1 Chemical composition and D_{10}, D_{50}, and D_{90} parameters of the coarse and fine Ti64 powder batches.

Powder	Coarse Ti64	Fine Ti64	Testing Method
Element (Wt.%)			
Al	6.394	6.409	ASTM E2371
V	3.920	3.933	
Fe	0.204	0.202	
Y	< 0.001	< 0.001	
O	0.096	0.118	ASTM E1409
N	0.015	0.014	
H	0.002	0.002	ASTM E1447
Others Each	< 0.080	< 0.080	ASTM E2371
Others Total	< 0.200	< 0.200	
Ti	Balance	Balance	-
Particle Size Distribution (PSD)			
D_{10}	23 µm	20 µm	ASTM B822
D_{50}	45 µm	34 µm	
D_{90}	57 µm	44 µm	
Span	0.76	0.71	

In the build layout, 32 net-shaped fatigue specimens (geometry according to ASTM E466 [52]) to be tested in the as-built surface condition were included (see Fig. 2(c)). In addition, 60 cylindrical rods were fabricated, among which, 24 rods were machined to the geometries of fatigue specimens (20 rods) according to ASTM E466 [52] (see Fig. 2(d)) and tension specimens (4 rods) according to ASTM E8M [53] (see Fig. 2(e)) and were tested in the machined surface condition. Two tensile tests were performed for per powder batch per location. The build layout also contained some half-built cylindrical bars (referred to hereafter as microstructural samples) which were used to characterize the microstructure representative of the build height at the gage of the

test specimens. The specimens were specifically placed in two locations, including the East, i.e., closer to the feedstock bin, and the West, i.e., farther away from the feedstock bin to investigate the effects of location on the mechanical properties as well.

Table 2 EOS M290 Infill and contour process parameters for Ti64 along with the calculated energy densities.

Parameter Set	Laser Power P (W)	Scanning Speed V (mm/s)	Hatching Distance H (mm)	Layer Thickness t (µm)	Energy Density E (J/mm^3)
Infill	280	1200	0.14	30	55.6
Contour	150	1250	--	30	--

After fabrication, parts were detached from the build plate then annealed at 900 °C for 1 hour and furnace-cooled in an argon environment. This heat treatment of L-PBF Ti64 has been reported to decompose its martensitic microstructure and result in lamellar α+β and slightly higher fatigue strength as compared to stress relief at 740 °C for about two hours [54]. Before the test, the machined specimens were polished using sandpapers with reducing grit. Tensile tests were performed in displacement-controlled mode with a nominal strain rate of 0.001 mm/mm/s according to ASTM E8M [53] via MTS Landmark servohydraulic axial test system equipped with a 100-kN load cell. An extensometer was attached to the specimen initially and was removed at 0.05 mm/mm strain to protect the extensometer from any damage. The tensile tests were continued until fracture in displacement-controlled mode. After the fracture, true fracture strain ε_f, 0.2% offset YS, and UTS were measured and calculated. The fracture surfaces of some tensile test specimens were examined using the Zeiss Crossbeam 550 scanning electron microscope (SEM).

In addition, fully-reversed fatigue tests ($R_\sigma = -1$) were conducted in the force-controlled mode for both as-built and machined specimens based on ASTM E466 [52] using an MTS Bionix Tabletop axial test system supplied with a 25-kN load cell. Different stress levels were applied on specimens to acquire properties in high- and mid- cycle fatigue (HCF and MCF) regimes. Test

frequency was chosen at each stress level to ensure a constant average cyclic strain rate for all specimens. Each test was continued until the complete separation of the specimen. After failure, both pieces of the fractured specimen were protected for further fracture surface analysis. All tests that endured 5×10^6 cycles (i.e., 10^7 reversals) were stopped and considered as run-out (no failure) tests. Fracture surfaces of fatigue specimens were later investigated via a Keyence VHX-6000 digital optical microscope. Using microscopy, the crack initiation sites were identified and the defect size was measured with the built-in software.

The R_a surface roughness, i.e., the arithmetical mean height of profiled lines, was evaluated in all East and West as-built specimens fabricated from either coarse or fine powder batches using the Keyence microscope. The measurements were performed in a 3-mm length in the gauge section from five different locations to verify the results. To capture the defect content, 2 machined fatigue specimens per powder type in each location (a total of 8 specimens) were selected and scanned via Zeiss Xradia 620 Versa at 140 kV voltage and 21 W power. The source and detector were positioned in a way to reach a voxel size of 6 μm. Finally, the Zeiss built-in software was used to reconstruct the images. Reconstructed images were then processed with ImageJ to assess the defect distributions. In addition, 3D visualizations were generated via Dragonfly software.

Microstructural samples were cut parallel to the building direction, mounted in the longitudinal plane, and were polished to achieve a mirror-like surface finish. After polishing, electron backscatter diffraction (EBSD) scans were performed via the Zeiss Crossbeam 550 SEM to obtain the microstructure. The Freeman Technology FT4 powder rheometer was also used to characterize the rheological properties of powder batches, which were sampled following ASTM B215 [55] before and after the sieving process from the feedstock bin. Powder characteristics including compressibility, permeability, cohesion, conditioned bulk and tapped densities (ASTM

B527 [56]), and shear stress (ASTM D7891 [57]) were quantified via FT4. Particle morphology and surface chemistry were also evaluated by the SEM and energy-dispersive X-ray spectroscopy (EDS). Lastly, the PSDs were assessed via a Beckman Coulter LS 13 320 laser diffraction particle size analyzer according to ASTM B822 [50].

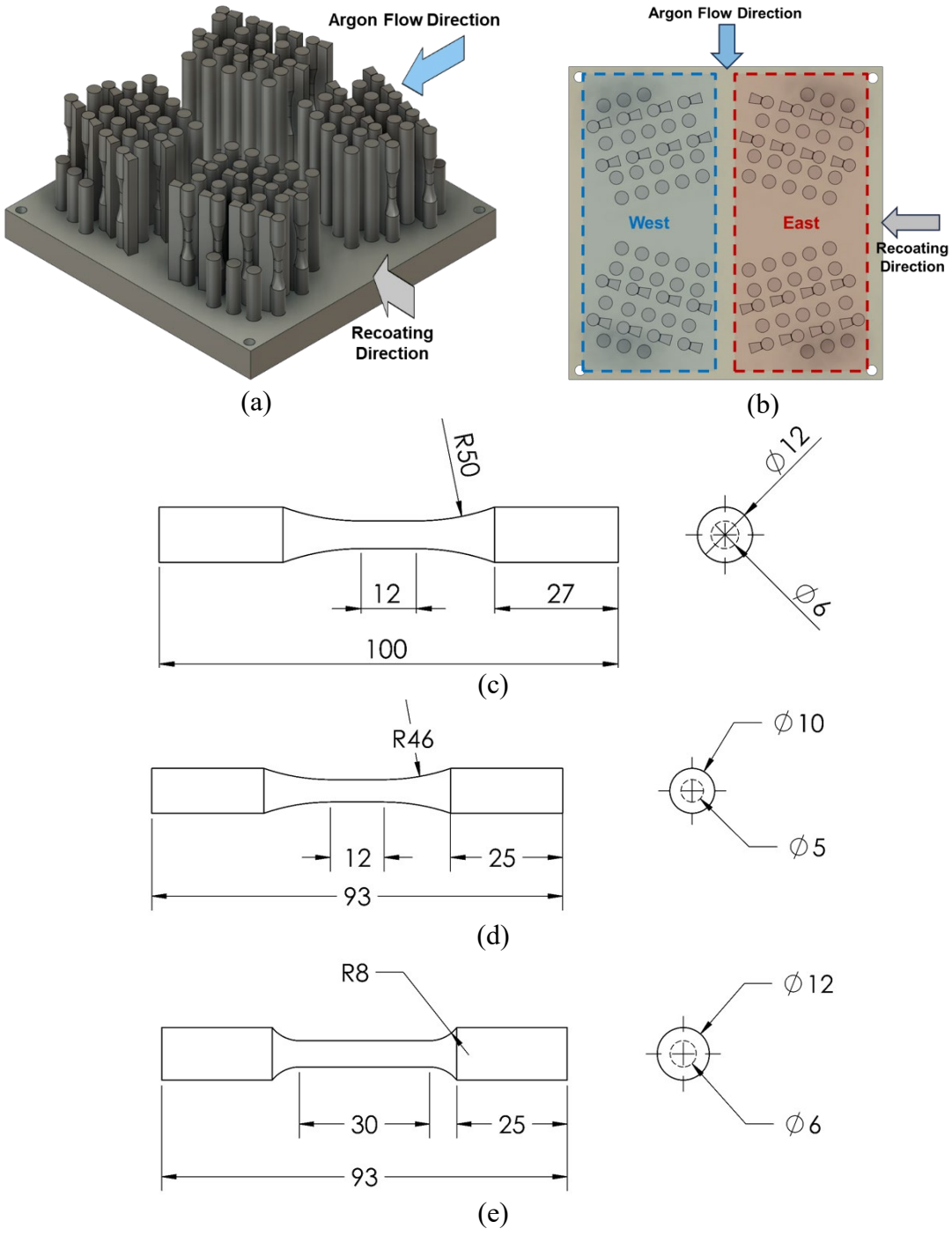

Fig. 2 Fabrication layout in (a) isometric and (b) top views. The layout consisted of (c) as-built fatigue specimens according to ASTM E466 with a gage diameter of 6 mm [52] and cylindrical bars which were machined to (d) fatigue specimens with a gage diameter of 5 mm according to ASTM E466 [52] and (e) round tension test specimens according to ASTM E8M [53].

2.3. Experimental Results

2.3.1. Powder Characteristics

The morphology of both powder batches in the unused (i.e., virgin) condition was assessed via the SEM and shown in Fig. 3(a)-(b). It appears that both coarse and fine batches consist of highly spherical particles that are relatively uniform in size, despite a few irregularly-shaped ones that may form due to the atomization process or powder handling. These features are consistent with the output of plasma atomization, which typically produces very spherical particles, narrow PSDs, and fewer internal defects (i.e., gas-entrapped pores in powder particles) [9,10,12]. In the magnified views in Fig. 3(a)-(b), some fine particles as well as satellites, are present in both batches. It needs to be emphasized that 2D morphological analysis may not completely represent the 3D features of powder particles. Ideally, 3D morphological analysis using X-ray CT is recommended [58–61] to obtain particle geometries accurately.

As seen in Fig. 3(c), the surface chemistry in terms of the major alloying elements (i.e., Ti, Al, and V), obtained from EDS and performed on the shaded particles in Fig. 3(a)-(b) revealed no significant difference between the fine and coarse powder particles. Moreover, there was a higher oxygen content in the unused fine powder than in the coarse one. Although the weight percentages of elements provided by EDS may not be exact, the qualitative comparison it offers is still valid. The PSD curves of both powder batches are also shown in Fig. 3(d). As seen in this figure, the coarse powder had a bimodal size distribution and contained more large particles (> 45 μm). In addition, more finer particles (< 20 μm) were present in the fine powder batch (12% in the fine vs. 8% in the coarse).

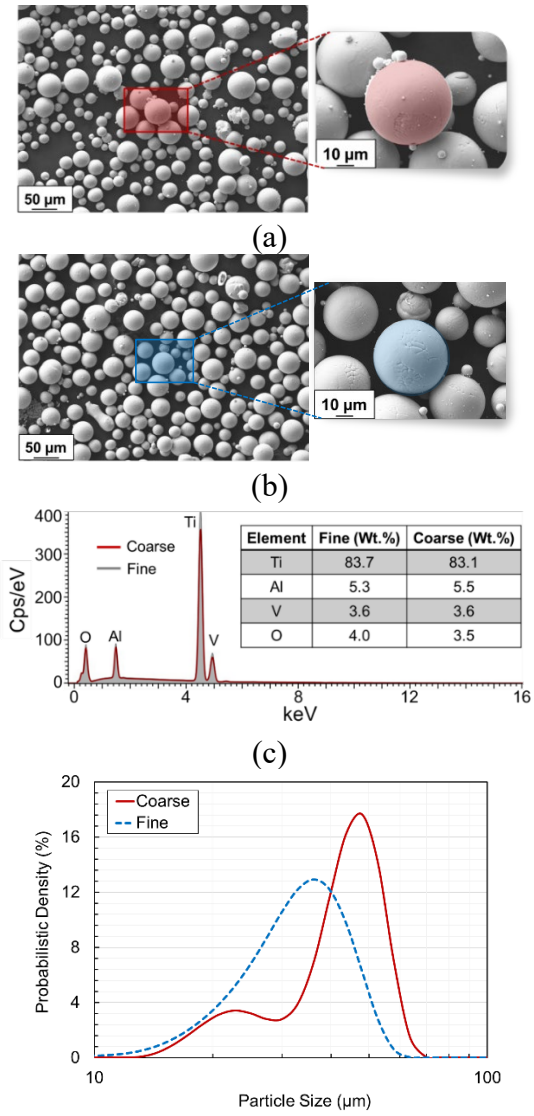

Fig. 3 Powder particles' morphology of the (a) coarse and (b) fine plasma atomized Ti64 powder batches as well as (c) the surface chemistry from shaded particles in the magnified images measured via EDS. The powder PSD curves for both batches are also shown in (d).

To achieve a better understanding of how the PSD and morphology can affect the powder flow behavior, the rheological properties of both powder batches were measured. A summary of all rheological properties obtained from FT4 along with their definitions is reported in Table 3. In this table, powder characteristics are given after the sieving process, as the powder that was used for the fabrication. A higher basic flowability energy value is typically associated with lower flowability. As reported in Table 3, both powder batches have comparable basic flowability energy

values after sieving, with that of the coarse powder being slightly higher. This trend correlates with the PSD spans of 0.71 and 0.76 for the fine and coarse powder batches, respectively (see Table 1). Generally, a powder with a lower span (i.e., narrower PSD) has higher flowability [33].

The specific energy, measured with basic flowability energy in the same test sequence, is also related to flowability. Since it is measured while the blade is moving upwards, specific energy represents the flowability in a low-stress environment. Specific energy values smaller than five can indicate powder with low cohesion. The very close basic flowability energy and specific energy measures of both batches indicate comparable flowabilities and cohesivity between them, which is also reflected in their identical cohesion values of 0.1 kPa.

Table 3 A summary of powder rheological and bulk characteristics obtained in this study along with the definition of powder rheological characteristics adapted from [62].

Powder Characteristic	**Fine Powder**	**Coarse Powder**
Basic Flowability Energy (mJ)	280 ± 3.6	282.0 ± 2.5
Specific Energy (mJ/g)	1.6 ± 0.2	1.8 ± 0.1
Conditioned Bulk Density (g/mL)	2.6 ± 0.2	2.8 ± 0.0
Tapped Density (g/mL)	2.8 ± 0.0	2.9 ± 0.0
Compressibility (%)	2.6 ± 0.5	3.3 ± 0.1
Cohesion (kPa)	0.10 ± 0.00	0.10 ± 0.02
Pressure Drop (mBar)	9.5 ± 0.6	7.1 ± 0.2
Aeration Energy (mJ)	5.3 ± 0.9	5.0 ± 0.3
Definition of Powder Rheological Properties		
Basic Flowability Energy: Amount of work done while moving the blade within the powder bulk in a downward motion		
Specific Energy: Amount of energy to move the blade within the powder bulk in an upward motion in an unconfined (i.e., low stress) environment as there is no constraint on top of the powder bulk		
Conditioned Bulk Density: The bulk density of the powder in a low-stress condition		
Tapped Density: The bulk density of the powder when it is consolidated		
Compressibility: Shows the change in volume as a function of applied normal stress		
Cohesion: Amount of shear stress needed to flow the powder while the applied normal stress is zero		
Pressure Drop: Indicates how easily the gas can permeate the powder while is under applied compression (3 kPa) and the gas flows from below the powder bulk		
Aeration Energy: Indicates how easily the powder fluidizes when it is subjected to gas flow		

While the fine and coarse powder batches had different PSDs, similar conditioned bulk and tapped densities were recorded, with slightly higher density values for the coarse powder batch. This was likely because powders with a wider PSD span can occupy space more efficiently and typically have higher theoretical packing densities, even though the actual powder bed density is typically lower than its theoretical packing density [63]. However, the compressibility, which measures how powder reacts to compaction under the recoater arm, of the coarse powder (3.3%) was slightly higher than the fine powder (2.6%), although both values were low. When agitated, powder particles tend to segregate into different size groups [64] (see schematic illustration provided in Fig. 4). For the coarse powder, the segregation depicted in Fig. 4 also tends to be more severe than the fine powder due to its wider PSD span, and it is more likely to contain regions of mixed particle sizes and agglomerates. As finer particles in a wide PSD powder batch typically tend to adhere to other particles due to their high surface/volume ratio and interparticle friction [10], they form agglomerates which have lower flowability and tend to create empty spaces around them. The empty spaces around these agglomerates most likely are the reason for the slightly higher compressibility of the coarse powder [10,33]. The more pronounced empty spaces within the coarse powder can form pathways of higher gas permeability which should lead to a lower pressure drop, which was indeed the case. As shown in Table 3, the coarse powder had a pressure drop of 7.1 mBar, while the fine powder had a pressure drop of 9.5 mBar.

Aeration energy is a measure of how easily the powder fluidizes when subjected to gas flow and is also relevant to the AM process. Lower aeration energy is generally desired for the PBF process to help achieve a more uniform powder bed with a higher powder bed density (PBD) and lower mechanical interlocking between powder particles [20]. Table 3 shows quite comparable aeration energies for both powder batches.

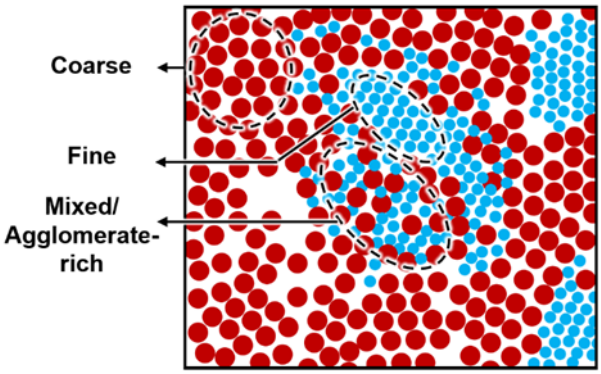

Fig. 4 Schematic illustration of the coarse powder bed particle arrangement.

2.3.2. Microstructure Characterization, Defect Distribution, and Surface Roughness

Upon investigation of the microstructural samples in the longitudinal plane (longitudinal direction aligned with build direction) of fabricated specimens from the coarse powder, a Widmanstätten microstructure was seen in the non-heat-treated (NHT) condition as shown by the inverse pole figure (IPF) maps in Fig. 5. Even though the characteristic cooling rate around the solidification temperature of L-PBF processes around 10^5 K/s can result in pure α' (and or α") martensites, the repeated reheating during the layer-by-layer fabrication likely have partially decomposed the martensitic phase [32]. Indeed, the EBSD scans revealed a β phase fraction of 1%, consistent with the values reported from other studies in the NHT condition [65]. No difference in phase fraction was detected between the specimens fabricated from the coarse and fine powder batches in the NHT condition. The remaining phases, occupying 99% of volume, are a mixture of α and α'(α"). Indeed, in the annealed condition, further decomposition of the martensitic phase resulted in a β phase fraction of ~29%.

Microstructures of the coarse (Fig. 5(a)) and fine (Fig. 5(b)) powder specimens in the NHT condition were obtained from the microstructural coupons placed in the East location. It is evident from the IPF maps that prior-β columnar grains are mainly elongated towards the building direction which is the primary path of heat dissipation [66]. Finally, the lath thickness was measured for the NHT and annealed coarse as well as the NHT fine conditions from the IPF maps.

As seen in Fig. 5(d), the lath thickness was slightly coarser for the fine powder batch in NHT condition. The large error bars are consistent with the significant variation in the lath thickness in each condition. Additionally, the mean lath martensite thickness was seen to slightly increase from the NHT to the annealed coarse condition.

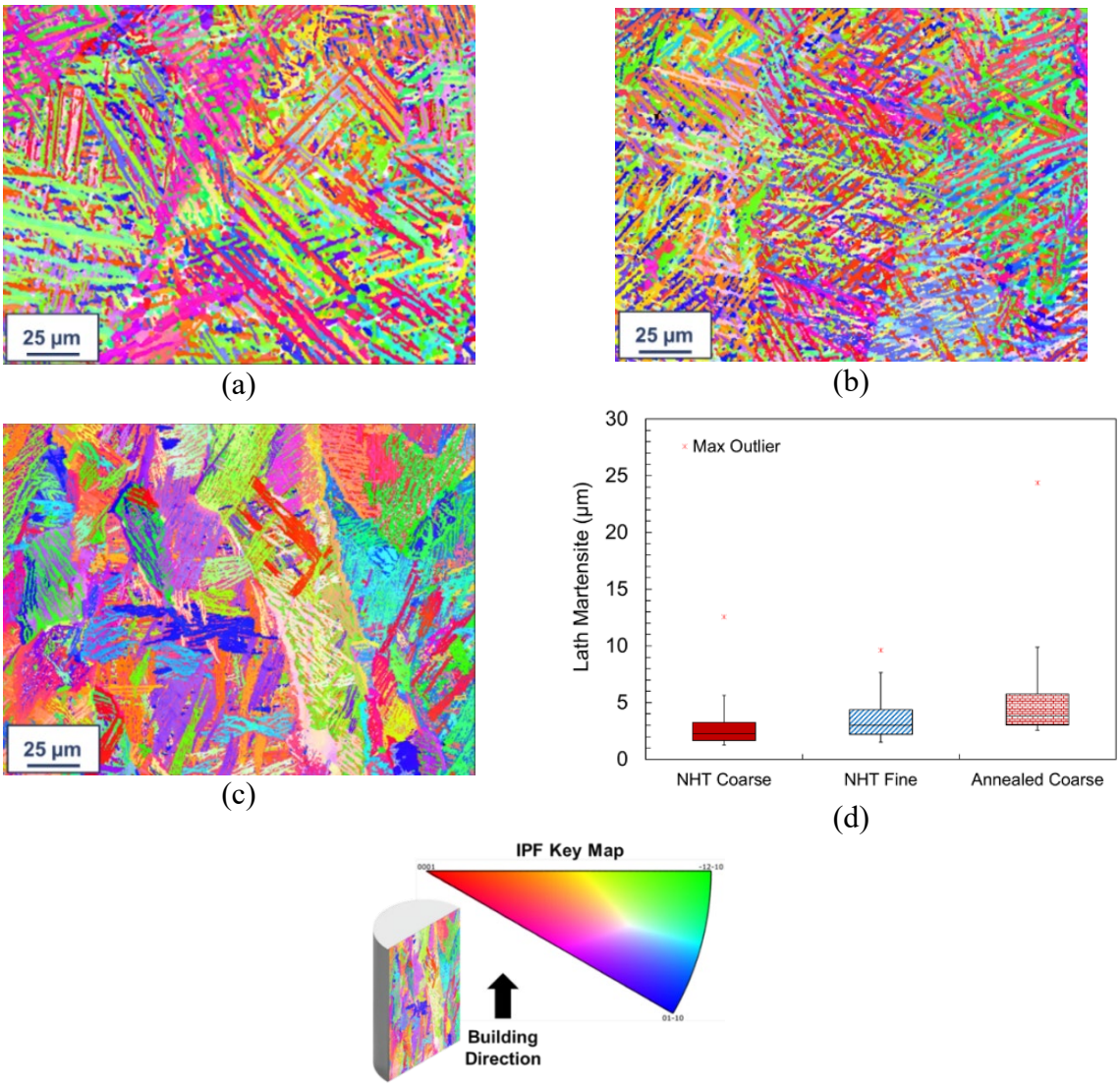

Fig. 5 Microstructure of L-PBF Ti64 for the (a) NHT coarse, (b) NHT fine, and (c) annealed coarse powder specimens along with (d) lath thickness for all the conditions.

To investigate defect distribution inside the specimens before testing, two specimens were selected from each location (i.e., East and West) of each powder batch for X-ray CT. The 3D visualizations performed are presented in Fig. 6(a). Additionally, a bar chart showing the size

distribution of defects normalized for a 10-mm^3 sample size inside the representative gage sections is presented in Fig. 6(b). Fig. 6(b) shows that the coarse powder specimens fabricated in the West location tend to yield fewer defects in all defect size ranges than the ones fabricated in the East location. In the case of the fine powder, it appears from Fig. 6(b) that the number of defects was less in these specimens as compared to their counterparts from the coarse powder regardless of the location. The larger population of defects in the coarse powder specimens can be attributed to the "empty spaces" formed from the non-uniformly distributed powder and the potentially higher cooling rates when this powder batch was used for the fabrication. Coarser powder tends to have higher cooling rates due to the lower surface-to-volume ratio of the larger powder particles which reduces the energy absorption efficiency [36,40]. The total number of defects in the 10-mm^3 volume of the gage section was 18 and 12 for the coarse powder specimens in East and West, and 4 and 2 for the fine powder in East and West locations.

Some very large defects, however, were still evident in these fine powder-fabricated specimens (the maximum defect sizes in μm observed in each specimen are marked on the ">40 μm" bar in Fig. 6(b)). The maximum volumetric defect sizes were 171 and 130 μm in the fine and 113 and 83 μm in the coarse powder specimens, depending on location. Note that the size of a volumetric defect was calculated as the diameter of the sphere with equal volume. It is also important to note that all specimens, regardless of the powder type or location, had overall densities greater than 99.99% based on the X-ray CT scans.

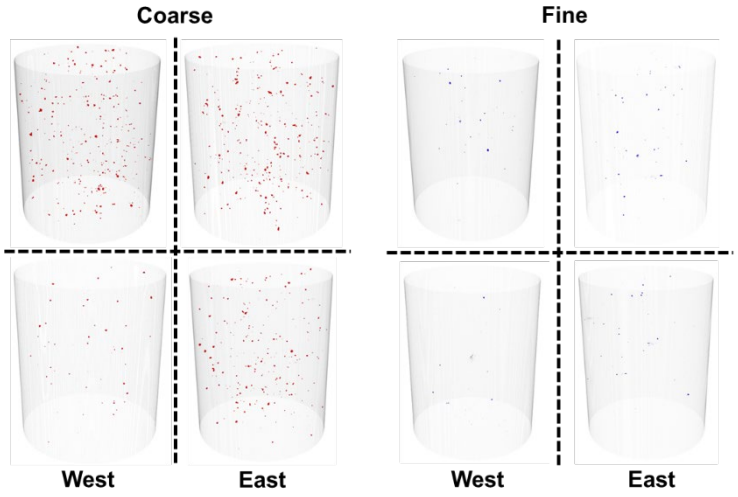

(a)

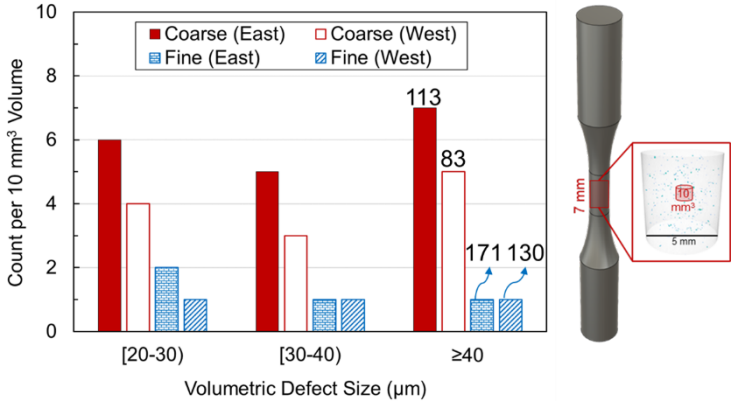

(b)

Fig. 6 3D visualizations of defect population in the coarse (depicted by red) and fine (illustrated by blue) powder specimens placed in different locations of the build plate, and (b) histograms demonstrating the volumetric defect in 10 mm3 sample size from the representative specimen gage sections. The maximum defect size (in µm) for each condition is labeled on the corresponding bar.

The surface roughness of all as-built specimens fabricated from coarse and fine powder batches in the gage sections was measured using R_a — the arithmetical mean height of line profiles. As shown in Fig. 7(a), even though the mean values of R_a showed slight variations as a function of build location as well as PSD, significant overlaps in the error bands are also evident. The specimens fabricated from the coarse powder had slightly higher surface roughness as compared to those from the fine powder which has been attributed to the higher energy density level required by coarser particles to achieve a full melting in some studies [9,40]. In addition, the surface profiles

of a coarse powder specimen and a fine powder specimen in the East location are shown in Fig. 7(b). A large amount of partially melted powder particles were seen to adhere to the surfaces of both specimens. However, they were more frequent and larger in the case of the coarse powder specimen, which further explained the higher measured surface roughness.

Within the build with fine powder, it was found that the West specimens had almost comparable surface roughness compared to the East ones. However, this location dependency of surface roughness was more for the specimens fabricated from the coarse powder. Such PSD-specific location dependency may be attributed to the possible segregation of finer and coarser particles given rise to the "front stress-free turning powder wedge" behavior proposed in some studies [41,43]. For instance, Jacob et al. [41] reported that during powder spreading, finer particles tend to move to the bottom of the powder bulk, and consequently, are deposited closer to the dispenser while coarser ones might deposit near the overflow bin (i.e., collector). Another possible reason may be that some of the West specimens (i.e., Southwest) were closer to the spatter-rich region in the L-PBF machine which has been shown to result in higher surface roughness values [67].

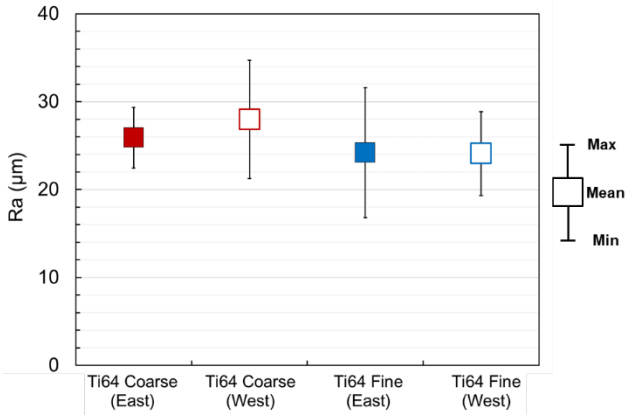

(a)

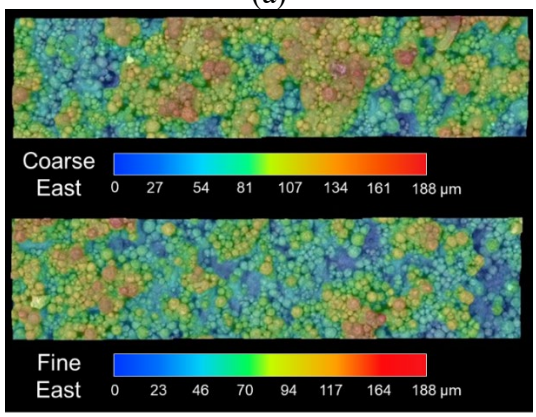

(b)

Fig. 7 (a) Ra values for the specimens manufactured from the coarse and fine powder batches in East and West locations, and (b) surface profile micrographs for a coarse and a fine powder specimen located in the East.

2.3.3. Tensile Behavior

Quasi-static tensile tests were performed on both sets of specimens fabricated from coarse and fine powder batches. As explained in the experimental setup, all tensile tests were paused at 5% strain to remove the extensometer to prevent damage, as such ε_f was measured after the tensile test. In Fig. 8(a), the tensile properties, including UTS, YS, and ε_f, measured from this study as well as the minimum requirements for L-PBF Ti64 specimens fabricated vertically (i.e., along the Z-axis) based on ASTM F2924 [68] are provided. Concerning the location, it seems that tensile properties including UTS, YS, and ε_f are independent of location on the build plate.

Regarding the effects of particle size on the tensile properties, it can be seen from Fig. 8(a) that there were negligible changes in UTS and YS between the specimens manufactured from fine and coarse powder batches. This behavior can be correlated well with the similar microstructure that was seen in the specimens fabricated from both batches. However, the ε_f in fine powder specimens was lower than the coarse powder specimens which might be due to the larger maximum defect sizes in fine powder specimens (see Fig. 6(b)) and the higher oxygen content in the fine powder (see Fig. 3). While a higher strength might be expected due to higher content of oxygen in fine powder, almost comparable strength was noted which can be attributed to the strengthening effect of slightly thinner lath martensite in the coarse powder [69,70]. The engineering stress-displacement behavior is also shown in Fig. 8(b) and (c) for the specimens tested from the East and West locations.

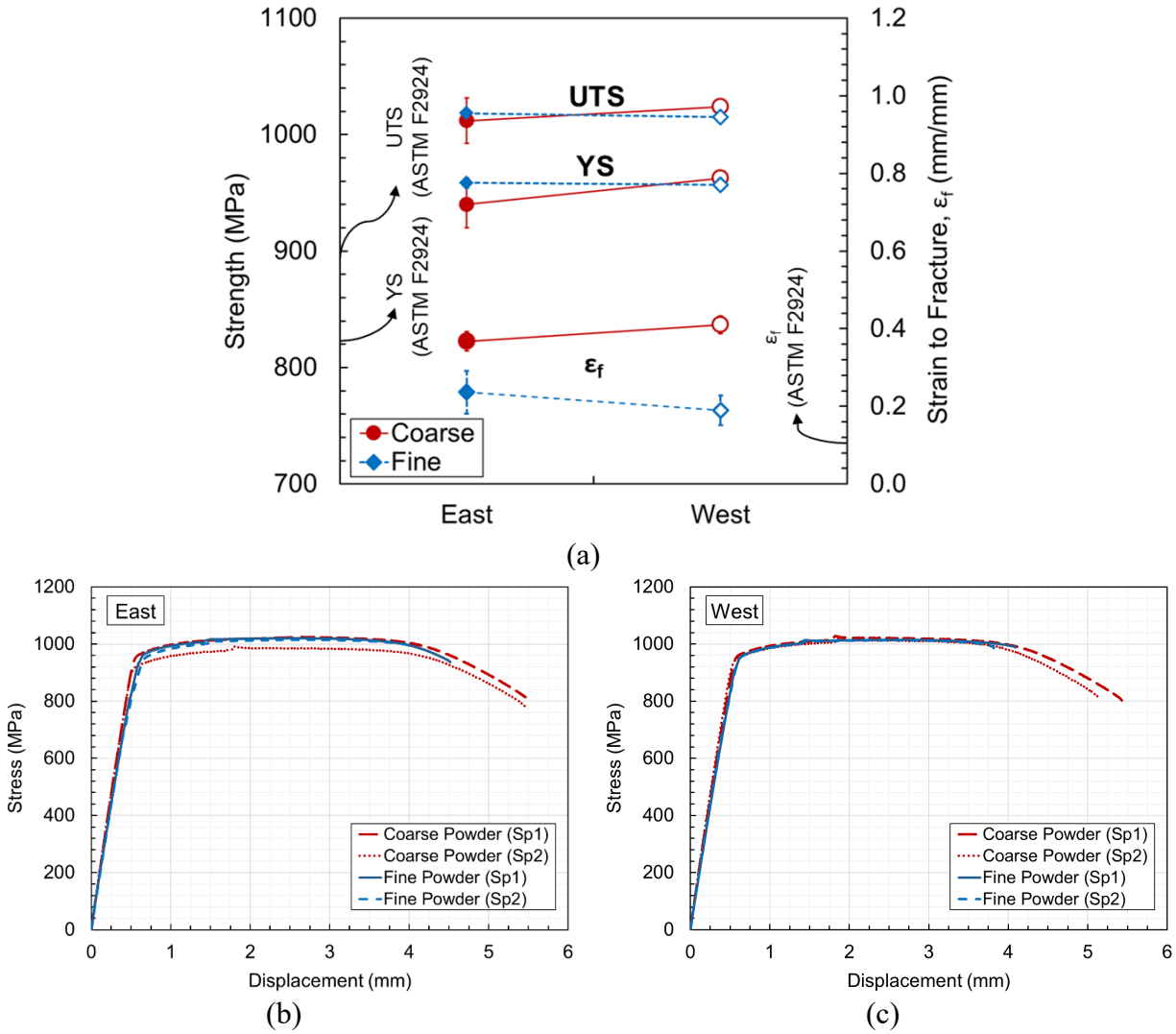

Fig. 8 (a) Quasi-static tensile properties of L-PBF Ti64 specimens fabricated from coarse and fine powder batches and different locations along with the minimum requirements according to ASTM F2924. All specimens have been annealed prior to testing. Since only two tensile tests were performed per condition, the two ends of an "error" bar represent the two measurements of a property for a given location and powder batch, while the markers represent the mean values and (b) and (c) engineering stress-displacement curves for both fine and coarse powder batches in the East and West, respectively.

2.3.4. Fatigue Behavior & Failure Analysis

The axial fatigue behaviors of both as-built and machined specimens from different locations on the build plate and fabricated from coarse and fine powder batches are presented in Fig. 9. It is evident from Fig. 9(a) that the difference between the fatigue lives of as-built specimens fabricated from both batches is relatively small in the MCF ($\leq 10^5$ reversals to failure) and HCF ($>10^5$

reversals to failure) regimes. In addition, regardless of the powder type, it seems that the West as-built specimens have slightly lower fatigue resistance compared with the East as-built ones in the HCF regime.

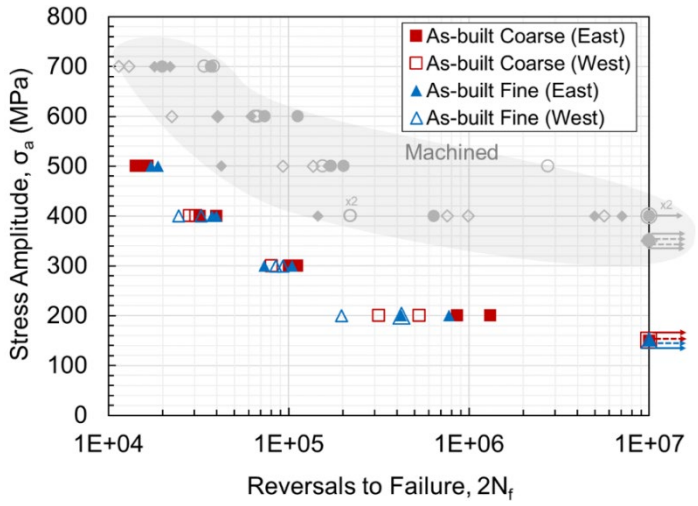

(a)

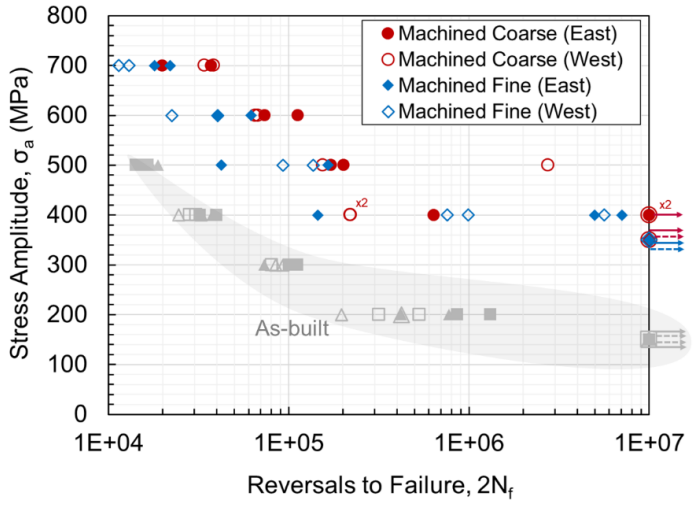

(b)

Fig. 9 Fatigue performance of L-PBF Ti64 specimens fabricated from coarse and fine powder batches from the East and West locations in their (a) as-built and (b) machined surface conditions. All specimens have been annealed before testing. The grayed-out markers in each subfigure represent the opposing surface condition for each comparison (i.e., machined in (a) and as-built in (b)).

In the machined condition (see Fig. 9(b)), it was seen that the coarse powder specimens have higher fatigue resistance as compared to fine powder specimens in the MCF regime. This behavior

was following the observations reported in [18], which can be attributed to the higher ductility of the coarse powder specimens. In low-cycle fatigue (LCF) and MCF regimes (i.e., higher stress levels), crack growth accounts for a more significant portion of the overall fatigue life [71]. Therefore, the higher ductility of the coarse powder specimens may imply higher fracture toughness and larger crack size at fracture which typically increases the crack growth life. At the lower stress level (i.e., 400 MPa), the coarse powder specimens still appear to outperform the fine powder ones (note the three runouts in coarse condition vs. no runouts in fine condition) despite the more significant data overlap. This is consistent with the observation that the largest defects in the fine powder specimens being larger than those in the coarse powder ones, although in general more volumetric defects were detected in coarse specimens. In addition, increasing scatter in data was noticed with decreasing stress levels, which can be ascribed to the more prominent effect of defects in these conditions [7,33,72]. As to location dependency in the machined specimens, no apparent trend was seen between the fatigue lives of East and West specimens manufactured from either powder batches. A summary of all force-controlled fatigue tests is reported in Table 4.

Table 4 A summary of fully-reversed (R_σ = -1) force-controlled fatigue tests for L-PBF annealed Ti64 specimens in both as-built and machined surface conditions.

Specimen ID	σ_a (MPa)	$2N_f$ - Fine (Reversals)	$2N_f$ - Coarse (Reversals)	Location	Surface Condition
019	400	24,538	30,634	West	As-built
008	400	32,712	28,332		
009	300	92,984	80,398		
106	300	84,678	N/A		
010	200	196,858	316,330		
017	200	422,610	532,308		
018	150	10,000,000	10,000,000		
087	500	17,284	14,250	East	
034	500	18,822	16,524		
042	400	39,650	39,856		
077	400	37,628	32,170		
043	300	73,322	111,686		
078	300	104,584	100,376		

033	200	420,944	1,318,620		
086	200	773,836	862,818		
079	150	10,000,000	10,000,000		
044	150	10,000,000	10,000,000		
104	700	11,388	38,324	West	Machined
011	700	12,996	34,098		
014	600	40,338	67,876		
112	600	22,510	65,350		
110	500	93,098	2,744,548		
012	500	136,838	155,384		
013	400	757,194	219,854		
111	400	990,378	220,690		
098	400	5,630,226	10,000,000		
015	350	10,000,000	10,000,000		
037	700	21,996	37,250	East	
085	700	17,992	19,958		
038	600	40,142	112,776		
082	600	61,686	73,630		
040	500	165,706	201,716		
084	500	42,282	172,172		
039	400	4,992,374	10,000,000		
083	400	145,146	639,024		
076	400	7,049,054	10,000,000		
044	350	10,000,000	10,000,000		

While fracture surfaces of all specimens were characterized from the digital optical microscope, only a few notable fractography images were presented in this article (see Fig. 10 and Fig. 11). Fig. 10(a), (b), and (c) present fracture surfaces of as-built specimens tested at σ_a= 300 MPa and a frequency of 4 Hz for the coarse powder in East and West as well as the fine powder in East, respectively. As seen in these figures, cracks initiated in multiple locations in each specimen from the rough surfaces of both coarse and fine powder specimens in East and West locations, resulting in similar fatigue lives within the range of 80,398 and 104,584 reversals to failure. It is well established that rough surfaces of AM parts, which are mainly derived from partially-melted powder particles and the stair effect due to the layer-by-layer fabrication, can

behave like micro notches [73]. These micro notches on the surface can drastically deteriorate the fatigue resistance of AM parts when they are subjected to cyclic loading conditions.

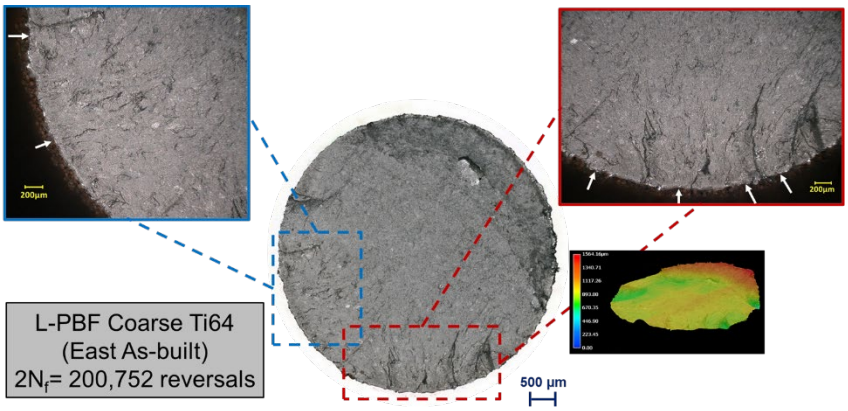

(a)

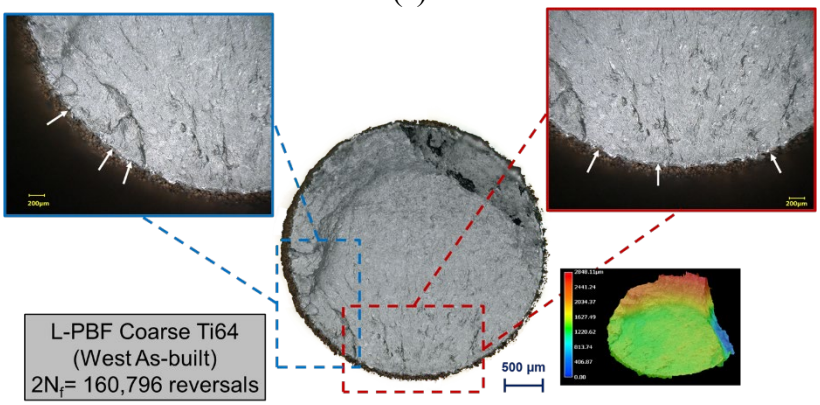

(b)

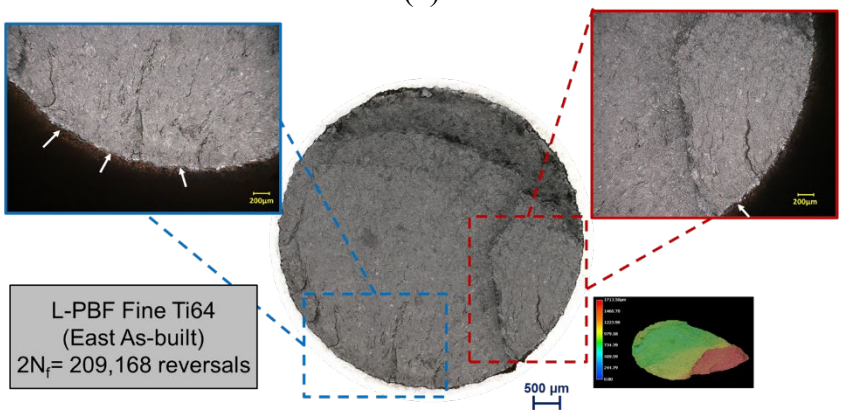

(c)

Fig. 10 Fracture surfaces of L-PBF annealed Ti64 specimens in their as-built surface conditions for the coarse powder specimens in (a) East and (b) West, as well as (c) fine powder specimen in the East. All specimens were tested at σa= 300 MPa. Crack nucleation sites are indicated with white arrows.

In the machined condition, however, as the surface micro notches are removed, cracks mainly start from the internal or near-surface volumetric defects (i.e., gas-entrapped pores and lack-of-fusion defects). Fig. 11(a)-(d) shows the fracture surfaces of the coarse and fine powder specimens from the East and West locations and tested at σ_a= 500 MPa. It is evident that cracks initiated from near-surface gas-entrapped pores in the two coarse powder specimens in East and West with fatigue lives of 201,716 and 155,384 reversals to failure, respectively. The equivalent defect size (i.e., $\sqrt{area}$ μm) was also calculated based on Murakami's principles [74], and it is labeled on each image. Unlike the coarse powder specimens, in the fine powder ones, cracks mainly initiated from internal defects (see Fig. 11(c)-(d)). Although these defects were farther away from the surface of the specimens, the defect sizes were appreciably larger than the coarse powder specimens, resulting in fatigue lives of 165,706 and 136,838 reversals to failure in the East and West specimens, respectively.

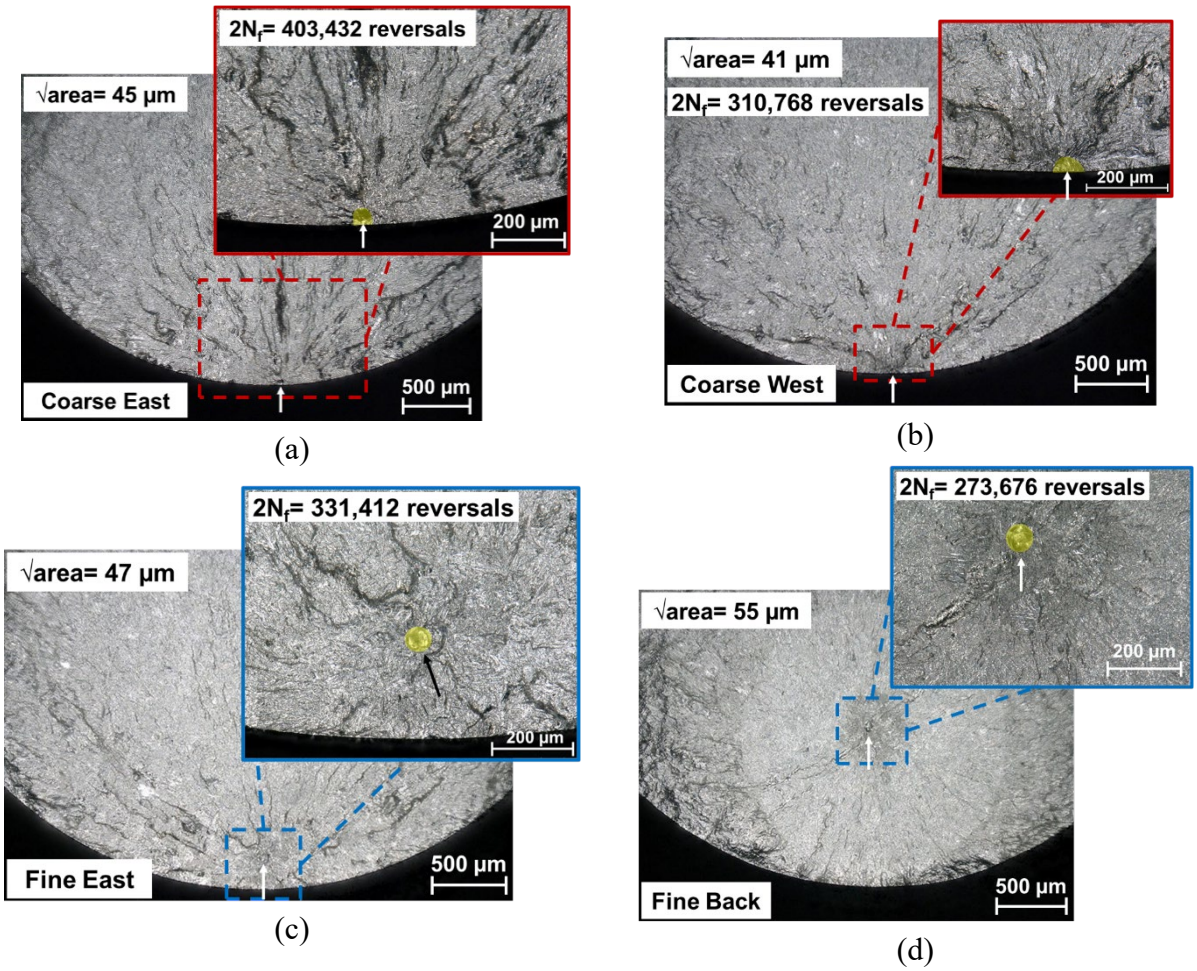

Fig. 11 Fractures surfaces of L-PBF annealed Ti64 specimens in the machined surface condition for the coarse powder specimens in (a) East and (b) West, as well as the fine powder specimens in (c) East and (d) West. All specimens were tested at σa= 500 MPa. In these images, the crack initiation sites are also portrayed with yellow shade in the magnified views. Arrows are also placed toward the crack initiating defects in all images.

2.4. Discussion on Experimental Results

2.4.1. Effect of powder characteristics on the surface and volumetric defects

On average, the coarse powder specimens had slightly higher R_a values as compared to the fine powder specimens (see Fig. 7(a)). The higher R_a values of the coarse powder specimens can be explained by the existence of larger particles in the coarse batch, which typically have a lower absorptivity. Therefore, particles on the surface may not completely melt resulting in a higher surface roughness [40] (see Fig. 7(b)). Concerning the effects of part location, it was noted that the coarse powder specimens located in the West had generally higher R_a values as compared to

the East ones. However, this difference was less obvious for the fine powder specimens due to its slightly lower mechanical interlocking (i.e., lower specific energy and basic flowability energy) and consequently better flowability, and more uniform powder bed [20]. In addition, the narrower PSD span of the fine powder could also reduce the severity of particle size segregation during spreading.

As evident in Fig. 6(a) & (b), the coarse powder specimens contained a higher number of defects though the maximum defect size for fine powder specimens was larger. The higher defect population in the coarse powder specimens could have been derived from multiple factors. First, the coarse powder had an inferior packing state as compared with the fine powder batch due to its more severe powder size segregation. Therefore, when the regions of low packing densities in the coarse powder batch are melted, porosity is more probable to form. This is exacerbated by the fact that coarser particles require more input energy to completely melt [40] due to their lower absorptivity [75] associated with their lower surface-to-volume ratio. Effectively, when the regions of coarser particles in the powder bed are melted, the cooling rate is higher, leading to the formation of more defects [4].

Interestingly, the maximum defect sizes detected by the X-ray CT were 130~171 μm in the fine and 83~113 μm in the coarse powder specimens. Observing larger-sized defects in the fine powder specimens which possessed a superior packing state was rather surprising. The presence of substantially large defects in the fine powder specimens appears to be the result of spattering. Indeed, the crack initiation sites in the fatigue specimens and fracture nucleation sites of the tensile specimens fabricated from the fine powder were rich in Si, which could have been induced by spatters resulting in the formation of large pores (see Fig. 12). The Si is often added to Ti-6Al-4V to enhance its resistance to oxidation and creep, as well as to increase its tensile strength [76,77].

The Si-rich regions in Ti64 tend to form a mixture of $TiSi_x$, TiO_2, and SiO_2 phases [78]. Among the compounds, the melting point of $TiSi_x$ is substantially lower than Ti (liquidus temperature of 1330 °C for Ti-Si alloy compared to 1670 °C for Ti); besides, the SiO_2 phase has a decomposition temperature of only 1861 °C in oxygen lean environments (similar to the build chamber which is purged in argon) [79] (note that the boiling point for Ti is over 3200 °C). When interacting with laser, the Si-rich powder particles would likely melt early, and the contained SiO_2 phase rapidly decompose into Si and gaseous O_2. The explosive formation of the gaseous O_2 within the melted Si-rich powder particles was likely the cause of the Si-rich spatters observed within the specimens. Both batches had approximately the same level of Si, yet the fine batch had higher oxygen pickup due to the higher surface-to-volume ratio. The higher oxygen content in the fine powder most likely had formed more SiO_2, which results in more spatter in the fine powder specimens. Indeed, other possible factors may also exist resulting in the observation of larger defects in the case of fine powder which necessitates further investigations.

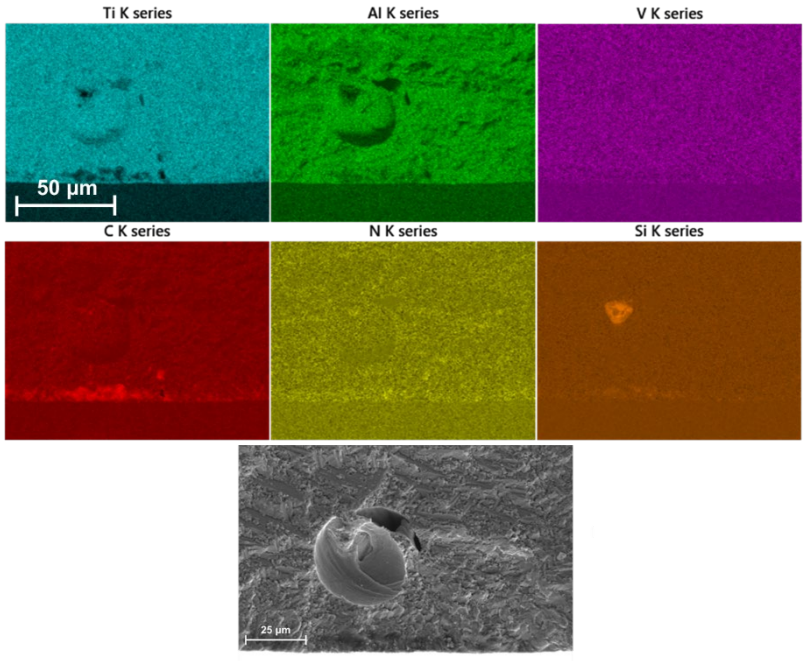

Fig. 12 EDS maps on the fracture surface of an L-PBF annealed Ti64 specimen manufactured from the fine powder.

Concerning the effects of location, it was observed that the number of defects in the specimens manufactured from the coarse powder and placed in the West was, to some extent, lower as compared to their counterparts located in the East. Such location dependency of defect population may be attributed to the possible segregation of finer and coarser particles by spreading, i.e., the "front stress-free turning powder wedge" behavior proposed in some studies [41,43] and somewhat lower flowability of the coarse powder. Finer particles tend to be deposited closer to the dispenser, while coarser ones can be spread further due to their wider PSD, resulting in the formation of more loosely packed regions in the East. In contrast, the fine powder specimens located in the East and West had almost similar number of defects, which could be ascribed to its more uniform PSD (i.e., lower span) and consequently, the higher powder flowability.

2.4.2. Effect of powder characteristics on tensile behavior

As seen in Fig. 8, the coarse and fine powder specimens had comparable UTS and YS. Tensile YS is primarily governed by the microstructure of the parts and is not expected to be different between the specimens fabricated from the two powder batches as there were no significant changes in the microstructure (see IPF maps shown in Fig. 5). In addition, since Ti64 is well known for its low strain hardenability, the UTS is typically not much higher than the YS and is not sensitive to ductility. In terms of ductility, it was observed that the coarse powder specimens possess superior ε_f which is consistent with the observations reported in [18,40]. The lower ductility of fine powder specimens can be attributed to the presence of larger volumetric defects due to spattering and their higher oxygen content which likely have increased the material's sensitivity to defects.

Fracture surfaces of the tensile specimens, presented in Fig. 13, revealed different fracture mechanisms for the coarse and fine powder specimens, with the former being ductile and the latter being brittle. The fracture of the coarse powder specimens occurred after the onset of necking and

its surface resembles the classic cup and cone feature, which had a fibrous central region surrounded by an annular shear lip (see Fig. 13(a)). The fibrous region is the result of the nucleation, growth, and subsequent coalescence of the voids during the tensile loading driven by the hydrostatic tension in the neck. Some of the voids were nucleated in a homogenous fashion and appeared as dimples on the fracture surface. Others grew from volumetric defects which are indicated by black arrows in Fig. 13(a).

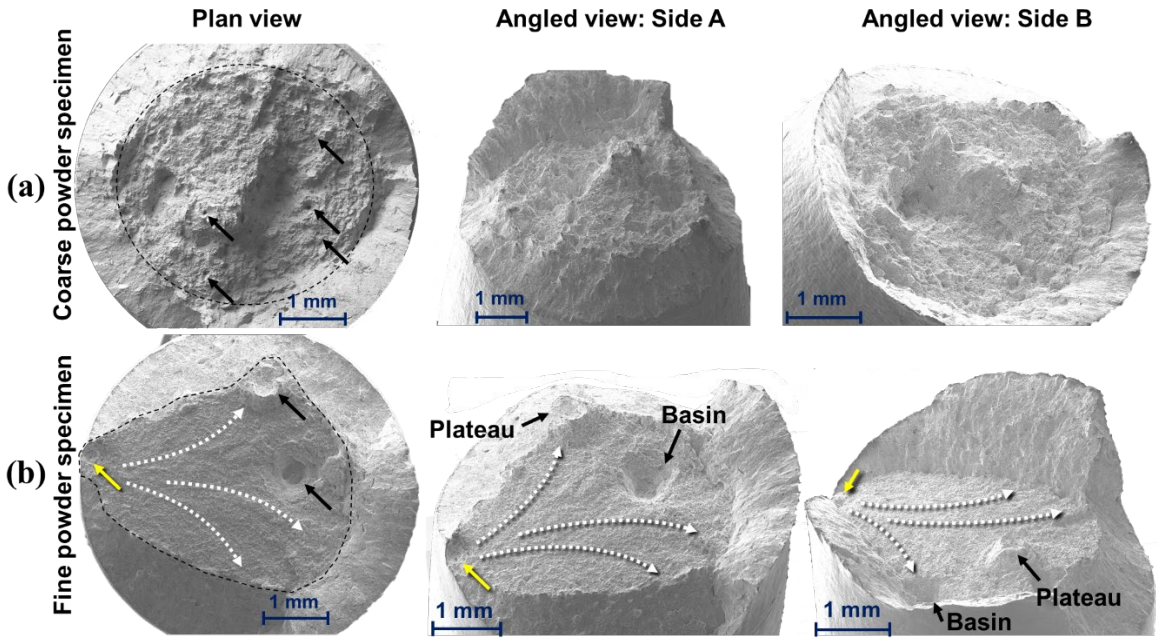

Fig. 13 Fracture surfaces of L-PBF annealed Ti64 tensile specimens in the (a) coarse and (b) fine powder specimens. Black arrows indicate the location of pores, while the yellow arrow in (b) points to the defect responsible for the onset of fracture for the fine powder specimen. The white dashed arrows in (b) mark the direction of fracture.

In contrast to the coarse powder specimens, the fracture of the fine powder specimens occurred without clear evidence of necking and under a different mechanism. As shown in Fig. 13(b), the fracture surface lacked a central symmetry and featured a central flat region that was open to the specimen's external surface from one side. Relatively large defects, such as the one indicated by the yellow arrow in Fig. 13(b), were always observed at the opening. The flat region was partially surrounded by the shear lips. Closer inspection also revealed that the river marks [80] on the flat

regions converged toward its opening to the specimen surface, suggesting the opening to be the initiation site for fracture. The initiation of fracture was likely due to the close interaction between the defect (indicated by the yellow arrow in Fig. 13(b)) and the specimen surface. The flat region is the plane strain portion of the unstable propagation of the tensile crack, while the shear lip is the plane stress portion. Occasionally, a large defect could be found in the interior of the fracture surface residing either on a "plateau" or in a "basin" (see Fig. 13(b)). In such cases, although secondary cracks initiated from these internal defects, their propagation was suppressed by the main crack. These defects did not reside on the same plane with the main crack, therefore the secondary cracks formed plateaus/basins when they joined with the main crack.

The difference in the fracture mechanisms in the two specimen batches is likely due to the different defect and oxygen contents. In coarse powder specimens, the maximum size of the defects was significantly smaller and the oxygen fraction was lower than those in the fine powder specimens. Therefore, even though the number of defects per volume was higher than that of the fine powder specimens, the surface cracks formed due to the near-surface defects in coarse specimens, if any, did not have sufficient stress intensity factors under loading to induce fracture. This permitted necking and resulted in the typical ductile fracture. Conversely, the much larger although fewer defects in the fine powder specimens (where the oxygen content was higher) formed cracks that were large enough to induce surface-originated, brittle mode fracture. Despite the low number of defects per volume, the probability of finding a large defect near the specimen surface was still relatively high.

2.4.3. Effect of powder characteristics on fatigue behavior

When the fatigue performance of specimens in their as-built surface condition was investigated, negligible changes between the coarse and fine powder specimens were noted (see Fig. 9(a)). This observation was following the R_a results which showed almost identical values for

both batches (see Fig. 7(a)). In the case of location, some improvement in fatigue resistance of as-built coarse specimens located in the East was seen as compared with the ones in the West in the HCF regime ($\geq 10^5$ reversals to failure), which was consistent with the higher R_a of coarse powder specimens in the West location. The higher fatigue resistance of coarse powder specimens in the East can be attributed to the more prominent effects of surface roughness in the HCF regime [71]. The similar trend was less pronounced for the fine powder due to its slightly higher flowability, which also agreed with the R_a results in Fig. 7(a). Regardless of the powder and the location, cracks initiated from the surface of as-built specimens, resulting in final fatigue failures (see Fig. 10).

In the machined surface condition, a higher fatigue resistance was generally observed for the coarse powder specimens (see Fig. 9(b)), which was more discernible at higher stress levels, i.e., $\sigma_a \geq 500$ MPa. The fatigue lives on these stress levels are mostly in the MCF regime, where the crack propagation stage occupies a significant portion of the total fatigue life. The coarse powder specimens provided slightly better ductility which may be beneficial for their MCF resistance. At lower stress levels (such as $\sigma_a = 400$ MPa), the advantage of the coarse powder specimens became less clear. Nevertheless, it is still important to note the two coarse powder specimens from the East and one from the West reached run-out at this stress level, while none of the fine powder specimens did. In the HCF regime (such as at the stress level of $\sigma_a = 400$ MPa), fatigue life is governed by crack initiation which often occurs at defects. The reason for the significant overlap in fatigue data at this stress level may be explained by the uncertainty in the maximum defect size in each specimen. This is evident from the defect size (measured by $\sqrt{area}$ μm) reported in Fig. 11, where both larger and small fatigue critical defects could present in either batch of specimens even though those in fine specimens were generally larger.

To formally assess the uncertainty in the size of crack initiating defects in both batches of specimens, $\sqrt{area}$ for these defects projected onto the loading plane was measured from the fracture surfaces following Murakami's approach [74], and its distribution was analyzed using extreme value statistics [32,81]. Since only the information of crack initiating defects were involved in the analyzes, the outcome could shed light on the size ($\sqrt{area}$) of the most detrimental defects within a batch of specimens [82]. Although the analysis was performed on fatigue specimens, the knowledge can provide insights towards the statistics of extreme defects in larger components fabricated with the same process parameters, as long as the surface to volume ratio is similar [32]. Gumbel distribution, which was shown to describe the size distribution of extreme defects well [32], has been adopted in this study following the approach established in Refs. [82,83].

The empirical cumulative distribution functions (ECDF) for all crack initiating defects for both fine and coarse powder specimens in machined conditions are shown in Fig. 14(a) according to the extreme value statistics by Gumbel [82–85]. Note here that all of these defects were volumetric ones which were ranked according to their $\sqrt{area}$ from small to large. As shown, the Gumbel ECDF is presented as the reduced variate:

$$Y_i = -\ln\left(-\ln(F_i)\right) \quad (1)$$

where $F_i = i/N + 1$, with i being the rank of the current crack initiating defect, and N is the total number of crack initiating defects identified in each specimen batch (there were only one or a few of these defects per specimen). If the relation between the $\sqrt{area}$ and the reduced variate Y_i is linear, then the distribution follows the Gumbel distribution. Agreeing with the literature [18,32,86], Fig. 14 (a) shows that the size distribution of crack initiating defects well obeys the

Gumbel distribution (R^2 = 0.9554 and 0.9484 for coarse and fine powder specimens, respectively), whose cumulative distribution function is given as:

$$F\left(\sqrt{area}\right) = \exp\left(-\exp\left(-\frac{\sqrt{area}-\lambda}{\delta}\right)\right) \quad (2)$$

where λ and δ are the location and scale parameters of the extreme value distribution. The location parameter (λ) gives the $\sqrt{area}$ value that corresponds to the peak of the corresponding probability density distribution (PDF) function, which is given as:

$$G\left(\sqrt{area}\right) = \exp\left(-\left(\left(\frac{\sqrt{area}-\lambda}{\delta}\right) + \exp\left(-\frac{\sqrt{area}-\lambda}{\delta}\right)\right)\right) \quad (3)$$

The scale parameter (δ) represents the spread of data, i.e., larger δ corresponds to wider distribution, and is used to "scale" the standard Gumbel distribution to best fit a data set. The location and scale parameters in the Gumbel distribution functions are given in Table 5 for both coarse and fine specimens. As seen in Fig. 14(a), the largest crack initiating defects in the coarse and fine powder specimens were 64 and 109 μm, respectively. In addition, the corresponding probability distribution functions (PDFs) are shown in Fig. 14(b). As shown, 90% of defects in coarse powder specimens were smaller than 54 μm whereas they were smaller than 80 μm in fine powder specimens. The statistical analysis confirmed the speculation made above that, going from the coarse powder to the finer powder, the size of crack initiating defects increases. However, the most probable ranges of the crack initiating defect size from the coarse and fine powder specimens significantly overlap, which can explain the fatigue results observed for the machined specimens at σ_a = 400 MPa. Although the precise fitting parameters shown in Table 5 may slightly vary depending on the population of the critical defects analyzed—fitting parameters are generally more reliable with larger population—the observations made above are nevertheless valid since each specimen set contained >15 analyzed defects (see Fig. 14(a)).

Table 5 Location (λ) and scale (δ) parameters of the Gumbel's extreme value distribution obtained based on the $\sqrt{area}$ of the projected defects onto the loading plane from the fracture surfaces.

Gumbel Distribution Function Parameters	Fine Powder	Coarse Powder
Location Parameter, λ	42.9	36.4
Scale Parameter, δ	16.7	8.0

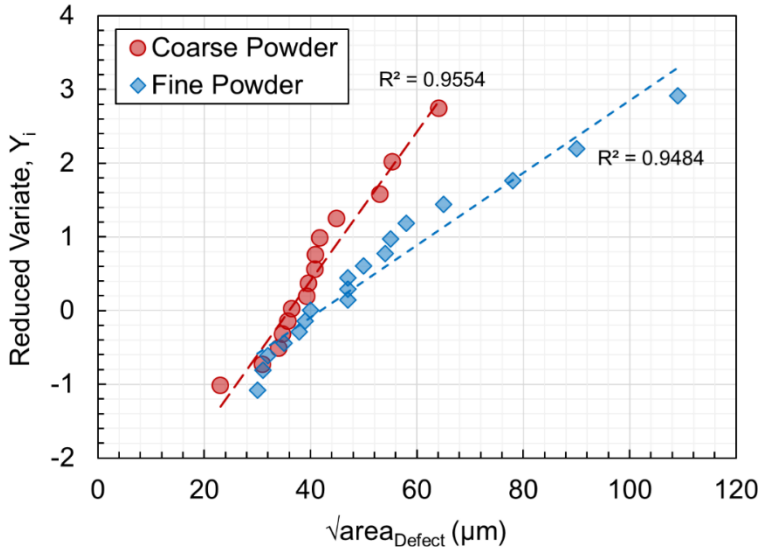

(a)

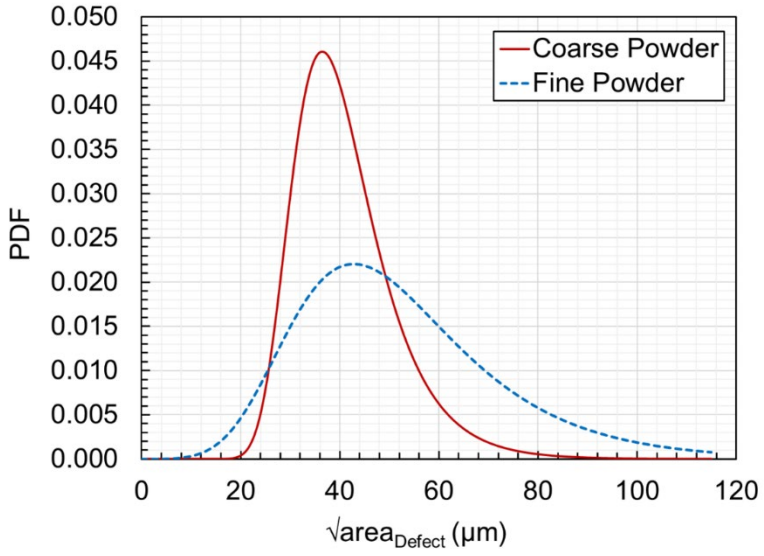

(b)

Fig. 14 (a) Estimation of the largest extreme value distribution and (b) probability density function (PDF) for crack initiating defects based on Gumbel's extreme value statistics and Murakami's $\sqrt{area_{Defect}}$ approach [74] in coarse and fine powder specimens.

2.5. Conclusions

In this study, plasma atomized Ti64 powder batches with PSDs of 15-45 μm and 15-53 μm were used to investigate the effects of particle size on the mechanical performance of parts fabricated by the L-PBF AM technique. Parts were fabricated in different locations on the build plate to study the location dependency of mechanical properties. Overall, slightly higher ductility and fatigue resistance were observed for the specimens manufactured from the coarse powder. Additional conclusions based on the experimental results can be drawn as:

- No difference in the fatigue performance of specimens in the as-built surface condition was noted due to different powder PSDs. In all as-built specimens, fatigue failures initiated from the micro notches on the surface.
- More defects were seen in the coarse powder specimens due to the inferior packing state and lower heat absorptivity of coarser powder particles. However, the maximum defect size was still larger in the fine powder specimens, which was ascribed to the powder spattering during the fabrication.
- Negligible changes were noted in the YS and UTS resulting from the similar microstructure in the coarse and fine powder specimens. Ductility, however, was larger in the coarse powder specimens as they had generally smaller defects.
- Higher fatigue resistance was observed for the coarse powder specimens which was correlated with the higher ductility and smaller-sized defects affecting the MCF and HCF regimes, respectively. While the fatigue life is majorly spent in the crack growth regime at higher stress levels, the crack initiation often dominates the fatigue life at longer life regimes.

- The largest prospective defect size assessed by the Gumbel distribution showed an increase in defect size using the fine powder compared to the coarse one. In addition, 50% of the critical defects in the specimens manufactured from both powder batches had somewhat comparable sizes.

To summarize, it was observed that powder rheological analyses are capable of interpreting and predicting the fatigue behavior of AM parts manufactured from powder batches with different PSDs. In addition, it was noticed that the coarse powder, which showed an inferior packing state compared to the fine batch can still result in almost comparable mechanical properties, and even superior ductility, as well as fatigue resistance in the MCF and HCF regimes. This shows that by carefully selecting the appropriate PSD, it is feasible to improve the part performance. On the other hand, using a less expensive powder with larger and wider particle size distribution may not affect the mechanical performance of the AM parts; however, this observation may be material and AM system dependent.

3. Ti-6Al-4V Powder Reuse in Laser Powder Bed Fusion (L-PBF): The Effect on Porosity, Microstructure, and Mechanical Behavior

3.1. Introduction

In powder bed fusion (PBF) additive manufacturing (AM) technologies, functional parts can be fabricated from the powder feedstock. Due to the use of powder beds in such technologies and the fact that the fabricated parts only occupy a small fraction (typically < 25%) of the bed volume, a significant amount of used powder can remain after fabrication. In the applications where the use of unused (i.e., virgin) powder is not mandatory, it is economically appealing to reuse/recycle the used powder for subsequent fabrications to reduce the costs associated with new powder purchase and handling. However, the characteristics of used powders may be significantly different from their unused counterparts which can influence the defect-/micro-structure and result in inconsistencies in the mechanical properties of the fabricated parts.

Careful evaluation of the effect of powder reuse on the powder feedstock-defect-/micro-structure-part performance relationships thus becomes crucial [32]. In fact, America Makes and the American National Standards Institute (ANSI) have listed powder reuse as one of the main AM technical gaps in their Standardization Roadmap for AM [87]. As such, some studies have already attempted to pave the way toward a thorough understanding of the effects of powder reuse on powder characteristics and mechanical properties of AM parts manufactured via electron powder bed fusion (E-PBF) with Ti-6Al-4V (Ti64) [13–15,88,89], Inconel 718 (IN718) [90], and Ta [91] powders as well as laser powder bed fusion (L-PBF) with Ti64 [7,24,92–95], steels [33,96–100], IN718 [27,101], AlSi10Mg [102–104], and Hastelloy X [105] powders. However, understanding regarding the powder reuse effect on parts' mechanical properties, especially fatigue, and their location dependency is still lacking, as detailed in the forthcoming text.

During AM process fabrication, powder particles near the parts experience exceeding temperatures [3]. Among them, the smaller ones tend to either melt or be attached to larger particles (forming agglomerates) which are then removed during sieving. Accordingly, the fraction of small particles in a powder batch tends to decrease with limited reuse, and narrow the span of particle size distribution (PSD) [7,13,14,33], typically improving the flowability and powder bed packing state [7,13,14,27,33,96], which can result in less defects in the fabricated parts. However, smaller agglomerates (especially the partially melted ones) can remain even after sieving, and their fraction can increase with reuse. Therefore, the flowability of excessively reused powder is expected to decrease, which can lead to a poorer and more location-dependent powder bed packing state, and, accordingly, higher and more location-dependent defect content in the fabricated parts [33,106]. Although the existence of the non-spherical particles due to powder reuse has been confirmed by several studies [13,91,97,105], to what extent these particles contribute to the aforementioned location-dependency is still not well understood.

In addition to particle morphology, reuse can also increase the O concentration in powder particles [7,13,14,24,88–91,98,105]. This again is likely due to the repeated thermal exposure of powder particles near the fabricated parts, which permits the reaction between metal particles and O_2 adsorbed on their surfaces during powder handling [107]. The increased O content in the reused powder may not only lead to a higher concentration of O interstitial atoms in the fabricated parts but also increase the tendency of spattering during fabrication [90,97,98], which can form large defects and nonmetallic inclusions in the fabricated material. The spattering-induced melt pool ejecta (typically oxide-coated metal particles), upon landing back onto the powder bed, can lead to the formation of lack-of-fusion defects due to poor wetting with melts which may increase the O content of the parts in the vicinity [67]. Although shield gas (such as Ar) flow in the build

chamber is typically utilized to remove most of the ejecta as they form, some may still land on the powder bed in the downstream locations [67,106]. Therefore, it can be hypothesized that the defect and O contents for parts fabricated at downstream locations are higher, and the upstream-downstream location dependency is expected to increase with reuse. However, the testing of such hypotheses is still lacking in the literature.

The powder reuse-induced variations in the defects contents and microstructure (primarily O concentration) in the fabricated parts can influence their mechanical properties. For instance, higher ultimate tensile strength (UTS) and yield strength (YS) [13,14,24,88,105] and lower tensile ductility [15,24,88,91,97,105] of a wide range of materials, including Ti64 and AlSi10Mg, are typically seen with powder reuse. The higher strengths are generally ascribed to the additional solid solution effect associated with increased O content. The reduced ductility is typically due to the increased defect content, serving as the inception point of fracture [108].

The role of defects is more accentuated in fatigue properties. As a result, the variations in parts' defect content and their location dependency due to powder reuse can translate to relatively large changes in fatigue lives. For instance, an improvement in the high-cycle fatigue performance was observed in Refs. [7,33,93] due to powder reuse, which was associated with a better packing state of reused powder resulting in fewer and smaller defects. Opposite results (i.e., reduction of fatigue performance with reuse) were also reported in Refs. [14,15] due to the formation of lack-of-fusion defects which were ascribed to excessive reduction of fine particles and low aspect ratio (minimum to maximum dimension) powder particles that passed through the sieve. Under high strain-rate loadings, understanding the role of variations from powder reuse induced micro-/defect-structures is still largely lacking, although some data is available for the high strain-rate fracture

behavior of some additively manufactured (AM) alloys [109–112] (see Section 8.4 in Supplement A for further details).

The current study aims to investigate the effects of powder reuse on mechanical properties, including tensile, fatigue, and high strain-rate fracture behavior of L-PBF Ti64 parts. Any observed variations will be discussed and correlated with powder characteristics, including its flowability, packing state, and chemical composition, as they are affected by powder reuse. In addition, location dependency of mechanical properties with respect to gas flow and powder recoating directions will be investigated. Finally, statistical analysis will be performed to explain the variations in fatigue properties. Following the Introduction, the article will be arranged as follows: Methodology, Experimental Results, Discussion, and Conclusions.

3.2. Methodology

Plasma atomized Ti64 Grade 5 from the AP&C with a nominal PSD of 15-53 µm was used to fabricate parts using the EOS M290, an L-PBF machine, in an Ar environment employing the EOS recommended process parameters as listed in Table 6. The chemical composition, reported by the manufacturer and measured based on the ASTM F2924 [68], is provided in Table 7.

Table 6 EOS Ti64 Grade 5 HiPer 40 µm process parameters and the calculated energy density.

Parameter Set	**Infill**	**Contour**
Laser Power, P (W)	280	240
Scanning Speed, V (mm/s)	1300	900
Hatching Distance, h (µm)	120	(single contour)
Layer Thickness, t (µm)	40	40
Energy Density, E (J/mm^3)*	44.87	-
Power Density, E' (J/mm^2)**	-	6.67

* $E=P/(V\times h\times t)$
** $E'=P/(V\times t)$

Table 7 Chemical composition for AP&C plasma atomized Ti64 Grade 5 reported by the manufacturer.

Chemical Composition

Element	Min (Wt.%)	Max (Wt.%)
Oxygen (O)	-	0.20
Aluminum (Al)	5.50	6.75
Vanadium (V)	3.50	4.50
Iron (Fe)	-	0.30
Carbon (C)	-	0.08
Nitrogen (N)	-	0.05
Hydrogen (H)	-	0.02
Yttrium (Y)	-	0.01
Other elements, each	-	0.10
Other elements, total	-	0.40
Titanium (Ti)	Balance	

As seen in Fig. 15, the build layout consisted of 48 larger square bars with a volume of 13×13×100 mm^3 and 24 smaller square bars with a volume of 9×9×90 mm^3. The build layout also had 16 net-shaped high strain-rate fracture specimens. A half-built square block was also placed in each quadrant for microstructural analyses. All the coupons located on top of the central line were considered the north group, which was closer to the gas inlet nozzle, and the ones below the line and closer to the gas outlet nozzle were grouped as south. All parts were fabricated on support structures.

Lastly, the build plate contained 9 X-ray computed tomography (XCT) coupons for defect characterization across the build plate (i.e., NW, N, NE, W, C, E, SW, S, and SE) for rapid qualification of the print quality. The build plate density (i.e., defined as the fraction of the build plate area occupied by parts) was 12% which was well below 25% recommended by the EOS to prevent the excessive formation of byproducts (e.g., spatter) [21]. The specimen IDs were also labeled on each specimen in Fig. 15. For the reuse strategy, all the powder was collected from the build plate and overflow bin, sieved using an 80-µm filter, and blended with the unused powder remaining from the previous fabrication. This process was conducted without adding any unused

powder until the remaining powder was not sufficient for subsequent iterations. For each set, ~20 kg of powder was used to cover the whole build plate and fabricate the parts. The initial amount of powder (i.e., 65 kg) was adequate to fabricate 8 times. Each fabrication was ~100 hours of exposure (i.e., a total of 800 hours) which is among the highest exposure hours in the literature [12].

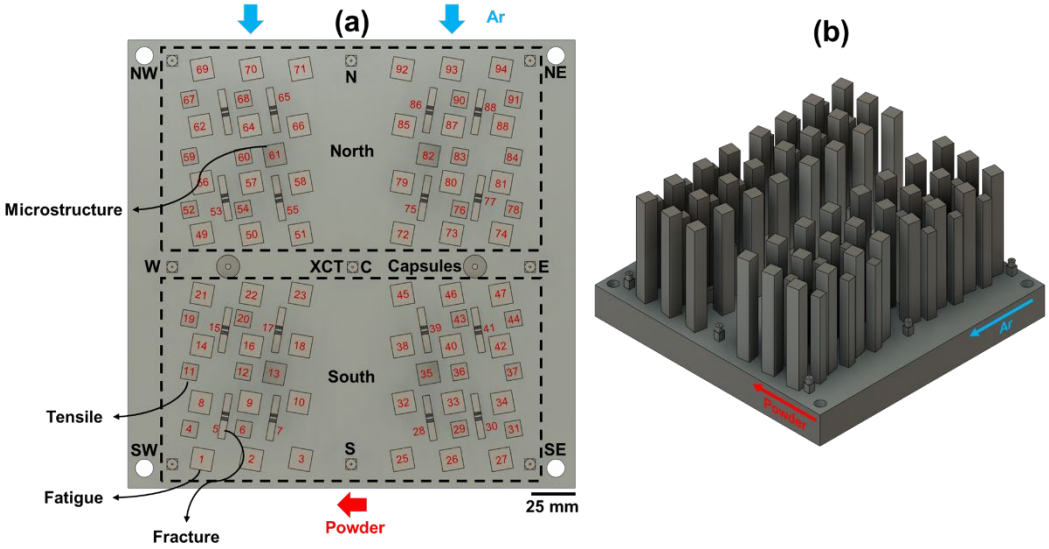

Fig. 15 The (a) top and (b) isometric view of the build layout.

After fabrication, the XCT and microstructure coupons were removed from the build plate in the non-heat-treated (NHT) condition. The remaining were stress-relieved (SR) at 704 °C for 1 hour, followed by furnace cooling in Ar. After SR, the parts were removed from the build plate. The large and small square bars were machined to the geometry of fatigue, and tensile specimens, based on ASTM E466 and E8M [52,53], respectively, as shown in Fig. 16. This figure also shows the geometry of high strain-rate fracture specimens and XCT coupons.

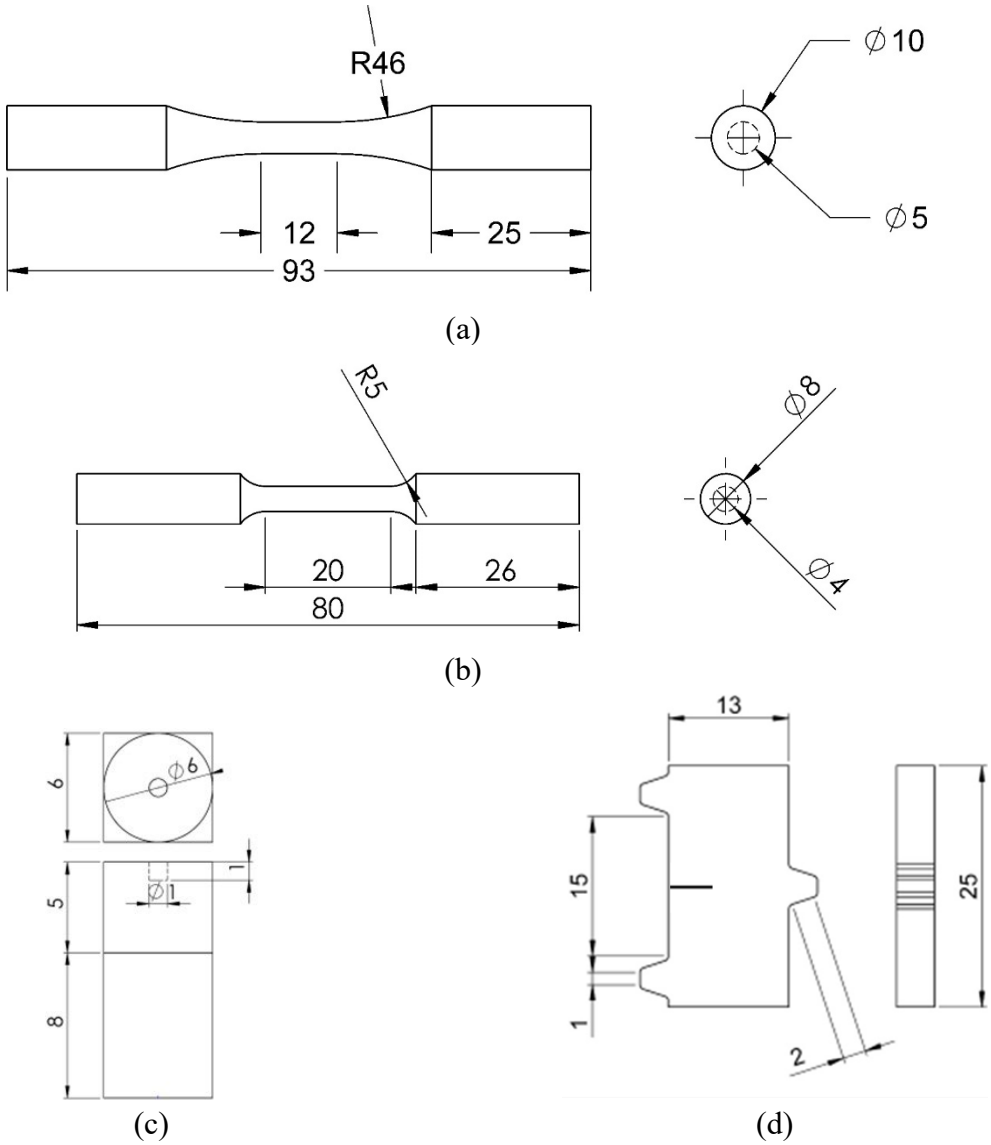

Fig. 16 The geometries of (a) round fatigue specimens with 5-mm straight gage diameter according to ASTM E466 [52], (b) round tension test specimen with 4-mm straight gauge diameter according to ASTM E8M [53], (c) XCT coupon, and (d) high strain-rate fracture specimen. All dimensions are in mm.

After machining, tension tests were conducted in displacement control mode using an MTS Landmark load frame with 100 kN load cells without further polishing. The strain-rate was kept constant at 0.001 mm/mm/s based on ASTM E8M [53]. An extensometer was used to record the strain, and it was removed post yielding at 0.05 mm/mm. High strain-rate fracture tests were performed using a Kolsky bar apparatus with a striker velocity of ~40 m/s. The Digital Image Correlation (DIC) method coupled with ultrahigh-speed photography was employed to obtain

time-resolved in-plane deformations on the specimen surface. A Kirana-05M camera (924×768 pixels) fitted with an 80-400 mm focal length lens and adjustable bellows was used to record speckle images at a rate of 400,000 frames per second.

The experimentally measured displacements from DIC were exported into Finite Element (FE) nodes as boundary conditions to evaluate the fracture properties of interest, namely the *J*-integral [112,113] (further details are provided in Section 8.4 in Supplement A). Fully-reversed fatigue tests ($R_\sigma = -1$) were run via the MTS Landmark and MTS Bionix Tabletop load frames. The force-controlled tests were conducted at 400, 500, 600, and 700 MPa stress levels with 6, 5, 4, and 3 Hz frequencies, respectively, to probe fatigue behavior in the mid-cycle and high-cycle fatigue regimes (MCF and HCF) based on ASTM E466 [52]. The different frequencies were used to ensure approximately the same cyclic strain rates at all stress levels. Failure was defined as the complete fracture of each specimen, and tests that did not fail before 5×10^6 cycles (i.e., 10^7 reversals) were considered run-out.

Using a Zeiss Crossbeam 550 scanning electron microscope (SEM), all fracture surfaces and the microstructure of Ti64 specimens were investigated. The crack-initiating defect sizes were evaluated with the FIJI software [114]. The chemical composition on the fracture surfaces near the defects was also obtained by the Oxford energy-dispersive X-ray spectroscopy (EDS) instrument. The microstructure in the NHT condition was also investigated for all prints via electron channeling contrast imaging (ECCI) using the SEM. The images were obtained from the longitudinal plane (i.e., along the building direction). A Zeiss Xradia 620 Versa was utilized for XCT scans to examine the defect content within the specimens using a source voltage of 140 kV, power of 21 W, and a voxel size of 5 μm. The 3D visualizations and defect distributions were obtained via Dragonfly Pro and FIJI, respectively.

Before each fabrication, the powder was sampled according to ASTM B215 [55] from the feedstock bin. Some heat-affected (HA) powder with particles ejected from the melt pools and near the gas flow outlet nozzle (see Fig. 64 in Supplement A) were also collected for further investigations. All powder PSDs were analyzed using a Beckman Coulter LS 13 320 Particle Size Analyzer using the laser diffraction method. The concentration of interstitial elements (including O and N) in powder batches was analyzed using LECO 736 Series Inert Gas Fusion according to ASTM E1409 [46]. Powder rheological characteristics were measured via an FT4 powder rheometer according to ASTM D7891 [57] and the FT4 manual [62]. Powder characteristic measurements were repeated four times to ensure repeatability.

3.3. Experimental Results

3.3.1. Powder Characteristics

As seen in Fig. 17(a), the PSDs of the feedstock (i.e., the powder used for fabrication) indicated a slight increase in particle size with powder reuse. In addition, the corresponding D_x-values are reported in Fig. 17(c). The D_x indicates that the x% of the particles have an equivalent diameter smaller than the D-value [10,31]. The gradual increase of the D-values can be ascribed to the removal of fine particles, which are easier to melt and be attached to other particles and part surfaces [21]. Closer inspection of the PSDs showed a secondary peak in PSD of Print 8 powder between 80-100 µm. This peak corresponded to ~1% of the total population of Print 8 powder particles. This observation was quite interesting as the sieve used for filtering the particles had a nominal size of 80 µm. Therefore, it may be that some of these particles had low aspect ratios (the ratio of minimum to maximum orthogonal dimensions) and passed through the sieve (e.g., elongated particles and agglomerates) [14]. The particle size span (i.e., D_{90}-D_{10}/D_{50} [20]), which characterizes the width of the PSD peak, did not change with the powder reuse (i.e., 0.8 for all

batches). The HA powder (i.e., the powder after fabrication and near the gas outlet) PSDs were consistently larger than the feedstock in all prints (see Fig. 17(b)).

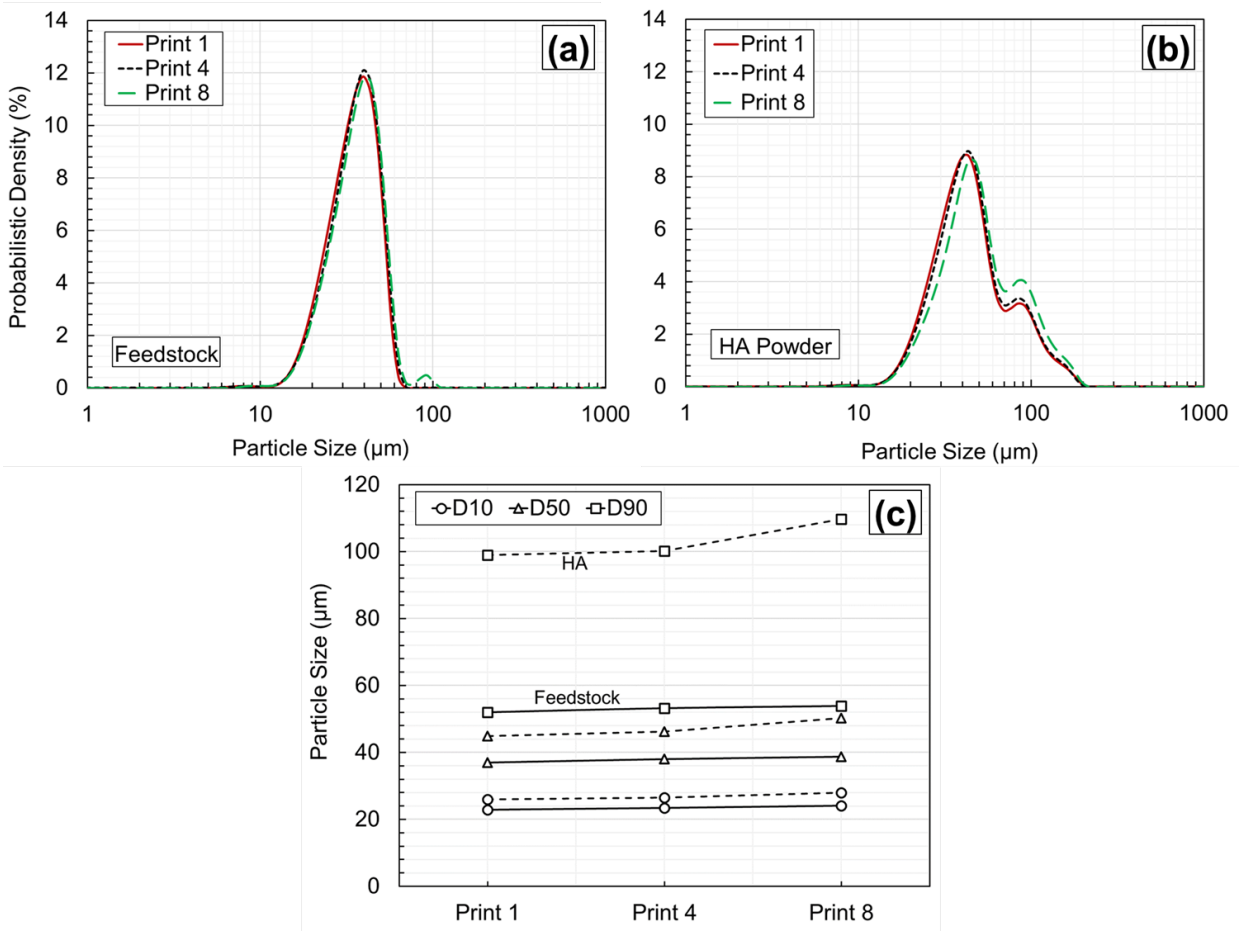

Fig. 17 PSD of the (a) feedstock and (b) HA powder samples, as well as the corresponding D-values of the (c) feedstock and HA powders. The solid and dashed lines correspond to feedstock and HA powders in (c), respectively.

The D_{90} value was exceedingly high in the HA powder, which was attributed to the presence of very large particles that were either large, resolidified melt pool ejecta or large agglomerates of smaller particles due to heat exposure [115–117] (see Fig. 17(a-c)). The HA powder span was twice the powder feedstock (i.e., 1.6), showing a wide range of particle sizes. The particle circularity and aspect ratio were evaluated from the 2D images of the powder with microscopy (see Fig. 18). Some non-spherical elongated particles were observed in Print 8. The aspect ratios of particles 1, 2, and 3 in Print 8 (see Fig. 18(c) & (d)) were 0.5, 0.4, and 0.4, with circularities of

0.7, 0.6, and 0.7, respectively. Such low aspect ratio particles or agglomerates could possibly form due to the collision of melt pool ejecta in the chamber environment [115]. These particles were more frequently seen in the Print 8 powder due to longer exposure to the laser [14]. Such agglomerates could pass through the sieve and, with sufficient quantity, compromise powder spreading and bed packing, potentially resulting in poorer mechanical properties of AM parts [115].

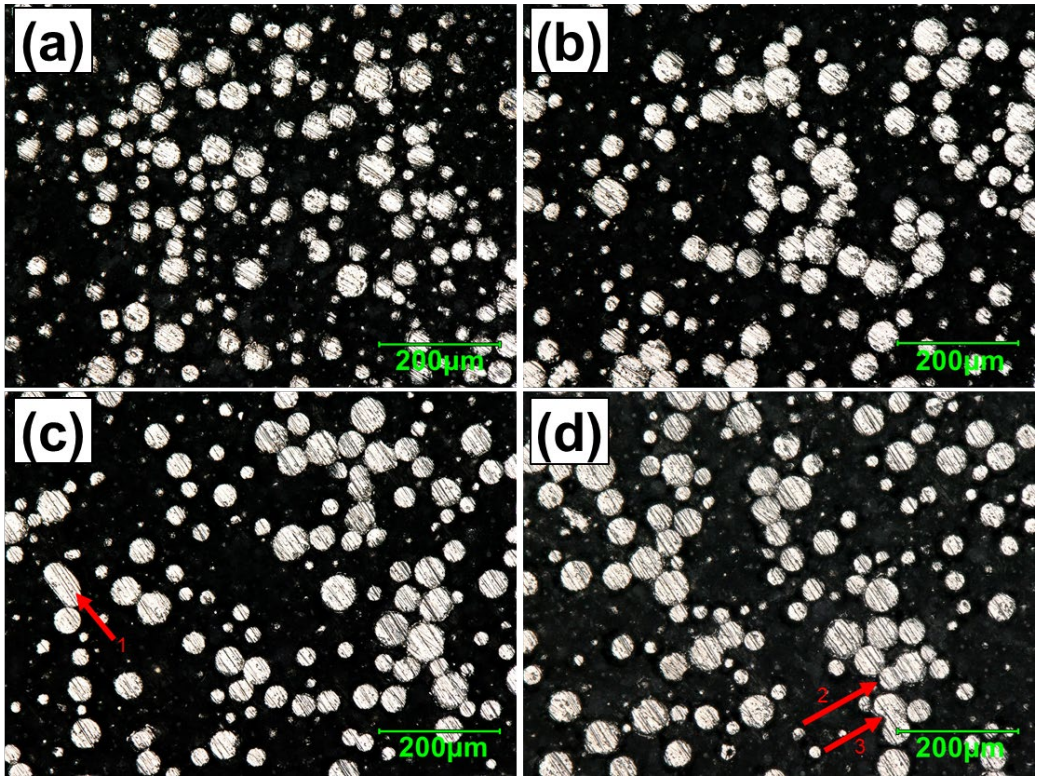

Fig. 18 Polished powder particle cross-sections for Prints 1 in (a), 4 in (b), and 8 in (c) and (d). The red arrows are pointed toward the low aspect ratio particles.

The powder feedstock rheological characteristics were evaluated and reported in Table 8. The basic flowability and specific energies can quantify the powder flowability by measuring the energy required for the blade to move respectively downward or upward within the powder bulk [19,31]. While the basic flowability energy did not exhibit significant change, the specific energy slightly decreased with powder reuse, indicating some improvement in the powder flowability on

the powder bed during fabrication [20]. This flowability improvement with powder reuse was also observed in cohesion values. The cohesion evaluates the powder flow behavior when sheared. Lower cohesion can represent a lower resistance to flow and a more uniform powder bed, yielding less east-to-west location dependency of the parts on the build plate [19,20,31,33,62].

The powder bed packing state improved with powder reuse. This behavior was noted by evaluating the powder compressibility and conditioned bulk density. The former indicates the volume change when the powder is compressed [31], and the latter is measured when the powder bulk is in a low-stress condition (i.e., loosely packed) [19,31]. Therefore, the reducing compressibility and increasing conditioned bulk density at higher print numbers shown in Table 8 indicated the improving packing state of metal powder bed with reuse [7,20,33]. This observation was consistent with the increasing pressure drop values as reuse times increased [62]. A higher pressure drop can indicate a more tightly packed powder bed; i.e., a better packing state [31,33].

Table 8 A summary of powder rheological and bulk characteristics for Prints 1, 4, and 8.

Powder Characteristic	**Print 1 (Unused)**	**Print 4 (3x-Reused)**	**Print 8 (7x-Reused)**
Basic Flowability Energy, BFE (mJ)	277.75 ± 16.51	289.00 ± 13.06	288.25 ± 8.97
Specific Energy, SE (mJ/g)	1.81 ± 0.11	1.53 ± 0.05	1.56 ± 0.03
Conditioned Bulk Density, CBD (g/mL)	2.73 ± 0.01	2.75 ± 0.01	2.76 ± 0.01
Tapped Density, BDtap (g/mL)	2.83 ± 0.02	2.83 ± 0.01	2.84 ± 0.01
Compressibility, CPS (%)	2.85 ± 0.23	2.37 ± 0.43	2.01 ± 0.24
Cohesion, c (kPa)	0.14 ± 0.01	0.10 ± 0.02	0.09 ± 0.03
Pressure Drop, PD (mBar)	6.60 ± 0.48	6.92 ± 0.54	7.38 ± 0.36
Aeration Energy, AE (mJ)	5.38 ± 0.88	5.44 ± 0.28	5.44 ± 0.44

As seen in Fig. 19(a), the concentrations of interstitial elements (i.e., O and N) in the powder increased by powder reuse. The O and N concentrations of the HA powders were also investigated (see Fig. 19(b)). In the HA powder, the concentration of N significantly increased beyond the threshold value with Print 8, whereas the concentration of O did not change significantly and

maintained around the threshold value. Therefore, it was deduced that the increase of O and N in the reused feedstock batches was due to the HA particles which passed through the sieve and mixed with the feedstock powder. It is noteworthy that the amounts of O and N in the feedstock powders were still well below the maximum permitted amount per ASTM F2924 [68]. Some studies have associated the increase in elements such as O and N with a decrease in Ti melting temperature and consequently unstable molten flow, leading to rougher surfaces and interrupted powder flow [118,119].

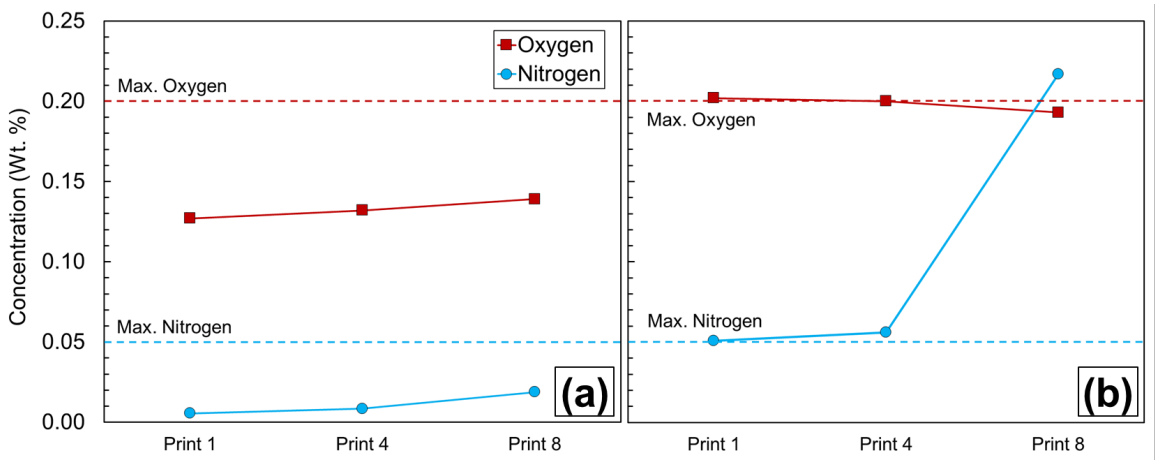

Fig. 19 The concentration of interstitial elements (O and N) in the (a) feedstock and (b) HA powders with respect to powder reuse. The feedstock and HA powders were collected before and after fabrication, respectively.

3.3.2. Defect Content and Microstructure

The XCT witness coupons were used to track any discernible trends of build quality with respect to powder reuse and location on the build plate. Defects smaller than four times voxel size (i.e., 20 µm) were removed to avoid false detection from noise. Upon XCT characterization, some high-density pixels were also detected. Some studies have correlated these dense pixels with secondary phase particles [120]. Since none of the fatigue failures initiated from such inclusions, they were excluded from the XCT analysis to only characterize the defect content. The results were then clustered in [20, 30), [30, 40), and [40, ∞) µm size ranges and reported in Fig. 20.

As seen in Fig. 20, there was generally a decreasing trend in the number and equivalent sphere diameter (i.e., the diameter of a sphere whose volume equals that of the defect's) of the defects by reusing the powder up to Print 4. However, further powder reuse up to Print 8 increased both defect diameter and number compared with Print 4. In addition, no clear trend in defect content was observed in the direction of the powder delivery (i.e., recoater direction), although some minor particle segregation was previously observed (see Fig. 17(c)). However, consistent with the results in [106], the number of defects increased along the gas flow direction, which may be attributed to melt pool ejecta not being properly removed from the build chamber by the gas flow and landing in such regions. This increase was more apparent for Print 8. The maximum defect size did not show a clear trend with respect to powder spreading direction. Although not significant, it somewhat increased in the gas flow direction, especially for the reused powder.

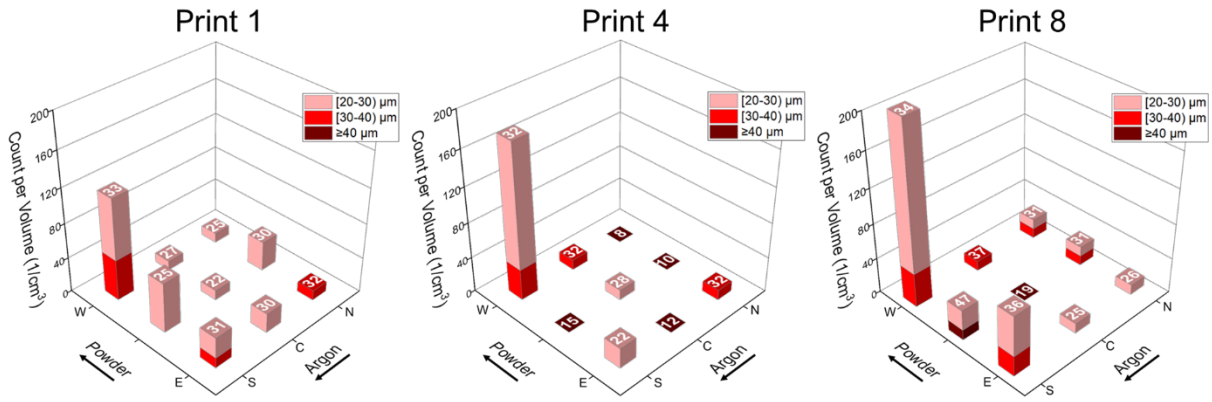

Fig. 20 3D bar charts indicating defect distributions in the XCT coupons across the build plate with powder reuse and the maximum defect size labeled on each bar.

As seen in the ECCI micrographs shown in Fig. 21, the changes in microstructure with powder reuse were negligible in the NHT condition. In Prints 1, 4, and 8 specimens, the darker phases appeared to be martensitic (i.e., α' and α") due to high cooling rates associated with L-PBF technology [32]. Although the rapid cooling was expected to generate purely martensitic microstructure, the repeated reheating due to the consolidation of the subsequent layers may have

partially decomposed the microstructure to α+β. Indeed, the phases with brighter contrast appeared to be β due to the partial decomposition. The grain size was almost comparable for all powders.

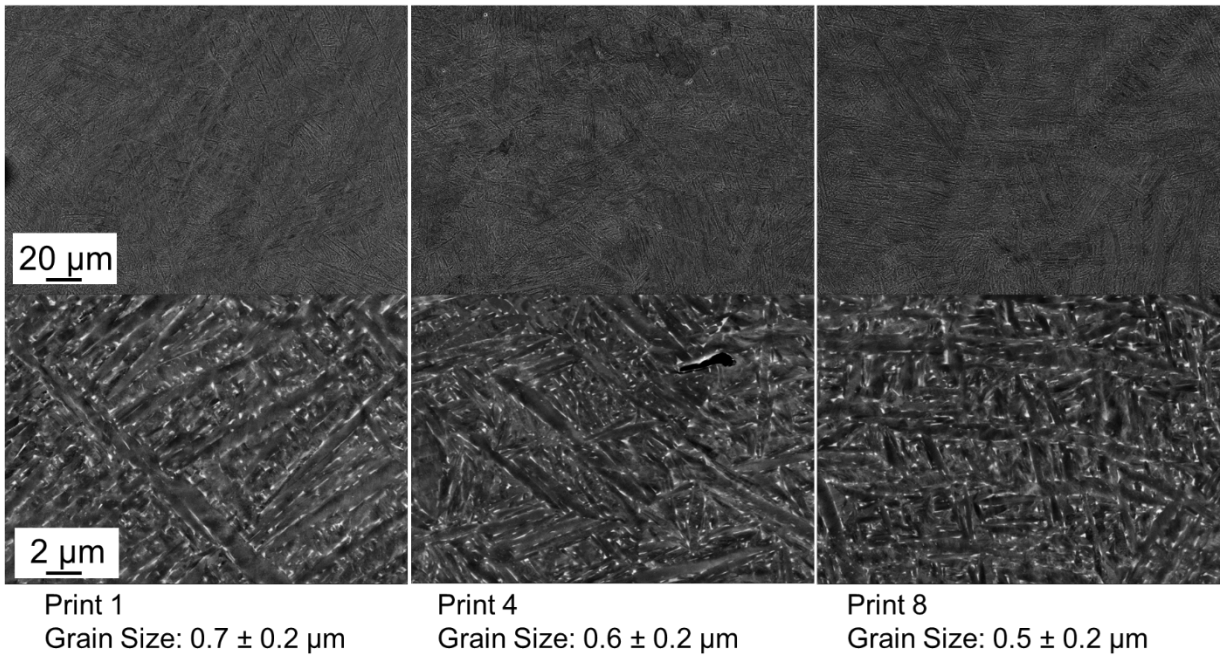

Fig. 21 The microstructure of L-PBF Ti64 in the NHT condition for Prints 1, 4, and 8.

3.3.3. Tensile Behavior

Tensile properties, including UTS, YS, and ductility (ε_f) were obtained for all tension test specimens to analyze their location dependency and the effect of reuse. Here, only the north and south locations, i.e., the upstream and downstream locations of the shielding gas flow, were of focus since no general trends in defect content were observed in the powder spreading direction (i.e., east to west). Accordingly, there were six specimens per reuse condition and location (i.e., north and south). As seen in Fig. 22(a), the UTS in the south was slightly higher than the north specimens regardless of the powder condition. In addition, an increasing trend in UTS was observed with powder reuse in both the north and south specimens. The YS also showed the same trend for both the location and the powder reuse (see Fig. 22(b)), which can be due to the low hardening rate of Ti64. As shown in Fig. 22, the microstructure of fabricated parts was not affected

by powder reuse. Therefore, the added strength with reuse was ascribed to some increase in O concentration in the powder (see Fig. 19(a)) and in the specimens. It is generally known that O concentration can increase strength and reduce ductility [95,105,121]. Indeed, unlike tensile strength, the ε_f somewhat decreased with powder reuse (see Fig. 22(c)). This decrease was more drastic for the specimens in the south. Noting that the defect content was expected to improve at Print 4 (see Fig. 20)—yet the ductility still reduced; thus, the role of O concentration in the powder (see Fig. 19(a)) may have been significant. Nevertheless, the tensile ductility observed in the south locations for Print 8 was substantially lower than all other conditions, which could have been contributed by the relatively high defect content witnessed in the south of Print 8.

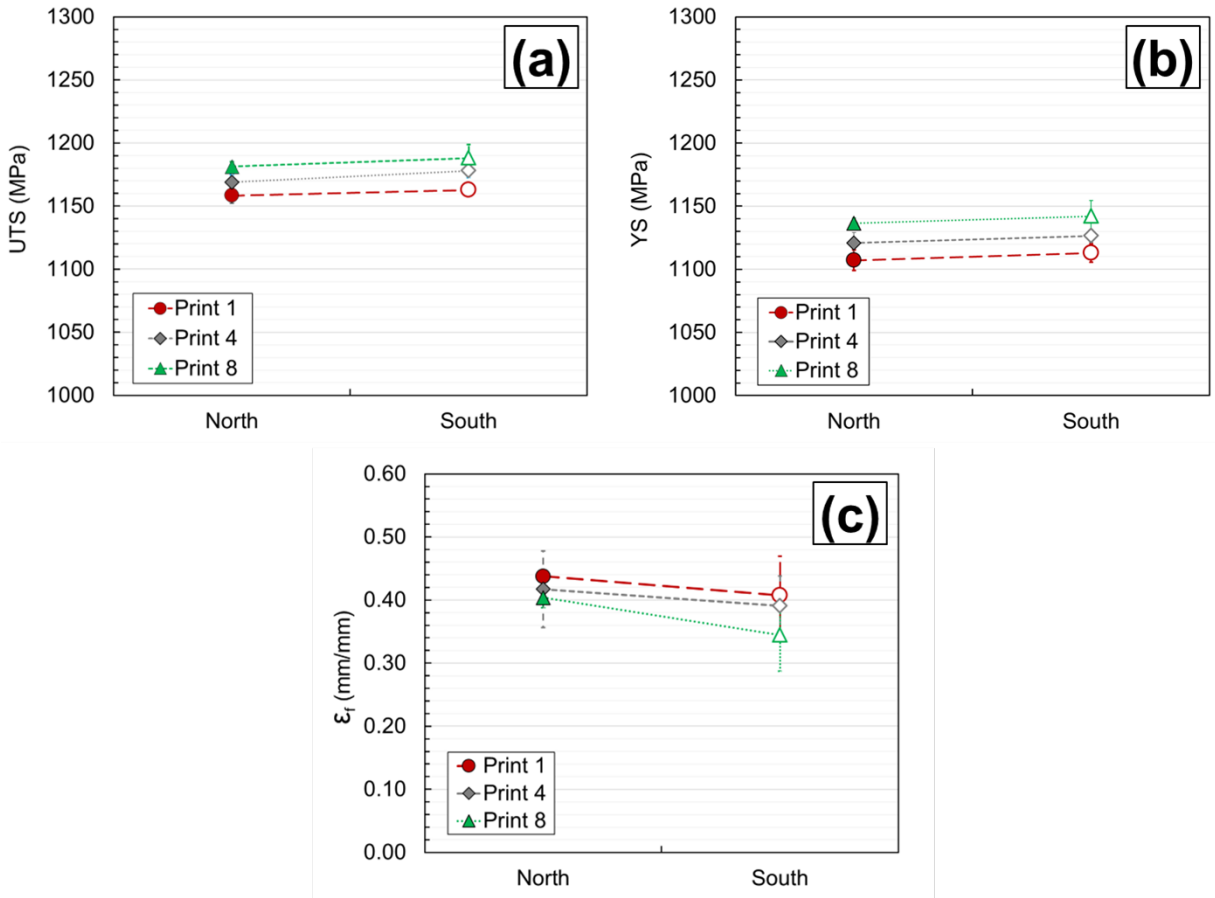

Fig. 22 Tensile properties, including (a) UTS, (b) YS, and (c) εf obtained for different prints and locations on the build plate.

3.3.4. High Strain-Rate Fracture Behavior

The *J*-integral or the energy release rate histories for the horizontally built specimens (Loading axis and crack were perpendicular to the build plate) from Prints 1, 4, and 8 (six specimens per condition) are shown in Fig. 23. From the DIC images, crack initiation was identified in each experiment, and that image or dataset was identified as $t = 0$ μs to create a common reference time for comparing all experiments. Therefore, negative and positive time instants represent the response before and after the crack initiation, respectively. It can be noted that the whole fracture event, from initial contact to crack initiation and growth, lasted ~60 μs. The data in Fig. 23(a) corresponds to the specimens from the north in each print. The *J*-integral values overlapped until crack initiation (or time $t \sim 0$ μs), and the variations were approximately parabolic. However, the values showed differences at crack initiation.

The *J*-integral at crack initiation was the highest for specimens from Print 8 at 19.4 kJ/m^2, followed by Print 4 at 19.2 kJ/m^2, and Print 1 at 18.6 kJ/m^2. The crack propagation behaviors had a similar response for all prints. Hence, considering all three, Prints 4 and 8 had 3% and 4% higher critical energy release rates than Print 1. The crack growth resistance curves under dynamic loading conditions are shown in Fig. 23(b). The crack growth was stable, as reflected by the non-negative slope of the resistant curve ($dJ/da \sim 0$) after crack initiation. The slopes after crack initiation also remained the same for all prints with just the difference in magnitude due to the higher critical energy release rate for Prints 4 and 8.

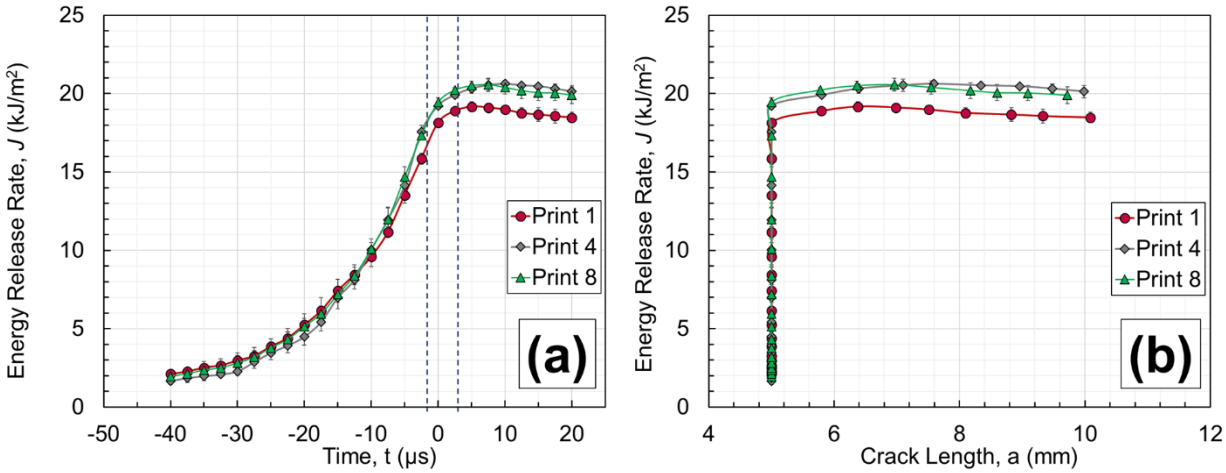

Fig. 23 The J-integral histories (a) and crack growth resistance curves (b) for Ti64 specimens from Prints 1, 4, and 8. All data is from the specimens in the north.

The similarity of fracture behaviors of Ti64 specimens fabricated from different locations on the build plate in Print 1 is shown by the *J*-integral histories in Fig. 24(a) and crack growth resistance curves in Fig. 24(b). As shown, there was no significant difference in the critical energy release rate for the specimens from different locations, i.e., no location dependency. Specifically, a maximum of 2% difference was observed between the south and north in Print 1. However, the experimental error was also ~2%. Similar behavior was also observed for Prints 4 and 8 (See Fig. 70 and Fig. 71 in Supplement A). A summary of high strain-rate fracture results is reported in Fig. 25. In this figure, critical energy release rates are shown for specimens fabricated in north and south locations, and their values are listed in the table next to the figure. It can be observed that the difference in fracture properties because of the location was within the experimental error (~2%). However, a discernible difference was observed between Print 1 and Prints 4 and 8. The difference between Prints 4 and 8 was still within the experimental error.

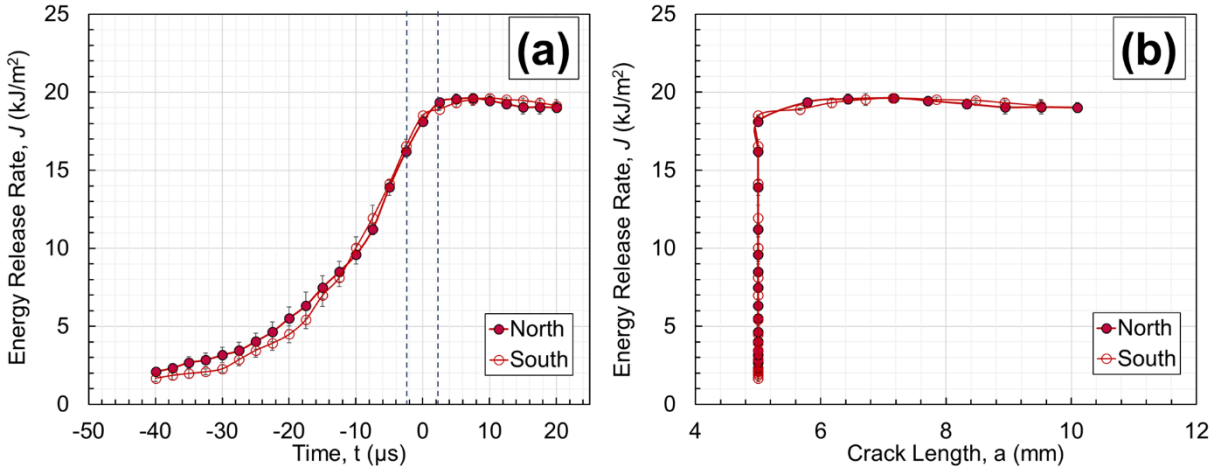

Fig. 24 The J-integral history (a) and crack growth resistance curves (b) for Ti64 specimens from Print 1 in the north and south locations of the build plate.

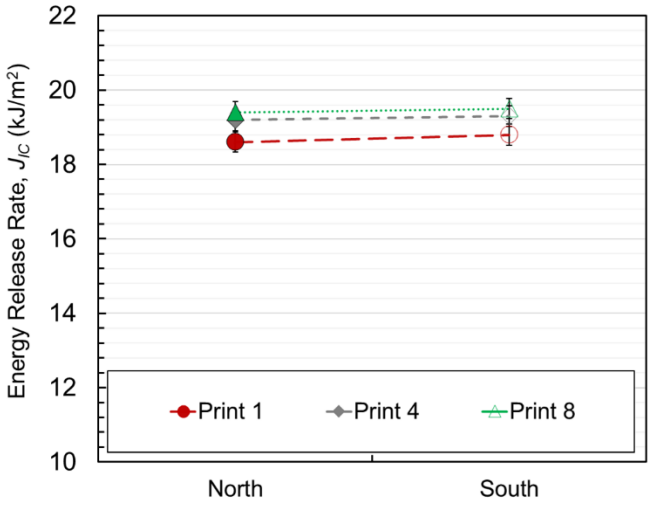

J_{IC} (kJ/m²)	North	South
Print 1	18.6	18.8
Print 4	19.2	19.3
Print 8	19.4	19.5

Experimental error~0.3 (2%)

Fig. 25 A summary of the critical energy release rate for Ti64 specimens for different powders and locations on the build plate.

3.3.5. Fatigue Behavior & Failure Analysis

Since defect contents only showed significant variation along the gas flow direction (see Fig. 20), fatigue performance was merely compared between the north and south specimens. Among the specimens located in the north, the ones in Print 4 had somewhat better fatigue performance, followed by Prints 1 and 8 (see Fig. 26). However, in the south, Print 1 outperformed Print 4 and 8. The better fatigue performance for the reused powder in the north agreed with the results in [7], which might have been due to the better packing state of reused powder (see Table 8). The reduced

fatigue performance in the north for Print 8 was perhaps due to the increased spattering activities caused by the increased O content in the powder. South locations were at the downstream of the shielding gas, and the effect of spattering was, therefore, more significant. As a result, reduced performance in the south was seen as early as Print 4. Location dependency of fatigue behavior for specimens from Prints 1, 4, and 8 was characterized and presented in Fig. 27. The specimens fabricated in the south generally had lower fatigue lives irrespective of the powder reuse.

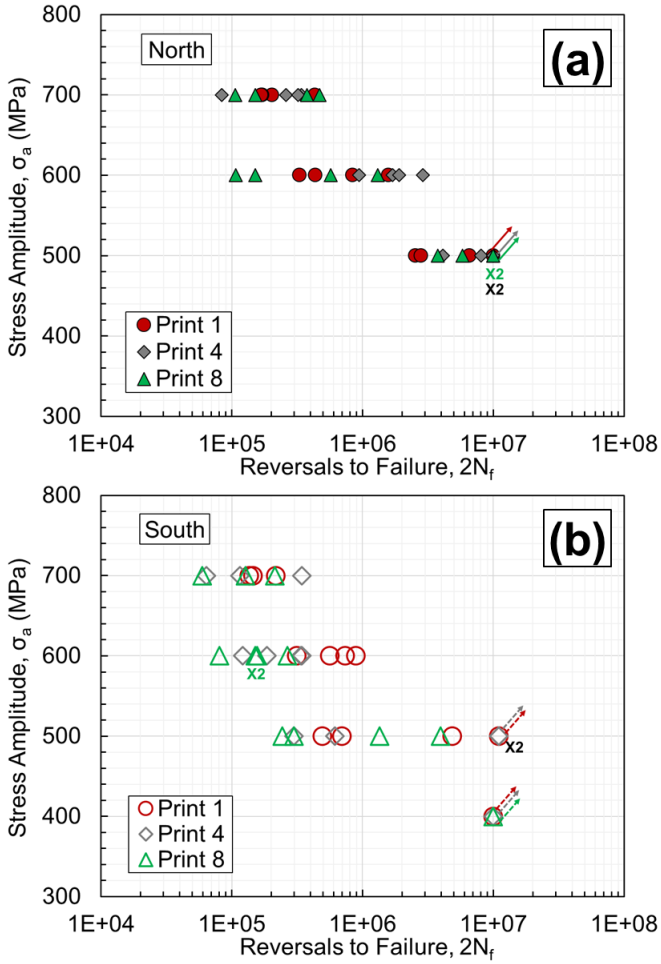

Fig. 26 Stress-life fatigue behavior of L-PBF Ti64 Grade 5 specimens from Prints 1, 4, and 8 in (a) north and (b) south.

The south-to-north difference was less significant in Print 1. As the powder was reused, the gap became more distinct in Print 4. With continued reuse, the gap appeared to become small again in Print 8. This interesting behavior may be related to changes in defect content within the

specimens in the north and south due to powder reuse. As briefly discussed in the Introduction, the increased O concentration in powder with reuse tends to induce more frequent spattering, which can form more defects of larger size. Due to the shield gas flow, more pronounced excessive defect formation first occurred at the downstream locations (south), and as O concentration increased, it proliferated gradually to the north. This hypothesis is tested in Section 4 with complete information on critical defects' size.

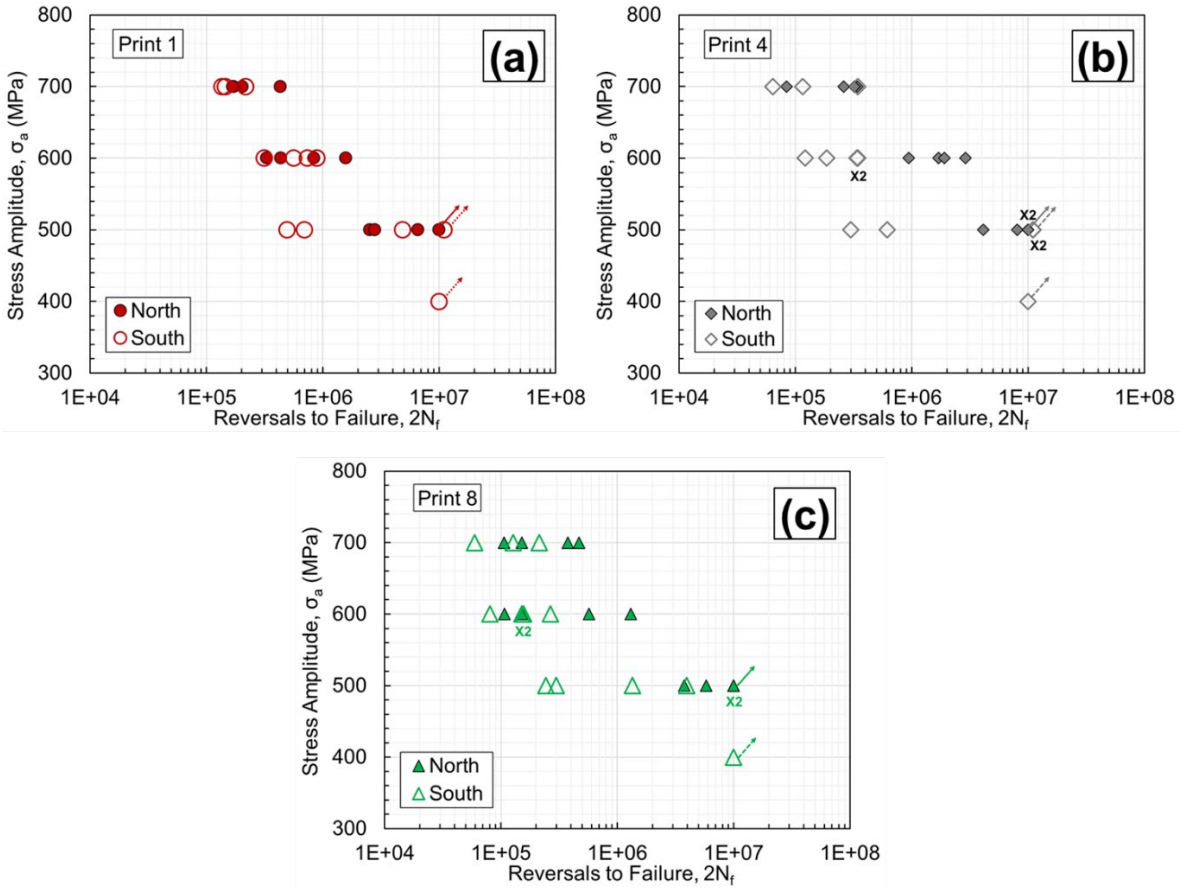

Fig. 27 Stress-life fatigue behavior of L-PBF Ti64 Grade 5 specimens from Prints (a) 1, (b) 4, and (c) 8 in the north and south regions.

A summary of all force-controlled fatigue tests is reported in Table 9. Fracture surfaces of all fatigue specimens were examined, and the size and location of the crack initiating defects are also listed in Table 9. In this table, the defect size was measured based on Murakami's approach. In this method, defects were classified based on their location from the surface (i.e., internal or at the

surface). When the defect is neither internal nor at the surface, i.e., sub-surface, the whole defect and the adjacent area between the defect and surface were considered, provided that its size is larger than the distance to the free surface [122]. Some notable fracture surfaces are also shown in Fig. 28. One of the specimens of interest was Sp. 1, which was located the closest to the shielding gas outflow nozzle and had lower fatigue life than other specimens at the same stress level. As seen in these figures, all failures initiated from irregular-shaped lack-of-fusion defects, typically larger for the specimens located in the south (i.e., Sp 1 and 27). It was reported that excess O content (e.g., in the form of oxides) could also promote the formation of such lack-of-fusion defects, possibly via spattering, in Ti64 [89].

Table 9 A summary of fully-reversed ($R\sigma = -1$) force-controlled fatigue tests for L-PBF Ti64 specimens in machined surface conditions for Prints 1, 4, and 8 with the corresponding equivalent defect size and location, including internal (I), surface (S), and sub-surface (SS).

ID	σ_a (MPa)	Print 1		Print 4		Print 8	
		$2N_f$ (Reversals)	Size (μm), Location	$2N_f$ (Reversals)	Size (μm), Location	$2N_f$ (Reversals)	Size (μm), Location
South							
22	400	> 10,000,000		> 10,000,000		> 10,000,000	
01	500	491,454	81, I	299,142	162, I	242,984	151, I
27	500	694,022	93, I	615,804	82, I	297,506	153, I
38	500	4,855,624	34, I	> 10,000,000		1,346,636	102, SS
18	500	> 10,000,000		> 10,000,000		3,937,652	42, I
03	600	314,492	129, I	185,184	105, I	151,290	125, I
42	600	561,396	49, I	338,338	159, I	265,448	171, SS
14	600	737,294	65, SS	120,800	116, SS	155,806	121, I
25	600	886,098	46, I	343,684	108, I	80,364	99, SS
09	700	135,700	79, I	63,978	127, SS	59,608	106, I
33	700	145,022	57, I	115,778	95, I	126,954	69, I
46	700	216,606	59, I	343,570	45, I	213,604	52, I
North							
69	500	2,540,668	71, I	8,064,276	49, I	3,767,278	67, I
94	500	2,791,038	81, I	4,116,082	56, I	5,801,358	41, I
79	500	6,544,252	47, I	> 10,000,000		> 10,000,000	
58	500	> 10,000,000		> 10,000,000		> 10,000,000	
81	600	328,582	32, S	944,152	20, I	150,684	41, I
92	600	434,968	33, S	1,904,194	56, SS	568,282	74, I

56	600	840,764	53, I	1,700,638	76, SS	106,902	36, I
71	600	1,572,070	50, I	2,879,354	36, I	1,307,644	52, I
73	700	167,730	112, S	321,576	23, I	106,318	41, I
87	700	171,618	28, I	260,672	23, I	468,616	34, I
50	700	203,216	31, I	339,696	34, I	150,650	28, S
64	700	431,318	31, I	83,640	36, I	375,512	37, I

As evident in Fig. 28 and Table 4, the size of defects increased with reusing the powder for the south specimens compared to Print 1. The equivalent defect size was measured based on Murakami's approach [4,31,74] and found to be 81, 162, and 151 μm, respectively, for Print 1, 4, and 8 specimens. This observation was consistent with the O pickup noted with powder reuse, which could have resulted in more spatter. In addition, due to the higher probability of spatters landing in the south region, the defects in these specimens were somewhat larger (see Table 9). The equivalent defect size in the Print 1-south specimens was 81 and 93 μm, respectively, whereas it was 71 and 81 μm for the case of Print 1-north specimens.

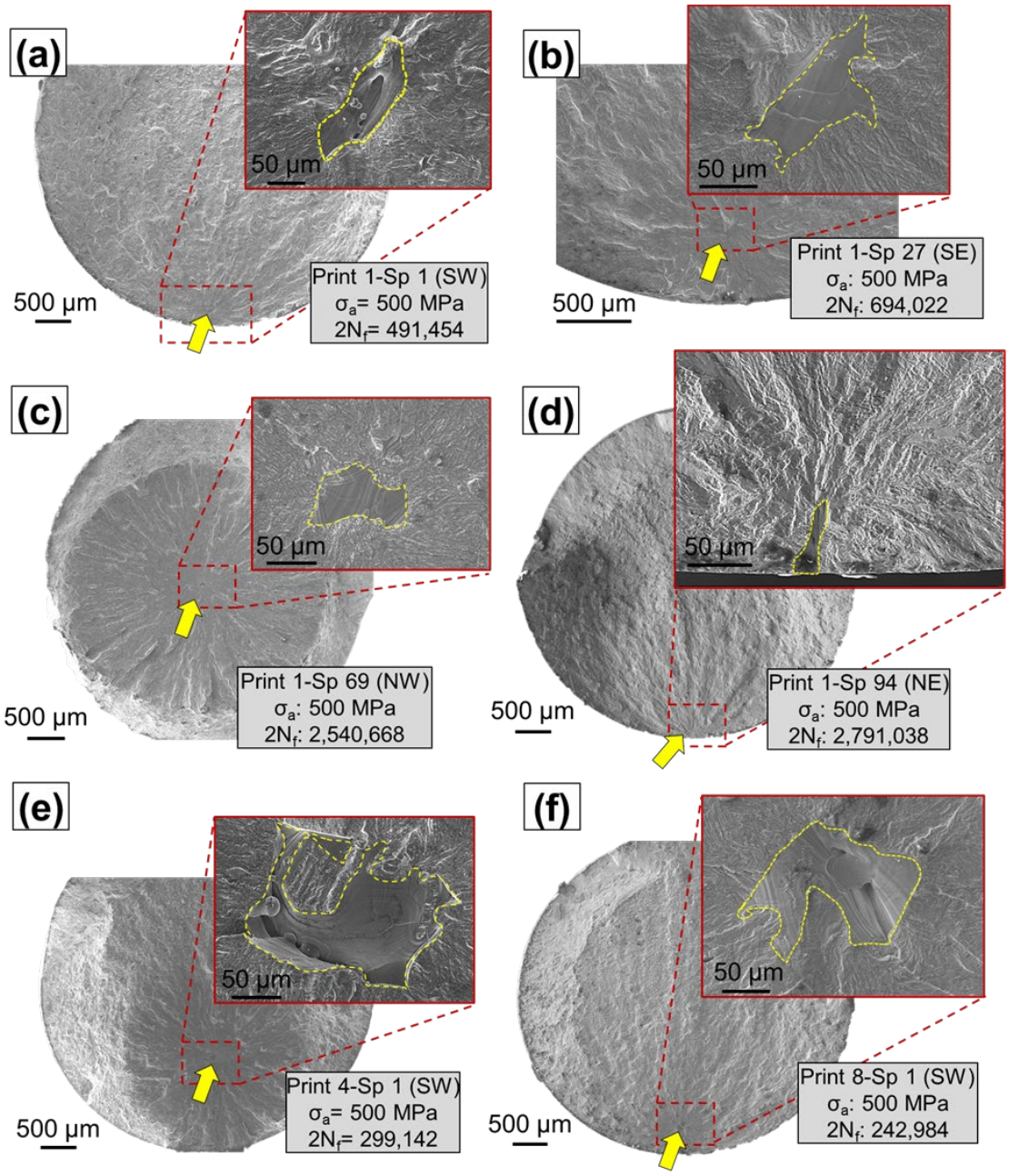

Fig. 28 Fracture surfaces of fatigue specimens including (a) Print 1-Sp1, (b) Print 4-Sp1, (c) Print 8-Sp1, (d) Print 1-Sp27, (e) Print 1-Sp 69, and (f) Print 1-Sp 94. All specimens were tested at 500 MPa stress amplitude. The fatigue life corresponding to each specimen is labeled on each figure. The yellow arrows indicate the crack initiation sites, and the crack-initiating defects are enclosed by yellow dashed lines in the zoomed-in images.

3.4. Discussion on Experimental Results

It is well established that the size of critical defects resulting in fatigue failures follows the largest extreme value Gumbel distribution [86]. In this regard, $\sqrt{area}$ of defects were measured

based on Murakami's approach [122]. Then, the defects were ranked based on their size from the smallest to the largest one. Lastly, the reduced variate (Y_i) was obtained by:

$$Y_i = -ln\left(-\ln\left({}^{i}/_{N+1}\right)\right) \quad (1)$$

where *i* is the rank and N is the total number of critical defects. The plots of the reduced variates of different prints for both north and south locations are presented in Fig. 29(a) & (b), respectively. As seen in Fig. 29(a), the critical defects in the fatigue specimens well obeyed the largest extreme value Gumbel distribution with R^2 values greater than 0.80 for all conditions. In addition, it was seen that in the north, the smallest critical defects occurred in Print 4 specimens. In the south, however, the largest defect was in Print 8, followed by Print 4, which were both considerably larger than that of Print 1. The cumulative and probability density functions (CDF and PDF) were also evaluated using equations (2) and (3) according to ASTM E2283 [81]:

$$PDF(x) = {}^{1}/_{\delta}\left[exp\left(-{}^{\left(\sqrt{area_{defect}}-\lambda\right)}/_{\delta}\right)\right] \times exp\left[-exp\left(-{}^{\left(\sqrt{area_{defect}}-\lambda\right)}/_{\delta}\right)\right] \quad (2)$$

$$CDF(x) = exp\left[-exp\left(-{}^{\left(\sqrt{area_{defect}}-\lambda\right)}/_{\delta}\right)\right] \quad (3)$$

where the λ and δ are location and scale parameters, respectively, and their values are reported in Table 10 [31,81].

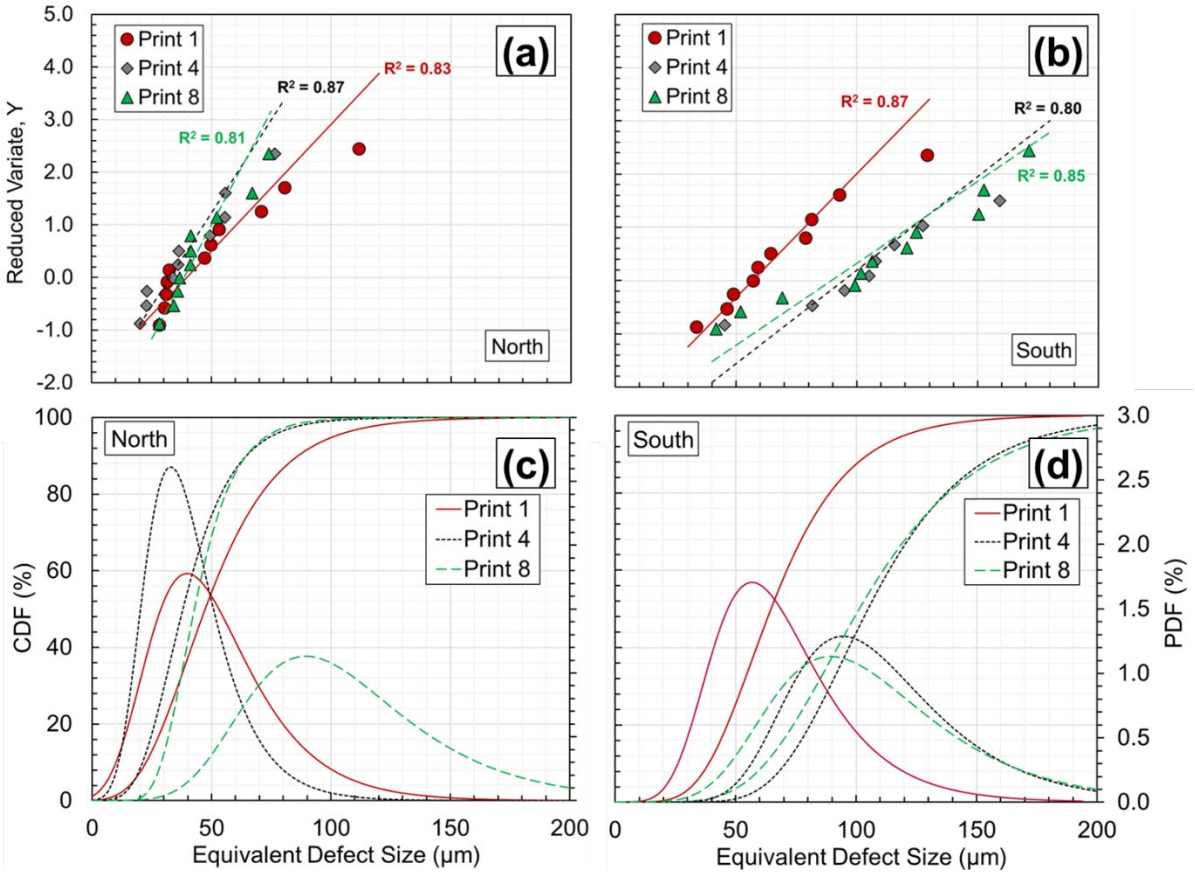

Fig. 29 The extreme value Gumbel distributions of critical defect size for Prints 1, 4, and 8 specimens in the (a) north and (b) south and the corresponding CDF and PDF in the (c) north and (d) south.

Table 10 Location (λ) and scale (δ) parameters of the Gumbel's extreme value distribution.

Gumbel Parameters	**Print 1**		**Print 4**		**Print 8**	
Build Plate Location	North	South	North	South	North	South
Location Parameter, λ	40	57	33	95	39	89
Scale Parameter, δ	21	22	14	29	12	33

The statistics of fatigue critical defect size, presented in Fig. 29, appeared to be in good agreement with the orders of data presented in Fig. 27 that the difference in fatigue life between north and south was small in Print 1, which became larger in Print 4 and small again in Print 8. In order to better quantify the change in location dependency, the log-normal distributions of fatigue lives for all prints and locations at the stress amplitude of 600 MPa were indicated in Fig. 30. The reused fatigue life improved in the north of Print 4, which was noted in Fig. 26, and clearly evident

in Fig. 30. Comparing the PDF curves in Fig. 29(c) & (d), it is evident that the ranges of critical defects in both north and south were essentially identical for Print 1.

This indicates the fabrication with unused powder had very limited spatter. As the powder was reused, the O pickup in the powder could result in more significant spattering, leading to more and larger defects in the downstream locations. Indeed, the critical defects in the south of Print 4 became significantly larger, while those in the north did not experience much change. Excessive O pickup due to further reuse of the powder exacerbated the spattering in both south and north locations. This could be the case for Print 8, where the size ranges of the critical defects in both north and south were similarly large. This observation on the equivalent diameter of critical defects matched the fatigue behavior.

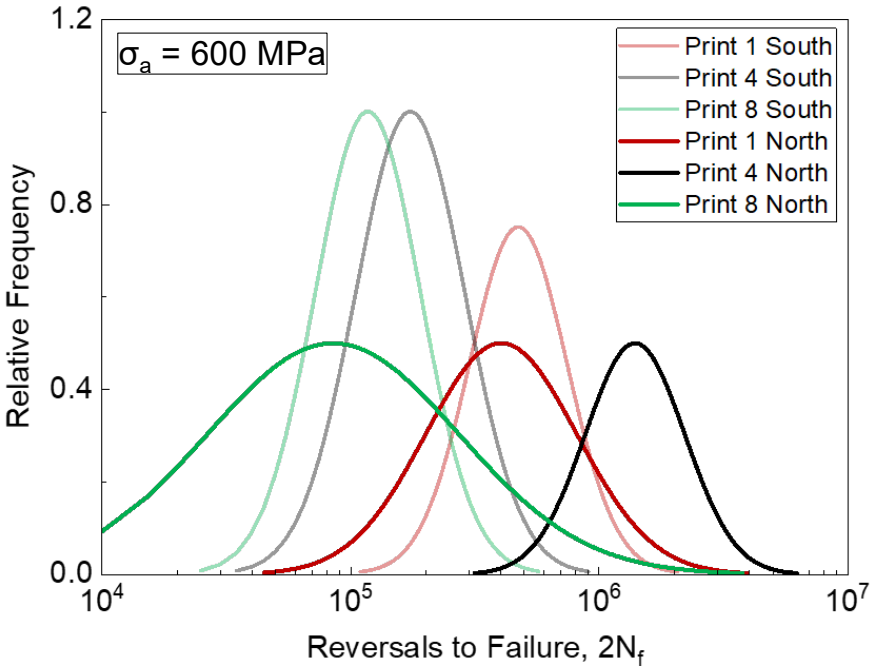

Fig. 30 The log-normal distribution of fatigue lives for Prints 1, 4, and 8 in the north and south at the stress amplitude of 600 MPa.

3.5. Conclusions

This study investigated the effects of reusing plasma atomized Ti-6Al-4V Grade 5 powder in an L-PBF system on microstructure, porosity, and mechanical properties. In addition, parts were

distributed across the build plate to evaluate the effect of location on the part mechanical performance. The following conclusions were drawn based on the experimental results and analysis:

- Powder reuse (up to 7x) increased the powder D-values and uniformity, resulting in higher flowability and packing state.
- Reusing the powder did not affect the microstructure. Based on the X-ray computed tomography scans performed on the witness coupons, the defect size and count generally increased in the direction of gas flow, which was attributed to the spattering during fabrication. Limited powder reuse up to 3 times appeared to decrease the defect content; however, it increased again with further reuse.
- The yield and ultimate tensile strength gradually increased with powder reuse due to higher oxygen concentration in reused powders. In addition, specimens closer to the gas flow outlet (i.e., downstream/south) had higher strength due to more heat-affected powders in this zone and, consequently, higher oxygen content. Tensile ductility had an opposite trend, indicating lower ductility for the specimens manufactured from reused powder and/or closer to the gas flow outlet.
- The high strain-rate fracture behavior of specimens from the reused powder showed a higher critical energy release rate (3-4%) because of the increased yield strength. However, no location dependency effect on the fracture behavior was noticed.
- Although limited powder reuse could moderately reduce defect content in parts and improve the fatigue performance of the specimens closer to the gas flow inlet, it generally decreased fatigue resistance due to higher oxygen content and spattering when reuse was excessive and/or fabrication was at downstream locations.

The knowledge obtained in this study can provide further insight into different sources of variabilities (i.e., location and powder) of part performance. Controlling or monitoring such variabilities during the L-PBF fabrication can result in more reliable parts or ones with more predictable mechanical properties, which is essential for the qualification and certification of AM parts in load-bearing critical applications [123,124].

4. Fatigue Behavior of Additively Manufactured 17-4 PH Stainless Steel: The Effects of Part Location and Powder Re-use [33]

4.1. Introduction

Additive manufacturing (AM) is an advanced manufacturing technology, which provides the opportunity to fabricate complex components directly from a 3D CAD model and material feedstock (i.e., powder or wire) in a layer by layer process. Powder is used as the feedstock in powder bed fusion (PBF) techniques, which are one of the most widely used AM methods [10]. One of the major challenges associated with powder feedstock, however, is the handling of previously used and recovered feedstock. A significant portion of the powder bed envelope is unfused after part fabrication and, for economic reasons, is often sieved and re-used for several iterations before being discarded. Currently, the effect of powder re-use on the resulting fatigue behavior of parts fabricated with increasingly re-used powder is not well understood. A common procedure to re-use metal powder is to collect all the powder in the collector bin and unconsolidated powder in the build envelope after fabrication, pass the collected powder through a sieve screen to remove large spatter particles and break down any agglomerates (i.e., clusters of small particles adhered to larger particles [10]), and mix to uniformity with an appropriate amount of additional powder to perform the next build.

While re-using the powder is a common practice, there are limited studies on how re-using the powder can alter the powder characteristics, and consequently, the mechanical performance of the fabricated part [10]. Some studies have been conducted in an effort to understand the effects of powder re-use on powder characteristics [22,58,117,125–128]. Effects of powder re-use on Ti-6Al-4V and Inconel 718 using electron beam powder bed fusion (EB-PBF) process were studied in [127], and no significant changes in flowability, morphology, and particle size distribution (PSD) with re-using for five and six times, respectively for Ti-6Al-4V and Inconel 718, were

observed. It was, however, found that the number of possible re-using times for Ti-6Al-4V can be limited to the amount of oxygen concentration due to its increase with powder re-use [127].

Cordova et al. [22] also studied the effects of re-using LB-PBF Inconel 718, Ti-6Al-4V, AlSi10Mg, and Scalmalloy on powder characteristics including morphology, flowability, microstructure, and chemical composition. Finer particles were reported to get eliminated with re-using the powder, leading to larger average particle sizes which was more drastic for AlSi10Mg. Some changes in morphology such as particles becoming more elongated were observed in the re-used Inconel 718 and AlSi10Mg. In addition, a general increasing trend of flowability was noticed for re-used powder as compared to unused powder for all the materials. While in these studies different powder features (including PSD, particle shape, chemistry and flowability) were characterized [22,58,117,125–128], the effects of powder re-using on the mechanical properties were not investigated.

Some studies have been recently conducted to understand the effects of powder re-use on the mechanical properties of the fabricated parts [7,13,15,23,96,97,129–132]. For instance, Popov et al. [15] observed shorter fatigue lives for specimens fabricated from EB-PBF 69-times re-used Ti-6Al-4V powder compared with the ones from unused powder. The shorter fatigue lives for the EB-PBF parts fabricated from re-used Ti-6Al-4V powder were explained by the particles' surface oxidation which led to lack of fusion defects in parts. While no changes in the microstructure of the fabricated parts were reported, a decrease in ductility of specimens fabricated by re-used powder was observed. In another study, the effects of re-used nickel alloy powder in LB-PBF on tensile properties were investigated [130]. Oxygen content increased with re-using the powder in LB-PBF. The increase in oxygen level resulted in lower ductility and toughness of the LB-PBF

parts fabricated from re-used nickel alloy. However, the ultimate tensile strength (UTS) and yield strength (YS) remained comparable for specimens from unused and re-used powder batches.

Tang et al. [13] also observed oxygen pickup with re-using Ti-6Al-4V powder in EB-PBF which was explained to be the reason for increases in UTS and YS. The PSD became narrower with the powder re-use due to the reduction in finer particles. Fewer satellites (i.e., fine particles adhered to larger particles during atomization [10]), and consequently, fewer agglomerates were found in the re-used batch. Powder flowability was observed to increase with continuously re-using the powder due to satellites removal and longer exposure of the powder to elevated temperatures, which can decrease moisture content, and consequently, increase the flowability.

While Popov et al. [15] reported a lower fatigue performance for specimens manufactured via EB-PBF 69-times re-used Ti-6Al-4V powder as compared to the ones from unused powder, Carrion et al. [7] observed some improvements in the high cycle fatigue (HCF) behavior of LB-PBF Ti-6Al-4V specimens by heavily re-using the powder. The higher fatigue performance of specimens from re-used powder was due to the fact that cracks initiated from smaller gas-entrapped pores. The existence of less and smaller defects within the specimens fabricated from re-used powder was explained by the combination of better powder flowability and less compressibility of the re-used batch. The improved flowability resulted in a more uniform powder layer on the build plate with fewer and smaller empty spaces within the powder bulk, resulting in lower compressibility, and consequently, smaller defects within the fabricated parts.

In addition, no significant changes in the microstructure and tensile behavior of LB-PBF Ti-6Al-4V parts were observed due to powder re-use [7]. Similar fatigue lives were also obtained for the parts fabricated from unused and re-used powder batches in the as-built surface condition which was explained by the crack initiation from rough surfaces inherent to AM [3,73]. The effect

of re-using 17-4 PH stainless steel (SS) powder in an LB-PBF process and nitrogen atmosphere for 15 and 11 times was investigated in two separate studies [96,129]. While no significant changes in the tensile behavior of parts were observed, it was reported in both studies that the apparent density and flowability of the powder could increase with re-using the powder.

Previous studies reported flowability as an important powder characteristic which can significantly affect the parts mechanical properties [7,129]. Flowability, however, is a complicated characteristic since it is dependent on several other powder characteristics (e.g., particle size, shape, bulk or surface chemistry, etc.) [9]. Therefore, several powder characteristics are often analyzed to illustrate flowability [117,133]. Additionally, powder characteristics can vary across the build plate due to the mechanism of powder distribution in PBF machines (i.e., spreading a powder layer upon the build plate using a recoater/wiper). Such variations in powder characteristics contribute to the complexity of understanding how the powder specification and re-use affect the mechanical performance of parts fabricated by PBF methods. Such powder characteristics can also affect the spreadability of the powder on the build plate; therefore, mechanical properties of parts fabricated in different locations of the build plate may be different [134].

It has been established that re-using powder can significantly alter the powder characteristics. Such variations may, in turn, affect the mechanical properties and challenging the qualification and certification of AM parts, specifically in safety critical applications [123,124]. Therefore, this study investigates the effects of powder re-use on the defect distribution and mechanical properties including tensile and fatigue behavior of parts fabricated from 17-4 PH SS via LB-PBF. In addition, the location of AM parts on the same build plate may contribute to variations in the final microstructural characteristics as well as mechanical performance of parts fabricated via LB-PBF.

Hence, the location dependency of LB-PBF parts and how re-using the powder may affect this location dependency will also be evaluated in this study.

4.2. Experimental Program

In this study, argon-atomized 17-4 PH SS powder produced from LPW Technology Ltd. was used. The initial particle size distribution (PSD) was reported by the manufacturer to be between 15 and 45 μm. The chemical composition of the powder provided by the manufacturer is reported in Table 11. The study was started with an initial amount of 80 kg to guarantee 15 consecutive builds. After each fabrication, all the powder was collected from the overflow bin and build envelope and filtered through an 80-μm sieve to ensure the removal of spatters and breaking down of agglomerates. After sieving, all the powder was thoroughly mixed with the unused powder in the feed bin and a sample was taken at equal increments throughout the depth of the powder according to ASTM B215 [55] standard for powder characterizations.

Table 11. Chemical composition of the argon-atomized 17-4 PH SS provided by LPW Technology Ltd.

Elements	**C**	**Cr**	**Ni**	**Cu**	**Mn**	**Si**	**Nb**	**Mo**	**N**	**O**	**P**	**S**	**Fe**
Wt. %	0.01	16.3	4.18	4.1	0.22	0.4	0.25	0.02	0.04	0.05	0.012	0.004	Bal.

Two different layouts, defined as full and half, were designed (see Fig. 31(a) and (b)). The full layout was used for batches 1, 5, 10 and 15, while the half layout was used for the interval builds (i.e., batches 2, 3, 4, 6, 7, 8, 9, 11, 12, 13, and 14). The full layout contained 38 specimens including net-shape round specimens with a uniform gage section according to ASTM E606 [135] (see Fig. 32(a)), 11-mm square rods to be further machined to the final shape and geometry of round specimens with uniform gage section based on ASTM E606, and round tension test specimens for tensile testing according to ASTM E8 [53] (see Fig. 32(b)). The maximum testing strain was selected to be 0.004 mm/mm; therefore, the risk of buckling under compression portion

of fully reversed loading was very small. This allowed the diameter of round specimens with uniform gage section to be reduced from the standard recommended 6.25 mm to 5 mm to save in material and ensure completion of 15 builds.

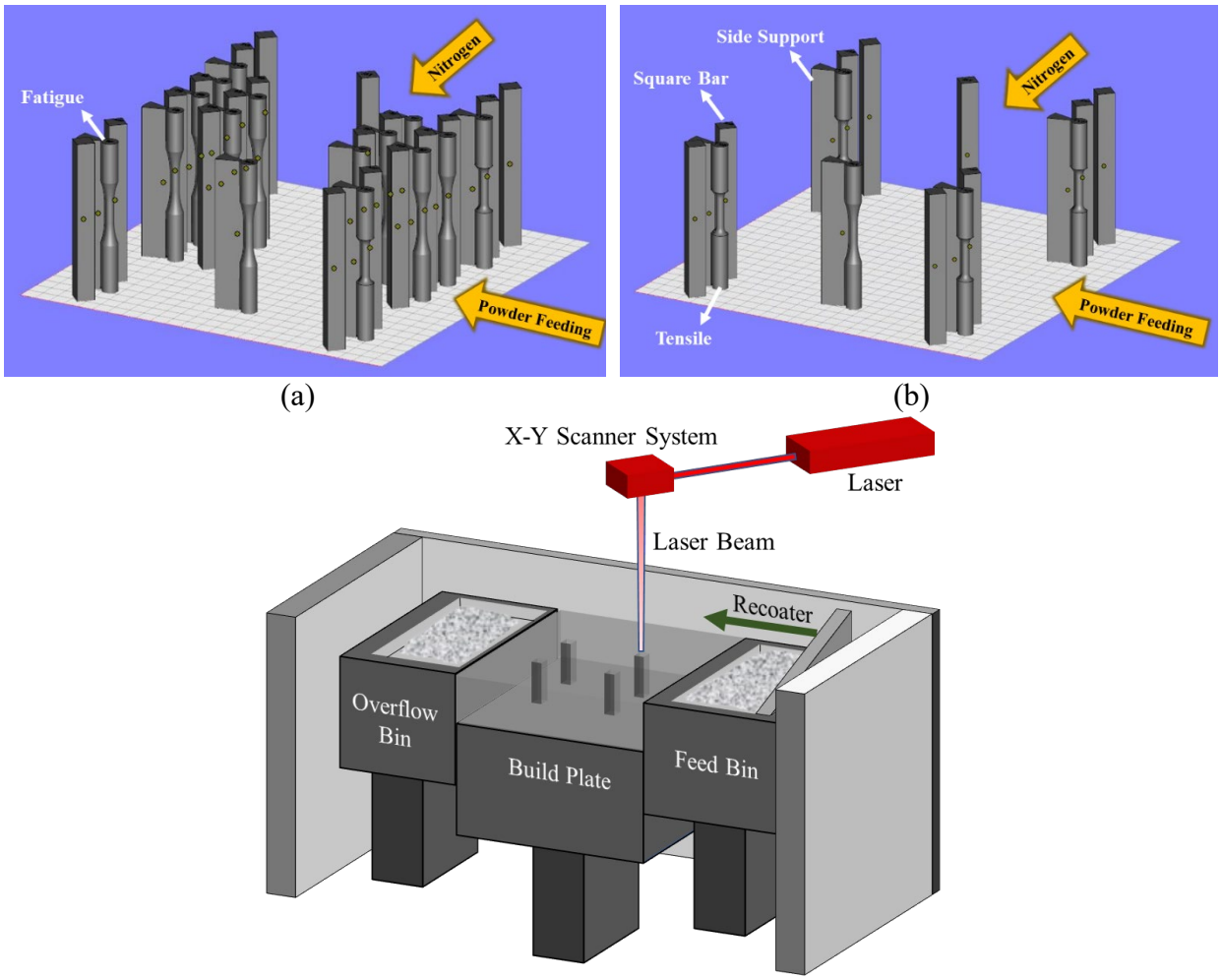

Fig. 31 (a) Full print layout used for Batch 1 (unused), Batch 5 (re-used 4 times), Batch 10 (re-used 9 times) and Batch 15 (re-used 14 times), (b) half print layout used for interval prints, and (c) a schematic of laser beam powder bed fusion (LB-PBF) system.

Side supports were fabricated in conjunction with the net-shape specimens (see Fig. 31(a) and (b)) to prevent deflection during contact with the recoater, and thus, disturbance of the powder near the specimens. The number of specimens on the half layouts was lowered from 38 to 18 specimens. Approximately 2.5 kg and 1.5 kg powder amounts were used for the fabrication of each

full and half print layouts, respectively. Most specimens were located on two ends of the build plate. Front specimens were closer to the feed bin and back specimens were further away from the feed bin (see Fig. 31(c)). This front and back specimen layout was designed in order to study the effects of part location upon the build plate on the final mechanical properties. Although there were two specimens located in the middle section of the build plate in both layouts, they were not used in this study.

All builds were fabricated using an EOS M290 machine in a nitrogen atmosphere with the manufacturer recommended 17-4 PH SS performance process parameters, reported in Table 12. All the specimens were subjected to CA-H1025 heat treatment. This heat treatment consists of solution treatment at 1050 ˚C for 30 minutes, air cooling to room temperature, with a subsequent aging at 552 ˚C for 4 hours and air cooling to room temperature. This heat treatment was selected since it was shown to be effective in homogenizing the microstructure and improving the fatigue performance of LB-PBF 17-4 PH SS specimens [136]. Net-shape round specimens were tested after heat treatment without any further surface treatments; therefore, they are referred to as as-built specimens in this study. However, the square rods were machined to the final specimen dimensions, as shown in Fig. 32(a), followed by further surface polishing to achieve R_a= 0.5-0.6 µm , and are referred to as machined specimens.

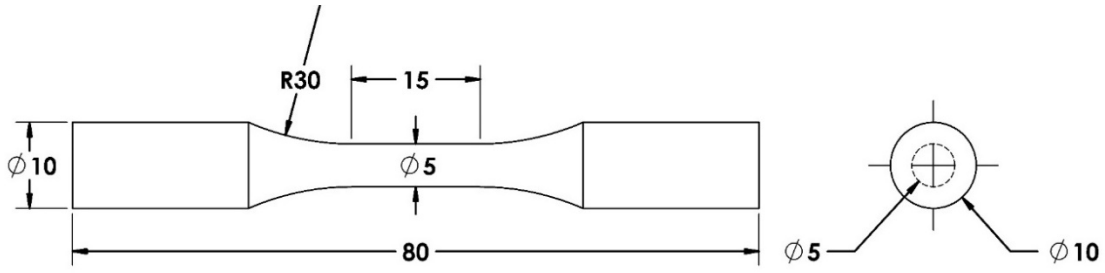

(a)

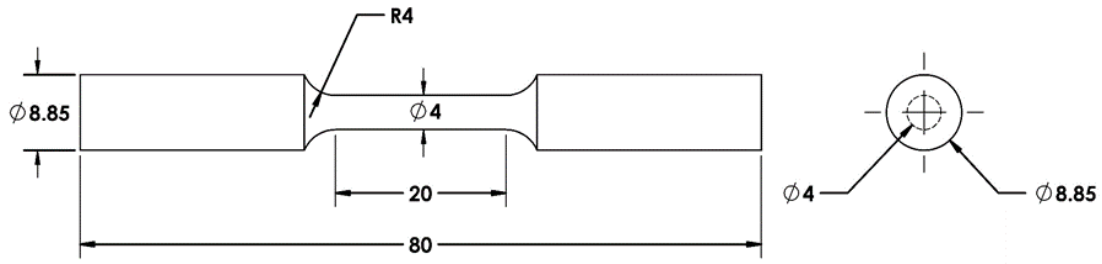

(b)

Fig. 32 (a) Round specimens with a uniform gage section for strain-controlled fatigue testing according to ASTM E606 [135], and (b) round tension test specimens for tensile testing according to ASTM E8 [53] (all dimensions are in mm).

Table 12. EOS recommended major process parameters utilized to fabricate LB-PBF 17-4 PH SS parts.

Laser power	**Scanning speed**	**Hatch distance**	**Layer thickness**	**Layer rotation angle**	**Stripe width**
220 W	755.5 mm/s	100 µm	40 µm	67°	100 mm

Powder characteristics including apparent and tapped density (i.e., the density when the powder is compacted), compressibility, shear stress [57], and cohesion were evaluated using Freeman Technology FT4 rheometer. PSD and shape morphology were analyzed via Malvern Morphology G3SE by static image analysis according to ASTM E2651 [137]. Particle shape parameters including circular equivalent (CE) diameter (i.e., the diameter of a circle with the same area as the particle's projected area on the normal plane [138]), circularity (defined as circle equivalent perimeter divided by the actual perimeter), and elongation (i.e., 1-width/length) were also measured. The powder shape morphology was also obtained with scanning electron microscopy (SEM) in order to compare unused and re-used powder batches. In this paper, the powder samples used for the full layouts are categorized into Batch 1 (i.e., unused), Batch 5 (re-used 4 times), Batch 10 (re-used 9 times), and Batch 15 (re-used 14 times).

Quasi-static tensile tests were performed via an MTS servo-hydraulic load frame with a 100 kN capacity according to ASTM E8 [53] on three specimens at a strain rate of 0.001 s^{-1}. Strain-controlled tensile tests were performed up to 0.045 mm/mm, followed by extensometer removal, and continued in displacement control until specimen failure. Fully reversed strain-controlled fatigue tests ($R_\varepsilon = -1$) according to ASTM E606 [135] were conducted on as-built specimens at two different strain amplitudes, ε_a, of 0.004 mm/mm and 0.002 mm/mm to study low and high cycle fatigue regimes, respectively. Strain amplitudes of 0.0025 mm/mm, 0.003 mm/mm, and 0.004 mm/mm in fully reversed condition ($R_\varepsilon = -1$) were used for machined specimens to evaluate their high, intermediate (or mid), and low cycle fatigue regime behaviors, respectively. In this study, low cycle fatigue (LCF) and high cycle fatigue (HCF) regimes are associated with high and low strain amplitudes. At least, two specimens were tested at each strain level to check the repeatability of the results. The frequency at each strain level was adjusted to maintain similar average cyclic strain rates among all tests to minimize any variations due to strain dependent deformation effects.

Fracture surfaces were analyzed via a Keyence VHX-6000 digital microscope to investigate the shape and size of the crack initiation sites. In addition, porosity measurements were carried out by serial cross-section analysis of specimens from Batch 1 and Batch 15 and analyzed using the Keyence VHX-6000 digital microscope at 500X to compare the porosity of the produced parts. Surface roughness of the specimens was also measured using Mahr MFW-250, which consists of a stylus instrument traversing perpendicular to the surface at constant speed to measure the surface profile for calculating the roughness parameters.

4.3. Experimental Results

4.3.1. Powder Characteristics

One of the most important characteristics of the powder particles is their size and shape morphology which may affect physical properties of the powder such as flowability. The PSD diagrams of Batches 1, 5, 10 and 15 are shown in Fig. 33. An enhanced view of PSD for finer particles (smaller than 15 μm) is also included. Although the variation in PSD between powder batches does not appear to be significant, powder re-use results in the PSD diagram to become somewhat narrower (the width of PSD was 45 μm for Batch 1 and 41 μm for Batch 15) and the circular equivalent (CE) diameter slightly decreases with continued powder re-use (it was measured as 30.8 μm for Batch 1 and 28.4 μm for Batch 15).

The difference in CE diameters can be related to the sieving and manufacturing processes. The large agglomerates can get detached or break down by the filtration. The reduction of large agglomerates was verified by D_{90} measurement which gives the particle size below which 90% of the sample lies [10]. The D_{90} was measured to decrease from 43.40 μm in Batch 1 to 40.20 μm in Batch 15. Very fine particles can also spatter (be ejected) from the build plate when the laser scans that area and/or they may be included in the melting and subsequent solidifying process [7]. The number of very fine particles (smaller than 15 μm) was found to decrease with re-using the powder from 9% to 6% of the powder samples. Therefore, as the satellites are shed from the agglomerates, the CE diameter will become more representative of the parent particle rather than the cluster of particles. Powder flowability and packing state may improve by the reduction of very fine particles and large agglomerate due to relatively high interparticle frictional forces of fine particles and void spaces between agglomerates [7,10,13].

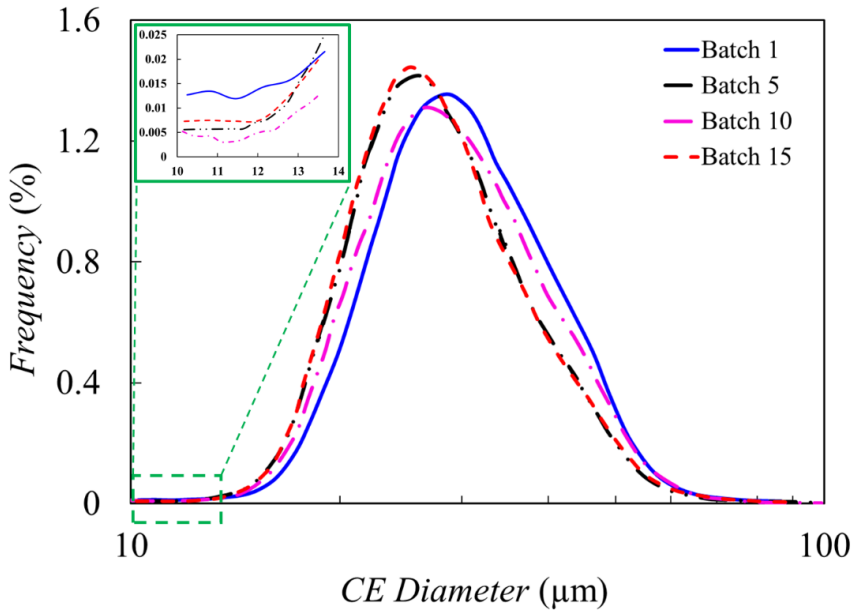

Fig. 33 Particle size distribution (PSD) of Batch 1 (unused), Batch 5 (re-used 4 times), Batch 10 (re-used 9 times), and Batch 15 (re-used 14 times) showing the PSD becomes slightly narrower and shifts to the left by re-using the powder.

The shape morphology of powder particles captured via SEM is shown in Fig. 34. No apparent change in shape can be observed as a result of continuous powder re-use. It can also be observed that most particles remained spherical after re-using the powder. This was verified by measuring the particles' circularity which was comparable for all the powder batches (0.87-0.88). Elongated particles can cause friction between particles which may impede the flow [10]. Therefore, having less elongated particles in the powder batch can contribute toward a better powder flowability. Needles have elongation (1-width/length) values approaching to 1. The particles' elongation was measured to be 0.20 for Batch 1 and 0.19 for Batch 15. Hence, no effect of re-using the powder on elongation was found in this study.

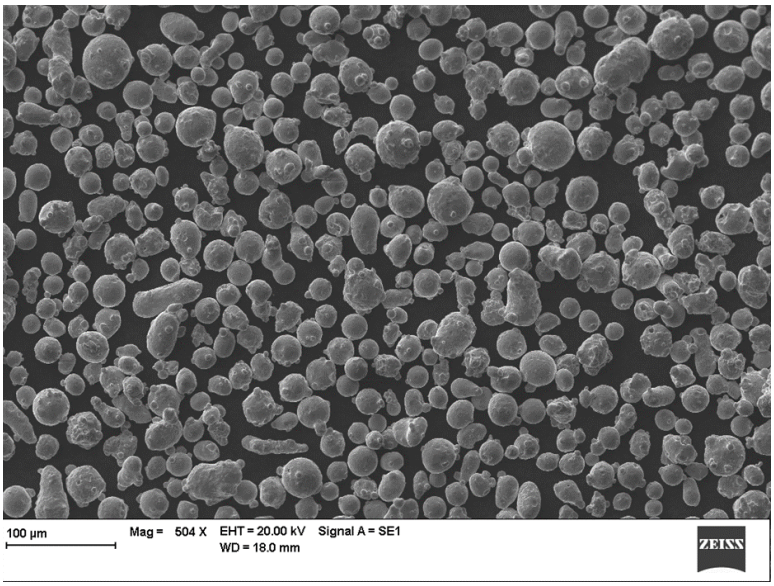

(a)

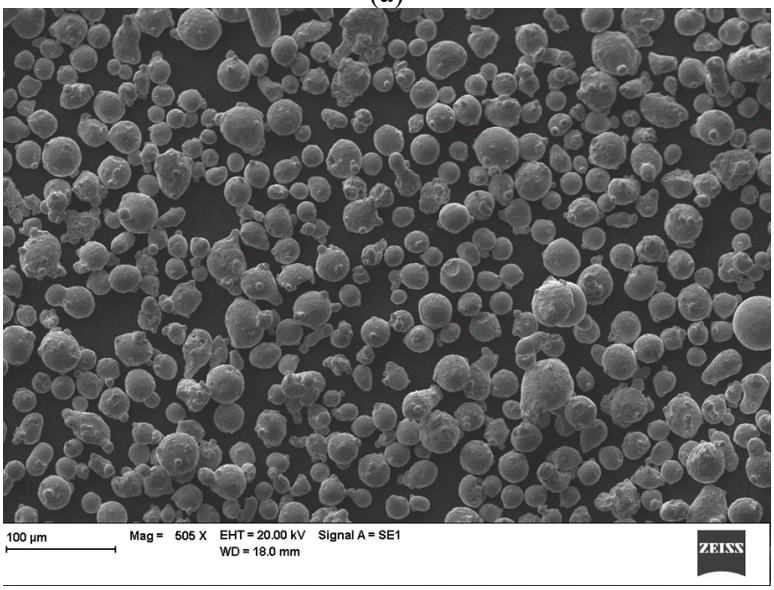

(b)

Fig. 34 Powder shape morphology for (a) Batch 1 and (b) Batch 15 obtained via SEM.

Apparent/bulk and tapped density values of the powder batches have been listed in Table 13. The bulk density shows an increase with continuous powder re-use. Tapped density was also increased slightly with re-using the powder. The increase in bulk and tapped densities can be due to existence of fewer agglomerates in the re-used powder batch resulting in less empty spaces within the powder batch. It should be noted that although finer particles can fill in the void/empty spaces between the larger particles [10], they may also adhere to large particles due to their larger

interparticle frictional forces and cohesivity [7], form more agglomerates, and leave void spaces in the powder bulk. As a result, the larger apparent and tapped density values of the re-used powder batches can be due to a more uniform particle size distribution and better packing state.

The existence of more void spaces within the powder bulk can lead to more gas entrapment during melting/solidification, which can form gas-entrapped pores in the material during melting/solidification process. The compressibility of a powder bulk can increase due to more void spaces between the powder particles. Hence, the compressibility of all batches was measured, and it was observed that the compressibility of Batch 1 was 4.65 % compared with 1.97 % for Batch 15. This means that Batch 1 is more compressible. The higher sensitivity of Batch 1 to compression can indicate the existence of more void spaces within the Batch 1 powder bulk. As a result, it may be postulated that the existence of more agglomerates and very fine particles, and subsequently, higher cohesion within Batch 1 can result in more empty spaces entrapped within the powder bulk [7,10].

Table 13. Apparent/bulk and tapped density values of Batches 1, 5, 10, and 15.

Powder batch	**Batch 1**	**Batch 5**	**Batch 10**	**Batch 15**
Bulk density (g/ml)	3.87	4.03	4.14	4.19
Tapped density (g/ml)	4.37	4.38	4.40	4.44

To verify this understanding, permeability of different powder batches was quantified. Permeability indicates how easily a gas (i.e., nitrogen) can flow through a material (i.e., powder) [138]. Permeability is inversely correlated with pressure drop due to applied normal stresses on the powder bulk [7,138]. This means that powder with a greater pressure drop is the least permeable one. As seen in Fig. 35, pressure drop in Batch 15 is higher than all the other batches. This may imply that the Batch 15 is the least permeable powder. As it was explained by the differences in compressibility values between different powder batches, nitrogen gas can flow

more easily within Batch 1 and least easily within Batch 15. The higher permeability of nitrogen within Batch 1 is mainly due to more empty spaces and less barriers due to agglomerations existence within the powder batch, which leads to a relatively smaller pressure drop (see Fig. 35), less apparent and tapped densities (see Table 13), and more compressibility. However, in Batch 15, with less agglomerates, there are fewer empty spaces, and therefore, gas has more difficulties going through the powder batch, which in turn increases the pressure drop.

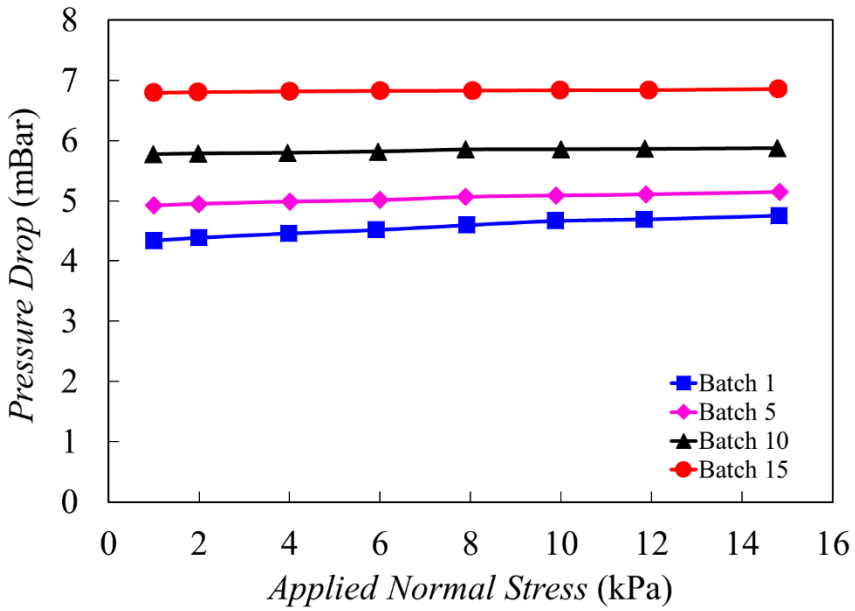

Fig. 35 Pressure drop versus applied normal stress on the powder bulk for Batches 1, 5, 10, and 15 showing the highest pressure drop for Batch 15 and the lowest for Batch 1.

A method to show the higher cohesion and interparticle frictional forces within Batch 1 compared with other batches is to perform shear cell test. In shear cell test, powder is sheared to obtain its shear strength properties [139]. Higher shear strength represents higher resistance for powder to flow [138], and thus, less flowability resulting in less uniform powder distribution on the build plate. Shear cell tests were performed according to ASTM D7891 [57] at applied normal stresses up to 2 kPa. It can be observed from Fig. 36 that Batch 1 has the highest shear stress under different normal stress levels. Additionally, the cohesion within each powder batch was measured to be 0.250 kPa for Batch 1 compared with 0.128, 0.158, and 0.160 kPa respectively for Batches

5, 10, and 15. This shows that at a constant applied normal stress (e.g., powder stored in the feed bin can experience a consolidation stress), Batch 1 requires more shear stress in order to flow due to higher cohesivity.

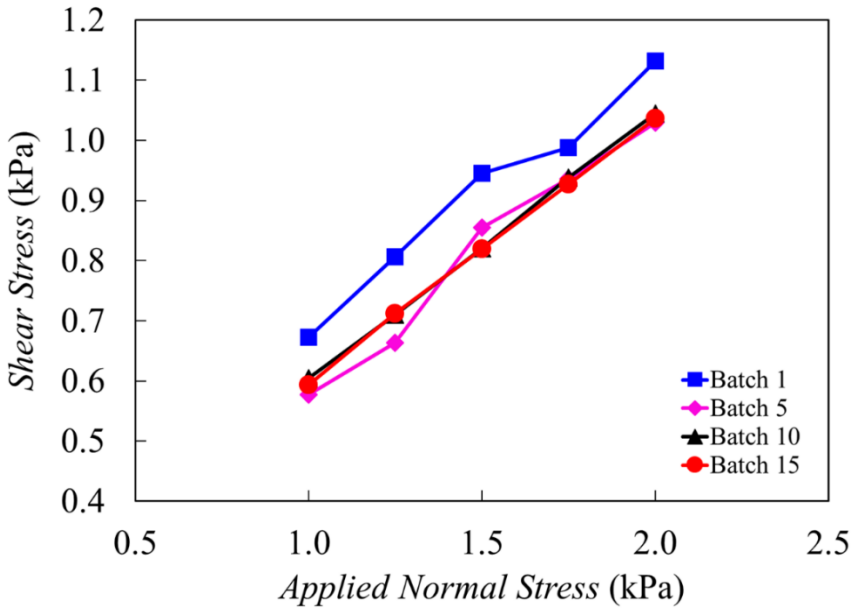

Fig. 36 Shear stress versus applied normal stress on the powder bulk for Batches 1, 5, 10, and 15 showing a higher shear stress for Batch 1 as compared to the other batches.

4.3.2. Porosity within the Fabricated Parts

Pores at the gage section of representative specimens fabricated from Batch 1 (i.e., unused) and Batch 15 (i.e., re-used 14 times), one from the front and one from the back of the build plate, were measured via digital microscopy and their size distributions are presented in Fig. 37. Porosity measurements were conducted on three different cross sections at the gage of each representative specimen. Pores with diameters smaller than 5 µm were disregarded from this analysis since they have relatively small probabilities to initiate a fatigue crack considering the maximum pore sizes observed. The average and maximum pore diameters for the specimen from Batch 1 (see Fig. 37 (a)) in front were found to be 9.4 and 26.6 µm, respectively. Similar analysis on the gage section of a specimen from Batch 1 in back (see Fig. 37 (b)) resulted in average and maximum pore dimeters of 10.4 and 33.7 µm.

The number of pores was also obtained and found to be relatively higher for the specimen in back compared with the front one (~14% increase). Comparable procedures were also performed on specimens from Batch 15 in front and back (see Fig. 37(c) and (d)). It was found that the number of pores was relatively lower for the specimen in back by 5%. However, the average and maximum pore diameters were still larger in the specimen from Batch 15 in back compared with the specimen in front. The average and maximum pore diameters were 9.2 and 24 μm for the specimen in front and 9.8 and 29.8 μm for the specimen in back. It should be noted that the number of pores reported is the average of the number of pores found on each section. It is also worth noting that the maximum pore size reported in Fig. 37 is the maximum found on the 3 sections cut from each specimen and does not necessarily represent the maximum pore size in the specimen.

It can be concluded that the pore sizes are relatively larger for the specimens fabricated from Batch 1 compared with the counterparts from Batch 15. The decrease in pore sizes of specimens fabricated from re-used powder can be related to the lower compressibility, and consequently, the better packing state of re-used powder compared with the unused powder which results in denser parts. In addition, the number and size of pores for the unused powder specimen in back were relatively larger than the specimen in front. However, the differences between the number and size of pores in front and back specimens were decreased with continuously re-using the powder which indicates more layer uniformity of re-used powder. Hence, it can be assumed that powder flowability improved by continuous powder re-use, which resulted in the reduction of finer particles and agglomerates, as discussed in the previous section.

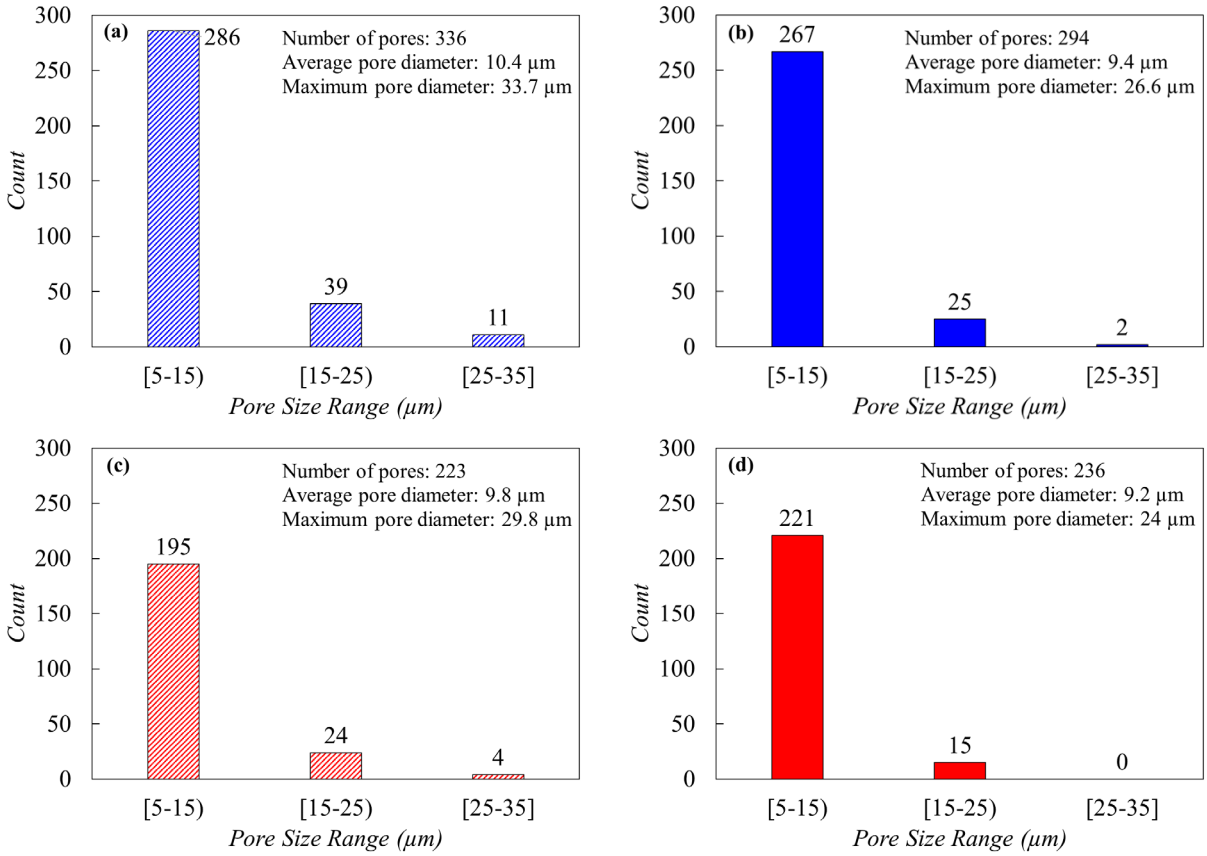

Fig. 37 Pore size distribution obtained from multiple cross sections at the gage of the specimens from (a) Batch 1 in back, (b) Batch 1 in front, (c) Batch 15 in back, and (d) Batch 15 in front.

4.3.3. Tensile Behavior

Tensile behavior of LB-PBF 17-4 PH SS specimens fabricated from Batches 1, 5, 10, and 15 from different locations (one from back and two from front for each batch) in as-built condition is shown via engineering stress versus engineering strain and engineering stress versus displacement curves in Fig. 38(a) and (b), respectively. One curve for each batch is presented in these figures due to negligible changes on tensile behavior as a result of specimen's location on the build plate. As seen in Fig. 8, no significant effect on tensile properties including UTS and YS was observed due to powder re-use either. The UTS was found to remain comparable around 1203 MPa for Batch 1 and 1193 MPa for Batch 15 [129]. The YS was also measured according to 0.2% offset

approach, and it was found to be 1155 and 1138 MPa for Batch 1 and 15, respectively. It should be noted that the tensile properties were obtained from the previous work of authors [129].

True fracture strain, ε_f, was also measured by $ln(\frac{A_0}{A_f})$, in which A_0 and A_f are initial and fracture cross-sectional areas of the gage [71]. The true fracture strain was found to be 0.35 and 0.40 for specimens fabricated from Batch 1 and 15, respectively, showing relatively higher ductility with continuously re-using the powder which can be related to the lower porosity in specimens from re-used powder. Since no difference in microstructure of the specimens fabricated from unused and re-used powder was expected due to powder re-use and heat treatment [7,136], changes in material strength were expected to be negligible. A summary of the main tensile properties is provided in Table 14.

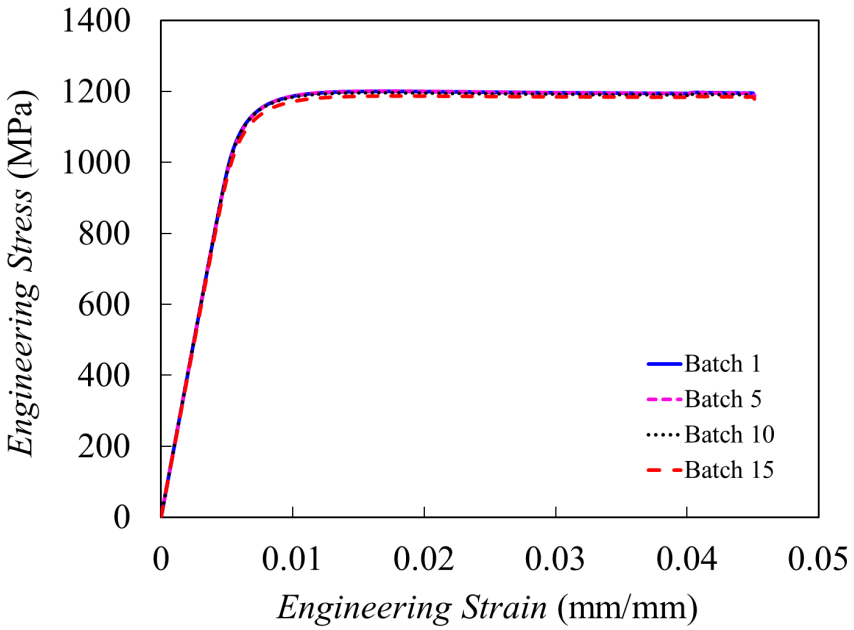

(a)

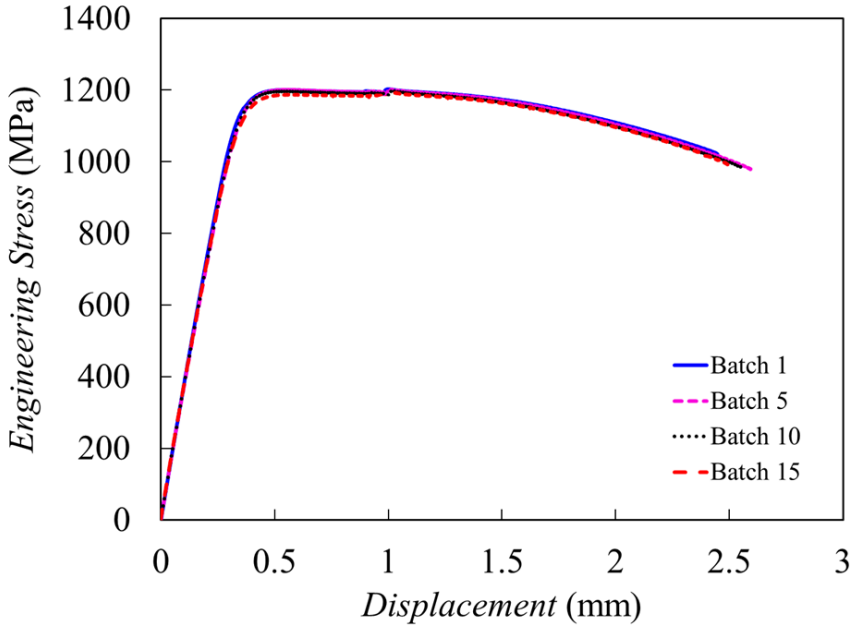

(b)

Fig. 38 Tensile behavior of LB-PBF CA-H1025 17-4 PH SS specimens fabricated from Batches 1, 5, 10, and 15 in the as-built surface condition: (a) engineering stress-strain and (b) engineering stress-displacement curves adapted from [129].

Table 14. LB-PBF CA-H1025 17-4 PH SS tensile properties obtained from as-built specimens [129].

Batch	***UTS* (MPa)**	***YS* (MPa)**	**ε_f (mm/mm)**
1	1203	1155	0.35
5	1201	1151	0.42
10	1198	1156	0.44
15	1193	1138	0.40

4.3.4. Fatigue Behavior

Strain-controlled fully reversed ($R_\varepsilon = -1$) tests were performed on both as-built and machined specimens fabricated from unused and re-used powder batches. The effect of specimen location on the build plate on the fatigue behavior was also investigated by comparing samples from the same batch, however, with different locations; i.e., front or back. A summary of strain-controlled fatigue test results for specimens fabricated from 17-4 PH SS via LB-PBF in as-built and machined conditions and heat treated utilizing CA-H1025 procedure is presented in Table 15 and Table 16, respectively. Results are categorized for different batches and from two different

locations (i.e., front versus back). Cyclic modulus of elasticity of the stable cycle, E', strain amplitude, ε_a, mid-life stress amplitude, σ_a, and mean stress, σ_m, as well as number of reversals to failure, $2N_f$, are included in Table 15 and Table 16. It is important to mention that no substantial plastic deformation occurred for any of the LB-PBF 17-4 PH SS specimens in this study.

Table 15. Strain-controlled fully reversed fatigue test results obtained from LB-PBF CA-H1025 17-4 PH SS specimens in as-built surface condition.

Surface condition	Location	E' (GPa)	ε_a (mm/mm)	σ_a (MPa)	σ_m (MPa)	$2N_f$ (Reversals)
Batch 1						
As-built	Back	194	0.0040	797	44	6,154
As-built	Front	198	0.0040	801	-5	9,844
As-built	Front	201	0.0020	407	-5	174,348
As-built	Back	199	0.0020	401	-3	200,654
As-built	Back	201	0.0020	405	-5	203,878
Batch 5						
As-built	Front	196	0.0040	801	-11	10,178
As-built	Back	196	0.0040	801	-8	10,480
As-built	Front	188	0.0020	382	-2	58,550
As-built	Front	201	0.0020	407	4	62,434
As-built	Back	199	0.0020	403	-4	98,038
As-built	Front	199	0.0020	401	-1	191,532
Batch 10						
As-built	Back	196	0.0040	793	-4	9,370
As-built	Front	196	0.0040	797	-4	11,150
As-built	Front	199	0.0020	401	4	75,996
As-built	Front	198	0.0020	402	-1	117,696
As-built	Back	198	0.0020	398	-2	209,518
Batch 15						
As-built	Back	196	0.0040	797	-1	12,982
As-built	Front	197	0.0040	801	-10	13,450
As-built	Front	200	0.0020	400	-3	97,847
As-built	Front	200	0.0020	403	-5	230,788
As-built	Back	199	0.0020	401	-1	235,294

Table 16. Strain-controlled fully reversed fatigue test results obtained from LB-PBF CA-H1025 17-4 PH SS specimens in machined surface condition.

Surface condition	Location	E' (GPa)	ε_a (mm/mm)	σ_a (MPa)	σ_m (MPa)	$2N_f$ (Reversals)
Batch 1						
Machined	Back	200	0.0040	812	17	10,564
Machined	Back	201	0.0040	811	-9	14,146
Machined	Front	200	0.0040	814	-16	63,300
Machined	Front	199	0.0040	805	-14	69,988
Machined	Back	199	0.0030	603	-4	76,638
Machined	Back	203	0.0030	612	-3	97,828
Machined	Back	205	0.0025	512	11	100,492
Machined	Back	205	0.0025	518	-41	193,634
Machined	Front	201	0.0030	609	-1	287,624
Machined	Front	197	0.0030	603	-24	459,082
Machined	Front	203	0.0025	510	-6	1,747,292
Machined	Front	201	0.0025	508	12	9,194,508
Batch 15						
Machined	Back	196	0.0040	801	-14	24,978
Machined	Back	202	0.0040	826	-33	31,044
Machined	Front	203	0.0040	823	10	59,298
Machined	Front	204	0.0040	823	-11	66,154
Machined	Back	204	0.0030	619	-2	118,476
Machined	Front	203	0.0030	615	1	119,494
Machined	Back	199	0.0030	599	-2	150,470
Machined	Front	205	0.0030	621	15	304,992
Machined	Back	203	0.0025	514	18	4,523,250
Machined	Back	199	0.0025	505	1	6,379,896
Machined	Front	202	0.0025	508	-4	15,084,902
Machined	Front	202	0.0025	510	-16	18,417,542

Strain-life comparison of specimens in the as-built condition form different batches is shown in Fig. 39. Fatigue lives are presented on a semi-log plot with strain amplitude, ε_a, on Y axis and number of reversals to failure, $2N_f$, on X axis. Specimens were tested in two different strain levels. As seen in Fig. 39, no effect of powder re-use was observed on the fatigue life of specimens with as-built surface condition. In addition, no effects of location (i.e., front versus back location) on fatigue life of LB-PBF specimens in the as-built surface condition can be observed from this figure. Therefore, no specific trend in fatigue life as a result of re-using the powder nor location was observed when specimens were kept in their as-built surface condition.

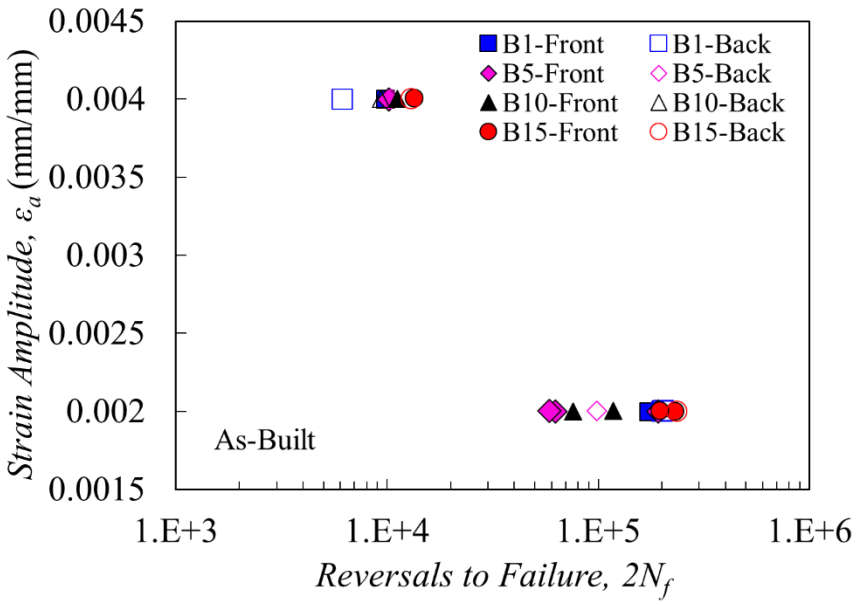

Fig. 39 Strain-life fatigue behavior of LB-PBF CA-H1025 17-4 PH SS specimens in the as-built surface condition fabricated from Batch 1 (B1), Batch 5 (B5), Batch 10 (B10), and Batch 15 (B15) in front and back locations.

Strain-life fatigue behavior comparison of LB-PBF CA-H1025 17-4 PH SS specimens from Batch 1 and Batch 15 fabricated in front location (i.e., closer to the feed bin) and in machined surface condition is shown in Fig. 40(a). Due to the stochastic nature of the defect size and number in the specimens, the fatigue lives show greater scatter in the machined surface condition as compared to the as-built surface condition. It can be seen that continuously re-using the powder did not affect the fatigue behavior in low cycle fatigue (LCF) and mid cycle fatigue (MCF) regimes. In the high cycle fatigue (HCF) regime, however, a gap between fatigue lives of machined specimens fabricated from Batch 1 and Batch 15 can be observed. In this regime, fatigue life appears to be improved by re-using the powder. A similar trend was also observed in Fig. 40 (b) for the machined specimens fabricated from Batch 1 and 15 in the back location (i.e., further away from the feed bin). As shown in Fig. 40 (b), the variation between the results is not significant in LCF and MCF regimes, although it can be seen that specimens fabricated from Batch 15 had slightly longer fatigue lives compared with the ones from Batch 1. However, the HCF lives were

improved by continuously re-using the powder. In addition, the difference observed in the HCF data between specimens fabricated by unused and re-used powder batches in the back location was more significant as compared to the counterparts from front location (compare Fig. 40(a) and (b)).

The effect of part location on the build plate on the fatigue lives of LB-PBF CA-H1025 17-4 PH SS machined specimens is shown in Fig. 41(a) and (b), respectively for Batch 1 and Batch 15. The effect of powder re-use on the fatigue behavior of specimen is ruled out by considering the specimens from the same batch but different locations. As it can be observed from Fig. 41(a) and (b), the fatigue lives of specimens from front location are relatively greater than the ones from back location, independent of strain level. It can be observed from Fig. 41(b) that the gap between fatigue lives of front and back location specimens was reduced with continuous re-use of the powder. It may be presumed that specimens from front location consistently have a greater fatigue life compared with the ones from back location; however, such differences are reduced by re-using the powder.

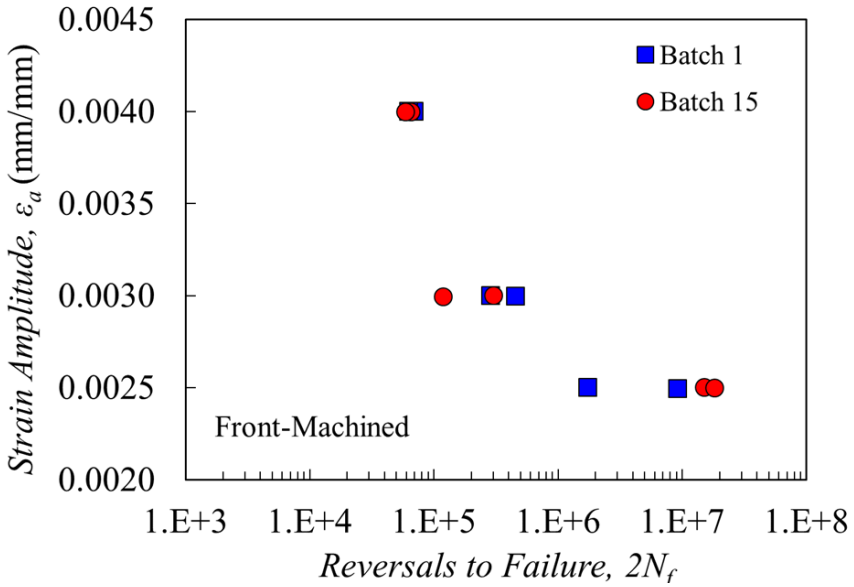

(a)

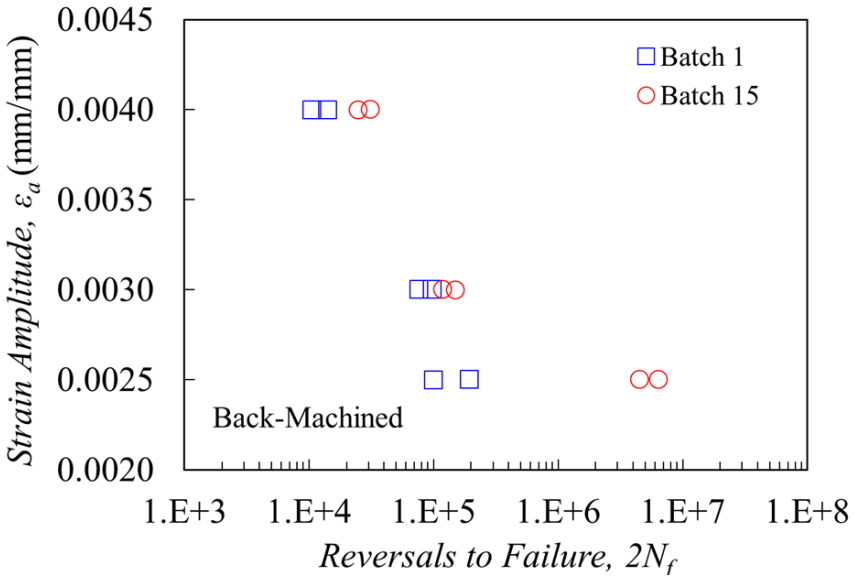

(b)

Fig. 40 Strain-life fatigue behavior of LB-PBF CA-H1025 17-4 PH SS specimens in machined surface condition fabricated from Batch 1 and Batch 15 in (a) front and (b) back locations.

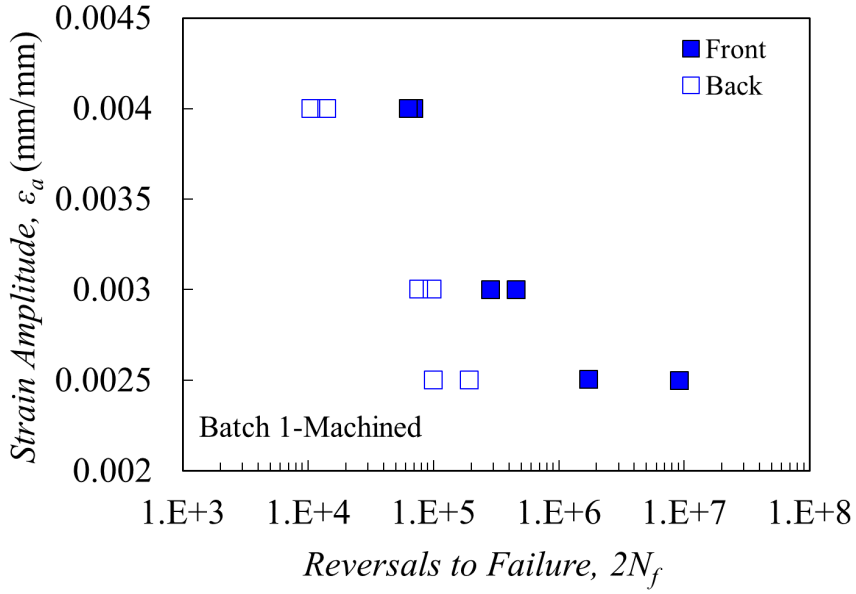

(a)

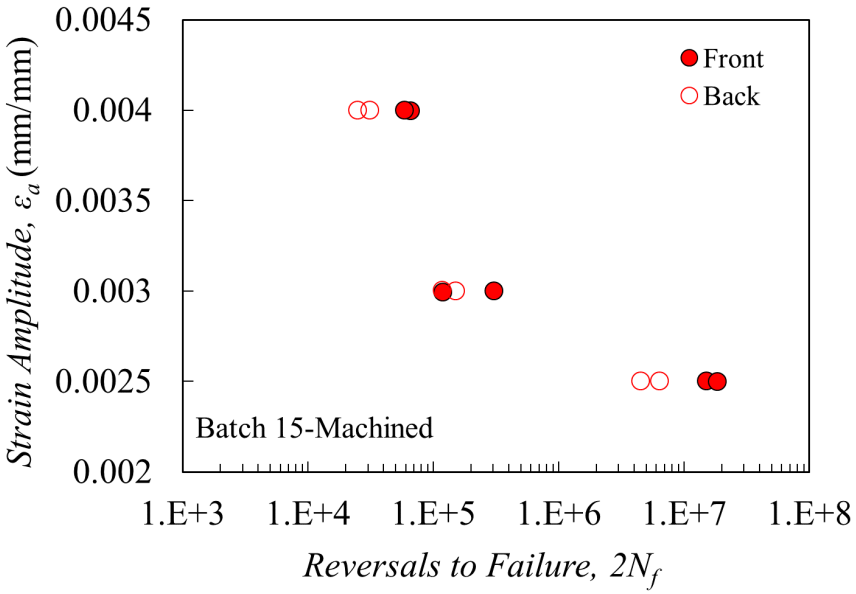

(b)

Fig. 41 Strain-life fatigue behavior of LB-PBF CA-H1025 17-4 PH SS specimens in machined surface condition fabricated from (a) Batch 1 and (b) Batch 15 in front and back locations.

4.3.5. Failure Analysis

Fractography analysis via digital microscopy was performed on the fracture surfaces of as-built and machined specimens from different locations. It was observed that in all as-built specimens, cracks started from the micro notches on the surface of the specimens due to rough surfaces inherent to the LB-PBF process. This was consistent for specimens from different batches

regardless of the powder re-using iteration or specimen location. Fracture surface of an as-built specimen fabricated from Batch 1 in front and tested at ε_a =0.004 mm/mm with 9,844 reversals to failure is shown in Fig. 42(a). A focused view of the fracture surface is also presented in the excised area. As shown in this figure, cracks have initiated from multiple locations and even different layers (shown by white arrows), propagated, coalesced to form a larger crack and continued to propagate until the part failed.

The fracture surface of a Batch 1 counterpart from the back location at ε_a =0.004 mm/mm with 6,154 reversals to failure is shown in Fig. 42(b). A similar trend was observed that cracks initiated from multiple locations at different layers and coalesced before final part failure. In Fig. 42(c), a specimen fabricated from Batch 15 and front location at ε_a =0.004 mm/mm is shown with 13,450 reversals to failure. Although this specimen had a longer fatigue life compared with its counterpart from Batch 1 at the same strain level, a similar trend in fatigue failure was observed in which cracks initiated from multiple locations and different layers. Similar failure mechanism was also observed for the specimens tested at ε_a =0.002 mm/mm. All cracks initiated from multiple locations on the surface, although there was more scatter in data at this strain level.

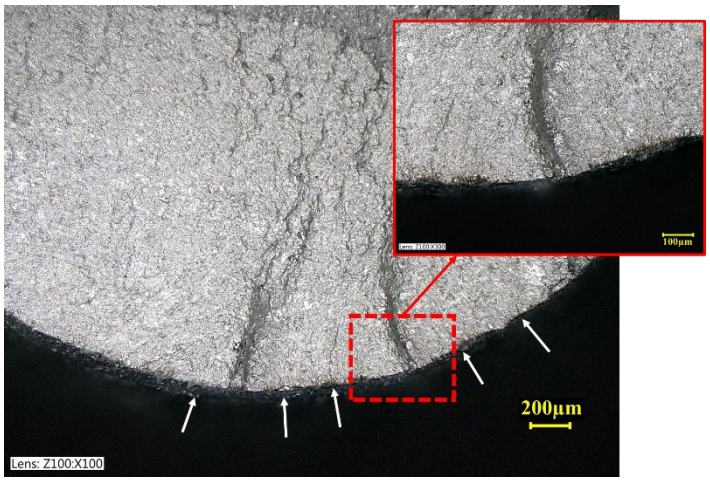

(a)

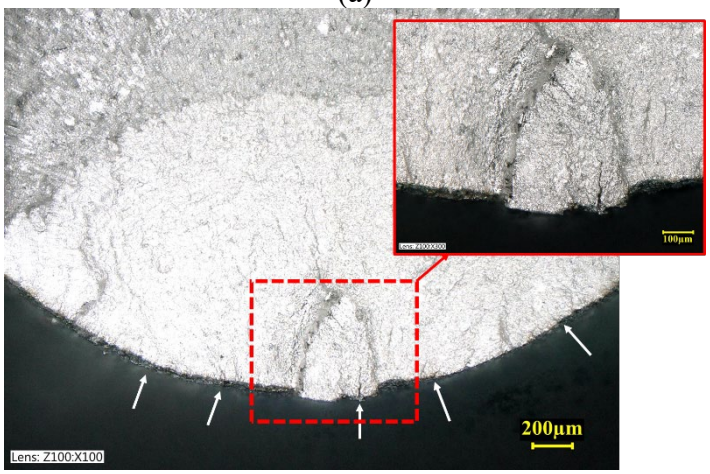

(b)

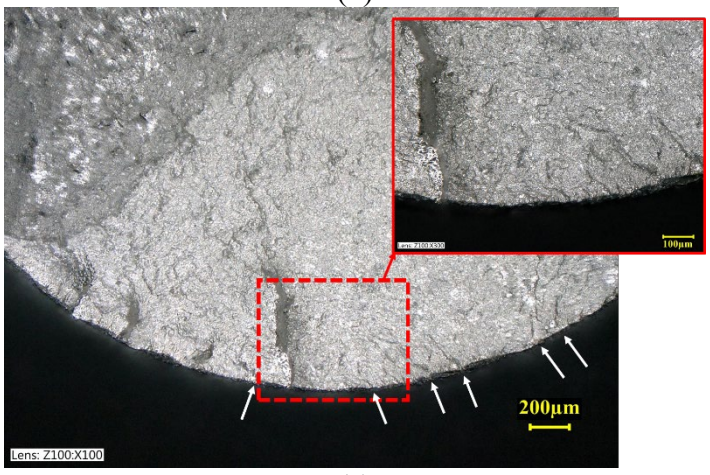

(c)

Fig. 42 Fracture surfaces of LB-PBF CA-H1025 17-4 PH SS specimens in as-built surface condition from (a) Batch 1 and front with 9,844 reversals to failure, (b) Batch 1 and back with 6,154 reversals to failure, and (c) Batch 15 and front with 13,450 reversals to failure, all tested at 0.004 mm/mm strain amplitude.

A comparable procedure was performed for specimens in the machined surface condition from different locations and powder batches to analyze their fracture surfaces. It was observed that cracks usually started from internal pores or the pores that were brought closer to the surface due to machining. As seen in Fig. 13(a), cracks initiated from two gas-entrapped pores close to the surface of a specimen fabricated from Batch 1 in front with 1,747,292 reversals to failure at ε_a =0.0025 mm/mm. The crack initiation site is illustrated with white arrow. A close-up of the crack initiation site is also shown in the same figure detailing the characteristics of the defects associated with crack initiation. In the close-up, it can be observed that the crack initiated from the two gas-entrapped pores with spherical shape and in proximity of each other which were brought close to the surface by machining.

Fig. 43(b) shows a specimen from the same powder batch however from the back location and 100,492 reversals to failure at the same strain amplitude of ε_a =0.0025 mm/mm. Cracks were observed to be initiated from a lack-of-fusion (LoF) defect shown by white arrow which was brought to the surface by machining. Additionally, multiple LoF defects were observed on the fracture surface of this specimen which are shown by yellow arrows. Interestingly, no LoF defect was found during the porosity analysis for which the results are presented in Fig. 37. This can be explained by the fact that LoF defects are slit shaped and do not have much heights and they occur between two consecutive layers, which is 40 μm (as the powder layer thickness) for the LB-PBF 17-4 PH SS specimens fabricated in this study. The porosity size distributions in this study were performed by randomly cutting the gage section of representative specimens throughout the gage length and in radial direction and observing the cut section under microscope to count and measure pores. Considering the shape and spacing of these potential LoF defects, it is very easy to miss them during the porosity analysis performed in this study.

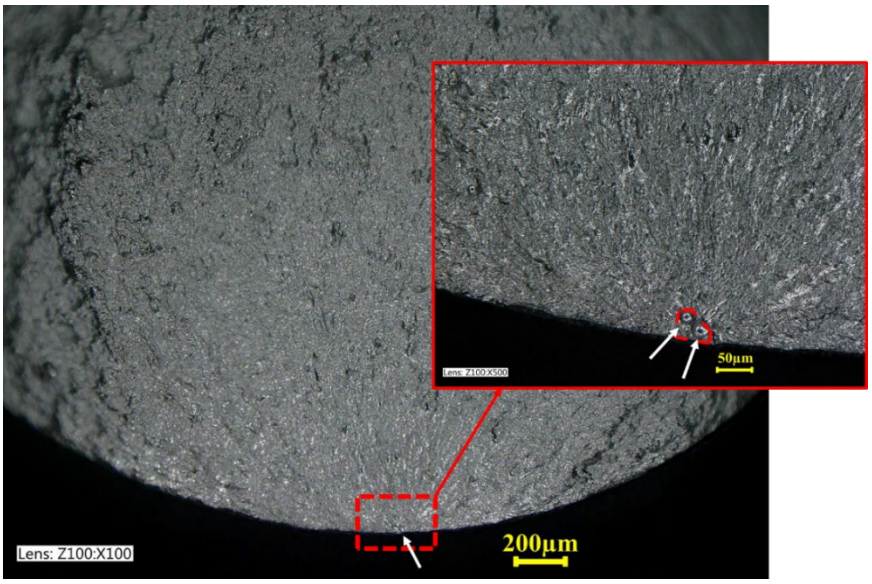

(a)

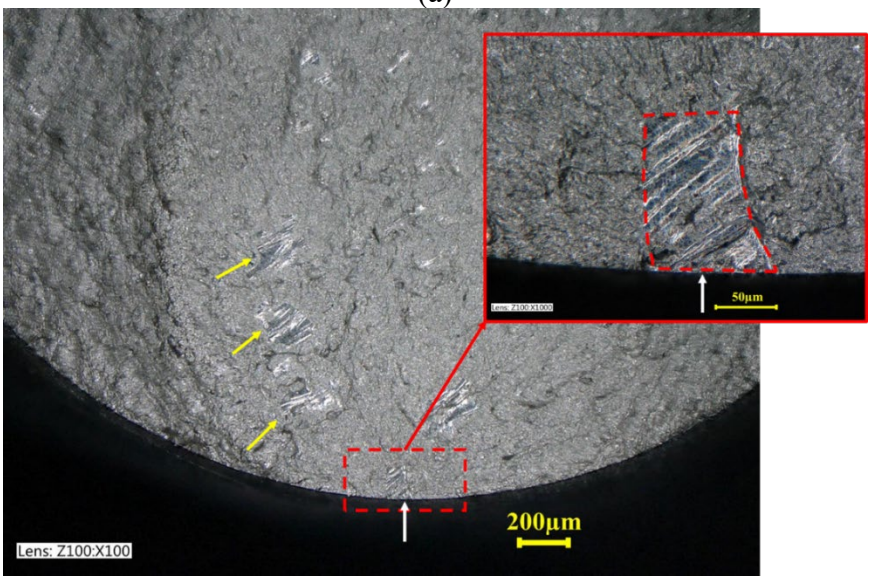

(b)

Fig. 43 Fracture surfaces of LB-PBF CA-H1025 17-4 PH SS specimens in machined surface condition fabricated from (a) Batch 1 and front with 1,747,292 reversals to failure, and (b) Batch 1 and back with 100,492 reversals to failure, both tested at 0.0025 mm/mm strain amplitude.

Fracture surfaces of machined specimens from Batch 15 fabricated in front and back locations were also analyzed using the same approach. Fracture surface of LB-PBF specimen fabricated from Batch 15 in front at ε_a =0.0025 mm/mm with 15,084,902 reversals to failure is presented in Fig. 14(a). An enhanced view of the crack initiation site is also included. It can be observed that cracks initiated from a spherical pore close to the surface, shown by white arrow, of the front

location specimen resulting in the part failure. Similar analysis on the fracture surface of a machined specimen from Batch 15 and fabricated in the back location at ε_a =0.0025 mm/mm with 4,523,250 reversals to failure at the same strain amplitude is shown in Fig. 44(b). This image indicates that the cracks initiated from an internal LoF defect, which led to the part failure. The LoF defect is also shown by white arrow.

It was observed that failure was occurred comparably in the specimens fabricated from Batch 1 and 15 and from the front location (see Fig. 43(a) and Fig. 44(a)). In these specimens, failure was due to crack initiations from gas-entrapped pores. However, in the specimens fabricated from Batch 1, cracks consistently initiated from larger gas-entrapped pores under the same strain amplitudes. In addition, the cracks were observed to initiate from gas-entrapped pores (usually spherical) in the specimens located in the front location regardless of the powder batch used. However, failure occurred by larger irregular shaped LoF defects in the specimens from the back. Therefore, it may be assumed that even on the same build plate, parts can have distinctly different performances due to the variation of powder characteristics in different locations.

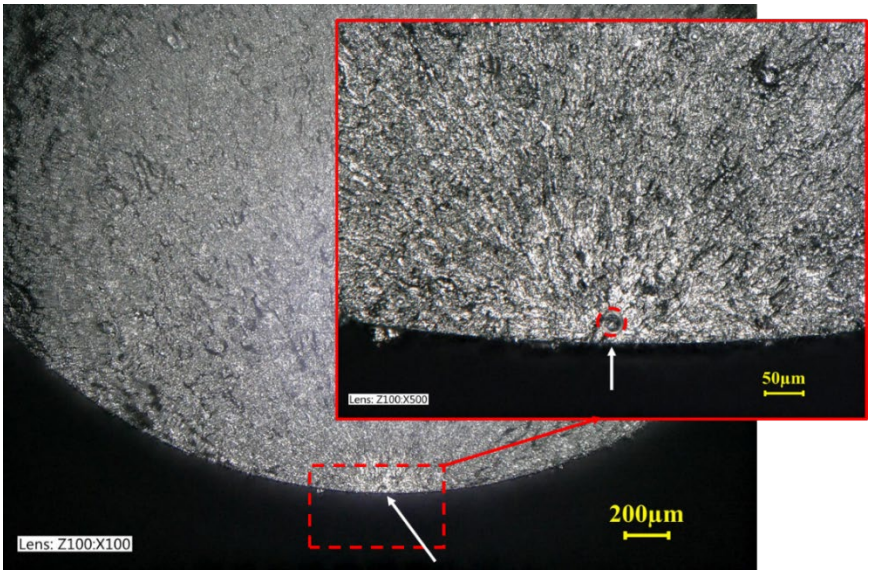

(a)

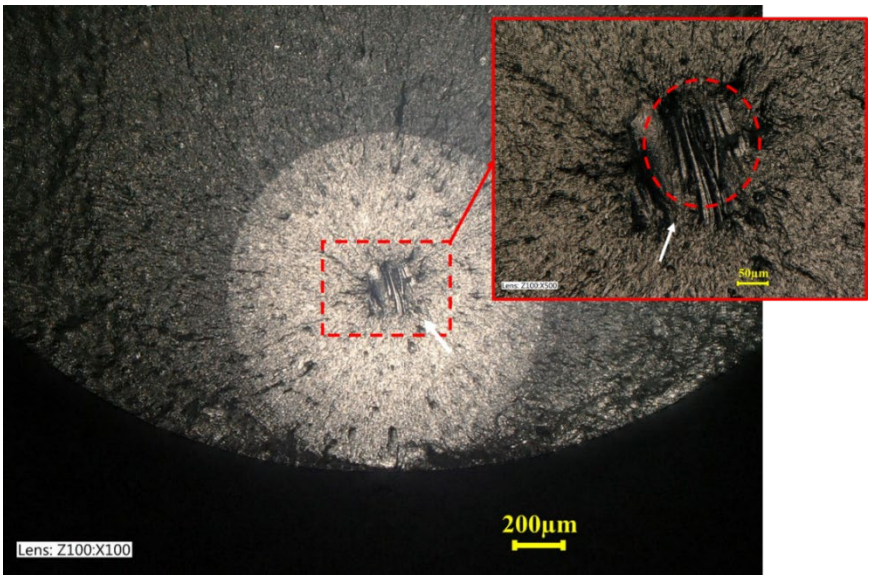

(b)

Fig. 44 Fracture surfaces of LB-PBF CA-H1025 17-4 PH SS specimens in machined surface condition fabricated from (a) Batch 15 and front with 15,084,902 reversals to failure, and (b) Batch 15 and back with 4,523,250 reversals to failure, both tested at 0.0025 mm/mm strain amplitude.

The cracks initiated similarly from LoF defects in the specimens fabricated in the back of the build plate from both Batch 1 and Batch 15. However, as shown in Fig. 43(b), the LoF defect was larger compared with the defect in the specimen fabricated from Batch 15 and same location (see Fig. 44(b)). This trend was observed for all the specimens analyzed in this study. The specimen fabricated from Batch 1 and from the back had a much shorter fatigue life as compared to the specimen from Batch 15 and the comparable location at the same strain amplitude. Therefore, in all the specimens with similar location and strain amplitude, cracks initiated from relatively larger defects (i.e., gas-entrapped pore or LoF) in the specimens fabricated from unused powder compared with the specimens from re-used powder. The larger defects in specimens fabricated from unused powder resulted in shorter fatigue lives compared with the counterparts fabricated from re-used powder. Moreover, in the specimens from the same batch, the defects were gas-entrapped pores in the specimens in front while there were more LoF defects in the specimens located in back.

4.4. Discussion on Experimental Results

Tensile monotonic behaviors of specimens from different batches were presented in Fig. 38 and Table 14. No significant variation in tensile properties including UTS and YS due to powder re-use nor location was observed. Similar observations have been made for specimens fabricated from unused and re-used powder via LB-PBF Ti-6Al-4V [7], Inconel 718 [131], and 17-4 PH SS [96] showing comparable tensile strength with re-using the powder. Comparable tensile behaviors obtained in this study may be resulting from the limited effects powder re-using has on the microstructure and chemical composition of the fabricated parts [7,15]. However, the true fracture strain was observed to slightly increase with continuously re-using the powder, which may be explained by relatively less porosity in specimens fabricated from re-used powder as compared to the ones fabricated from unused powder, as evident from Fig. 37.

Fatigue testing of CA-H1025 17-4 PH SS parts fabricated via LB-PBF in the as-built surface condition showed no significant trend in fatigue life as a result of powder re-use (see Fig. 39). The reason can be explained by crack initiation sites from rough surfaces of as-built specimens, which act as micro-notches and dominate the fatigue behavior [73] (see Fig. 42). Although average surface roughness, R_a, is not the most representative surface parameter for the fatigue behavior [140], R_a was measured for 12 specimens from different batches and locations, and all the measurements were around 7-9 μm. Not only did the surface roughness dominate the effects of powder re-use, but it also surpassed the effects of front and back locations (see Fig. 39) when the specimens were kept in their as-built surface condition.

In the machined surface condition, there was an observable difference between the fatigue lives of parts fabricated from Batch 1 and Batch 15 at the same location (see Fig. 40(a) and (b)) in the HCF regime. An improved fatigue resistance was observed for the specimens fabricated from

Batch 15 at $\varepsilon_a = 0.0025$ mm/mm compared with the ones from Batch 1 at the same strain level. This behavior may be explained by the importance of the crack initiation stage in the HCF regime, which dominates the fatigue degradation process [71]. Cracks typically initiate from defects especially the ones that are closer to the surface or brought to the surface by machining. Therefore, the projected area of the crack-initiating defect on the loading plane from the fractography analysis was measured and the defect size was calculated based on Murakami's approach [74]. In this approach, the defect size is presented by the square root of the projected area on the loading plane.

The defect diameter in the normal plane was measured to be 73 μm (surface defect) for the specimen fabricated from unused powder in front with 1,747,292 reversals to failure (see Fig. 43(a)). This defect was much larger than the maximum pore size observed in Fig. 7(a) since the crack initiated from two gas-entrapped pores close to each other, and both pores were considered to estimate the effective defect diameter. It should be noted that the maximum pore size reported in Fig. 37 is the maximum found from a 2D analysis by limited sectioning and does not necessarily represent the maximum defect size in the specimen. The defect diameter was 34 μm for the specimen fabricated from re-used powder and on the front of the build plate, resulting in 15,084,902 reversals to failure (see Fig. 44(a)).

Comparably, the defect diameters were calculated for the specimens fabricated from Batch 1 and Batch 15 in the back. The defect diameter was measured to be 90 μm (surface LoF defect) for the specimen fabricated from Batch 1 in back location with 100,492 reversals to failure (see Fig. 43(b)), while it was 69 μm (internal LoF defect) for the specimen fabricated from Batch 15 in the back with 4,523,250 reversals to failure (see Fig. 44(b)). Internal defects are considered to be more than the estimated defect diameter away from the surface, while a defect is known as a surface defect when its distance to the surface is less than its diameter. In the case of surface defects, the

area between the defect and surface of the part is also considered in the area calculations. Therefore, internal defects with comparable sizes to surface defects are expected to be less detrimental to fatigue failures. In addition, the average diameter of crack-initiating defects for all the specimens fabricated from unused powder in front and back at $\varepsilon_a = 0.0025$ mm/mm was 60 μm and 88 μm, respectively. The average diameter of crack-initiating defects of all re-used powder specimens at $\varepsilon_a = 0.0025$ mm/mm was relatively smaller than unused powder specimens, and measured to be 31 μm and 64 μm respectively for front and back specimens.

Additionally, it was observed from Fig. 37 that the maximum pore diameters are consistently smaller in the specimens fabricated from Batch 15 compared with Batch 1; about 9% and 12% smaller for the specimens in front and back, respectively. Moreover, the average pore diameters slightly decreased for the specimens fabricated from Batch 15 compared with the specimens from Batch 1 independent of location. The decrease in maximum and average pore sizes of the Batch 15 specimens can be attributed to the lower compressibility of Batch 15 as compared to Batch 1, derived from the reduction of agglomerates by powder re-use. This reduction in compressibility insinuates that the powder is naturally in a better packed state with fewer gaps between powder particles. This more uniform packing state during the melting and solidifying process can attribute to the smaller defect sizes observed in the specimens fabricated from the re-used powder batch [7]. The decreased defect size in specimens fabricated from re-used powder results in them having longer fatigue lives as it takes longer time to develop stable cracks when pores are smaller.

The non-uniform packing state of unused powder was also verified by permeability results. The higher permeability of Batch 1 showed that the gas can flow easier through the powder due to less barriers and more empty spaces within the batch. The gas in these empty spaces may not completely escape the melt pool during melting and solidification in the AM process, and can be

entrapped, introducing more gas-entrapped pores in the final fabricated parts. The reason for the smaller LoF defects, observed in the specimens fabricated from re-used powder compared with unused powder specimens (see Fig. 43(b) and Fig. 44(b)) is still unclear to authors. However, the thermal properties of the powder batches such as thermal conductivity may improve with re-using the powder [7] which may be attributed to the less compressibility and empty spaces of the re-used powder batch as compared to the unused one. Thus, the increase in thermal conductivity can lead to an increased energy absorption of the powder, resulting in a more stable melt pool and a better fusion between layers.

The difference in fatigue lives of the specimens from different locations can be illustrated based on the fact that powder is spread on the build plate using a recoater/wiper in the LB-PBF process. Therefore, some variations in powder characteristics in different locations can be expected as a result of spreading. These variations were also indicated by observing different types of defects on the fracture surface of machined specimens from the back compared with the counterparts from the front of the build plate. As seen in Fig. 43(b) and Fig. 44(b), the defects in specimens fabricated in the back were LoF, while in the specimens from the front, failure happened from gas-entrapped pores (see Fig. 43(a) and Fig. 44(a)). Additionally, the defect diameters (based on Murakami's approach [74]) of the specimens fabricated from Batch 1 and Batch 15 in the back were measured to be 90 μm and 69 μm, respectively, as compared to the counterparts in front with defect areas of 73 μm for Batch 1 and 34 μm for Batch 15. The smaller defect size in specimens fabricated in front compared to the ones fabricated in the back of the build plate (also see Fig. 37) explains the longer fatigue lives observed for specimens fabricated in front (see Fig. 41).

The observed difference between the defect distribution and size in the specimens from the same batch but fabricated in different locations can be attributed to the powder flowability. The

presence of large agglomerates in the powder batch can disrupt the smooth flow of powder across the build plate by moving in lumps and leaving empty spots on the build plate [7,10]. Additionally, fine particles may deteriorate powder flowability due to higher interparticle frictions and cohesion between fine particles and their tendency to agglomeration [9,10,130,133,141–145]. Therefore, the unused powder with more very fine particles and large agglomerates had inferior flowability, resulting in poor powder spreadability and layer uniformity on the build plate. However, by continuously re-using the powder, the number of large agglomerates and fine particles decreased leaving particles with more comparable sizes in the re-used batch (see Fig. 33). Therefore, flowability improved by powder re-use resulting in less difference in fatigue lives of specimens from the re-used powder batch in different locations compared with specimens from unused powder, as evident from Fig. 41(a) and (b).

The improved flowability of the powder by re-using can be also understood by comparing the permeability and cohesion of different powder batches (see Fig. 35 and Fig. 36). Permeability decreased from Batch 1 to Batch 15 which can be related to the reduction of large agglomerates from the batch. In addition, powder cohesion, which evaluates the tendency of fine particles to agglomerate [10], decreased with powder re-use. Therefore, the combination of decreased permeability and lower cohesion can indicate that there are fewer fine particles as well as agglomerates within the re-used powder resulting in better flowability of this batch. It should be noted that the longer exposure of re-used powder to higher temperatures, and consequently, less moisture content, might have also contributed to some extent to the more flowability of re-used batch [10,13]. In the absence of humidity, re-used powder particles are less prone to agglomeration resulting in a more uniform powder layer on the build plate, and consequently, a smaller gap between the fatigue lives of front and back specimens in low, mid and high cycle fatigue regimes.

4.5. Conclusions

In this study, effects of powder re-use on mechanical properties of parts fabricated from 17-4 PH SS via LB-PBF additive manufacturing process were studied. In addition, the dependency of the mechanical properties on the location of the specimen on the build plate was also investigated. Specimens were fabricated and tested in two surface conditions; as-built and machined. The powder was continuously re-used in order to fabricate 15 consecutive sets. Powder characteristics were also analyzed in relation to the observed mechanical properties. Overall, the experimental results in this study have shown that both location of the specimen on the build plate and the powder characteristics, as they get affected by the powder re-use, can be influential on the fatigue performance of LB-PBF fabricated materials. In addition, based on the results, the following conclusions can be made:

1. The high cycle fatigue behavior of machined LB-PBF CA-H1025 17-4 PH SS specimens was observed to improve by continuously re-using the powder. Specimens fabricated from heavily re-used powder (re-used for 14-times) had a better fatigue strength in the high cycle regime than the specimens fabricated from unused powder.
2. The improved fatigue behavior in the high cycle regime was related to the reduced compressibility of the powder after re-using due to the reduction of agglomerates. Less agglomerates in the re-used powder reduces the presence of empty spaces in the powder bulk which could have resulted in generation of larger and more pores during fabrication.
3. Fatigue behavior of parts in the machined surface condition was observed to be dependent on the part location on the build plate with relatively higher fatigue lives for the specimens closer to the powder feed bin compared with the ones further away from

the feed bin. However, the location dependency of the fatigue behavior was decreased with re-using the powder.

4. Powder flowability improved by continuously re-using the powder due to the reduction of fine particles and agglomerates in the re-used powder batches. This improved flowability was argued to be the main reason for the reduction in the location dependency of the fatigue behavior.
5. Fatigue behavior of parts in the as-built surface condition was insensitive to powder re-use or part location upon the build plate. Relatively high surface roughness as a result of the LB-PBF process was the dominating factor affecting the fatigue degradation in both high and low cycle fatigue regimes.
6. No significant variation in tensile properties including yield and ultimate tensile strengths was observed as a result of powder re-use or specimen location on the build plate. Elongation to failure was observed to slightly increase by powder re-using and its effect on reducing the porosity.

In closing, the findings of this study indicate that powder characteristics can vary not only for successive builds but also for different locations on a single build; thus, highlighting the importance of standardizing powder handling and re-using/reconditioning practices. The existence of standardized practices can ensure repeatable quality builds across the build plate and on multiple platforms. Therefore, further studies are needed to better understand how each powder characteristic contributes to variations in defect formation and mechanical performance to be able to propose effective powder handling and re-use procedures/standards.

5. Mechanical Properties of Laser Powder Directed Energy Deposited NASA HR-1 Superalloy: Effects of Powder Reuse and Part Orientation

5.1. Introduction

NASA HR-1 is a γ'-strengthened, Fe-Ni superalloy that NASA originally developed in the 1990s and primarily used in liquid hydrogen rocket engines [146], whose components, such as hot gas manifolds and regeneratively-cooled nozzles, are exposed to high-pressure hydrogen environment during normal operations. This alloy has a combination of properties desirable for this type of applications, including good resistance to hydron embrittlement (HE) and corrosion as well as adequate strength and ductility. This alloy was essentially developed to replace the commonly used materials in such applications, including stainless steels (SS), A286, and JBK-75, which have good HE resistance but lack strength [147]. In addition, the high thermal conductivity and excellent low-cycle-fatigue (LCF) performance of NASA HR-1 have made this material more suitable for such harsh environments [2,146,148–150].

This Fe-based superalloy was typically processed via a conventional manufacturing route that involves vacuum induction melting or vacuum arc melting followed by hot- or cold- rolling to fabricate individual parts, which are then assembled and/or brazed into engine components. The significant cost and lead-time for tooling, brazing, and assembly associated with this route make additive manufacturing (AM) approaches that can fabricate integral components with complex internal features [2,146,151] especially appealing. Among different AM methods, both laser powder bed fusion (L-PBF) and laser powder directed energy deposition (LP-DED) have been experimented with NASA HR-1. Nevertheless, the dimensions of most liquid hydrogen rocket engine components (on the order of meters) well exceed the build volume of L-PBF systems (typically well below 1 m^3) and make LP-DED technologies, that can fabricate geometric features as small as 1 mm [146], an ideal choice.

The geometric resolution and build rate of LP-DED correlate with the size of the melt pool, which is in turn governed by the laser power and spot size. For instance, small melt pools are required when fine features (such as thin walls) are fabricated, and large melt pools are needed when a high build rate is desirable. However, achieving higher geometric resolution is often traded-off with exceedingly low powder capture efficiency (defined as the fraction of the powder that is consolidated into the deposited part [152]) due to the smaller melt pools used – as low as 5% [28] compared to the 40-80% reported for normal deposition conditions [28,29]. To circumvent cost associated with new powder purchase, the uncaptured powder is commonly recycled to be used for subsequent depositions with or without rejuvenation (i.e., mixing used powder with the unused one).

Recycled powder, however, typically has different characteristics from its unused (i.e., virgin) state. For instance, coarsening of particle size distribution (PSD) with the reduction of finer particles had been observed due to reuse of various alloys during LP-DED, including Ti-6Al-4V after 10-time reuse and rejuvenated with unused powder at a 1:1 ratio [29], austenitic 316L SS after 9- and 2-times reuse without rejuvenation [28,153], or Ni-based superalloys after 5-time reuse [154]. Such variations in PSD and other powder characteristics' changes such as O content may lead to build-to-build variations in micro-/defect-structure and mechanical performances of the fabricated parts. For example, reduced tensile ductility values were reported in Refs. [28,30,153] when the specimens were deposited using reused 316L SS powder, and were attributed to the more frequently formed and larger Si- and Mn- oxides in these specimens as compared to their counterparts fabricated with unused powders.

These reported changes in the microstructure and tensile properties of Ti-6Al-4V [29,155], 316L SS [28,30,153], and Ni-based superalloy parts [154], call for careful evaluation of powder

reuse's impact on the structural integrity of NASA HR-1 components before LP-DED and the associated reuse practice are adopted to these high-value space applications. Given the recent success in re-flight of space hardware demonstrated by certain private space companies, the influence of powder reuse on the fatigue performance of LP-DED fabricated parts is of particular interest.

The present study aims to investigate the effects of powder reuse on tensile and fatigue properties of LP-DED NASA HR-1 specimens, which is currently lacking in the literature. The knowledge gained in this investigation will also contribute to the high-priority powder reuse technical gap identified by America Makes & ANSI Additive Manufacturing Standardization Collaborative (AMSC) Roadmap [87]. Moreover, the anisotropy in micro-/defect-structure and mechanical properties and how it is influenced by powder reuse will be investigated by excising the specimens parallel and perpendicular to the building direction. Following the introduction, the methodology and experimental results, including powder characteristics as well as defect content, tensile and fatigue properties of LP-DED NASA HR-1 specimens are presented. Subsequently, results are discussed, and some conclusions are made.

5.2. Methodology

In this study, rotary-atomized NASA HR-1 powder with a nominal PSD of 45-105 μm was employed in its unused condition for Print 1 via an RPM Innovations (RPMI) 557 LP-DED machine with 350 W laser power. As shown in Fig. 45, thin walls were deposited in a box-shaped structure and removed from the substrate using a bandsaw. Based on the heat treatment schedule developed by NASA [148], the boxes were stress-relieved at 900 °C for 1.5 hours in argon, furnace cooled, and homogenized at 1163 °C for 6 hours in a vacuum, and furnace cooled. Subsequently, they were solution treated at 1065 °C for 1 hour, argon quenched, aged at 690 °C and 621 °C for 32 hours, and furnace cooled.

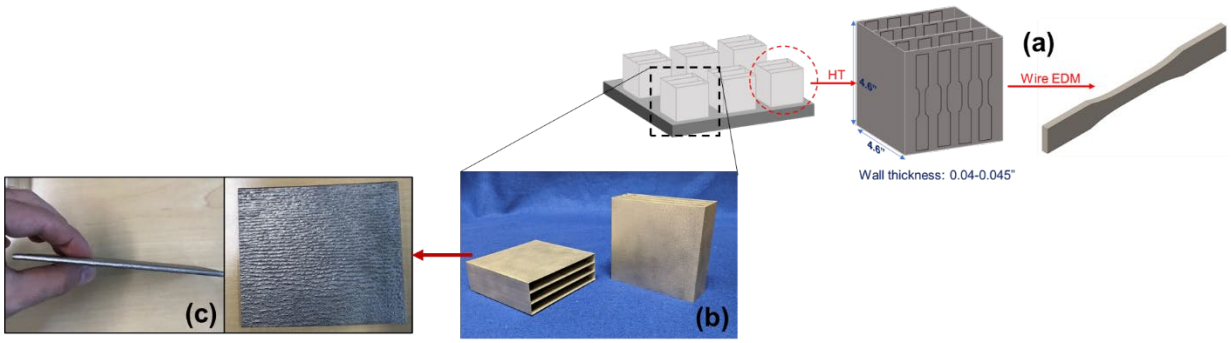

Fig. 45 A schematic of the LP-DED NASA HR-1 thin walls in (a) and the thin walls after fabrication in (b) and (c).

After each print, the extra powder was collected, sieved using a 100 µm sieve, and reused for the next iteration without adding unused powder. As the powder was consumed by repeated reuse, the number of boxes fabricated per print was reduced to ensure the powder was sufficient for each iteration, namely 7, 7, 4, 3, 2, and 1 box for Prints 1, 2, 3, 4, 5, and 6, respectively. Then, flat tensile and fatigue coupons were excised from the thin walls by cutting both parallel and perpendicular to the building direction (see Fig. 46). The tensile and fatigue test specimens were designed based on ASTM E8 and E466 standards [52,53], as illustrated in Fig. 47(a) and (b). It needs to be noted that there were no fatigue specimens available from Print 6 in parallel orientation. The specimens were tested in their as-built surface conditions, and no post-fabrication surface treatments were conducted. The reason was that this material is often used in its as-built condition after deposition.

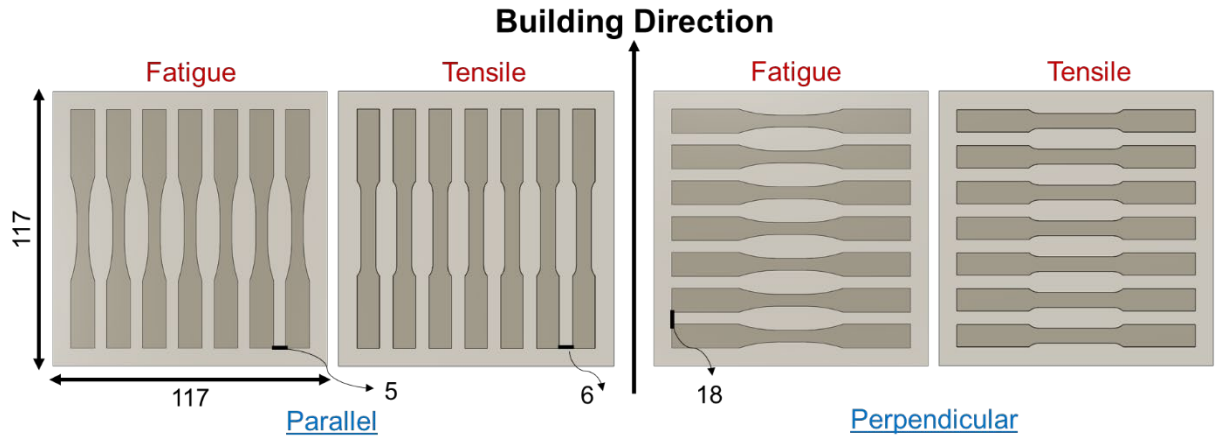

Fig. 46 Schematic of the orientations of fatigue and tensile test specimens excised parallel and perpendicular to the building direction from the thin walls with 0.1 mm linear and 0.5° angular tolerances. The dimensions are in mm.

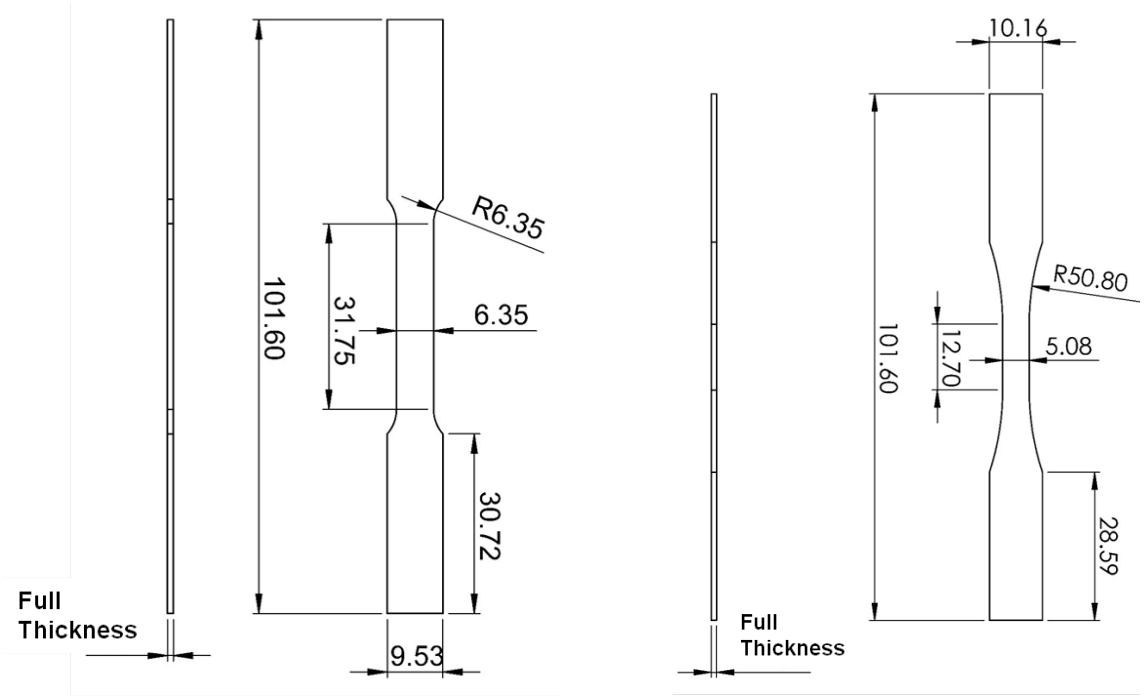

(a) (b)

Fig. 47 The geometries of ASTM E8 subsize rectangular tension test specimen in (a) and ASTM E466 fatigue specimen with tangentially blending fillets between the uniform test section and the ends in (b). All dimensions are in mm.

Tensile tests were conducted on an MTS Bionix Tabletop Test System, equipped with a 25 kN load cell. Tests were performed displacement-controlled with a nominal strain rate of 0.001

mm/mm/s according to the ASTM E8 [53]. The local strain information was collected with an MTS extensometer attached to the specimen. After yielding, the extensometer was removed at 0.05 mm/mm (5%) strain and the tests continued to fracture. After the fracture, the ultimate tensile strength (UTS), yield strength (YS), percent elongation to failure (%EL), strain hardening exponent (n), and strength coefficient (K) were obtained. For each reuse condition, three specimens were tested. Fatigue tests were also conducted using the same load frame according to ASTM E466 [52]. The test mode was force-controlled in order to avoid potential mean stress relaxation occurring during strain-controlled testing of thin walls [71]. A stress ratio, R_σ, of 0.1 was used to prevent specimen buckling. Tests were continued until the final fracture and the number of reversals to failure ($2N_f$) were recorded. Tests that did not fail before 10^7 reversals were considered as "run-out."

After fatigue and tensile failures, fracture surfaces were investigated via a Zeiss Crossbeam 550 scanning electron microscope (SEM) to identify the crack initiation sites and tensile fracture mechanisms. The same microscope was also used with an Oxford electron backscatter diffraction (EBSD) detector to characterize the microstructure of fatigue specimens. Surface roughness was evaluated using a Keyence VHX-6000 digital optical microscope on three specimens per reuse condition. The defect content within the fatigue specimens was analyzed via a Zeiss Xradia 620 and a voxel size of 6 μm. After scanning, 3D images were reconstructed using Dragonfly software, and sphere equivalent diameters of the volumetric defects were obtained using the ImageJ software [156]. The powders which were used for each iteration were sampled prior to fabrication. These samples were analyzed using a Freeman Technology FT4 powder rheometer to characterize the powder's flow and packing behavior. Each powder sample was evaluated at least three times to verify the results. The PSD of each powder and its morphological aspects (including circularity

and elongation) were measured by a Malvern Morphology G3SE analyzer via static image analysis. The powder flowability was also evaluated using a Hall Funnel according to ASTM B213 [157] to obtain the Hall flow rate (HFR). Lastly, the O content in the parts was determined using the inductively coupled plasma (ICP) method [158].

5.3. Experimental Results

5.3.1. Powder Characteristics

The powder rheological characteristics as the result of each use/reuse were evaluated in terms of flow characteristics, including basic flowability energy (BFE), aeration energy (AE), and cohesion and packing state, including compressibility and pressure drop. The BFE represents the work done to move a blade with a standard geometry as specified by [62] through powder bulk in a downward motion [31,62]. A lower BFE represents a powder with lower resistance to flow [20]. As seen in Fig. 48(a), the BFE was somewhat similar for all samples. The AE, which indicates the resistance of powder to fluidization by the gas flow, did not show any clear trend with powder reuse (see Fig. 48(b)). This behavior indicates a similar tendency to agglomeration in all samples [20,31,62]. The cohesion, however, showed a rather sharp decrease trend in Print 6 (i.e., 5-times reused powder). Cohesion is the amount of shear stress to flow the powder, and lower values represent lower mechanical interlocking [20,31,62].

The compressibility indicates the volume change under pressure and lower values can indicate a powder with a better packing state and lower entrapped gas within the powder bulk [20,31,62]. As evident in Fig. 48(e), the compressibility did not follow a specific trend with powder reuse. Although Prints 3 and 6 powders had the lowest compressibility, their values still overlapped with the scatter bands of other prints. Pressure drop can show the permeability of the gas through the powder; higher numbers may represent a powder with a tighter particle arrangement and lower compressibility [31,62]. No obvious trends of variation were noted for the pressure drop in Fig.

48(f), although higher pressure drop values (such as those seen for Prints 3 and 6) often corresponded with higher compressibility values shown in Fig. 48(e).

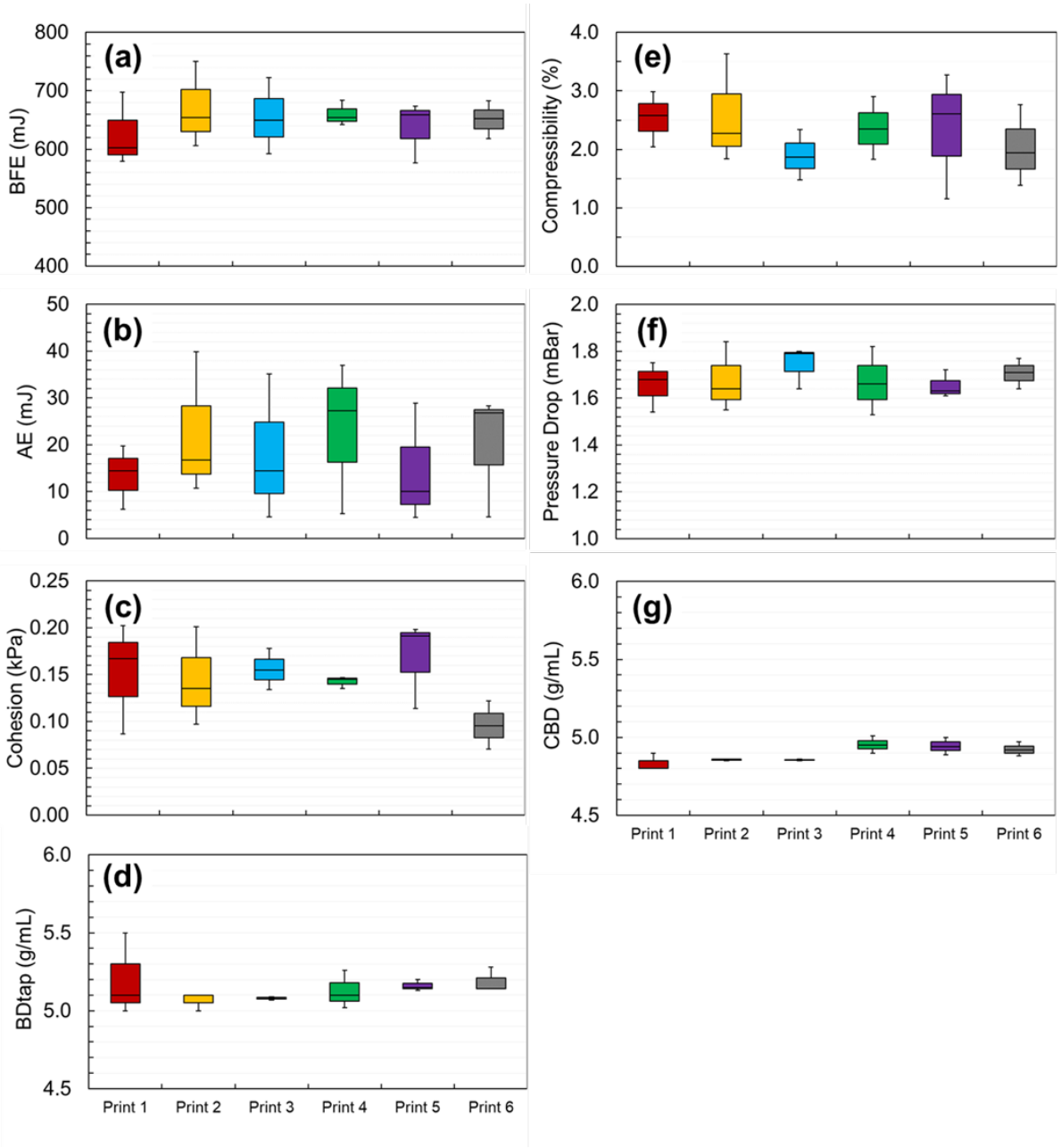

Fig. 48 Rheological properties including (a) BFE, (b) AE, (c) cohesion, (d) compressibility and (e) pressure drop for Print 1, 2, 3, 4, 5, and 6 powder samples.

Lastly, the conditioned bulk density (CBD) and tapped density (BDtap) of all samples were evaluated (see Fig. 48(g) and (d)). The CBD is evaluated when the powder is in a loose condition, whereas the BDtap is the density of the powder in a compacted condition [31]. The CBD slightly

increased by continuously reusing the powder (~1.6%); however, there was no particular trend in BDtap. The Hausner ratio ($^{BDtap}/_{CBD}$), and Carr index $\left(^{BDtap-CBD}/_{BDtap}\right)\times 100$ were also evaluated [20]. The Hausner ratios closer to one and lower Carr indices indicate better flowability. As is evident in Table 17, the changes did not follow a clear trend which matched the results in Fig. 48. The HFR, with a lower value representing better powder flowability, was also measured according to the ASTM B213 [159]. As seen in Table 17, there was no change in HFR values.

Table 17 The Hausner ratio, Carr index, and HFR for all the powder samples.

Density	**Print 1**	**Print 2**	**Print 3**	**Print 4**	**Print 5**	**Print 6**
Hausner ratio	1.07	1.04	1.04	1.04	1.04	1.05
Carr index	6.92	4.14	4.14	3.51	4.26	5.20
HFR (s/50g)	13±0	13±0	13±0	14±0	14±0	14±0

PSD was evaluated and reported in Fig. 49**(a)**. This figure shows that the PSD coarsened with the continuous reuse of the powder, which was concomitant with the reduction in the fraction of fine particles and the increase of the mean particle size (D_{50}). The particle circularity (i.e., the circle equivalent perimeter divided by the actual perimeter) and elongation (i.e., 1- width/length) were also evaluated. Powder reuse did not influence the circularity, and all powders had circularities ~ 0.93-0.95 (a circularity of 1 indicates a perfect circle). The particle elongation was also ~ 0.12-0.14 for all powders (needles have an elongation of 1). In all powders, a considerable amount of spherical, elongated, and agglomerated particles was present, which perhaps have contributed to the negligible effects of powder reuse on powder morphological features (see Fig. 49**(b)**).

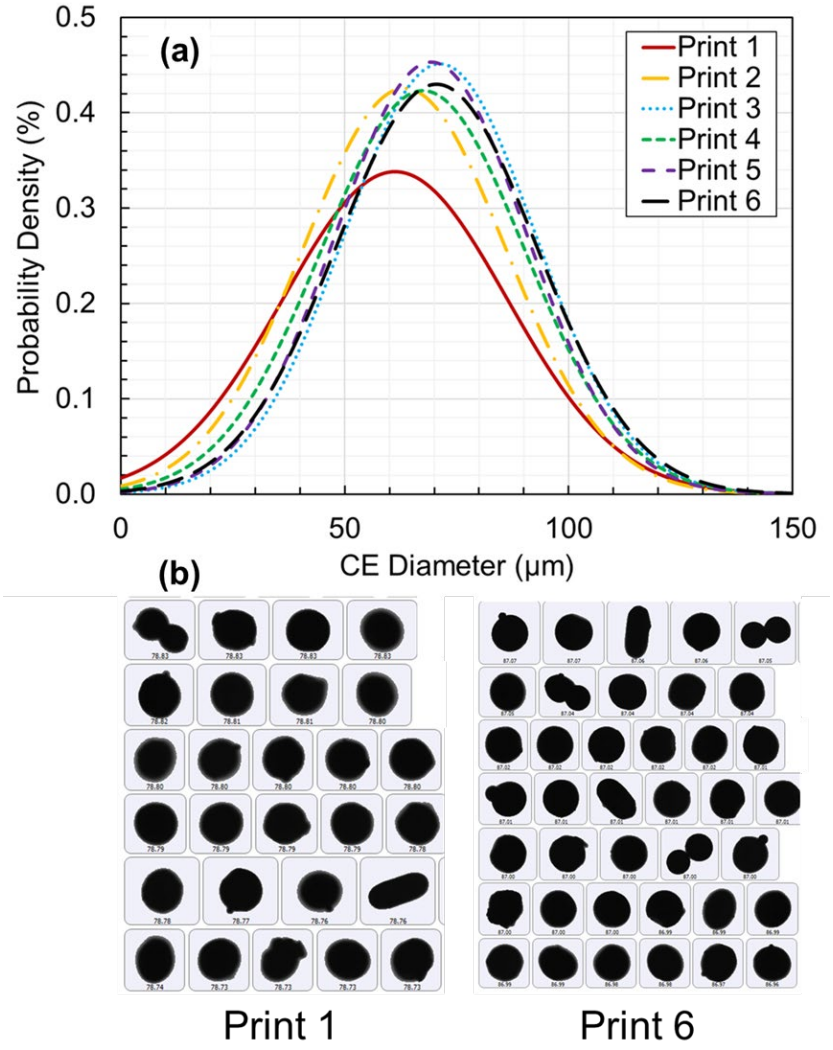

Fig. 49 (a) PSD of the Prints 1, 2, 3, 4, 5, and 6 powders, and (b) the typical particle shapes of Prints 1 and 6 powders.

5.3.2. Surface Roughness, Oxygen Pickup, and Defect-/Micro-Structure

The surface roughness was evaluated for the LP-DED NASA HR-1 specimens in both perpendicular and parallel orientations. As seen in Table 18, there were negligible changes between the arithmetical mean height of the profiled area (S_a) values resulting from powder reuse, considering the uncertainties associated with the measurement and the sample areas. The differences in S_a between parallel and perpendicular specimens were also negligible. The S_a values for all prints were around 15 μm. The O concentration was also analyzed in the LP-DED NASA

HR-1 specimens deposited from all powders. The results are reported in Table 19. The concentration of O did not show any particular trend with powder reuse. Therefore, it can be assumed that no O pickup in powder occurred during powder reuse and handling, indicating the robustness of the reuse practice.

Table 18 Effects of powder reuse and orientation on S_a.

Deposition	Print 1	Print 3	Print 4	Print 6
Perpendicular	15±1 µm	15±1 µm	16±1 µm	17±0 µm
Parallel	15±0 µm	15±1 µm	16±3 µm	N/A

Table 19 Concentration of O in the LP-DED NASA HR-1 specimens with powder reuse. The results are reported in parts per million (ppm).

Set	O (ppm)
Print 1	92.5 ± 1.5
Print 2	100.0 ± 3.0
Print 3	92.5 ± 0.5
Print 4	85.5 ± 0.5
Print 5	91.0 ± 6.0
Print 6	91.5 ± 1.5

The defect content within the deposited parts was investigated and illustrated in Fig. 50. It was observed that powder reuse and part orientation did not influence the defect content. Defects (mainly gas-entrapped pores) were randomly distributed within the LP-DED NASA HR-1 specimens in all prints. The sphere equivalent diameters of the defects were obtained based on the defect volumes to assess the probability density distributions (PDFs). As seen in Fig. 50, there was no difference among the PDFs, and the 10^{th}, 50^{th}, and 90^{th} percentile defect sizes were somewhat comparable and are ~18 µm, ~50 µm, and ~92 µm, respectively.

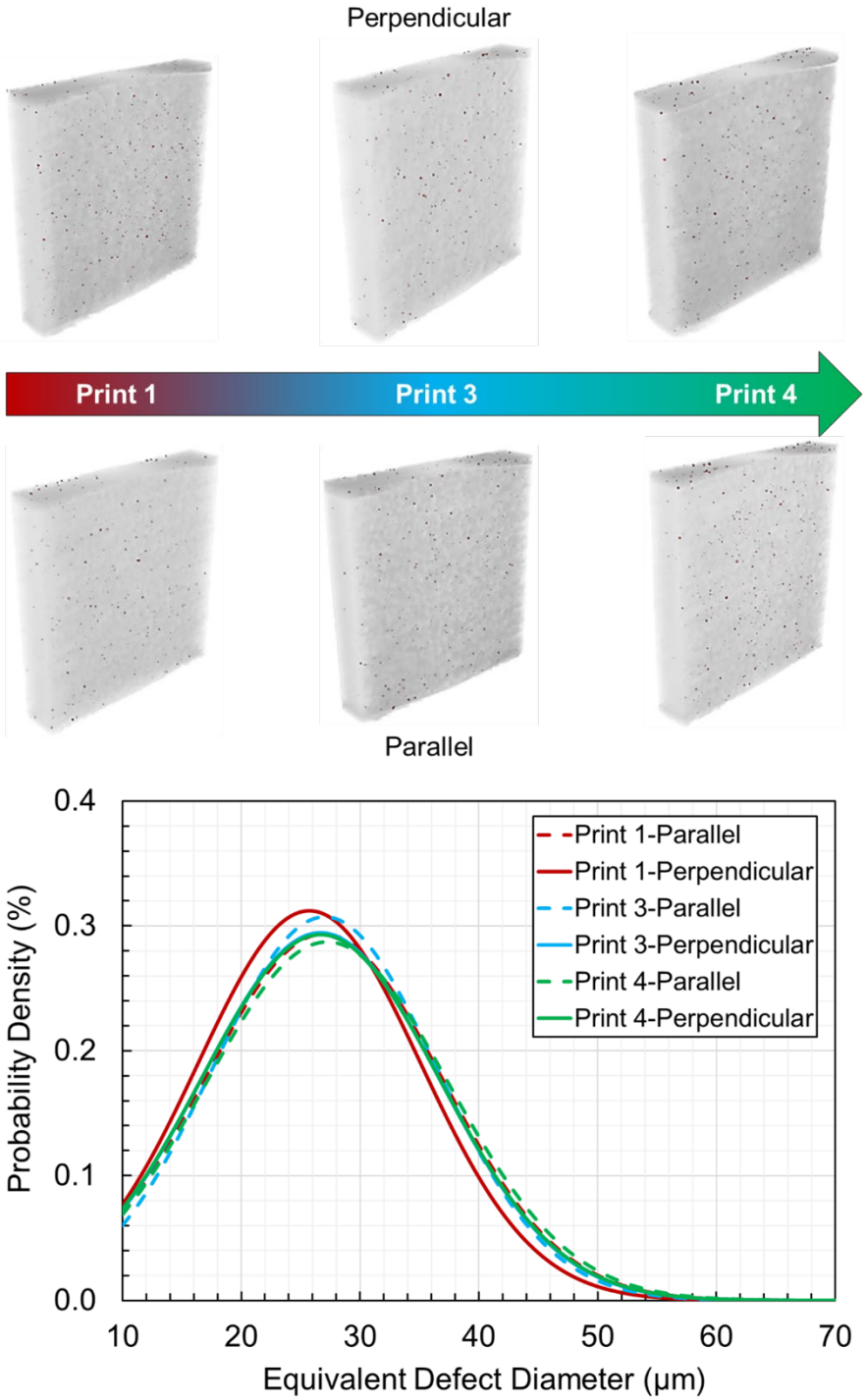

Fig. 50 The defect contents and their corresponding probability distributions in Prints 1, 3, and 4 specimens for both perpendicular and parallel orientations.

Lastly, the microstructure was investigated along the building direction. In Fig. 51, the inverse pole figure (IPF) and phase maps for each condition are shown. This image shows that the

microstructure was almost similar for all conditions, regardless of the powder reuse condition or specimen orientation. No columnar grains and signs of dendritic microstructure (i.e., presence of low angle grain boundaries, and intragranular misorientation) were noted, which may have been removed due to the heat treatment [148]. In all conditions, the grains were almost equiaxed with the amount of annealing twin boundaries (Σ3) being comparable, showing complete homogenization and recrystallization by heat treatment. In addition, the phase structure was completely face-centered cubic (FCC) and ~0.1% body-centered cubic (BCC) and did not change with powder reuse or specimen orientation. The size distributions of the grains visible in Fig. 51 were also compared in Fig. 52. As shown, no powder reuse and specimen orientation effects were observed on the grain size. The mean grain size was ~45-50 μm for all conditions with the most probable grain size being ~130-150 μm. Therefore, it may be assumed that the changes in powder characteristics due to reuse did not generate changes in microstructure significant enough to be carried through heat treatment.

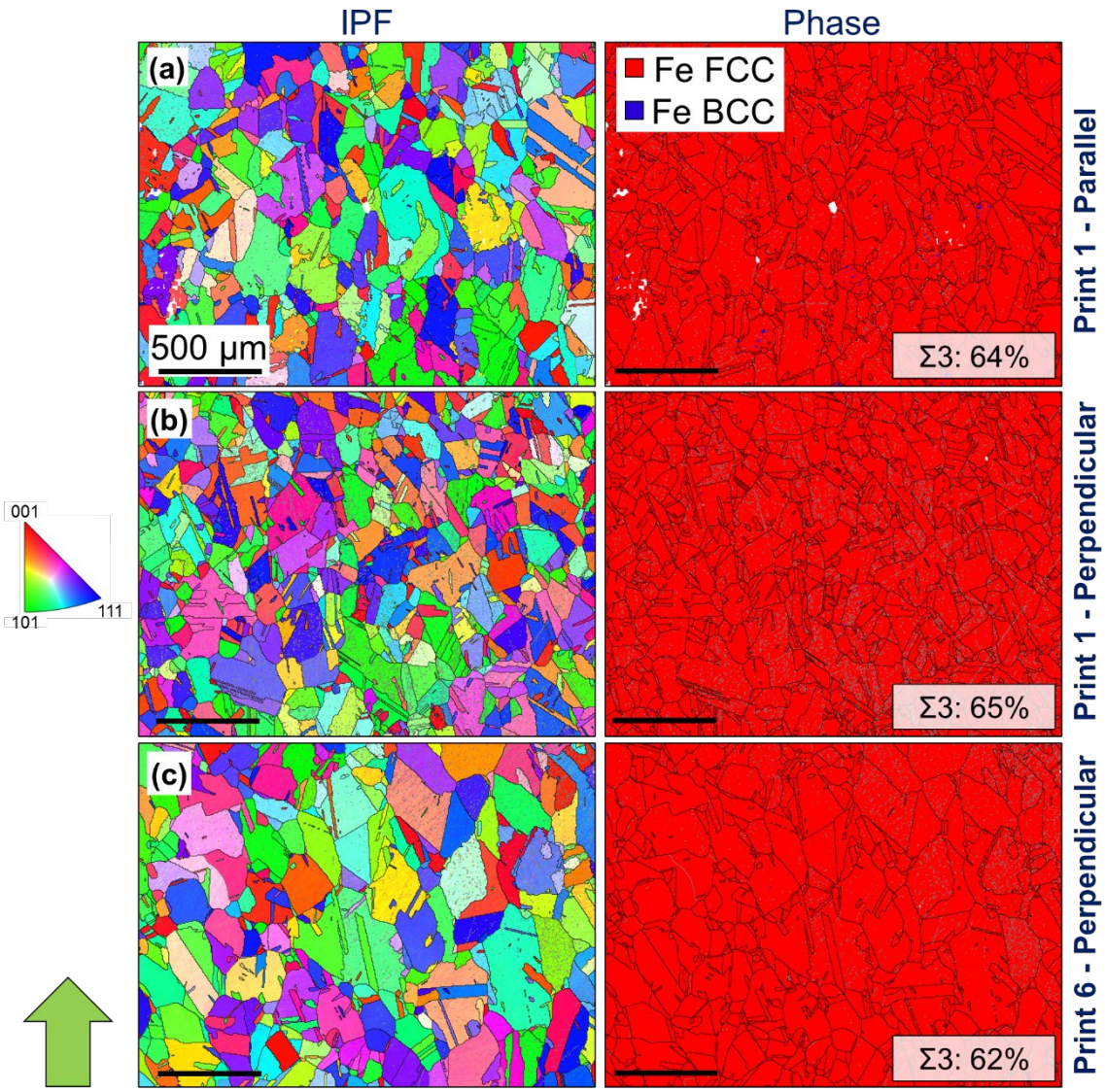

Fig. 51 The IPF and phase maps for LP-DED NASA HR-1 (a) Print 1 – Parallel, (b) Print 1 – Perpendicular, and (c) Print 6 – Perpendicular fatigue specimens in the heat-treated condition. The fractions of annealing twin boundaries (Σ3) are also labeled on each panel. The green arrow illustrates the building direction.

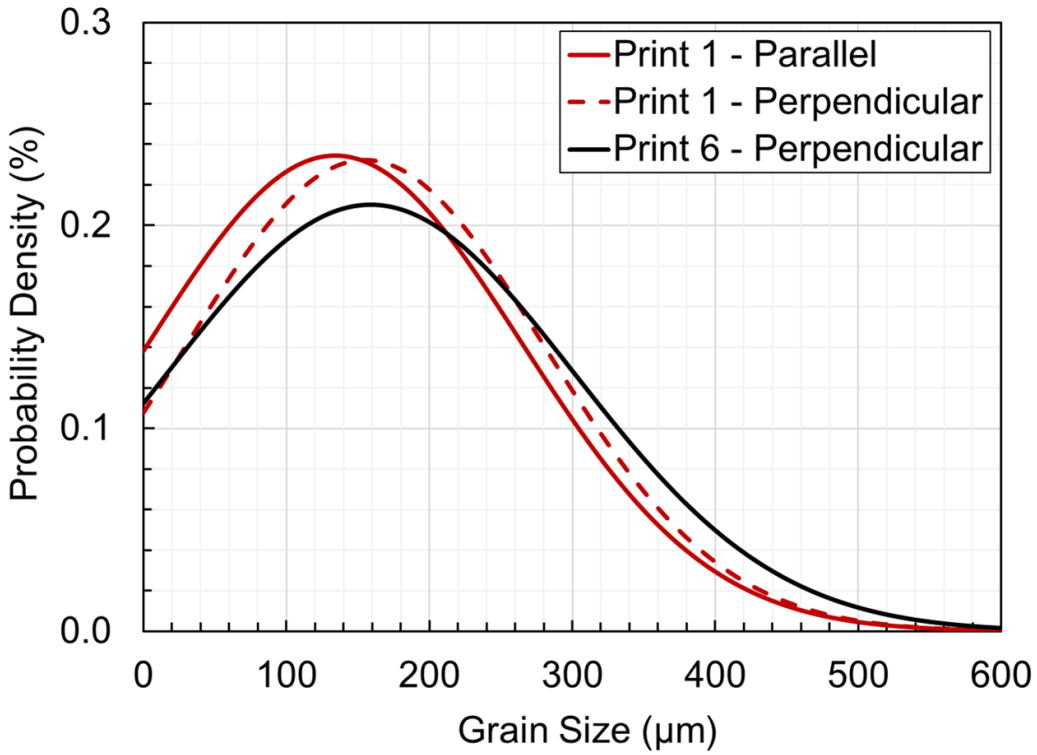

Fig. 52 Grain size distribution in LP-DED NASA HR-1 fatigue specimens.

5.3.3. Tensile Behavior & Failure

A side-by-side comparison tensile test results between different orientations is provided in Fig. 53. As is evident in this figure, when the specimens were cut perpendicular to the building direction, the UTS slightly increased with reusing the powder; however, YS did not change significantly. On the other hand, no clear trend was noted for specimens cut parallel to the building direction. In both conditions, the UTS and YS were almost comparable, however, with less scatter in parallel specimens. The ductility of the specimens as measured by %EL showed no clear trend in the perpendicular condition, and all the prints had somewhat similar values. In addition, powder reuse did not affect the tensile ductility of parallel specimens. However, more variation was noted among the specimens within some prints. The tensile ductility of parallel specimens was also generally lower than the perpendicular specimens, consistent with the results in Ref. [160]. Lastly,

the perpendicular specimens had a slightly lower strain hardening exponent than the parallel specimens (see Table 20).

Table 20 Tensile properties of LP-DED NASA HR-1 specimens for Prints 1, 2, 3, 4, 5, and 6.

Deposition	UTS (MPa)	YS (MPa)	%EL	K (MPa)	n	E (GPa)
Perpendicular						
Print 1	925±24	455±20	34±1	1083±36	0.16±0	171±8
Print 2	961±26	459±27	34±2	1149±46	0.16±0	183±6
Print 3	942±37	455±33	35±2	1094±53	0.16±0	185±6
Print 4	971±25	470±26	34±2	1161±31	0.17±0	185±5
Print 5	994±16	479±27	35±2	1204±36	0.17±0	199±5
Print 6	983±24	470±27	35±0	1176±34	0.16±0	186±3
Parallel						
Print 1	968±9	457±4	30±4	1164±16	0.18±0	178±12
Print 2	986±11	477±13	33±0	1210±24	0.17±0	181±4
Print 3	923±6	427±5	33±7	1121±7	0.18±0	186±+9
Print 4	952±6	448±4	34±1	1189±17	0.18±0	180±3
Print 5	955±14	468±23	31±3	1191±16	0.18±0	186±8
Print 6	943±5	443±2	30±2	1156±16	0.18±0	187±2

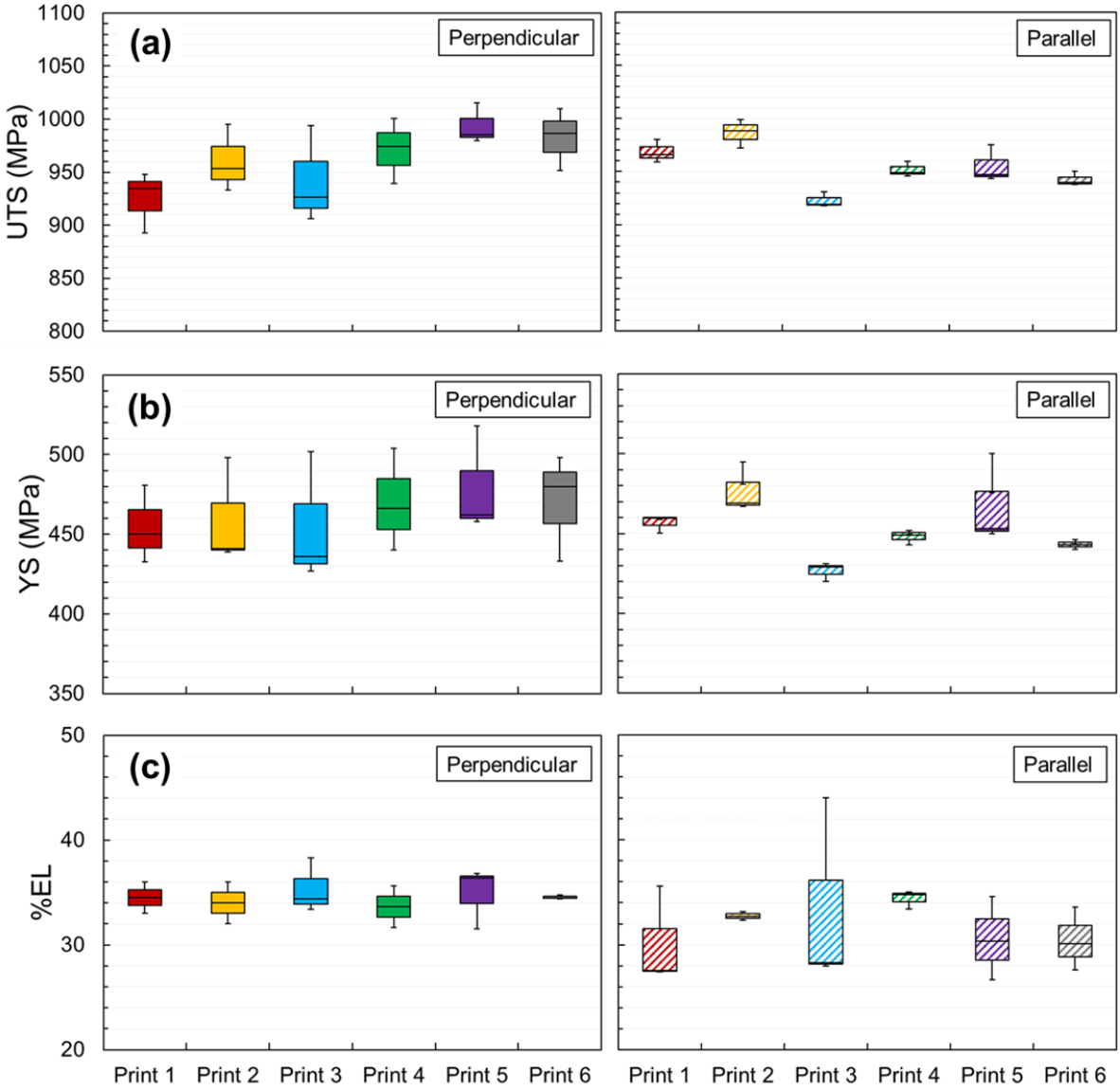

Fig. 53 The (a) UTS, (b) YS, and (c) %EL of Prints 1, 2, 3, 4, 5, and 6 specimens for both perpendicular and parallel orientations.

Tensile fracture surfaces were investigated with respect to powder reuse and orientation (see Fig. 54). Overall, no clear difference was noted among the fracture surfaces of all tensile specimens with respect to powder reuse or specimen orientation (i.e., perpendicular or parallel to the building direction). The fracture surfaces contained dimples and large volumetric defects in all conditions. While the shear lips were somewhat visible, indicating a ductile fracture, their areas were insignificant, possibly due to multiple initiation sites from the surface.

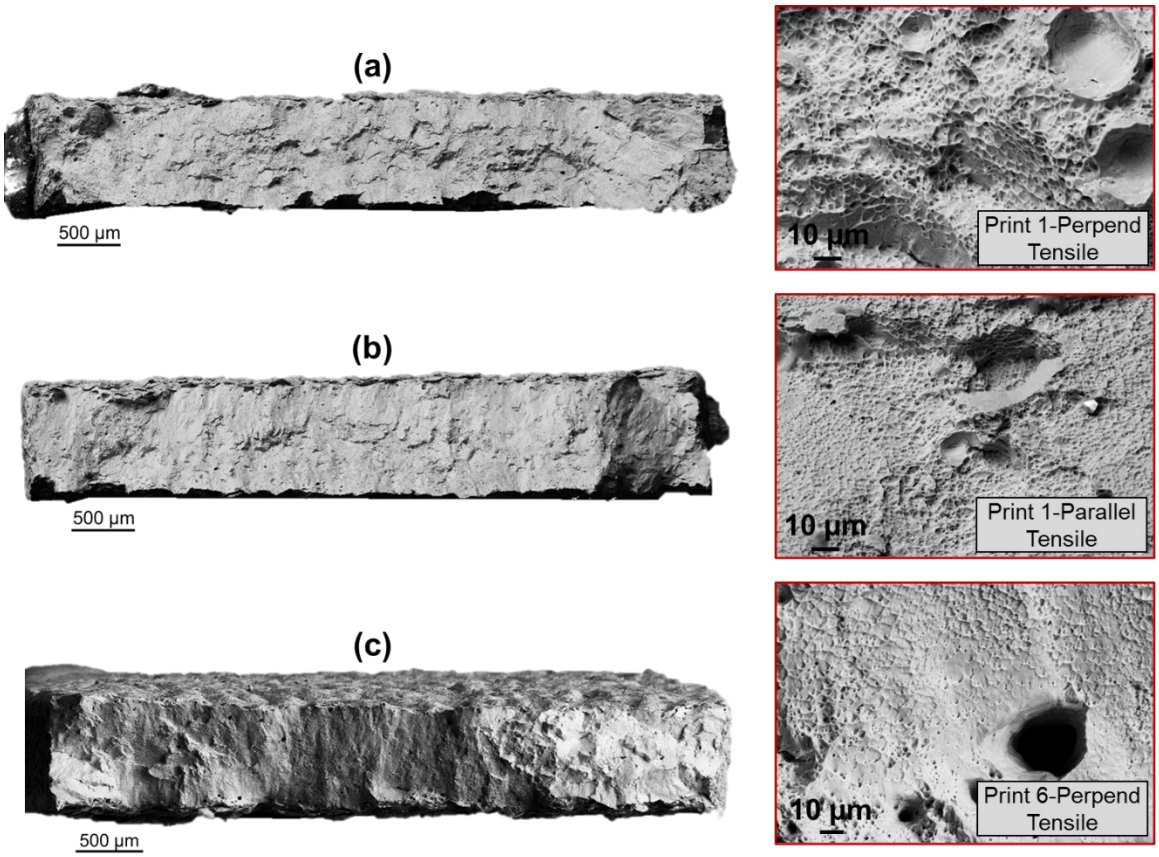

Fig. 54 Fracture surfaces of LP-DED NASA HR-1 for (a) Print 1-perpendicular, (b) Print 1-parallel, and (c) Print 6-perpendicular specimens.

5.3.4. Fatigue Behavior & Failure

Fatigue performance was evaluated for Prints 1, 3, and 4 for the specimens excised in both parallel and perpendicular directions and for Print 6 perpendicular specimens. Effects of specimen orientation are illustrated in Fig. 55. As seen in this figure, perpendicular specimens had slightly higher fatigue lives, with a factor of two, than the parallel ones in the LCF and mid-cycle-fatigue (MCF) regimes. In the high-cycle-fatigue (HCF) regime, the difference was still visible; however less notable compared with the scatter in data. Effects of powder reuse are shown in Fig. 56. As seen in this figure, the differences in fatigue lives among different prints (i.e., 1, 3, 4, and 6) were insignificant for both perpendicular and parallel specimens. A summary of all fatigue test results is provided in Table 4.

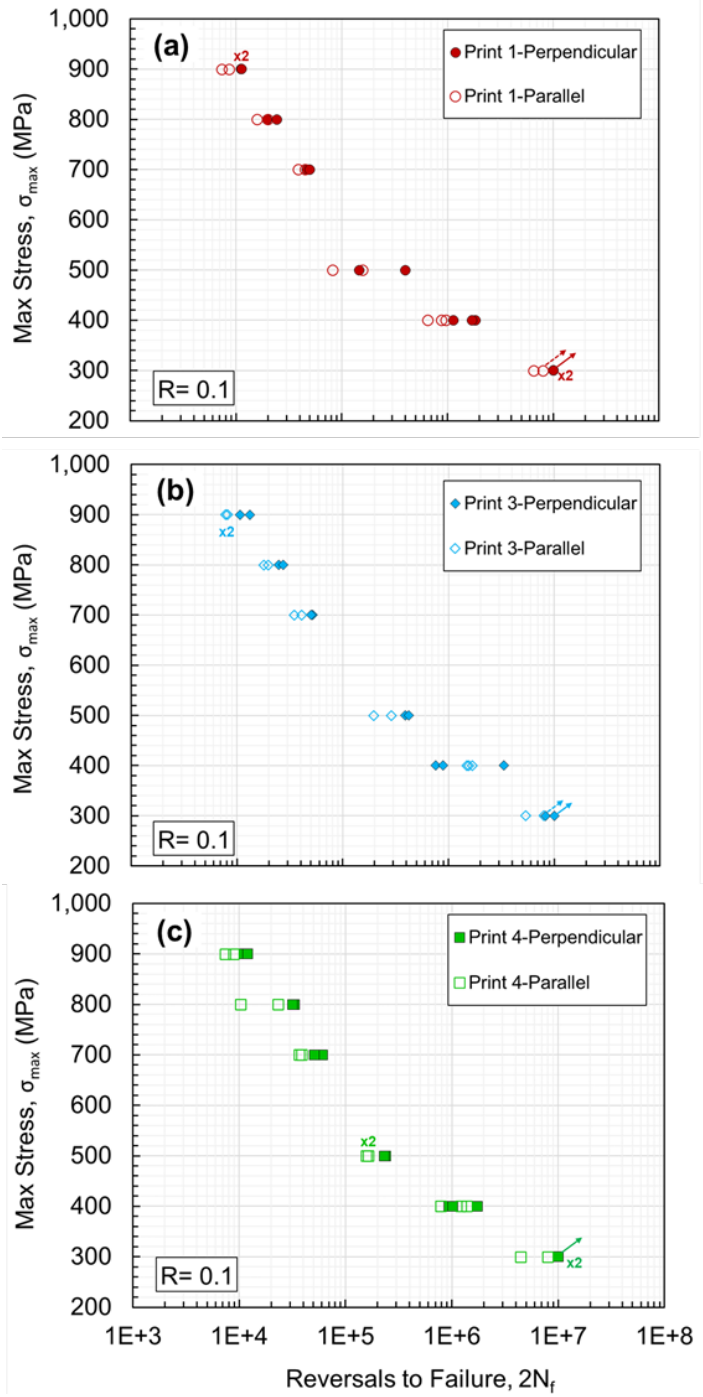

Fig. 55 Stress-life behaviors of (a) Print 1, (b) Print 3, and (c) Print 4 specimens in perpendicular and parallel orientations. All tests were force-controlled at $R_\sigma = 0.1$.

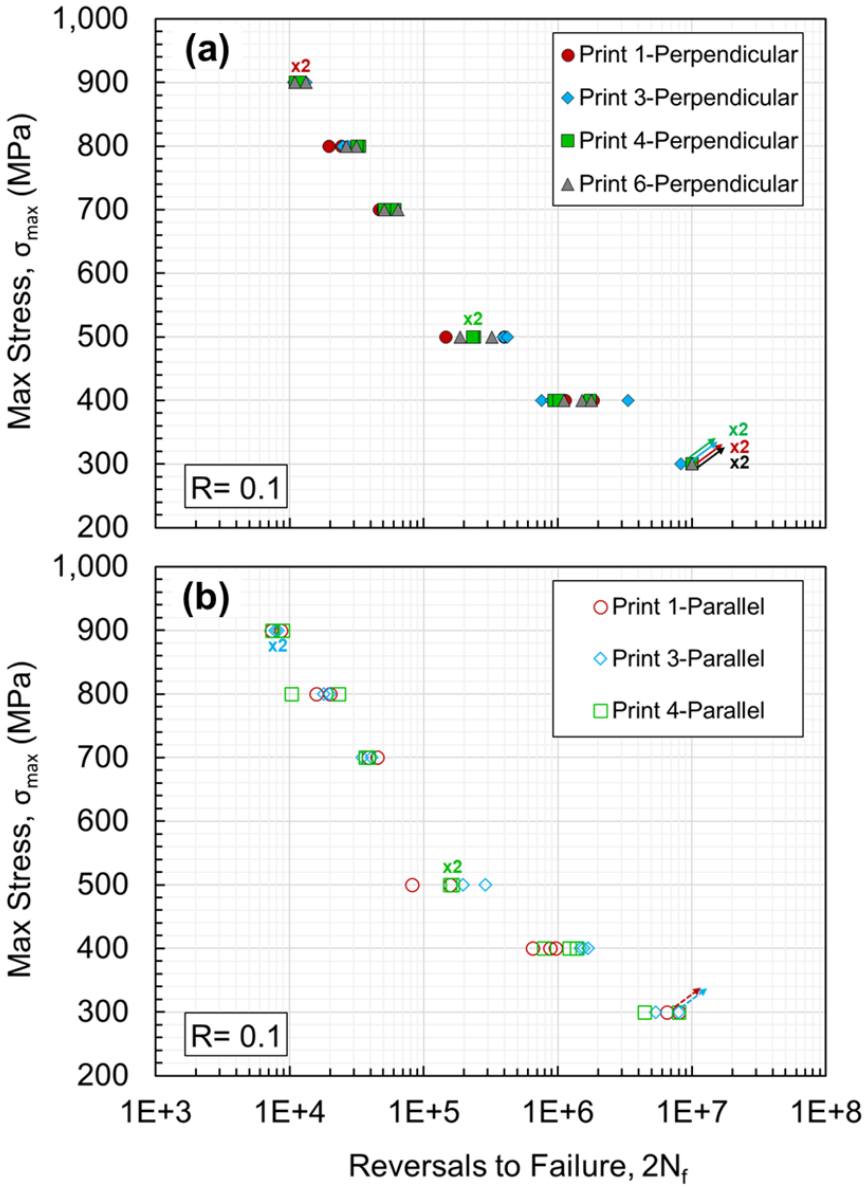

Fig. 56 Stress-life behaviors of Prints 1, 3, 4, and 6 specimens in (a) perpendicular and (b) parallel orientations. All tests were force-controlled at $R_\sigma = 0.1$.

Table 21 A summary of force-controlled fatigue test results ($R_\sigma = 0.1$) of LP-DED NASA HR-1 specimens for Prints 1, 3, 4, and 6.

σ_{max} (MPa)	$2N_{f,\ Perpendicular}$ (Reversals)	$2N_{f,\ Parallel}$ (Reversals)
	Print 1	
300	> 10,000,000	6,530,698
300	> 10,000,000	> 10,000,000
400	1,832,592	879,162
400	1,140,984	646,344
400	1,701,476	960,622

500	400,498	81,508
500	146,518	156,898
700	46,756	45,102
700	49,672	38,670
800	24,418	19,982
800	19,628	15,848
900	11,154	7,358
900	11,230	8,622
Print 3		
300	8,268,554	> 10,000,000
300	> 10,000,000	5,370,514
400	755,328	1,483,160
400	3,341,226	1,554,512
400	887,960	1,681,638
500	389,108	289,176
500	419,568	196,778
700	52,016	34,854
700	50,404	40,858
800	24,744	17,968
800	27,446	19,758
900	10,724	7,842
900	13,242	8,166
Print 4		
300	> 10,000,000	4,416,208
300	> 10,000,000	> 10,000,000
400	941,780	783,002
400	1,020,090	1,383,096
400	1,743,340	1,215,090
500	239,272	163,854
500	230,546	157,624
700	60,986	36,782
700	51,074	38,860
800	33,284	10,354
800	31,952	23,304
900	11,084	7,396
900	11,994	8,856
Print 6		
300	> 10,000,000	N/A
300	> 10,000,000	
400	1,522,910	
400	1,110,212	

400	1,781,876	
500	321,006	
500	186,326	
700	64,388	
700	50,776	
800	31,620	
800	26,494	
900	13,250	
900	10,918	

The fracture surfaces of some selected specimens were examined. All fatigue specimens, regardless of orientation, powder reuse, and stress level, had failure initiating from the surface. Some fracture surfaces of specimens tested at 500 MPa are shown in Fig. 57. Due to the presence of micro-notches on the surface, cracks were always initiated from the surface, as well as microstructural defects such as facets and gas-entrapped pores close to the surface, resulting in final fatigue failures [73,161]. In addition, dimples and striations were noted on fracture surfaces, which could indicate micro-void coalescence (MVC) fatigue crack growth mechanism, generally occurring in ductile materials [71].

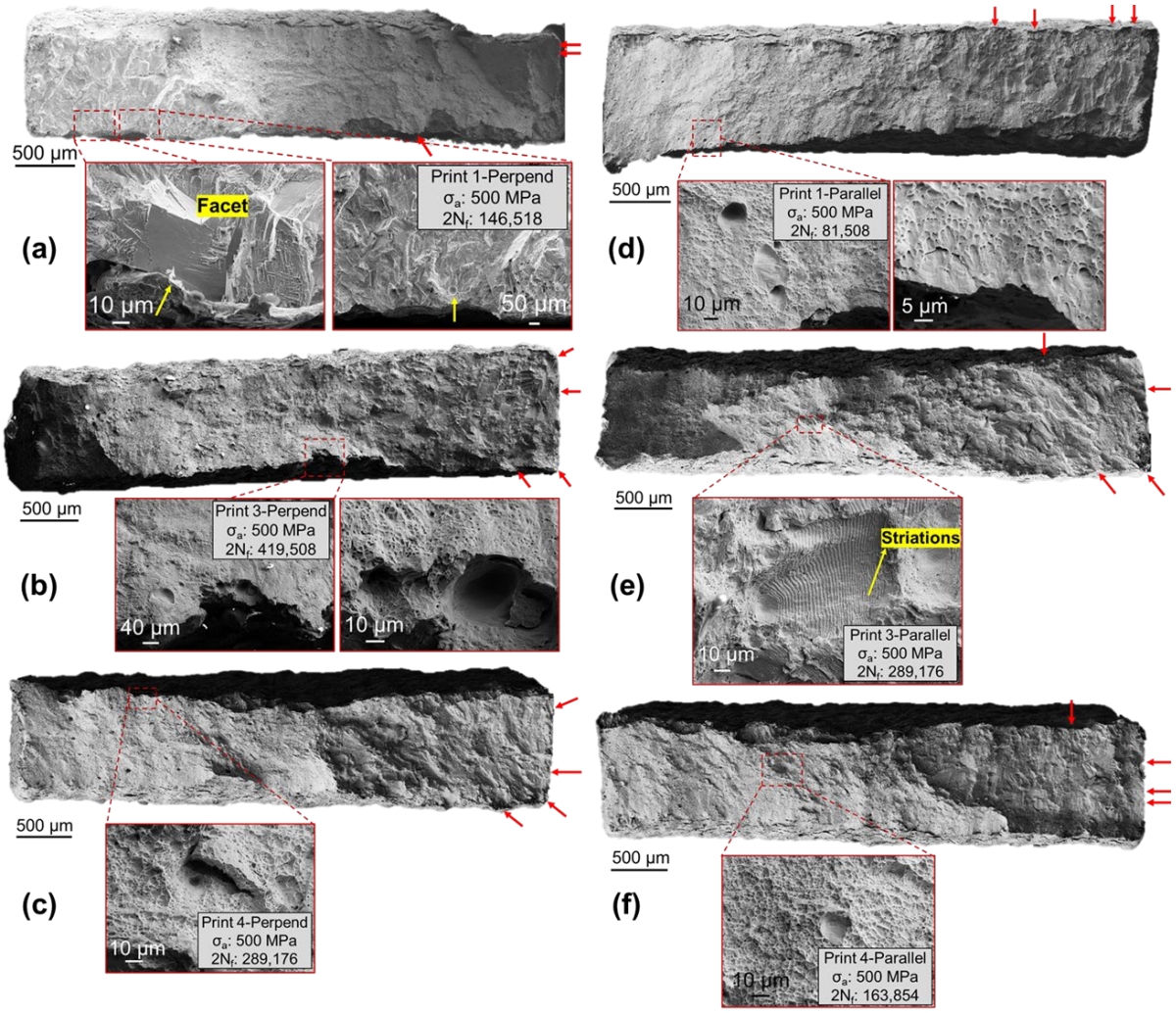

Fig. 57 Fracture surfaces of Prints 1, 3, and 4 fatigue specimens in (a-c) perpendicular and (d-f) parallel orientations. Crack initiation sites are illustrated with red arrows. Microstructural features are pointed with yellow arrows.

5.4. Discussion on Experimental Results

This study investigated the effects of powder reuse and specimen orientation on the mechanical properties of LP-DED NASA HR-1 parts. It was observed that powder characteristics, including flowability (see Fig. 48 and Table 17), did not change with powder reuse. This behavior might be counter-intuitive with PSD coarsening with powder reuse and reduction of finer particles [10]. However, it was noted that particle shape did not change with powder reuse, which dominated the effects of fine particles and their higher interparticle friction [26]. The similar powder flowability also resulted in similar defect content and surface roughness parameters in the LP-DED

NASA HR-1 parts with powder reuse (see Fig. 50 and Table 18). In addition, no change in O content was noted with powder reuse. Therefore, the comparable powder characteristics and chemical composition resulted in similar microstructures (see Fig. 51), consistent with the results in Ref. [28–31,33].

The similarities in the microstructure and O content, defects, and surface roughness resulted in somewhat comparable tensile strength with powder reuse (Fig. 53). Tensile ductility also did not change with powder reuse as the defect densities in all LP-DED NASA HR-1 specimens were higher than 99.997 ± 0.000 %, having minimal effects of defects on tensile ductility [162]. However, the specimens oriented parallel to the building direction had somewhat lower tensile ductility with more scatter among each batch than the perpendicular specimens. Similar observations were noted in Ref. [160], which reported that as-built specimens have generally lower effective Young's modulus due to undulations on the surface. When the layer orientation is normal to the tensile loading axis, such undulations will have additional weakening effects and result in lower tensile ductility.

The powder reuse did not influence the LCF and MCF performance of LP-DED NASA HR-1 specimens. This behavior can be explained by the similar microstructures of the parts. In the HCF regime, the powder reuse still did not reveal any clear trend in resistance to fatigue failures as the cracks always initiated from the micro-notches on the surface and dominated the fatigue failures (see Fig. 57). The surface roughness may get affected by powder characteristics. For instance, poor flowability may result in nonuniform powder deposition and higher surface roughness in some locations. However, powder flow did not change with reuse and resulted in similar S_a values (see Table 18). Unlike powder reuse, specimen orientation affected the fatigue performance.

In all prints, perpendicular specimens had somewhat higher LCF and MCF life than the parallel specimens. This behavior can be attributed to the more critical effects of surface undulations in parallel specimens when subjected to uniaxial tensile loadings due to accelerated crack initiation from the micro-notches [160]. The higher fatigue resistance of perpendicular specimens was also noted in the HCF regime; however, the difference was less significant compared with the scatter in the data. In this regime, the majority of fatigue life is spent in crack initiation, and therefore, micro-notches have more prominent effects [71]. To understand the effects of surface roughness parameters in different orientations, an effective elastic stress concentration factor, K_t, was used to estimate the fatigue performance based on Refs. [140,163], according to equations (1-3).

$$K_t = 1 + n(\frac{S_a}{\rho_{10}})(\frac{S_t}{SzISO}) \quad (1)$$

$$q = \frac{1}{1 + {\gamma}/{\rho_{10}}} \quad (2)$$

$$K_f = 1 + q(K_t - 1) \quad (3)$$

In the above equations, *n* corresponds to the stress state and equals 2 for the case of tension; γ is a material constant, and in some studies, the grain size was used as γ; S_t is the maximum distance between the peaks and valleys; S_{zISO} represents the 10-point height roughness [164]; and ρ_{10} evaluates the radii of the deepest valleys [140,163]. In addition, the following equations can be used to obtain the fatigue strength at 10^3 cycles, $\sigma'_{f,10^3}$, and endurance limit, σ_e,:

$$\sigma'_{f,10^3} = f * UTS \quad (4)$$

$$\sigma_e = k_a k_b k_c k_d k_e * 0.5 * UTS \quad (5)$$

Where f is the fraction of UTS at 10^3 cycles, and the Marin factors (k_a-k_e) can be estimated according to Ref. [165]. Therefore, the fatigue performance can be estimated by $\sigma'_{f,10^3}$ and σ_e. As

seen in Fig. 58. the fatigue performance estimation using the surface roughness parameters reasonably predicted the fatigue life with a factor of ± 3. All information for the fatigue life estimation is reported in Table 22.

Table 22 Surface roughness, fatigue parameters, and Marin factors used to estimate the fatigue performance of LP-DED NASA HR-1 Print 1 specimens.

Parameter	Print 1- Parallel	Print 1- Perpendicular
ρ_{10} (µm)	399	286
S_t (µm)	500	156
S_{zISO} (µm)	128	142
γ (µm)	63	56
q	0.86	0.84
K_t	1.29	1.12
K_f	1.25	1.10
f	0.81	0.81
$\sigma'_{f,10^3}$ (MPa)	784	762
K_a	0.45	0.45
K_b	1.00	1.00
K_c	0.85	0.85
K_d	1.00	1.00
K_e	0.87	0.87
S_e (MPa)	161	156

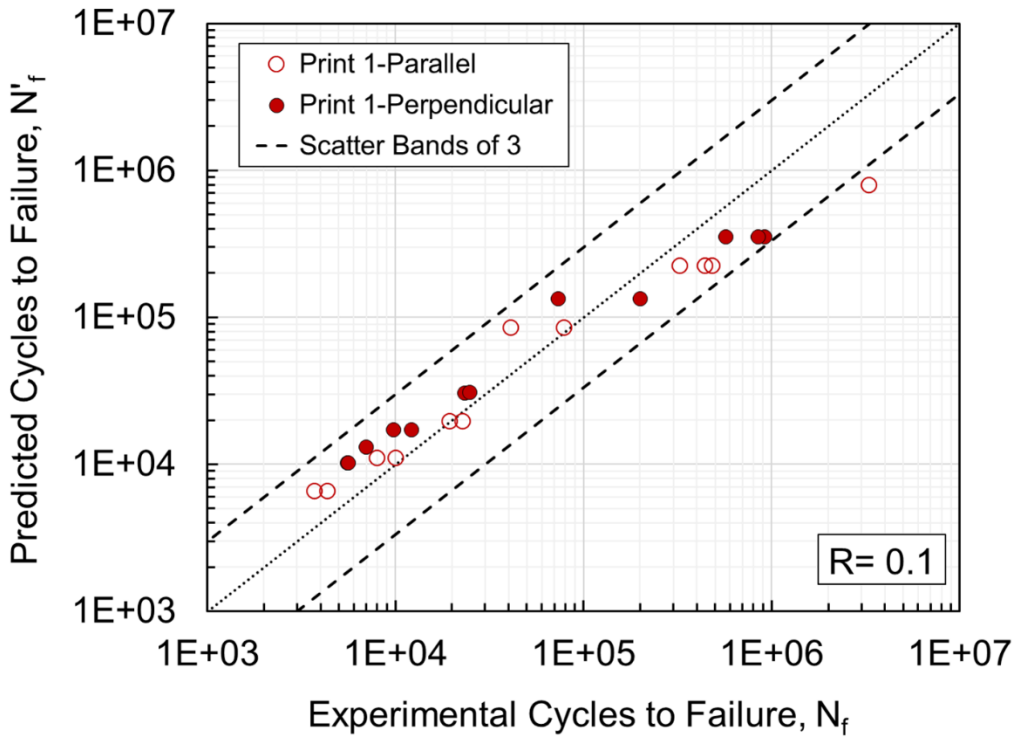

Fig. 58 Predicted fatigue life comparison with experiment for the NASA HR-1 Print 1 specimens in both parallel and perpendicular orientations.

5.5. Conclusions

This study investigated the effects of powder reuse and specimen orientation for LP-DED NASA HR-1 superalloy by examining the possible changes in microstructure, surface features, defect content, and mechanical properties as affected by reuse and orientation. Based on the results, the following conclusions can be drawn:

- The NASA HR-1 powder particle size distribution coarsened with powder reuse. However, the particle shape, including the circularity and elongation, did not alter.
- The similar powder flowability and O contents in the deposited materials resulted in comparable microstructures, defect contents, and surface roughness. All specimens had part densities higher than 99.997% and comparable 90th percentile sphere equivalent defect diameters.

- The heat treatment schedule completely diminished the material anisotropy, showing no effects of specimen orientation on the microstructure and grain size distribution of LP-DED NASA HR-1 specimens.
- Tensile strength did not vary with respect to powder reuse and specimen orientation due to similar, well-homogenized microstructures and O content. Tensile ductility also did not change with powder reuse. However, the specimens oriented parallel to the building direction showed slightly lower tensile ductility due to the more severe effect of surface undulations in parallel specimens.
- Fatigue performance was not affected by powder reuse in any fatigue life regimes, which was primarily ascribed to the similar surface roughness, defect contents and tensile properties of specimens from different prints. In addition, specimens perpendicular to the building direction showed somewhat higher fatigue performance due to the less detrimental effect of notches on the surface compared with parallel specimens.

6. Predicting Additive Manufacturing Powder Quality via an Artificial Neural Network

6.1. Introduction

Additive manufacturing (AM) has gained extensive attention from multiple industrial sectors, including biomedical and aerospace, due to compatibility with several alloys (e.g., titanium, stainless steel, aluminum, and nickel-based), lower fabrication lead time and structural weight, and more design freedom [3,12,32,166]. However, AM systems and parts demand different certifications from traditional methods (e.g., casting and forging), depending on the application criticality, which has hindered its broad adoption [167]. Indeed, certifying the AM systems requires a complete understanding of feedstock-process-structure-property-part performance relationships [1]. Notably, the feedstock-part performance correlation is one inseparable piece of such relationships, requiring in-depth analysis.

In several AM technologies, including laser or electron beam powder bed fusion (L-PBF or EB-PBF), laser powder directed energy deposition (LP-DED), and binder jetting, the material feedstock is in the form of powder. Hence, powder characteristics can significantly influence the mechanical properties of additively manufactured (AM) parts [9,10]. For instance, the powder is spread on the build plate in PBF technologies and compacted via a recoater/wiper/roller. Therefore, the powder's physical properties (e.g., packing state and flowability) can play a vital role in the quality of the AM process/parts. The packing state and flowability are primarily governed by the powder characteristics, including but not limited to particle shape and particle size distribution (PSD).

Some studies have reported the effects of particle shape and PSD on flowability, packing state, and mechanical properties. For instance, more spherical particles can generally result in superior flowability and packing state, smaller defects, and enhanced tensile properties [20,31]. Larger-sized particles can provide higher flowability, whereas finer particles can increase the part density

by filling the empty spaces between larger ones [19,31]. In addition, smaller defects and consequently higher fatigue lives were observed for the parts manufactured from the powders with lower span values (i.e., D_{90}-D_{10}/D_{50}) [33]. Although the effects of powder characteristics have been investigated, evaluating the flowability and packing state with a single metric can still be quite challenging [19]. Therefore, further investigation is needed to correlate different powder characteristics to assess powder flow and packing behavior.

In addition, merely focusing on experiments may not be cost-efficient [168,169]. For instance, evaluating rheological properties requires testing every powder batch multiple times to verify the results. Therefore, developing low-cost statistical methods, such as machine learning (ML) models, like neural networks, to assess powder quality can contribute to the faster adoption of AM technologies. To do this, some studies have combined 2D/3D image processing with clustering/regression algorithms to characterize the powder bed uniformity [170,171] or particle morphology [59,168,172–175]. However, there is no study on 3D image processing and evaluating powder flow and packing state. Therefore, the current study aimed to experimentally analyze the powder flow and packing and analytically score the powders based on their merit for AM technologies. Subsequently, an artificial neural network (ANN) was implemented to predict the score of several powders merely by evaluating their particle shape, PSD, and (potentially) rheological characteristics. Following the Introduction, Methodology, Results, Discussion, and Conclusions will be presented.

6.2. Methodology

A Freeman Technology powder rheometer (FT4) was used to determine powder rheological characteristics. The FT4 quantifies powder characteristics, including the basic flowability energy (BFE), specific energy (SE), aeration energy (AE), conditioned bulk density (CBD), tapped density (BDtap), compressibility (CPS), pressure drop (PD), and cohesion. The CPS is measured

as the ratio between powder bulk density in compressed and loose conditions. The PD illustrates how easily gas can permeate the powder bulk. Cohesion represents the shear stress required for the powder to flow. SE and BFE are measured when the FT4 blade travels upward or downward in the powder bulk, respectively. AE shows the resistance of the powder bed to fluidization when it is exposed to gas flow. The CBD is the bulk/apparent density of the powder in a loose (i.e., low-stress) condition, whereas the BDtap is the density in the consolidated state [20,31,62,176].

A few studies have attempted to correlate such powder characteristics via a single powder quality score [19,20,177]. For instance, in [19], the total score of the powder was defined as C_1×bulk score + C_2×rheological score + C_3×dynamic score, where C_1, C_2, and C_3 were weighting coefficients. In this equation, every property was normalized with its maximum value among different powder samples. Therefore, lower powder scores could indicate a more suitable powder for AM in terms of powder bed layer uniformity and defect content. In this study, as seen in Equ. (1), the bulk score was estimated by averaging the Hausner ratio (HR), defined as the ratio of BDtap to CBD and the Carr index (i.e., 100×(BDtap-CBD)/BDtap) similar to [19]. Typically, HRs higher than 1.40 and smaller than 1.25 can respectively indicate poor and superior powder flowability [10]. In addition, Carr indices lower than 10 represent excellent powder flowability.

$$Bulk\ score = (HR + Carr\ index)/2 \quad (1)$$

The rheological score was evaluated based on Equ. (2) by characterizing each sample at least three times to ensure the repeatability of the results. As seen in Equ. (2), an indirect PD effect on the rheological score was considered, whereas, in Ref. [20], a direct effect, and in Ref. [19], no effect was considered. Considering an indirect PD effect on the rheological score can be explained by the adverse correlation between PD and CPS. For instance, powders with a better packing state (i.e., lower CPS) generally present a tighter particle arrangement and, therefore, it becomes more

difficult for gas to permeate the powder bulk (i.e., higher PD) [20,33]. As the information regarding the dynamic score (e.g., angle of repose (AOR) and Hall flow rate [19]) was unavailable, it was neglected in this study. The total powder quality score was estimated by averaging the bulk (Equ. (1)) and rheological (Equ. (2)) scores.

$$Rheological\ score = (1/CBD + CPS + (1/PD) + SE + AE + BFE + Cohesion)/7 \quad (2)$$

Each powder sample was also mounted in an epoxy-resin solution and used for X-ray computed tomography (XCT). The XCT was conducted via a Zeiss Xradia 620 with 80 kV and 10 W and a voxel size of ~ 2 μm. The images were then reconstructed using the Zeiss built-in software and processed with ImageJ [156] and Dragonfly software for particle segmentation. At first, 3D images were converted to binary. Then, binarized images were used to calculate the Euclidean distance map. After creating the distance map, a threshold was considered to ensure one seed was selected for each particle and adjacent particles were not connected according to Ref. [59] in order to avoid the false detection of particles. Subsequently, the default watershed algorithm in Dragonfly was applied to the seeded images for segmentation. Finally, the $10^{th,}$ 50^{th}, and 90^{th} percentile particles' Feret diameters (i.e., $D_{f,10}$, $D_{f,50}$, and $D_{f,90}$) were obtained. In addition, the average sphericity (S_{avg}) and its standard deviation (S_{std}) were found by Equ. (3) where V is the volume and A is the surface area of each particle.

$$S = \frac{\pi^{1/3}(6 * V)^{2/3}}{A} \quad (3)$$

A feed-forward ANN multi-layer perceptron (MLP) model was used to predict the powder quality. This model generally consists of input, hidden, and output layers. The desired features (n) regarding powder characteristics are fed into the input layer. Therefore, the input vector has a $x =$

$(x_1, x_2, \dots, x_n)$ structure. Every x_i variable is then assigned a coefficient weight and transferred to the hidden layers. In these layers, there are perceptrons/neurons which are trained via a supervised-learning back propagation algorithm [178–181]. The back propagation algorithm generally contains two phases: forward and backward. In the forward phase, the input vector, x is routed in the model to the hidden and ultimately output layers. In this regard, an error is measured every time as the difference between the desired and actual outputs. In the second phase, i.e., backward, the error is moved backward in the model to alter the model parameters and increase its accuracy [178–181]. The neurons function to determine the weighting coefficients vectors, w, to calculate the sum of the input features and their corresponding weight coefficient. Note that each neuron will calculate a weight vector which has the length of its inputs; that is, each neuron in the first layer calculates n weights, then each one in the second layer calculates as many weights as there are neurons in the first layer (40 in this case), and so on.

Lastly, the processed data is routed to the output layer, and the output vector, y , is approximated with a continuous function. In this study, the MLP model was structured with an input, two hidden, and output layers. Each hidden layer contained 40 neurons, and sigmoid and relu (i.e., step) functions were employed for the first and second hidden layers, respectively. A linear activation function with a single neuron was also used for the output layer as the goal was to predict the powder quality with one numeric value. The initial weight coefficients were estimated via a truncated normal distribution (also known as he_normal). Moreover, the loss function was evaluated using the mean absolute percentage error (MAPE) after 1024 epochs and a batch size of 32. The MAPE was assessed according to Equ. (4), where N is the number of observations in the testing set.

$$MAPE = \frac{1}{N}\sum_{i=1}^{N}\left|\frac{(d_i - y_i)}{d_i}\right| \quad (4)$$

In this equation, the d_i and y_i are the true and forecasted responses, respectively. The model schematic is illustrated in Fig. 59. This figure shows that there were 14, 40, 40, and 1 neuron per input, first and second hidden, and output layers, respectively. It needs to be stated that the model contained 600 parameters in the first hidden layer (14 input × 40 neurons + 40 bias), 1640 parameters in the second hidden layer (40 input × 40 neurons + 40 bias), and 41 parameters in the output layer (40 input × 1 neuron + 1 bias). The number of neurons in each layer and the type of activation functions were obtained by experimentally evaluating the MAPE and selecting the values that minimized the MAPE. In addition, 1024 epochs were initially selected for the model; however, the model generally converged after 200 epochs.

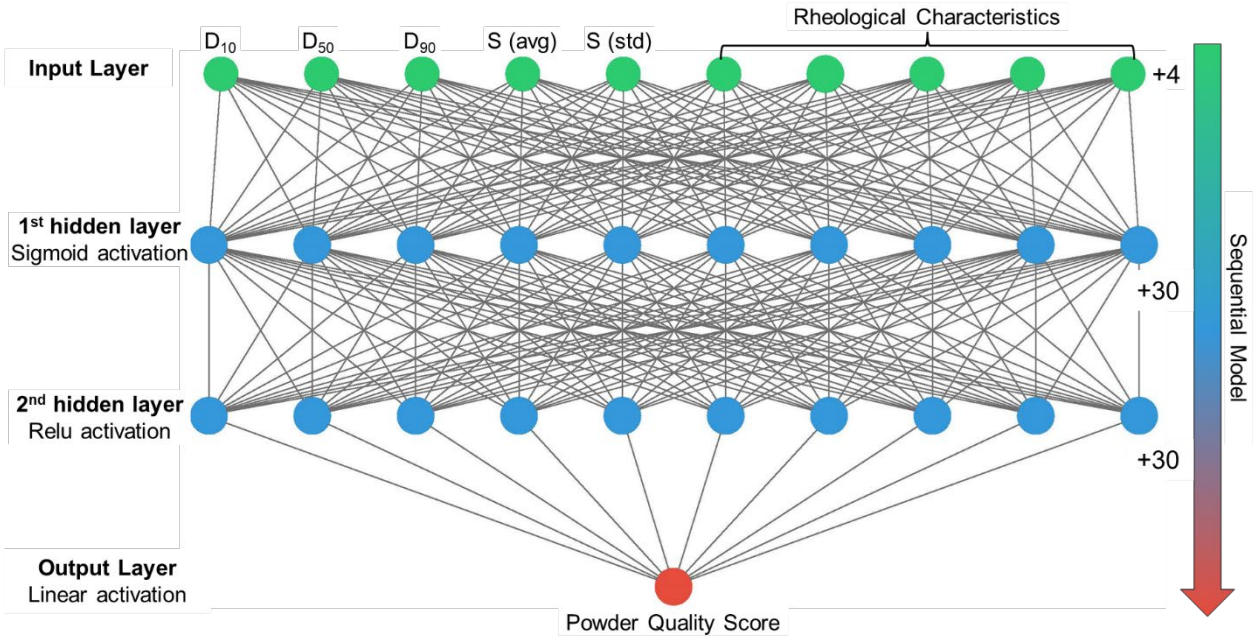

Fig. 59 The schematic of the ANN used in this study.

6.3. Results

6.3.1. Powder Scoring

The powder quality scores were evaluated for Ti-6Al-4V (Ti64) powder in its 0-times reused (0x-reused) as well as 3x- and 7x-reused conditions, and NASA HR-1 powder in its 0x-, 1x-, 2x-,

3x-, 4x-, 5x-reused states. Moreover, the quality scores of the powders used in [19,20,31,33] for AM fabrication were also evaluated. The bulk and rheological scores as well as the total score (i.e., the average of bulk and rheological scores) are reported in Table 23, which will be used in Section 0 for the ANN predictions.

Table 23 The bulk, rheological, and total scores for Ti64 and NASA HR-1 powders in their different reused conditions as well as the powders employed in Refs. [19,20,31,33].

Powder	Bulk Score	Rheological Score	Total Score
Ti64			
0x	1.00	0.99	1.00
3x	0.89	0.92	0.91
7x	0.89	0.85	0.87
NASA HR-1			
0x	1.00	0.92	0.96
1x	0.80	0.98	0.89
2x	0.79	0.90	0.85
3x	0.73	0.97	0.85
4x	0.80	0.93	0.86
5x	0.87	0.88	0.87
Ti64 [20]			
1	1.00	1.00	1.00
2	0.82	0.73	0.78
3	0.84	0.78	0.81
Ti64 [19]			
A	0.78	0.72	0.75
B	0.83	0.86	0.84
C	0.84	0.80	0.82
D	0.94	0.90	0.92
E	1.00	0.99	1.00
F	0.83	0.79	0.81
Ti64 [31]			
Fine	0.44	0.96	0.70
Coarse	0.47	1.00	0.74
17-4 PH (SS) [33]			
0x	1.00	1.00	1.00
14x	0.72	0.87	0.79

6.3.2. Image Processing

The segmentation process in Dragonfly was repeated for every 150 XCT slices, giving a total of 31 samples. The PSD and S were evaluated for each sample and reported in Table 24. The data

in this table was used as part of the input for the ANN. This table also includes the information collected about the powders from Refs. [9–12], which were later used for additional testing of the ANN. In addition, examples of Ti64 powder PSDs are also shown in Fig. 2 in their 0x-, 3x-, and 7x-reused conditions.

Table 24 Powder properties, including the $D_{f,x}$ values, and S obtained from the XCT using the watershed algorithm as well as the Refs. [19,20,31,33].

Powder (Sample No.)	**$D_{f,10}$**	**$D_{f,50}$**	**$D_{f,90}$**	**S_{avg} & S_{std}**
Ti64				
0x (#1)	23.86	37.34	59.73	0.95 ± 0.08
3x (#7)	22.91	36.64	58.89	0.95 ± 0.07
7x (#17)	17.48	28.47	52.60	0.96 ± 0.08
NASA HR-1				
0x (#21)	13.55	64.48	88.36	0.95 ± 0.11
1x (#23)	27.67	65.20	87.27	0.95 ± 0.11
2x (#25)	49.05	67.85	90.83	0.94 ± 0.13
3x (#26)	46.95	68.78	91.58	0.94 ± 0.12
4x (#28)	52.79	69.33	92.69	0.94 ± 0.13
5x (#30)	54.08	71.18	94.56	0.94 ± 0.13
Ti64 [20]				
1 (#32)	25.30	35.80	46.40	0.73 ± 0.18
2 (#33)	25.90	36.70	50.30	0.88 ± 0.15
3 (#34)	20.30	32.70	43.90	0.79 ± 0.16
Ti64 [19]				
A (#35)	46.30	63.15	91.30	0.90 ± 0.10
B (#36)	44.73	59.21	85.37	0.90 ± 0.10
C (#37)	42.84	55.24	72.95	0.90 ± 0.10
D (#38)	38.86	54.95	82.19	0.90 ± 0.10
E (#39)	27.82	44.19	68.10	0.90 ± 0.10
F (#40)	23.37	33.06	48.63	0.90 ± 0.01
Ti64 [31]				
15-45 µm (Fine) (#43)	21.75	34.85	47.86	0.95 ± 0.08
15-53 µm (Coarse) (#44)	23.84	45.43	57.28	0.95 ± 0.08
17-4 PH Stainless Steel (SS) [33]				
0x (#41)	14.19	32.16	70.78	0.87 ± 0.08
14x (#42)	15.70	31.01	59.69	0.88 ± 0.08

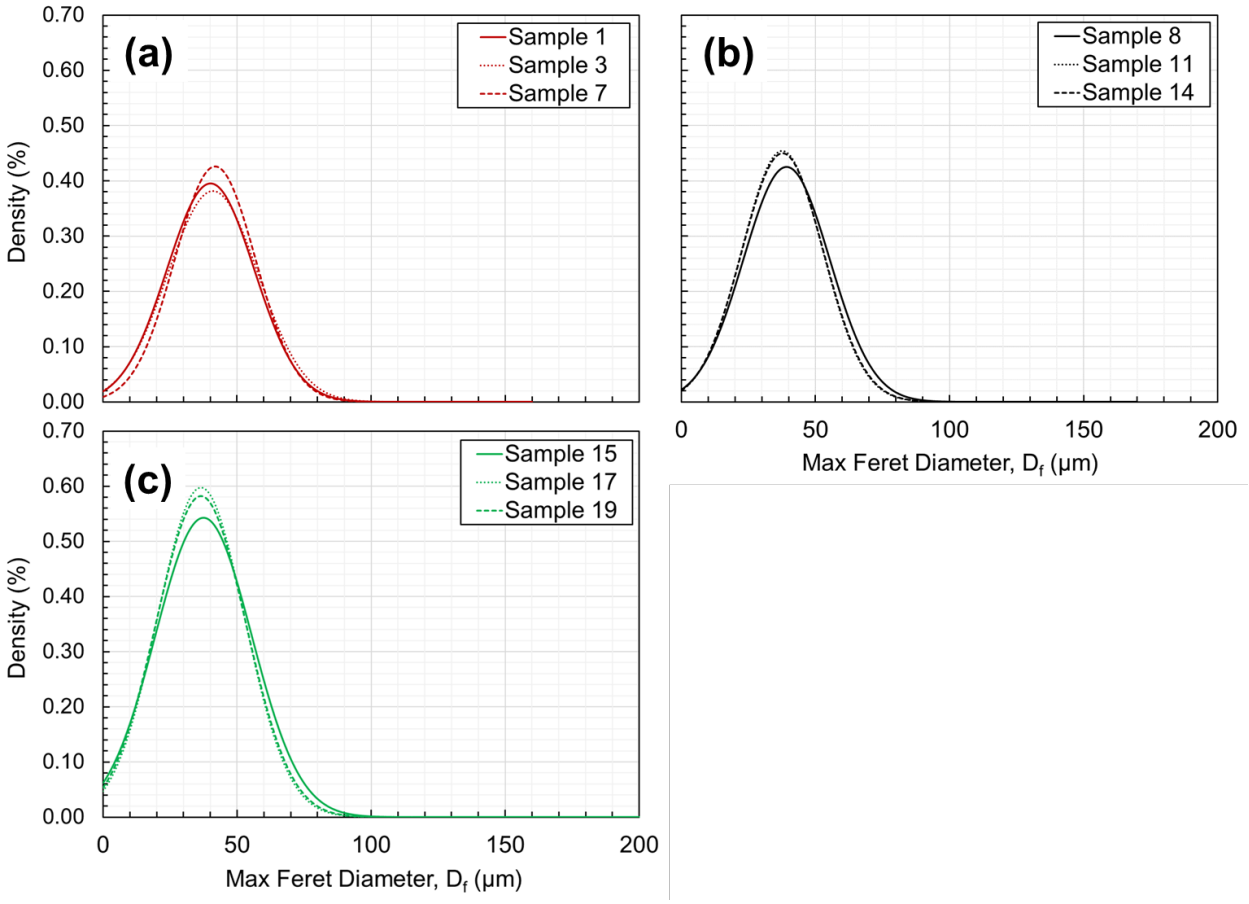

Fig. 60 Ti64 powder PSD in (a) 0x-, (b) 3x-, and (c) 7x-reused conditions obtained from the XCT analysis.

6.3.3. ANN Predictions

All the information obtained in Sections 6.3.1 and 0 was used as the ANN's input material (see the supplemental material for the ANN structure). The data was separated into two datasets. The first dataset (31 samples) only contained the 0x-, 3x-, and 7x-resued Ti64 and 0x-, 1x-, 2x-, 3x-, 4x-, and 5x-reused NASA HR-1 powders, which were used for training and testing. 70% of the first dataset was randomly selected to train the network, and the remainder was dedicated to testing. The dataset was input into the model to predict the total quality scores. As seen in Fig. 61, the predicted scores were compared with the test data. The model could effectively predict the total scores with high fidelity. The MAPE in this evaluation was ~ 1.3%. It needs to be stated that the MAPE value was computed by only considering the differences between predictions and the test

data and excluding the training set information. The same ANN model was also used to predict the total powder score for the data available in Refs. [19,20,31,33] in the second dataset. As seen in Fig. 62, the model could still reasonably predict the total powder quality scores. In this situation, the MAPE was higher and ~ 14.1%. A summary of all the predictions is reported in Table 25.

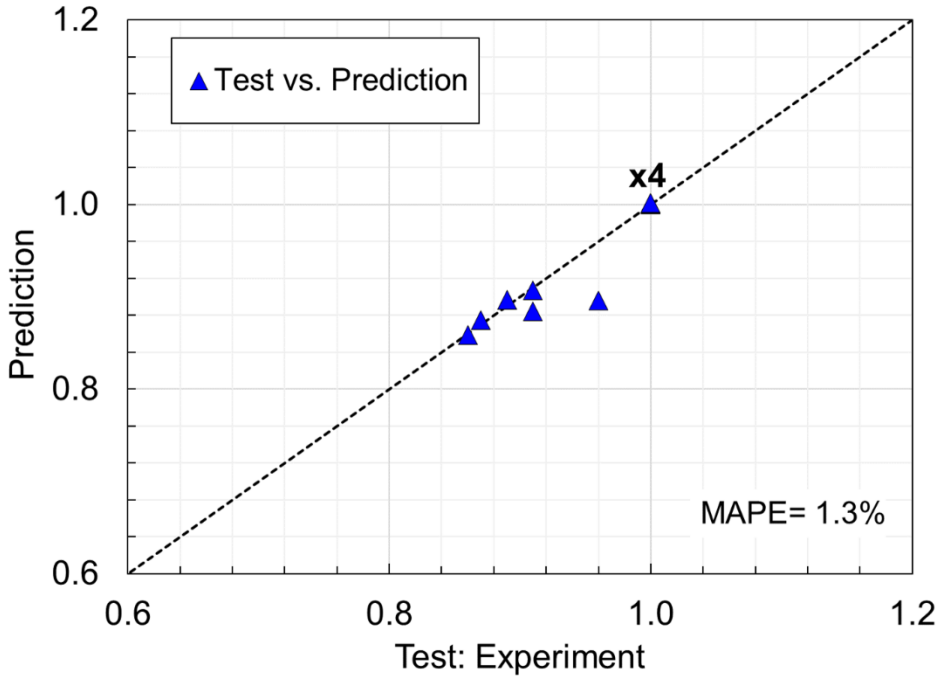

Fig. 61 Comparison between the experiment and ANN predictions.

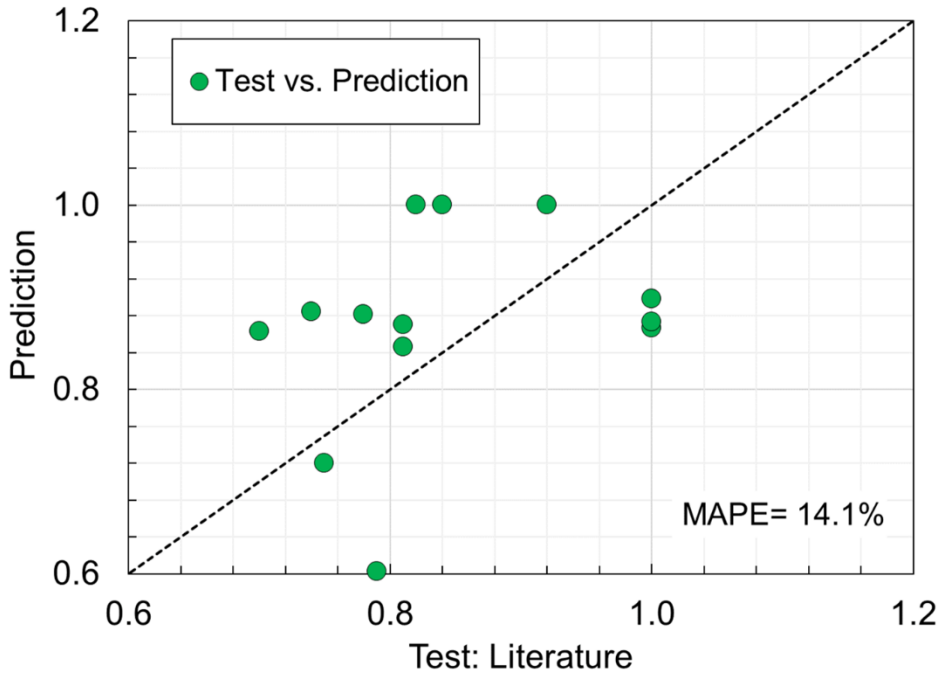

Fig. 62 Comparison between the data in Refs. [19,20,31,33] and ANN predictions.

Table 25 A summary of the total powder quality scores obtained from the experiment and ANN model.

Test	True Value	Prediction	Difference (%)
Experiment			
1	1.00	1.00	0.00
2	1.00	1.00	0.08
3	1.00	1.00	0.07
4	1.00	1.00	0.19
5	0.96	0.90	-6.62
6	0.91	0.88	-2.85
7	0.91	0.91	-0.33
8	0.89	0.90	0.73
9	0.87	0.87	0.56
10	0.86	0.86	-0.19
Literature [19,20,31,33]			
1	1.00	0.87	-13.32
2	1.00	0.87	-12.65
3	1.00	0.90	-10.17
4	0.92	1.00	8.70
5	0.84	1.00	19.05
6	0.82	1.00	21.95
7	0.81	0.85	4.45
8	0.81	0.87	7.47
9	0.79	0.60	-23.76
10	0.78	0.88	13.01

11	0.75	0.72	-3.99
12	0.74	0.88	19.45
13	0.70	0.86	23.33

6.4. Discussion

In this study, a powder metric was proposed to estimate the powder quality scores. This powder quality score originated based on the work done in literature [19,20], and further modifications were applied. It was noted that the proposed powder quality metric could effectively integrate all powder bulk and rheological characteristics. For instance, the total powder quality score for the 0x- and 14x-reused 17-4 PH SS powders were 1.00 and 0.79, respectively. Therefore, the lower quality score of 14x-reused powder could indicate its higher suitability for AM fabrication. This understanding of the powder score correlated well with the lower defect content and enhanced mechanical properties of L-PBF 14x-reused 17-4 PH SS specimens in Ref. [33]. In that study, larger and more frequent defects were reported for the specimens manufactured using the 0x-reused powder, resulting in lower fatigue performance than those fabricated using the 14x-reused one.

In some cases, such as the fine and coarse Ti64 powders used in Ref. [31], the total powder quality scores were 0.70 and 0.74, respectively. The fine powder's lower quality score matched its better packing state and identical flowability to that of the coarse powder in Ref. [31]. However, larger-sized defects were reported in Ref. [31] for the fine powder specimens, although they generally possessed fewer total defects. Such counter-intuitive understanding (i.e., better packing state but larger defects) was attributed to the higher oxygen (O) content when the fine powder was used for fabrication, promoting spattering during fabrication and resulting in large defects. It should be noted that the proposed powder quality metric in this study did not incorporate the effects of chemical composition on the bulk score. Therefore, one potential improvement of this method

is considering the detrimental effects of interstitial elements such as O and nitrogen (N) on material density.

Additionally, in this study, an artificial neural network was proposed to predict the powder quality scores solely by using the powder information, including its particle shape, PSD, and rheological characteristics. It was noted that the model could effectively predict the quality scores with a small MAPE value. This model was also applied to different powders used in the literature [19,20,31,33], and still, a reasonable prediction was obtained. However, the relative error was greater than for the powders tested as part of this study. Some sources of observing larger errors when the model was applied to literate data could include insufficient test data. Therefore, more experiments are suggested for training and testing the model. Another reason is that there are not many pieces of literature reporting such information. Lastly, some data points in the literature were missing, which were assumed an average value to run the model, but these can cause worse prediction quality.

Furthermore, an experiment was conducted on whether merely considering particle shape and PSD without considering the rheological characteristics can still efficiently predict the quality scores. In this situation, the MAPE was ~ 4.1%, indicating reasonable predictions with less powder information, which can further decrease experimental costs (see Fig. 63(a)). Interestingly, the MAPE decreased to ~ 11.1% for the literature data when rheological properties were not considered (see Fig. 63(b)), justifying that the previously observed larger error was likely due to the missing rheological data from the literature, which was replaced by averages to run the model.

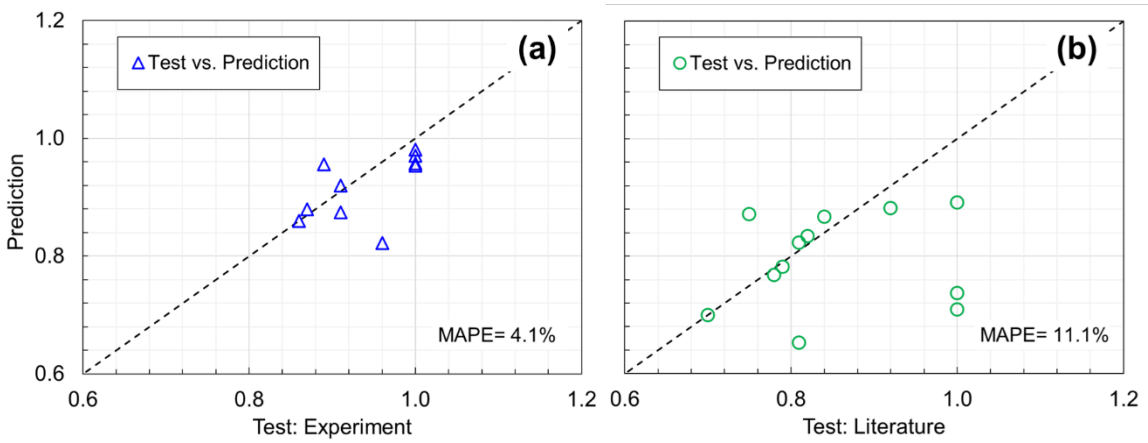

Fig. 63 Comparison between the test data and ANN predictions for the (a) experiments and (b) Refs. [19,20,31,33], without considering rheological characteristics.

6.5. Conclusions

This study investigated the feasibility of a powder quality metric and prediction using an ANN. Different powders were analyzed using XCT to obtain PSD and sphericity. The total powder quality score was defined as the average powder bulk and rheological scores. The bulk score was estimated via the HR and Carr index, which were obtained based on powder bulk and tapped densities. The powder rheological score was evaluated using rheological characteristics, such as BFE, SE, PD, CPS, cohesion, and AE, to correlate with the flowability and packing state of the powder. It was found that the current quality metric still needs further modifications. One suggestion was to consider the effects of chemical compositions, such as the concentration of O in the powder. Some powders such as Ti64 are sensitive to O, and a higher O content can jeopardize the final AM part quality and endanger build consistency and material ductility.

In addition, it was feasible to use the rheological characteristics, PSD, and particle shape to train and test an ANN model, enabling the powder quality score predictions with high fidelity. Developing such low-cost statistical tools is essential to decrease the AM costs to a competitive point to conventional manufacturing methods (e.g., casting and forging) [182,183]. These methods can significantly contribute toward faster adoption of AM and rapid qualification and certification

of AM powders/parts. It should be emphasized that feeding more samples into the ANN can result in higher accuracies being obtained. Therefore, systematic data storage is essential for AM to capture powder feedstock information. Moreover, in the situations where some data is missing, fewer input data that only includes the particle shape and PSD might be more practical and result in more accurate predictions.

7. Summary

In this dissertation, the effects of different powder characteristics on the mechanical properties of additively manufactured (AM) parts were investigated to shed light on the relationships between powder feedstock and part performance. The outcomes of this dissertation can contribute to our knowledge and faster industrywide adoption of laser-based additive manufacturing (AM) technologies utilizing powder feedstock. These understandings are vital as humans have encountered critical issues while living on Earth. These challenges include but are not limited to air pollution and depletion of energy sources. Scientists have declared two approaches to protect and preserve the Earth. One approach is to be efficient. Efficiency is defined as reducing our energy consumption by all means. For instance, we are now employing reusable launch space vehicles to decrease CO_2 generation. Heavy components are replaced with cellular structures to reduce the structural weight and fuel consumption.

The second approach is to investigate the viability of living in other complementary locations to Earth. Several government agencies and industrial sectors are currently exploring livability in remote colonies in outer space. Such colonies will need their manufacturing departments to generate parts and components as required due to the extensive costs of space travel. In addition, using the material resources in space is feasible instead of carrying them from the Earth. Therefore, AM technologies can play a beneficial role in both approaches. AM technology can be a green fabrication technology alternative to conventional subtractive methods. This technology can significantly decrease material waste, accounting for a significant portion of unsustainable energy and the supply chain, limiting it to on-demand production.

Moreover, AM technology can be employed to reuse/recycle raw materials. For instance, powder feedstock may be used several times without re-processing it. Functional parts can be repaired using AM without the need for reproduction. Therefore, AM technologies can decrease

our dependency on nonrenewable energy sources. However, there are also several challenges associated with this technology. The AM parts typically possess defects and anisotropic microstructures. Therefore, this distinct micro-/defect-structure needs to be thoroughly characterized. There are other challenges; for example, how often the powder feedstock can be reused or recycled. Which powder characteristics are more critical? How should the parts be located on the build plate concerning powder spreadability to ensure consistent mechanical properties? Can we decrease our experimental efforts and estimate the powder quality and mechanical properties using predictive models?

This dissertation aimed to address some of these questions by defining multiple objectives. The first objective was the effects of the particle size distribution (PSD) and particle shape on mechanical properties. To achieve this objective, two plasma atomized Ti-6Al-4V (Ti64) powders with normal and bimodal PSDs and with highly spherical particles were used. The normal PSD consisted of finer particles, whereas there was a peak of coarse particles in the bimodal PSD. Powder flowability and packing state, defect content, microstructure, and mechanical properties were investigated. It was found that a bimodal PSD of 15-53 μm (i.e., coarse powder) could result in similar flowability owing to the high sphericity of particles and a slightly lower packing state than the normal PSD of 15-45 μm (i.e., fine powder). The higher packing state of the fine powder also resulted in fewer defects in Ti64 parts manufactured with the laser powder bed fusion (L-PBF/LB-PBF). However, careful investigations revealed the existence of some large defects in the specimens manufactured using the fine powder.

Since the packing state of the fine powder was somewhat better, the chemical compositions were analyzed in both powders. It was noted that the fine powder had higher O content due to the higher surface-to-volume ratio of particles. Therefore, a higher spattering phenomenon (i.e.,

ejection of powder particles or liquid droplets from the melt pool) was anticipated when the fine powder was used for fabrication. The spattering resulted in large lack-of-fusion defects in the specimens. When fatigue resistance of the specimens after machining the surface was evaluated, the coarse powder specimens represented an improved mid-cycle-fatigue (MCF) performance and some improvement in the high-cycle-fatigue (HCF) regime. However, when the specimens were manufactured net-shaped and tested without any post-fabrication surface treatment, no difference in fatigue performance was observed, which was attributed to the two sets of specimens having similar surface roughness characteristics.

The ultimate tensile and yield strengths were almost comparable for specimens manufactured from both powders. The similar tensile strength was attributed to the microstructure, which did not change with altering the PSD of the powder. The tensile ductility, however, was higher for the coarse powder specimens. Although the coarse powder specimens had a higher number of defects, the defect sizes were smaller than the fine powder specimens. Such large defects in fine powder specimens resulted in somewhat lower ductility. In contrast, the tensile failure in coarse powder specimens was due to the coalescence of microvoids which ultimately resulted in dimples and a cup and cone tensile fracture. This study showed that statistical tools such as the Gumbel distribution could effectively interpret the distribution of critical defects and their effects on fatigue performance. The information obtained from the Gumbel distribution was used to predict the largest critical defects for each powder when used for fabrication.

Lastly, the mechanical properties of AM parts along the powder spreading direction were consistent, and no change was observed. Therefore, it was deduced that highly spherical powder particles could dominate the effects of PSD and result in a more uniform powder bed layer and no interruption in the powder spreadability. The outcomes of this study disclosed that using a wider

PSD which typically is less expensive, can still result in comparable or even superior mechanical properties provided that the PSD is wisely customized and carefully selected for each AM material system. When the effects of PSD and particle shape were understood, the changes in powder and mechanical properties with powder reuse were traced. In this regard, plasma atomized Ti64 powder with a nominal PSD of 15-53 μm was used to fabricate a set of specimens. After fabrication, the unused and used powder was collected and cleaned out of contamination using a sieve filtration for manufacturing additional specimens. This process was repeated until 8 sets were fabricated, and the powder was insufficient for subsequent iterations. It was noted that continuously reusing the powder could enhance the powder flowability due to the reduction of finer particles and packing state because of the reduction of agglomerates from the batch.

Interestingly, a lower defect content was observed in the witness coupons manufactured using the 3-times reused powder compared with the unused powder due to the improved packing state. However, as the powder was further reused (i.e., 7-times), the defect content increased again. Therefore, the chemical composition of the unused, 3-times, and 7-times reused powders were measured. It was noted that the O content gradually increased with powder reuse. Therefore, when considering the effects of powder reuse, the changes in chemical composition must also be considered. The increase in O content most likely resulted in more spattering during fabrication, and consequently, larger defects in the specimens placed downstream of the argon flow (i.e., near the gas outlet). These specimens possessed higher strength, lower ductility, and worse fatigue performance than those located upstream (i.e., near the gas inlet). The separation between the fatigue performance of upstream and downstream specimens was considerable for the 3-times reused powder. However, further powder reuse to 7-times increased spattering in all locations of the build plate, and the upstream specimens also showed relatively low fatigue performance.

Therefore, further powder reuse might be limited depending on the material, the packing state, flowability, and chemical composition.

The microstructure of the parts manufactured from unused and reused powders was similar. However, the tensile strength was slightly higher for the reused powder specimens due to the higher O content in the reused batch. The outcomes of this investigation showed some sources of variability during the AM fabrication, which needs to be understood. In addition, controlling such variabilities by altering the process parameters (e.g., argon flow speed, gas type, layer thickness, and laser power) can further contribute to the qualification and certification of AM parts. Different material systems, including argon atomized 17-4 precipitation hardened (PH) stainless steel (SS) powder, were also analyzed after identifying the effects of powder reuse with highly spherical powders. The powder fabricated using argon atomization is typically less expensive than plasma atomized powder and generally consists of spherical and irregular particles that might jeopardize the powder bed layer uniformity in the L-PBF process. Hence, 15 batches of specimens were manufactured in the east (i.e., closer to the feedstock bin) and west (i.e., farther away from the feedstock bin) of the build plate using the unused and continuously reused powders up to 14-times.

Powder flowability and packing state improved with powder reuse upon analyzing the powder characteristics, which was attributed to the reduction of finer particles and agglomerates. The higher packing state of reused powder enhanced the fatigue performance of L-PBF 17-4 PH SS parts due to smaller defects in the specimens. Unlike Ti64, the O content did not change with powder reuse practice; therefore, no effect on spattering was expected. The tensile strength was also similar between all batches. However, the tensile ductility was somewhat higher for the reused powder specimens, which could be attributed to the fewer and smaller-sized defects in these batches. In addition, the specimens in the east and west showed inconsistent fatigue performance

due to the irregularly-shaped particles in both batches, impeding the powder flow. This inconsistency was more severe for the unused powder and alleviated by continuously reusing the powder due to increased flowability resulting in a more uniform powder bed layer. The results of this investigation uncovered the importance of powder handling/reconditioning practices. Repeatable mechanical properties may be obtained by standardizing the powder reuse practices.

The investigation of powder characteristics' effects on mechanical properties was further expanded to the laser powder directed energy deposition (LP-DED) process. A significant amount of powder is accumulated after LP-DED fabrication when higher build feature resolutions are desired due to the low capture efficiency of LP-DED machines. Therefore, reusing the powder in LP-DED is inevitable to decrease the manufacturing costs. Thus, 6 sets of thin walls were manufactured from the NASA HR-1 superalloy. The NASA HR-1 thin walls are commonly used in liquid rocket engine applications, necessitating powder reuse inspections. In addition, the tensile and fatigue specimens were excised in multiple orientations, i.e., parallel and perpendicular to the building direction, to analyze the orientation effects as well. In LP-DED technology, the powder is blown instead of spreading as in L-PBF technology. Therefore, the powder packing state might not be as critical as the powder flowability. Regarding the powder flowability, a minor improvement was noted in the 5-times reused powder compared with the unused one, which was attributed to the PSD coarsening; the mean particle size increased, and finer particles decreased with reusing the powder.

No variation was noted in the chemical composition and the surface roughness due to the negligible changes in powder flowability with powder reuse and uniform powder deposition. No difference was observed in the tensile strength, which was attributed to the similar microstructures and O content of LP-DED NASA HR-1 parts. Tensile ductility did not change with powder reuse

in either orientation. However, the specimens cut parallel to the building direction (i.e., layers were normal to the tensile loading axis) generally showed a lower ductility than perpendicular specimens as a consequence of surface undulations in net-shaped specimens. The low-cycle-fatigue (LCF), MCF, and HCF performances were almost comparable for all the batches. Moreover, the critical defect sizes were similar in all prints, ascribed to the similar powder flowability.

Upon investigation of the fracture surfaces, it was noted that the fatigue crack growth mechanism was ductile for specimens from all powders due to microvoids and striations on the fracture surface. In addition, perpendicularly oriented specimens showed slightly higher fatigue performance than the parallel oriented ones, owing to the less weakening effect of surface undulations in this orientation. The outcomes of this investigation showed that the effects of powder flowability and packing state in LP-DED might differ from PBF technologies. In addition, several quality metrics are essential to evaluate powders for each AM process. In the previous chapter, it was noticed that such powder quality metrics could be well correlated with the observed mechanical properties.

In addition, to reduce the experimental costs regarding powder characterization and AM fabrications, an artificial neural network was created. This neural network could predict powder quality scores by inputting the powder information, including its PSD, particle sphericity, and rheological characteristics. This information can be obtained by 3D or 2D image processing of the powder particles and rheological analysis via a small powder quantity. It was observed that the proposed network could efficiently predict powder flow and packing behavior during fabrication. However, further modifications to the powder quality metric and training the model with more datasets can improve the model's accuracy. Overall, the lessons learned from this dissertation can

help us to select an appropriate powder for each AM process and understand the sources of variabilities to obtain more repeatable mechanical properties.

8. Supplement A

8.1. Heat-Affected (HA) Powder Collection

Some powder samples were collected from the regions in the proximity of the gas flow outlet/downstream to investigate the laser-powder interactions and how the particles change during the laser powder bed fusion (L-PBF) fabrication. The collection area is schematically illustrated in Fig. 64. This area was selected as the region of interest based on [67].

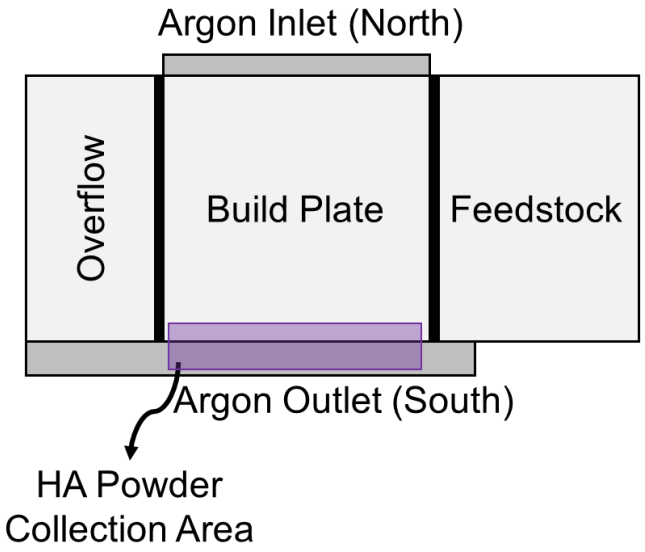

Fig. 64 Schematic illustration of HA powder collection area.

8.2. Surface Roughness of the L-PBF Ti-6Al-4V (Ti64) Parts

The arithmetical mean height of the profiled surface, S_a, was investigated on the X-ray computed tomography (XCT) coupons using a Keyence VHX-6000 digital optical microscope by considering a constant area on each side (4×0.85 mm^2). As seen in Fig. 65, the surface roughness generally increased with reusing the powder, meaning that the Print 1 coupons had the lowest S_a, followed by Print 4 and 8, which might be attributed to the PSD changes as well as melt pool instabilities due to increased O and N, as reported in [119]. Concerning the location on the build plate, coupons located at the center had the lowest S_a regardless of powder condition. The lowest surface roughness at this location can be attributed to the highest power density of the laser at the center and the complete melting of powder particles [184]. In addition, the surface roughness was consistently lower for the coupons located in the east compared with the counterparts in the west. The variation in surface roughness along the recoating direction can be due to the slight particle segregation on the build plate and colonies of coarser particles in the west [31]. However, no clear trend in surface roughness was observed in the direction of argon gas flow.

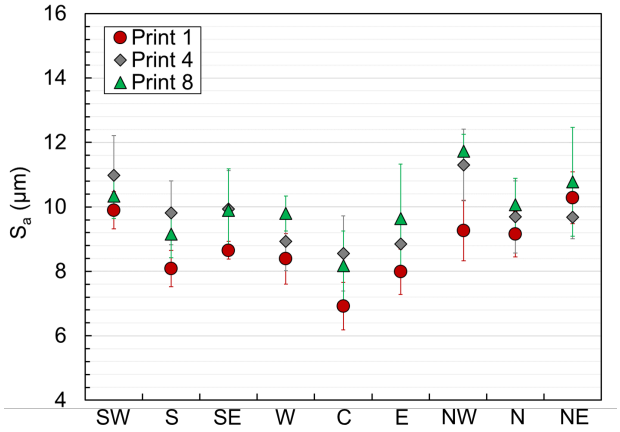

Fig. 65 The S_a values of the XCT coupons across the build plate for different prints.

8.3. Location of the Defects in XCT Coupons

The defect location inside XCT coupons was analyzed with respect to powder reuse and the location on the build plate. In this approach, the defect density heat maps were projected from the 3D reconstructed images onto the 2D plane. Therefore, all defects within the coupons at different layer heights and radial distances from the centerline were collected and presented. In Fig. 66, the x-axis represents the distance between the centerline and the edge, and the y-axis corresponds to the height along the building direction. No clear trend in defect location concerning powder reuse or the location on the build plate was observed. Most defects were at 1-2 mm proximity to the centerline.

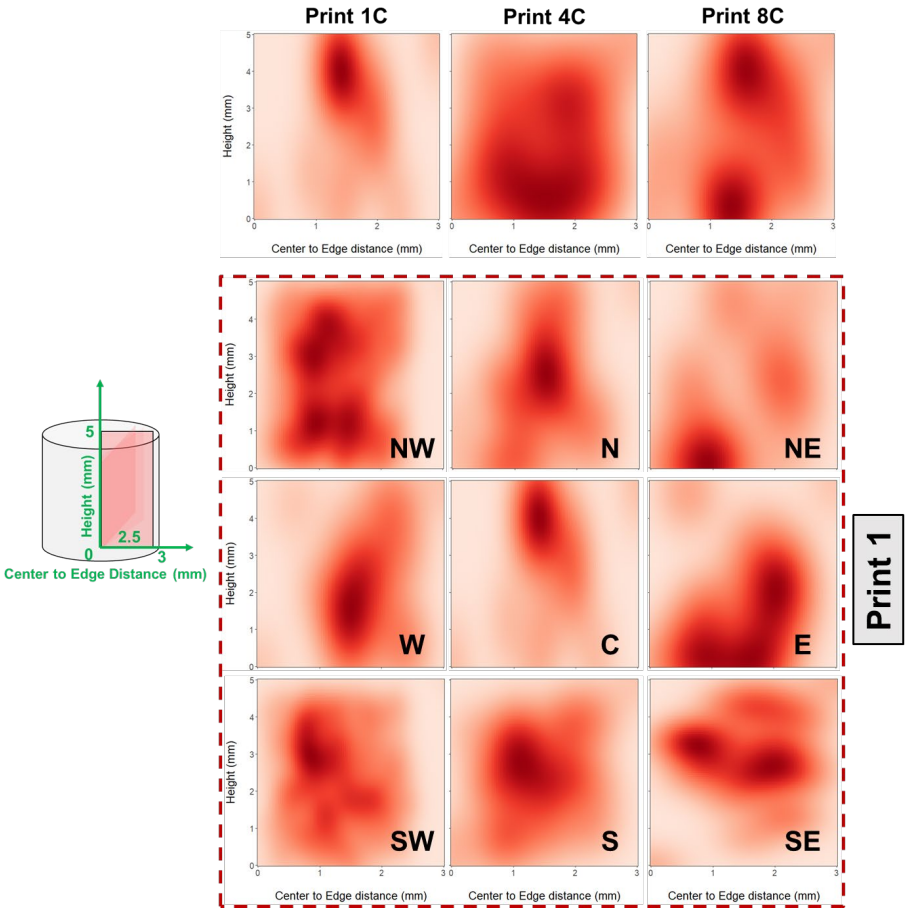

Fig. 66 2D-projected defect density heat maps from 3D images for different prints and locations on the build plate.

8.4. Details on High Strain-Rate Fracture Study

Currently, there is not much information about fracture toughness and the effects of strain-rate on AM Ti64 parts [109–111,185]. In [109], net-shaped compact tension (CT) specimens were fabricated in different build layer orientations and tested in SR and heat-treated (HT) conditions to obtain the fracture toughness, K_{IC}. A considerable variation was noted when the specimens were tested in their non-heat-treated condition, which was attributed to the microstructural anisotropy. However, this disparity was largely alleviated when the test specimens were stress relieved. When the specimens were heat-treated, the K_{IC} increased due to microstructural changes with heat treatment [32]. In another study [111], compression and tensile tests were performed at two different strain-rates, namely 0.001 s^{-1} (i.e., quasi-static) and 1000 s^{-1} (i.e., high strain-rate). The Ti64 material toughness (i.e., the area underneath the strain-strain curve) increased with the strain-rate, and ductility reduced under compression. Regarding the tensile loading, the effects of strain-rates were marginal, and its influence was only observed in the fracture path and surface morphology. In [111], the authors observed a cup and cone failure mode when the specimens were tested under quasi-static tensile conditions. On the other hand, the fracture surfaces were aligned with the maximum shear plane when tested at high strain-rates.

In the present work, the fracture behavior of L-PBF Ti64 parts was investigated under high strain-rate loading conditions (500 s^{-1}). The specimens were oriented horizontally (loading axis and crack were perpendicular to the build plate (Fig. 1(a)) on the build plate in different locations to study the effects of both powder reuse and location. A hybrid digital image correlation (DIC)-finite element (FE) approach was used to obtain the fracture parameters. Earlier techniques based on this concept have involved applying the measured displacements from full-field optical methods as boundary conditions into FE sub-models [186–189]. The particular hybrid methodology has been shown previously to capture the fracture parameters with a high degree of

fidelity in polymeric and metallic materials processed using traditional and AM methods under static and dynamic loading conditions [113,190,191].

High strain-rate fracture specimens for this study were built horizontally. That is, the loading axis was perpendicular to the build plate. The geometry of high strain-rate fracture specimens consisted of frustum-shaped pins to load the specimen in the symmetric three-point bend configuration. This design was favored over integrating the pins into the loading apparatus due to simplicity. The strategy of performing full-field optical measurements directly on the specimens facilitated this approach even though pins deform during the loading event. A crack of 6 mm in length and 150 μm in width was inserted into the specimen using a diamond saw. Subsequently, the specimens were sprayed with mists of black and white paint to create random speckles on one of the two surfaces to perform DIC and measure in-plane deformations.

A Kolsky compression pressure bar apparatus [112] was used for testing under high strain-rate conditions. Two C350 maraging steel long-bars of length 2.4 m and diameter 25.4 mm were used as incident and transmission bars. A maraging steel striker rod with a length of 305 mm and a diameter of 25.4 mm was propelled from the barrel of a gas gun to impact the incident bar and generate stress waves. The other end of the incident bar had a flat profile and was in contact with the central loading pin of the specimen. The opposing edge of the specimen with two loading pins was in contact with the flat profile of the transmission bar. All three loading pins were kept in contact with the two bars before the loading event. In order to hold the specimen between the two bars from slipping down due to gravity, a block of soft putty was used as a support. Due to the low acoustic impedance of the putty block, an approximately free surface condition was achieved. For acoustic symmetry relative to the loading axis, another putty block was pressed on the top edge of

the specimen. In all experiments, the striker velocity was set at ~40 m/s, and all the dynamic deformations were captured with a Kirana-05M ultrahigh-speed camera.

The DIC method was used to measure full-field in-plane deformations on Ti64 specimens in the vicinity of a growing crack tip [112,192–194]. The displacement components can be numerically differentiated to find spatial gradients of deformations and strain fields. The *J*-integral [195,196] can be calculated using the standard line integration approach using the expression,

$$J = \lim_{\Gamma \to 0} \int_{\Gamma} \left(W \delta_{1i} - \sigma_{ij} \frac{\partial u_j}{\partial x_1} \right) n_i dC, (i, j = 1,2; x_1 = x, x_2 = y) \qquad (1)$$

that requires spatial derivatives of displacement components. In the above equation, W is the strain energy density, σ_{ij} and u_j are the Cartesian components of Cauchy stress ($\sigma_{11} = \sigma_{xx}, \sigma_{12} = \sigma_{xy}$) and displacement components ($u_1 = u, u_2 = v$), respectively. In Eq. (1), n_i is the unit vector component normal to the counterclockwise contour path Γ, δ_{1i} is the Kronecker delta and dC is the incremental arc length along the contour path. The *J*-integral is often evaluated as a path-independent line integral. Instead, it can also be expressed as area integrals in planar geometries.

It should be noted that when compared to the traditional optical methods of finding fracture parameters by employing measured deformations in conjunction with the theoretical crack tip fields and over-deterministic least-squares analysis [192,193,197,198], the *J*-integral approach does not depend on fitting a field description to measurements. Moreover, in the traditional approach, the measured fracture parameters are generally sensitive to different factors, including the number of terms of the asymptotic displacement field employed, the rigid body motions suffered by the specimen during loading, the domain over which data is extracted, the out-of-plane displacements due to crack tip triaxiality. The results are also often sensitive to locating the crack tip amidst speckles and from the displacement field. Considering these issues, a more straightforward method of transferring the two measured orthogonal displacement data arrays from

DIC into a FE discretization as surface boundary conditions to compute the *J*-integral using the domain (area) integral representation of Eq. (1) is employed using,

$$J = \int_A \left(-W\delta_{1i} + \sigma_{ij} \frac{\partial u_j}{\partial x_1} \right) \frac{\partial q_1}{\partial x_1} dA, (i, j = 1,2) \qquad (2)$$

in the above equation, A is the area of the ribbon of elements encircling the crack tip, q_1 is a sufficiently smooth weighting function, and all other parameters are as defined previously.

During experiments, random speckle images were recorded by the camera in the reference (undeformed) and deformed states. These images were then segmented into subsets of gray scales for carrying out DIC. The displaced location of each subset in the deformed state is subsequently determined relative to its reference state using a grayscale correlation algorithm. The displacement data at the center of each subset is computed over the whole region of interest. To implement the proposed approach to compute the *J*-integral, the domain was discretized. The locations where displacements were determined matched the nodal locations in the FE model consisting of a square grid of quadrilateral elements parallel perpendicular to the specimen edges. However, it should also be noted that when the crack followed a kinked path relative to its initial orientation after crack initiation, the neighborhood of the crack (regions adjacent to the crack flanks) was discretized along with a band and the interpolated displacements obtained from DIC subsets were inputted at the FE nodes. The crack tip was modeled as a sharp discontinuity for simplicity. Since the measured displacements were used as input to the FE model to dictate the post-processing of DIC data and find the *J*-integral, the sharpness of the crack tip in the model is unimportant. A flowchart of all the steps followed during the *J*-integral evaluation is shown in Fig. 67. First, experimentally measured displacement components were imported as nodal boundary conditions. Then, the model was run using ABAQUS structural analysis software (v.16.1) after identifying the current crack tip position and its orientation to extract the energy release rate using in-built

algorithms. The stress-strain curves, obtained from the tensile tests, were used to run an elastoplastic analysis in FE and evaluate the *J*-integral.

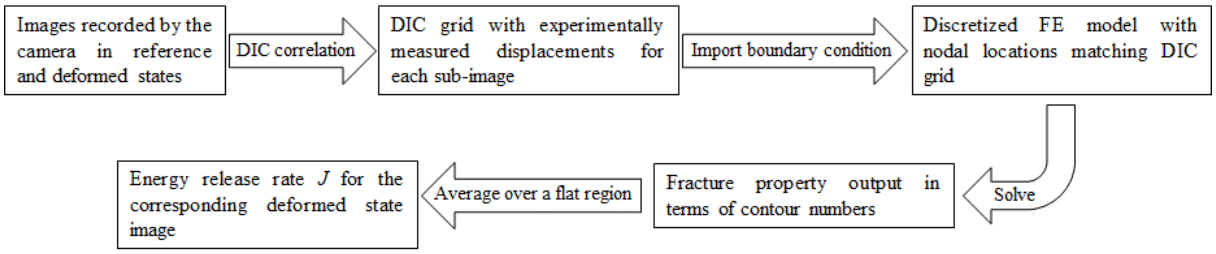

Fig. 67 Flowchart depicting the hybrid DIC-FE approach.

ABAQUS outputs fracture parameters for different rings/contours of elements around the crack tip. The first output corresponds to the ring of elements encircling the crack tip and the second one includes the first and the second rings, and so on. As the contour number increases, the radial extent of the domain around the crack tip used for computing the *J*-integral increases. Since the discretization corresponds to the overlap between neighboring subsets used while performing DIC (subset size = 25 pixels and adjacent subset overlap = 5 pixels, scale factor or the optical magnification ~ 30 μm/pixel), each additional ring corresponds to the radial increment of sub-image overlap × the scale factor. An example speckle image and displacement contours obtained from DIC are shown in Fig. 68. It can be observed that the *u*-fields are symmetric relative to the loading axis (along the *x*-axis). Similarly, *v*-fields are symmetric; however, they are antisymmetric in magnitude relative to the loading axis.

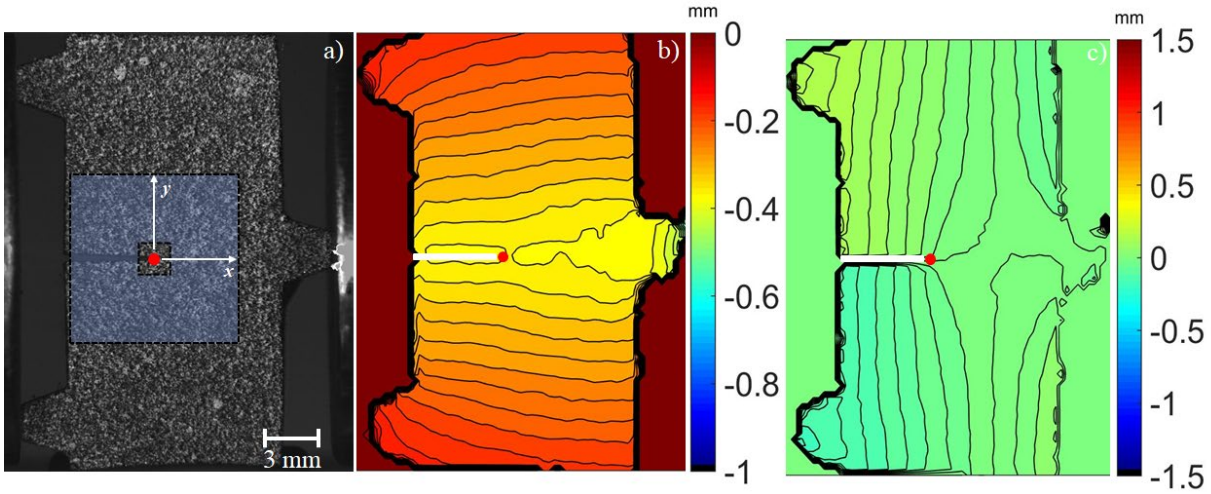

Fig. 68 (a) Speckle image captured at 400,000 fps, (b) u-field and (c) v-field displacement contours from DIC, contour interval = 20 μm. The particular time instant shown here is before crack initiation. Red dots indicate the crack tip location at this time instant.

An example plot of the *J*-integral values for different contours and radial distances from the crack tip at the instant of crack initiation is shown in Fig. 69. The values do not show path independence in the very close vicinity of the crack tip (for up to contour #7 or radial extent of ~1 mm) due to a combination of crack tip triaxiality, inelastic deformations violating small scale yielding assumptions, and the finite size of elements and shape functions used, among others. However, at larger distances of 1.5-5.5 mm (r/B ratio of 0.4-1.3, where r is the radial distance from the crack tip and B is the specimen thickness) away from the crack tip, the values are rather stable and nearly constant with an acceptable variation of ~5%. These stable values, averaged over contours 10-33 or 1.5 mm-5.5 mm (shaded region in Fig. 68), were recovered as the instantaneous *J*-integral. A summary of other experimental parameters used for 2D DIC is listed in Table 1.

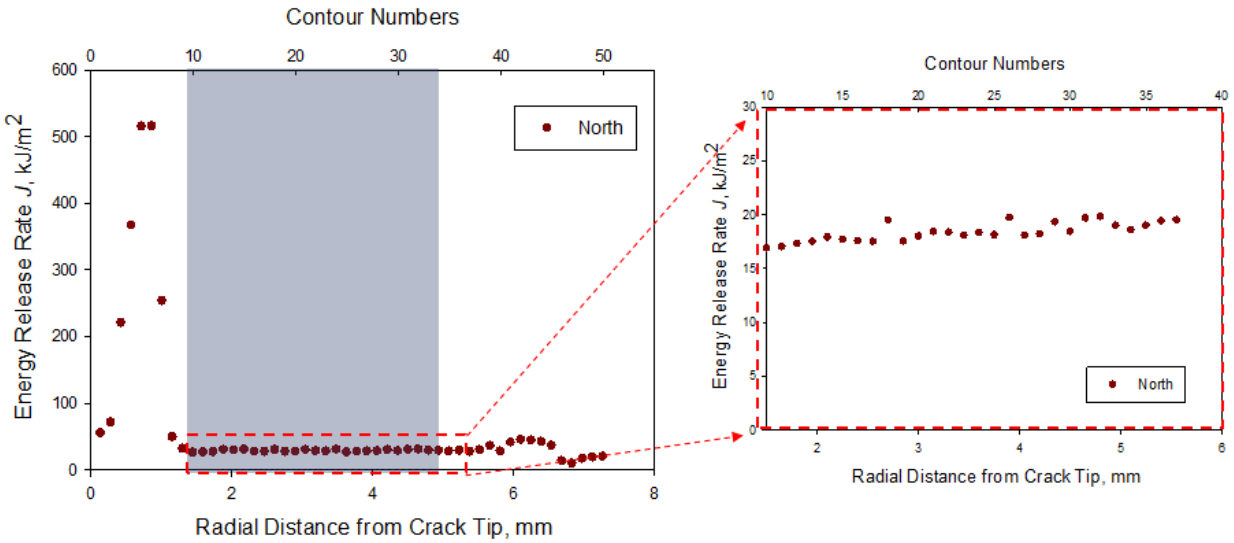

Fig. 69 Computation of the J-integral: Plot of J for different contour numbers (left). Contour #10-37, corresponding to 1.5-5.5 mm or r/B ratio of 0.4-1.3 are used consistently for all load steps. (The reported data corresponds to the shaded part where the J-value varies by < 5%). An enlarged view of the averaged plateau region is also shown on the right.

Table 1 DIC parameters summary.

Hardware Parameters		**Analysis Parameters**	
Camera Manufacturer Model Image Resolution	Kirana-05M 924×768 pixels	Software Manufacturer	Aramis® 6.2.0 GOM
Lens Focal Length	Nikon 80-400 mm	Image Filtering	None
FOV	33 mm × 26 mm	Sub-image/Subset	25 × 25
Image Scale	33.3 pixel/mm	Step Size	5
Stereo-Angle	N/A	Subset Shape Function	Affine
Stand-Off Distance	0.6 m	Data Processing and Filtering for QOIs	None
Image Acquisition Rate	400,000 fps	Noise-floor and Bias of QOIs	2 µm
Patterning Technique	Spray painted		
Approx. Feature Size	3 pixels		

Fig. S7 and S8 show the *J*-integral histories and crack growth resistance curves for Prints 4 and print 8, respectively. In both cases, the energy release rate had a monotonic increase until crack

initiation, followed by crack growth under steady-state conditions. Stable crack growth could be better inferred from the crack growth resistance curves. The fracture behaviors for Prints 4 and 8 followed the observed behavior of Print 1 with the exception of higher critical energy release rates in Prints 4 and 8. However, north and south specimens exhibited no difference when looking at the location dependency on the build plate for Prints 4 and 8. The same trend was also observed in Print 1.

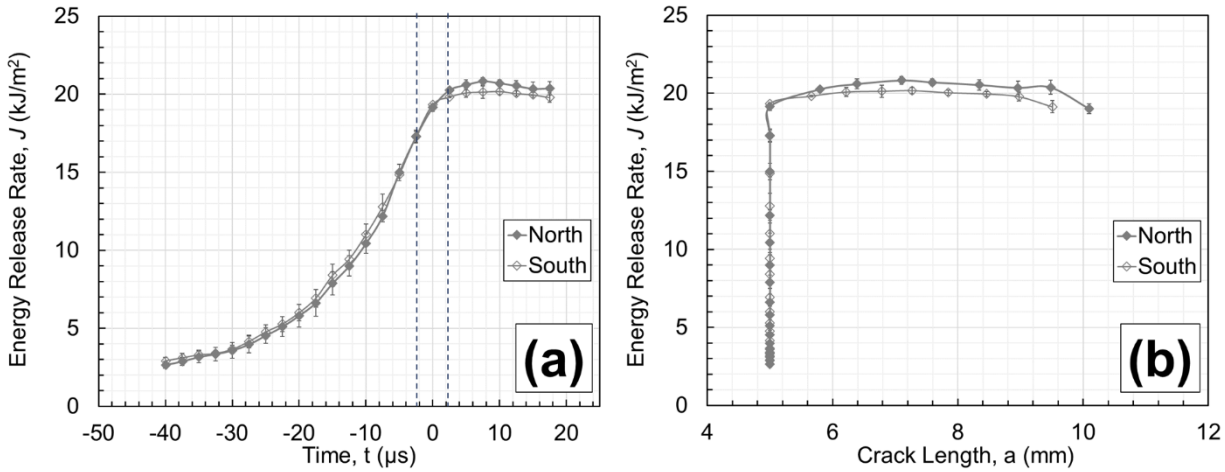

Fig. 70 The J-integral history (a) and crack growth resistance curves (b) for Ti64 specimens from Print 4 in the north and south locations of the build plate.

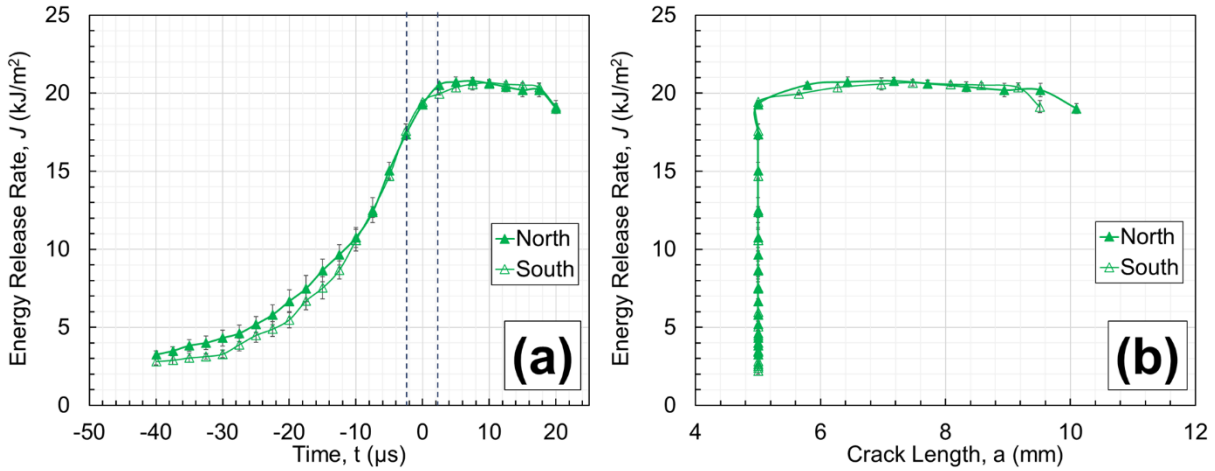

Fig. 71 The J-integral history (a) and crack growth resistance curves (b) for Ti64 specimens from Print 8 in the north and south locations of the build plate.

8.5. Chemical Composition on the Fracture Surface

The chemical composition on the fracture surfaces of fatigue specimens was investigated to understand why south specimens had relatively shorter fatigue lives. Some nonmetallic inclusions such as oxides (e.g., Al_2O_3), carbides (e.g., TiC), and ceramics (e.g., SiO_2) were detected at or close to the volumetric defects (see Fig. 72). These inclusions were most likley formed due to spattering [31], an unstable melt pool, or vapor-induced particle entrapment [199]. These spatter-induced inclusions could considerably degrade the fatigue performance regardless of their type by preventing the proper fusion between successive layers [120]. In addition, such nonmetallic inclusions were more frequently noted on the fracture surface of reused powder specimens in the south due to a higher probability of spatters and melt pool ejecta landing in the south region [106], accompanied by the higher O content of reused batches.

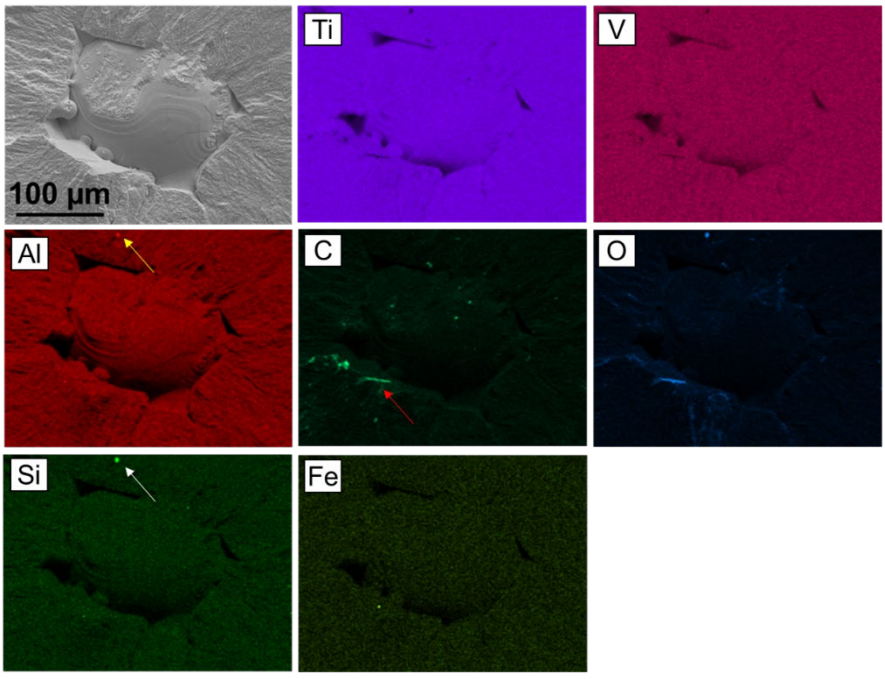

Fig. 72 Energy-dispersive X-ray spectroscopy (EDS) maps on the fracture surface of the L-PBF Ti64 Sp.1 from Print 4. The SiO2, Al2O3, and TiC nonmetallic inclusions are pointed with white, yellow, and red arrows.

9. Supplement B

The artificial neural network used in this dissertation to predict the powder quality score had a structure as follows:

Loading the required packages:

```
from pandas import read_csv
from matplotlib import pyplot
from keras.utils.vis_utils import plot_model
from tensorflow.keras.models import Sequential
from tensorflow.keras.layers import Dense
from sklearn.metrics import mean_absolute_error
from sklearn.metrics import mean_absolute_percentage_error
from sklearn.model_selection import train_test_split
from ann_visualizer.visualize import ann_viz
import pandas as pd
import numpy as np
import visualkeras
import tensorflow as tf
import math
import matplotlib.pyplot as plt
import graphviz
```

Creating the first dataset from the data and defining the input and output variables:

```
dataframe = pd.read_csv('MyCodes/Powder_Data.csv');
dataset = dataframe.values
dataset = dataframe.values
X = dataset [0:30,2:16]
y = dataset [0:30,26]
```

Splitting the dataset into training and testing data:

```
X_train, X_test, y_train, y_test = train_test_split(X, y, test_size=0.3, random_state=10)
X_train = np.asarray(X_train).astype(np.float32)
y_train = np.asarray(y_train).astype(np.float32)
X_test = np.asarray(X_test).astype(np.float32)
y_test = np.asarray(y_test).astype(np.float32)
n_features = X_train.shape[1]
```

Defining the artificial neural network based on a Keras model:

```
model = Sequential()
model.add(Dense(40,inputdim=n_features,activation='sigmoid',kernel_initializer='he_normal'))
model.add(Dense(40, activation='relu', kernel_initializer='he_normal'))
model.add(Dense(1, activation='linear'))
```

```
model.compile(loss='mse', optimizer='adam', metrics=['accuracy'])
history=model.fit(X_train,y_train,epochs=1024, validation_data=(X_test,y_test), batch_size=32,
verbose=0)
```

Predicting the powder score based on the input variables:

```
y_predict = model.predict(X_test)
print("Test=%s, Predict=%s" % (y_test[0:50], y_predict[0:50]))
mape= mean_absolute_percentage_error(y_test,y_predict)
print("Mean absolute percentage error (MAPE)=" , mape)
```

Evaluating the model loss:

```
plt.plot(history.history['loss'],label='Loss')
plt.plot(history.history['val_loss'], label='Loss Value')
plt.title('Model Loss')
plt.ylabel('Loss')
plt.xlabel('Epoch')
plt.legend(loc='upper right')
plt.show()
```

Creating the second dataset from the literature to predict powder quality score:

```
dataframe2 = pd.read_csv('MyCodes/Powder_Data.csv')
dataset2 = dataframe2.values
Xnew = dataset2 [31:44,2:16]
Xnew = np.asarray(Xnew).astype(np.float32)
ynew = dataset2 [31:44,26]
ynew = np.asarray(ynew).astype(np.float32)
ynew_predict = model.predict(Xnew)
ynew_predict = np.asarray(ynew_predict).astype(np.float32)
print("Data from Literature=%s, Prediction=%s" % (ynew[0:50], ynew_predict[0:50]))
mape= mean_absolute_percentage_error(ynew,ynew_predict)
print("Mean absolute percentage error (MAPE) of literature data=" , mape)

plt.subplots(figsize=(8, 6))
Line1= plt.plot(y_test, marker='o', color='r', linestyle='None', markersize = 10, label='Data')
Line2=plt.plot(y_predict,marker='^',color='b',linestyle='None',markersize=10,label='Predictio
ns')
plt.xlabel('Sample', fontsize=14, fontname="arial")
plt.ylabel('Powder Score',fontsize=14, fontname="arial")
plt.legend(fontsize=14, loc='best')
plt.tick_params(axis='both', length=5, width=1, which='both', labelsize=14, direction='in')
plt.title("Experimental Data", fontsize=14, fontname="arial")
plt.xlim([-1, 14]);
plt.ylim([0,1.2]);
```

```
plt.subplots(figsize=(8, 6))
Line3= plt.plot(ynew, marker='o', color='k', linestyle='None', markersize = 10, label='Literature
Data')
Line4=plt.plot(ynew_predict,marker="^",color='c',linestyle='None',markersize=10,
label='Prediction')
plt.xlabel('Sample',fontsize=14, fontname="arial")
plt.ylabel('Powder Score',fontsize=14, fontname="arial")
plt.legend(fontsize=14, loc='best')
plt.tick_params(axis='both', length=5, width=1, which='both', labelsize=14, direction='in')
plt.title("Literature Data", fontsize=14, fontname="arial")
plt.xlim([-1, 32]);
plt.ylim([0,1.2]);
plt.show()
```

10. References

[1] N. Shamsaei, A. Yadollahi, L. Bian, S.M. Thompson, An overview of Direct Laser Deposition for additive manufacturing; Part II: Mechanical behavior, process parameter optimization and control, Addit. Manuf. 8 (2015) 12–35.

[2] P.R. Gradl, C.S. Protz, Technology advancements for channel wall nozzle manufacturing in liquid rocket engines, Acta Astronaut. 174 (2020) 148–158.

[3] A. Yadollahi, N. Shamsaei, Additive manufacturing of fatigue resistant materials: Challenges and opportunities, Int. J. Fatigue. 98 (2017) 14–31.

[4] A. Soltani-Tehrani, R. Shrestha, N. Phan, M. Seifi, N. Shamsaei, Establishing specimen property to part performance relationships for laser beam powder bed fusion additive manufacturing, Int. J. Fatigue. 151 (2021) 106384.

[5] R. Shrestha, N. Shamsaei, M. Seifi, N. Phan, An investigation into specimen property to part performance relationships for laser beam powder bed fusion additive manufacturing, Addit. Manuf. 29 (2019) 100807.

[6] S.M. Thompson, L. Bian, N. Shamsaei, A. Yadollahi, An overview of Direct Laser Deposition for additive manufacturing; Part I: Transport phenomena, modeling and diagnostics, Addit. Manuf. 8 (2015) 36–62.

[7] P.E. Carrion, A. Soltani-Tehrani, N. Phan, N. Shamsaei, Powder Recycling Effects on the Tensile and Fatigue Behavior of Additively Manufactured Ti-6Al-4V Parts, JOM. 71 (2019) 963–973.

[8] P.E. Carrion, A. Soltani-Tehrani, S.M. Thompson, N. Shamsaei, Effect of Powder Degradation on the Fatigue Behavior of Additively Manufactured As-Built Ti-6Al-4V, Solid Free. Fabr. Proc. (2018).

[9] A.T. Sutton, C.S. Kriewall, M.C. Leu, J.W. Newkirk, Powder characterisation techniques and effects of powder characteristics on part properties in powder-bed fusion processes, Virtual Phys. Prototyp. 12 (2017) 3–29.

[10] J.H. Tan, W.L.E. Wong, K.W. Dalgarno, An overview of powder granulometry on feedstock and part performance in the selective laser melting process, Addit. Manuf. 18 (2017) 228–255.

[11] R.M. German, Powder metallurgy science, 105 College Rd. E, Princeton, N. J. 08540, U. S. A, 1984.

[12] P. Moghimian, T. Poirié, M. Habibnejad-Korayem, J.A. Zavala, J. Kroeger, F. Marion, F. Larouche, Metal Powders in Additive Manufacturing: A Review on Reusability and Recyclability of Common Titanium, Nickel and Aluminum Alloys, Addit. Manuf. (2021) 102017.

[13] H.P. Tang, M. Qian, N. Liu, X.Z. Zhang, G.Y. Yang, J. Wang, Effect of Powder Reuse Times on Additive Manufacturing of Ti-6Al-4V by Selective Electron Beam Melting, JOM. 67 (2015) 555–563.

[14] G. Soundarapandiyan, C. Johnston, R.H.U. Khan, C.L.A. Leung, P.D. Lee, E. Hernández-Nava, B. Chen, M.E. Fitzpatrick, The effects of powder reuse on the mechanical response of electron beam additively manufactured Ti6Al4V parts, Addit. Manuf. 46 (2021) 102101.

[15] V. V. Popov, A. Katz-Demyanetz, A. Garkun, M. Bamberger, The effect of powder recycling on the mechanical properties and microstructure of electron beam melted Ti-6Al-4V specimens, Addit. Manuf. 22 (2018) 834–843.

[16] J. Schiltz, F. Alamos, K. Kozlovsky, R. Attardo, B.A. Gatrell, J. Budzinski, C. Tomonto, J. McGuffin-Cawley, S.R. Schmid, Fatigue performance of direct metal laser sintered parts

using reused metallic feedstocks, 48 (2020) 814–820.
[17] K. Kassym, A. Perveen, Atomization processes of metal powders for 3D printing, Mater. Today Proc. 26 (2019) 1727–1733.
[18] Z.M. Jian, G.A. Qian, D.S. Paolino, A. Tridello, F. Berto, Y.S. Hong, Crack initiation behavior and fatigue performance up to very-high-cycle regime of AlSi10Mg fabricated by selective laser melting with two powder sizes, Int. J. Fatigue. 143 (2021) 106013.
[19] M. Habibnejad-korayem, J. Zhang, Y. Zou, Effect of particle size distribution on the flowability of plasma atomized Ti-6Al-4V powders, Powder Technol. 392 (2021) 536–543.
[20] S.E. Brika, M. Letenneur, C.A. Dion, V. Brailovski, Influence of particle morphology and size distribution on the powder flowability and laser powder bed fusion manufacturability of Ti-6Al-4V alloy, Addit. Manuf. 31 (2020) 100929.
[21] E. Santecchia, S. Spigarelli, M. Cabibbo, Material reuse in laser powder bed fusion: Side effects of the laser—metal powder interaction, Metals (Basel). 10 (2020) 1–21.
[22] L. Cordova, M. Campos, T. Tinga, Revealing the Effects of Powder Reuse for Selective Laser Melting by Powder Characterization, JOM. 71 (2019) 1062–1072.
[23] B.A. Hann, Powder Reuse and Its Effects on Laser Based Powder Fusion Additive Manufactured Alloy 718, SAE Int. J. Aerosp. 9 (2016) 2016-01–2071.
[24] F.J. Alamos, J. Schiltz, K. Kozlovsky, R. Attardo, C. Tomonto, T. Pelletiers, S.R. Schmid, Effect of powder reuse on mechanical properties of Ti-6Al-4V produced through selective laser melting, Int. J. Refract. Met. Hard Mater. 91 (2020) 105273.
[25] R. Harkin, H. Wu, S. Nikam, J. Quinn, S. McFadden, Reuse of Grade 23 Ti6Al4V Powder during the Laser-Based Powder Bed Fusion Process, Metals (Basel). 10 (2020) 1700.
[26] C. Rock, C. Ledford, M. Garcia-Avila, H. West, V.M. Miller, M. Pankow, R. Dehoff, T. Horn, The Influence of Powder Reuse on the Properties of Nickel Super Alloy ATI 718^{TM} in Laser Powder Bed Fusion Additive Manufacturing, Metall. Mater. Trans. B Process Metall. Mater. Process. Sci. 52 (2021) 676–688.
[27] F. Yi, Q. Zhou, C. Wang, Z. Yan, B. Liu, Effect of powder reuse on powder characteristics and properties of Inconel 718 parts produced by selective laser melting, J. Mater. Res. Technol. 13 (2021) 524–533.
[28] K.L. Terrassa, J.C. Haley, B.E. MacDonald, J.M. Schoenung, Reuse of powder feedstock for directed energy deposition, Powder Technol. 338 (2018) 819–829.
[29] J.N. Rousseau, A. Bois-brochu, C. Blais, J. Nicolas, A. Bois-brochu, C. Blais, J.N. Rousseau, A. Bois-brochu, C. Blais, Effect of oxygen content in new and reused powder on microstructural and mechanical properties of Ti6Al4V parts produced by directed energy deposition, Addit. Manuf. 23 (2018) 197–205.
[30] A. Saboori, A. Aversa, F. Bosio, E. Bassini, E. Librera, M. De Chirico, S. Biamino, D. Ugues, P. Fino, M. Lombardi, M. De Chirico, S. Biamino, D. Ugues, P. Fino, M. Lombardi, An investigation on the effect of powder recycling on the microstructure and mechanical properties of AISI 316L produced by Directed Energy Deposition, Mater. Sci. Eng. A. 766 (2019) 138360.
[31] A. Soltani-Tehrani, M. Habibnejad-Korayem, S. Shao, M. Haghshenas, N. Shamsaei, Ti-6Al-4V Powder Characteristics in Laser Powder Bed Fusion: The Effect on Tensile and Fatigue Behavior, Addit. Manuf. 51 (2021) 102584.
[32] J.W. Pegues, S. Shao, N. Shamsaei, N. Sanaei, A. Fatemi, D.H. Warner, P. Li, N. Phan, Fatigue of additive manufactured Ti-6Al-4V, Part I: The effects of powder feedstock, manufacturing, and post-process conditions on the resulting microstructure and defects, Int.

J. Fatigue. 132 (2020) 105358.
[33] A. Soltani-Tehrani, J. Pegues, N. Shamsaei, Fatigue behavior of additively manufactured 17-4 PH stainless steel: The effects of part location and powder re-use, Addit. Manuf. 36 (2020) 101398.
[34] L. Cordova, T. Bor, M. de Smit, M. Campos, T. Tinga, Measuring the spreadability of pre-treated and moisturized powders for laser powder bed fusion, Addit. Manuf. 32 (2020) 101082.
[35] M. Salarian, H. Asgari, M. Vlasea, Pore space characteristics and corresponding effect on tensile properties of Inconel 625 fabricated via laser powder bed fusion, Mater. Sci. Eng. A. 769 (2020) 138525.
[36] K. Riener, N. Albrecht, S. Ziegelmeier, R. Ramakrishnan, L. Haferkamp, A.B. Spierings, G.J. Leichtfried, Influence of particle size distribution and morphology on the properties of the powder feedstock as well as of AlSi10Mg parts produced by laser powder bed fusion (LPBF), Addit. Manuf. 34 (2020) 101286.
[37] P. Nandwana, M.M. Kirka, V.C. Paquit, S. Yoder, R.R. Dehoff, Correlations Between Powder Feedstock Quality, In Situ Porosity Detection, and Fatigue Behavior of Ti-6Al-4V Fabricated by Powder Bed Electron Beam Melting: A Step Towards Qualification, Jom. 70 (2018) 1686–1691.
[38] R. Molaei, A. Fatemi, N. Sanaei, J. Pegues, N. Shamsaei, S. Shao, P. Li, D.H. Warner, N. Phan, Fatigue of additive manufactured Ti-6Al-4V, Part II: The relationship between microstructure, material cyclic properties, and component performance, Int. J. Fatigue. 132 (2020) 105363.
[39] R. Shrestha, J. Simsiriwong, N. Shamsaei, Fatigue behavior of additive manufactured 316L stainless steel parts: Effects of layer orientation and surface roughness, Addit. Manuf. 28 (2019) 23–38.
[40] A.B. Spierings, N. Herres, G. Levy, Influence of the particle size distribution on surface quality and mechanical properties in AM steel parts, Rapid Prototyp. J. 17 (2011) 195–202.
[41] G. Jacob, C.U. Brown, A. Donmez, The Influence of Spreading Metal Powders with Different Particle Size Distributions on the Powder Bed Density in Laser-Based Powder Bed Fusion Processes, NIST Adv. Manuf. Ser. (2018) 100–17.
[42] ASTM International, B243-20 Standard Terminology of Powder Metallurgy, West Conshohocken, PA; ASTM Int. (2020).
[43] A. Amado, M. Schmid, G. Levy, K. Wegener, Advances in SLS powder characterization, in: 22nd Annu. Int. Solid Free. Fabr. Symp. - An Addit. Manuf. Conf. SFF 2011, 2011: pp. 438–452.
[44] S. Liu, Y.C. Shin, Additive manufacturing of Ti6Al4V alloy: A review, Mater. Des. 164 (2019) 107552.
[45] ASTM International, F3001-14 Standard Specification for Additive Manufacturing Titanium-6 Aluminum-4 Vanadium ELI (Extra Low Interstitial) with Powder Bed Fusion, West. (2014).
[46] ASTM International, E1409-13 Standard Test Method for Determination of Oxygen and Nitrogen in Titanium and Titanium Alloys by Inert Gas Fusion, West Conshohocken, PA; ASTM Int. (2016).
[47] ASTM International, E1447 Standard Test Method for Determination of Hydrogen in Titanium and Titanium Alloys by Inert Gas Fusion Thermal Conductivity/Infrared Detection Method, West Conshohocken, PA; ASTM Int. (2016).

[48] ASTM International, E1941 Standard Test Method for Determination of Carbon in Refractory and Reactive Metals and Their Alloys by Combustion Analysis, West Conshohocken, PA; ASTM Int. (2016).
[49] ASTM International, E2371-13 Standard Test Method for Analysis of Titanium and Titanium Alloys by Direct Current Plasma and Inductively Coupled Plasma Atomic Emission Spectrometry (Performance-Based Test Methodology), West Conshohocken, PA; ASTM Int. (2013).
[50] ASTM International, B822 Standard Test Method for Particle Size Distribution of Metal Powders and Related Compounds by Light Scattering, West Conshohocken, PA; ASTM Int. (2020).
[51] M. Tang, P.C. Pistorius, J.L. Beuth, P. Chris Pistorius, J.L. Beuth, P.C. Pistorius, J.L. Beuth, P. Chris Pistorius, J.L. Beuth, Prediction of lack-of-fusion porosity for powder bed fusion, Addit. Manuf. 14 (2017) 39–48.
[52] ASTM International, E466 Standard Practice for Conducting Force Controlled Constant Amplitude Axial Fatigue Tests of Metallic Materials, West Conshohocken, PA; ASTM Int. (2015).
[53] ASTM International, E8/E8M Standard Test Methods for Tension Testing of Metallic Materials, West Conshohocken, PA; ASTM Int. (2016).
[54] M. Frkan, R. Konecna, G. Nicoletto, L. Kunz, Microstructure and fatigue performance of SLM-fabricated Ti6Al4V alloy after different stress-relief heat treatments, Transp. Res. Procedia. 40 (2019) 24–29.
[55] ASTM International, B215 Standard Practices for Sampling Metal Powders, West Conshohocken, PA; ASTM Int. (2020).
[56] ASTM International, B527 Standard Test Method for Tap Density of Metal Powders and Compounds, West Conshohocken, PA; ASTM Int. (2020).
[57] ASTM International, D7891 Standard Test Method for Shear Testing of Powders Using the Freeman Technology FT4 Powder Rheometer Shear Cell, West Conshohocken, PA; ASTM Int. (2015).
[58] J.A. Slotwinski, E.J. Garboczi, P.E. Stutzman, C.F. Ferraris, S.S. Watson, M.A. Peltz, Characterization of Metal Powders Used for Additive Manufacturing, J. Res. Natl. Inst. Stand. Technol. 119 (2014) 460.
[59] X. Zhou, N. Dai, X. Cheng, A. Thompson, R. Leach, Three-dimensional characterization of powder particles using X-ray computed tomography, Addit. Manuf. 40 (2021) 101913.
[60] M. Mehrabi, A. Hassanpour, A. Bayly, An X-ray microtomography study of particle morphology and the packing behaviour of metal powders during filling, compaction and ball indentation processes, Powder Technol. 385 (2021) 250–263.
[61] B. Xie, Y. Fan, S. Zhao, Characterization of Ti6Al4V powders produced by different methods for selective laser melting, Mater. Res. Express. 8 (2021).
[62] Freeman Technology, FT4 Powder Rheometer - Summary of Methodologies, (2008).
[63] H.Y. Sohn, C. Moreland, The effect of particle size distribution on packing density, Can. J. Chem. Eng. 46 (1968) 162–167.
[64] M. Ghadiri, M. Pasha, W. Nan, C. Hare, V. Vivacqua, U. Zafar, S. Nezamabadi, A. Lopez, M. Pasha, S. Nadimi, Cohesive powder flow: Trends and challenges in characterisation and analysis, KONA Powder Part. J. 37 (2020) 3–18.
[65] T. Voisin, N.P. Calta, S.A. Khairallah, J.B. Forien, L. Balogh, R.W. Cunningham, A.D. Rollett, Y.M. Wang, Defects-dictated tensile properties of selective laser melted Ti-6Al-

4V, Mater. Des. 158 (2018) 113–126.
[66] M. Masoomi, S.M. Thompson, N. Shamsaei, Laser powder bed fusion of Ti-6Al-4V parts: Thermal modeling and mechanical implications, Int. J. Mach. Tools Manuf. 118–119 (2017) 73–90.
[67] R. Esmaeilizadeh, U. Ali, A. Keshavarzkermani, Y. Mahmoodkhani, E. Marzbanrad, E. Toyserkani, On the effect of spatter particles distribution on the quality of Hastelloy X parts made by laser powder-bed fusion additive manufacturing, J. Manuf. Process. 37 (2019) 11–20.
[68] ASTM International, F2924-14 Standard Specification for Additive Manufacturing Titanium-6 Aluminum-4 Vanadium with Powder Bed Fusion, West Conshohocken, PA; ASTM Int. (2014).
[69] D. Barba, C. Alabort, Y.T. Tang, M.J. Viscasillas, R.C. Reed, E. Alabort, On the size and orientation effect in additive manufactured Ti-6Al-4V, Mater. Des. 186 (2020) 108235.
[70] W. Xu, M. Brandt, S. Sun, J. Elambasseril, Q. Liu, K. Latham, K. Xia, M. Qian, Additive manufacturing of strong and ductile Ti-6Al-4V by selective laser melting via in situ martensite decomposition, Acta Mater. 85 (2015) 74–84.
[71] R.I. Stephens, A. Fatemi, R.R. Stephens, H.O. Fuchs, Metal fatigue in engineering, John Wiley & Sons, 2000.
[72] S. Romano, P.D. Nezhadfar, N. Shamsaei, M. Seifi, S. Beretta, High cycle fatigue behavior and life prediction for additively manufactured 17-4 PH stainless steel: Effect of sub-surface porosity and surface roughness, Theor. Appl. Fract. Mech. 106 (2020).
[73] J. Pegues, M. Roach, R. Scott Williamson, N. Shamsaei, Surface Roughness Effects on the Fatigue Strength of Additively Manufactured Ti-6Al-4V, Int. J. Fatigue. 116 (2018) 543–552.
[74] A. Fernandez, S.E. Pautler, Metal Fatigue Causing Cystoscope Rupture During Bladder Neck Incision, JSLS J. Soc. Laparoendosc. Surg. 15 (2011) 421–423.
[75] Y. Yang, D. Gu, D. Dai, C. Ma, Laser energy absorption behavior of powder particles using ray tracing method during selective laser melting additive manufacturing of aluminum alloy, Mater. Des. 143 (2018) 12–19.
[76] K. Maeda, S. Suzuki, K. Ueda, T. Kitashima, S.K. Bhattacharya, R. Sahara, T. Narushima, Experimental and theoretical study of the effect of Si on the oxidative behavior of Ti-6Al-4V alloys, J. Alloys Compd. 776 (2019) 519–528.
[77] T. Deng, S. Li, Y. Liang, L. Sun, Y. Zhang, Effects of scandium and silicon addition on the microstructure and mechanical properties of Ti-6Al-4V alloy, J. Mater. Res. Technol. 9 (2020) 5676–5688.
[78] M. Ipek, C. Bindal, S. Zeytin, G. Celebi Efe, M. İpek, Pack Siliconizing of Ti6Al4V Alloy, 132 (2017).
[79] H. Okamoto, O-Si (Oxygen-Silicon), J. Phase Equilibria Diffus. 28 (2007) 309–310.
[80] P. Moore, G. Booth, The Welding Engineer's Guide to Fracture and Fatigue, Elsevier, 2014.
[81] ASTM International, E2283 Standard Practice for Extreme Value Analysis of Nonmetallic Inclusions in Steel and Other Microstructural Features, West Conshohocken, PA; ASTM Int. (2019).
[82] S. Romano, A. Brandão, J. Gumpinger, M. Gschweitl, S. Beretta, Qualification of AM parts: Extreme value statistics applied to tomographic measurements, Mater. Des. 131 (2017) 32–48.
[83] S. Beretta, Y. Murakami, Largest-extreme-value distribution analysis of multiple inclusion

types in determining steel cleanliness, Metall. Mater. Trans. B Process Metall. Mater. Process. Sci. 32 (2001) 517–523.
[84] E.J. Gumbel, Statistics of Extremes, Columbia University Press, 1958.
[85] S. Romano, A. Brückner-Foit, A. Brandão, J. Gumpinger, T. Ghidini, S. Beretta, Fatigue properties of AlSi10Mg obtained by additive manufacturing: Defect-based modelling and prediction of fatigue strength, Eng. Fract. Mech. 187 (2018) 165–189.
[86] S. Beretta, C. Anderson, Y. Murakami, Extreme value models for the assessment of steels containing multiple types of inclusion, Acta Mater. 54 (2006) 2277–2289.
[87] America Makes & ANSI Additive Manufacturing Standardization Collaborative (AMSC), Standardization Roadmap for Additive Manufacturing - Version 2.0, 2018.
[88] R. Schur, S. Ghods, C. Wisdom, R. Pahuja, A. Montelione, D. Arola, M. Ramulu, Mechanical anisotropy and its evolution with powder reuse in Electron Beam Melting AM of Ti6Al4V, Mater. Des. 200 (2021) 109450.
[89] R. Schur, S. Ghods, E. Schultz, C. Wisdom, R. Pahuja, A. Montelione, D. Arola, M. Ramulu, A Fractographic Analysis of Additively Manufactured Ti6Al4V by Electron Beam Melting: Effects of Powder Reuse, J. Fail. Anal. Prev. 20 (2020) 794–803.
[90] H. Gruber, P. Karimi, E. Hryha, L. Nyborg, Effect of Powder Recycling on the Fracture Behavior of Electron Beam Melted Alloy 718, Powder Metall. Prog. 18 (2018) 40–48.
[91] Y. Guo, C. Chen, Q. Wang, M. Liu, Effects of reuse on the properties of tantalum powders and tantalum parts additively manufactured by electron beam powder bed fusion, Mater. Res. Express. 8 (2021).
[92] A. Soltani-Tehrani, M.S. Yasin, S. Shao, Shamsae, Effects of Powder Reuse and Spatial Location Dependency on the Powder Characteristics and Defect Structure of Additively Manufactured Ti-6Al-4V Parts, in: Proc. 32nd Annu. Int. Solid Free. Fabr. Symp. - An Addit. Manuf. Conf., 2021: pp. 1093–1103.
[93] V. Contaldi, P. Corrado, F. Del Re, D. Di Martino, P. Di Petta, B. Palumbo, F. Scherillo, A. Squillace, Direct metal laser sintering of Ti-6Al-4V parts with reused powder, Int. J. Adv. Manuf. Technol. (2022).
[94] M. Skalon, B. Meier, T. Leitner, S. Arneitz, S.T. Amancio-Filho, C. Sommitsch, Reuse of Ti6al4V powder and its impact on surface tension, melt pool behavior and mechanical properties of additively manufactured components, Materials (Basel). 14 (2021) 1–22.
[95] R. Harkin, H. Wu, S. Nikam, S. Yin, R. Lupoi, W. McKay, P. Walls, J. Quinn, S. McFadden, Powder Reuse in Laser-Based Powder Bed Fusion of Ti6Al4V—Changes in Mechanical Properties during a Powder Top-Up Regime, Materials (Basel). 15 (2022) 2238.
[96] G. Jacob, C.U. Brown, A. Donmez, S.S. Watson, M.A. Donmez, S.S. Watson, J. Slotwinski, Effects of powder recycling on stainless steel powder and built material properties in metal powder bed fusion processes, Gaithersburg, MD, 2017.
[97] F. Ahmed, U. Ali, D. Sarker, E. Marzbanrad, K. Choi, Y. Mahmoodkhani, E. Toyserkani, Study of Powder Recycling and its Effect on Printed Parts During Laser Powder-Bed Fusion of 17-4 PH Stainless Steel, J. Mater. Process. Tech. 278 (2019) 127177.
[98] H. Sun, X. Chu, Z. Liu, A. Gisele, Y. Zou, Selective Laser Melting of Maraging Steels Using Recycled Powders: A Comprehensive Microstructural and Mechanical Investigation, Metall. Mater. Trans. A Phys. Metall. Mater. Sci. 52 (2021) 1714–1722.
[99] J. Berez, C. Saldana, Fatigue of laser powder bed fusion processed 17-4 stainless steel using prior process exposed powder feedstock, J. Manuf. Process. 71 (2021) 515–527.
[100] C. Lu, R. Zhang, M. Xiao, X. Wei, Y. Yin, Y. Qu, H. Li, P. Liu, X. Qiu, T. Guo, A

comprehensive characterization of virgin and recycled 316L powders during laser powder bed fusion, J. Mater. Res. Technol. 18 (2022) 2292–2309.
[101] S. Kim, M. Goto, S. Kim, Effect of Powder Recycling on Environment-Assisted Fracture of Inconel 718 Alloy Fabricated by Laser Powder Bed Fusion, Metall. Mater. Trans. A Phys. Metall. Mater. Sci. 53 (2022) 211–224.
[102] F. Del Re, V. Contaldi, A. Astarita, B. Palumbo, A. Squillace, P. Corrado, P. Di Petta, Statistical approach for assessing the effect of powder reuse on the final quality of AlSi10Mg parts produced by laser powder bed fusion additive manufacturing, Int. J. Adv. Manuf. Technol. 97 (2018) 2231–2240.
[103] C. Weiss, C.L. Haefner, J. Munk, On the Influence of AlSi10Mg Powder Recycling Behavior in the LPBF Process and Consequences for Mechanical Properties, Jom. (2022).
[104] J.D. Carroll, A.N. Exil, S.A. DeJong, I.A. Valdez, C.M. Laursen, L.A. Deibler, C.B. Finfrock, B.L. Boyce, High-Throughput Statistical Interrogation of Mechanical Properties with Build Plate Location and Powder Reuse in AlSi10Mg, JOM. 73 (2021) 3356–3370.
[105] X. He, D. Kong, Y. Zhou, L. Wang, X. Ni, L. Zhang, W. Wu, R. Li, X. Li, C. Dong, Powder recycling effects on porosity development and mechanical properties of Hastelloy X alloy during laser powder bed fusion process, Addit. Manuf. 55 (2022) 102840.
[106] A. Mussatto, R. Groarke, R.K. Vijayaraghavan, C. Hughes, M.A. Obeidi, M.N. Doğu, M.A. Yalçin, P.J. McNally, Y. Delaure, D. Brabazon, Assessing dependency of part properties on the printing location in laser-powder bed fusion metal additive manufacturing, Mater. Today Commun. 30 (2022) 103209.
[107] C.L.A. Leung, S. Marussi, M. Towrie, R.C. Atwood, P.J. Withers, P.D. Lee, The effect of powder oxidation on defect formation in laser additive manufacturing, Acta Mater. 166 (2019) 294–305.
[108] T. Montalbano, B.N. Briggs, J.L. Waterman, S. Nimer, C. Peitsch, J. Sopcisak, D. Trigg, S. Storck, Uncovering the coupled impact of defect morphology and microstructure on the tensile behavior of Ti-6Al-4V fabricated via laser powder bed fusion, J. Mater. Process. Technol. 294 (2021) 117113.
[109] V. Cain, L. Thijs, J. Van Humbeeck, B. Van Hooreweder, R. Knutsen, Crack propagation and fracture toughness of Ti6Al4V alloy produced by selective laser melting, Addit. Manuf. 5 (2015) 68–76.
[110] A. Mohammadhosseini, S.H. Masood, D. Fraser, M. Jahedi, Dynamic compressive behaviour of Ti-6Al-4V alloy processed by electron beam melting under high strain rate loading, Adv. Manuf. 3 (2015) 232–243.
[111] O.L. Rodriguez, P.G. Allison, W.R. Whittington, H. El Kadiri, O.G. Rivera, M.E. Barkey, Strain rate effect on the tension and compression stress-state asymmetry for electron beam additive manufactured Ti6Al4V, Mater. Sci. Eng. A. 713 (2018) 125–133.
[112] J.P. Isaac, S. Lee, N. Shamsaei, H. V. Tippur, Dynamic fracture behavior of additively manufactured Scalmalloy®: Effects of build orientation, heat-treatment and loading-rate, Mater. Sci. Eng. A. 826 (2021) 141978.
[113] J.P. Isaac, S. Dondeti, H. V. Tippur, Fracture behavior of additively printed ABS: Effects of print architecture and loading rate, Int. J. Solids Struct. 212 (2021) 80–95.
[114] J. Schindelin, I. Arganda-Carreras, E. Frise, V. Kaynig, M. Longair, T. Pietzsch, S. Preibisch, C. Rueden, S. Saalfeld, B. Schmid, J.-Y. Tinevez, D.J. White, V. Hartenstein, K. Eliceiri, P. Tomancak, A. Cardona, Fiji: an open-source platform for biological-image analysis, Nat. Methods. 9 (2012) 676–682.

[115] A.T. Sutton, C.S. Kriewall, M.C. Leu, J.W. Newkirk, B. Brown, Characterization of laser spatter and condensate generated during the selective laser melting of 304L stainless steel powder, Addit. Manuf. 31 (2020) 100904.
[116] A.T. Sutton, C.S. Kriewall, S. Karnati, M.C. Leu, J.W. Newkirk, Characterization of AISI 304L stainless steel powder recycled in the laser powder-bed fusion process, Addit. Manuf. 32 (2020) 100981.
[117] V. Seyda, N. Kaufmann, C. Emmelmann, Investigation of Aging Processes of Ti-6Al-4V Powder Material in Laser Melting, Phys. Procedia. 39 (2012) 425–431.
[118] M. Khorasani, A.H. Ghasemi, U.S. Awan, E. Hadavi, M. Leary, M. Brandt, G. Littlefair, W. O'Neil, I. Gibson, A study on surface morphology and tension in laser powder bed fusion of Ti-6Al-4V, Int. J. Adv. Manuf. Technol. 111 (2020) 2891–2909.
[119] N. Emminghaus, C. Hoff, J. Hermsdorf, S. Kaierle, Residual oxygen content and powder recycling: Effects on surface roughness and porosity of additively manufactured Ti-6Al-4V, Addit. Manuf. 46 (2021).
[120] P. Caracciolo, Effect of Defect in Additive Manufacturing Products, in: Int. Conf. Addit. Manuf. 3D Print., Nottingham (UK), 2018.
[121] N. Derimow, N. Hrabe, Oxidation in Reused Powder Bed Fusion Additive Manufacturing Ti-6Al-4V Feedstock: A Brief Review, Jom. 73 (2021) 3618–3638.
[122] Y. Murakami, M. Endo, Effects of defects, inclusions and inhomogeneities on fatigue strength, Int. J. Fatigue. 16 (1994) 163–182.
[123] M. Seifi, M. Gorelik, J. Waller, N. Hrabe, N. Shamsaei, S. Daniewicz, J.J. Lewandowski, Progress Towards Metal Additive Manufacturing Standardization to Support Qualification and Certification, Jom. 69 (2017) 439–455.
[124] R. Russell, D. Wells, J. Waller, B. Poorganji, E. Ott, T. Nakagawa, H. Sandoval, N. Shamsaei, M. Seifi, Qualification and certification of metal additive manufactured hardware for aerospace applications, in: Addit. Manuf. Aerosp. Ind., 2019.
[125] J. Clayton, D. Millington-Smith, B. Armstrong, The Application of Powder Rheology in Additive Manufacturing, Jom. 67 (2015) 544–548.
[126] R. O'Leary, R. Setchi, P.W. Prickett, G. Hankins, N. Jones, An Investigation into the Recycling of Ti-6Al-4V Powder Used Within SLM to Improve Sustainability, 2nd Int. Conf. Sustain. Des. Manuf. 8 (2015) 377–388.
[127] P. Nandwana, W.H. Peter, R.R. Dehoff, L.E. Lowe, M.M. Kirka, F. Medina, S.S. Babu, Recyclability Study on Inconel 718 and Ti-6Al-4V Powders for Use in Electron Beam Melting, Metall. Mater. Trans. B. 47 (2016) 754–762.
[128] Y.Y. Sun, S. Gulizia, C.H. Oh, C. Doblin, Y.F. Yang, M. Qian, Manipulation and Characterization of a Novel Titanium Powder Precursor for Additive Manufacturing Applications, JOM. 67 (2015) 564–572.
[129] P. Dastranjy Nezhadfar, A. Soltani-Tehrani, A. Sterling, N. Tsolas, N. Shamsaei, Effects of Powder Recycling on the Mechanical Properties of Additively Manufactured Stainless Steel 17-4PH, Solid Free. Fabr. Proc. (2018) 1292–1300.
[130] A. Strondl, O. Lyckfeldt, H. Brodin, U. Ackelid, Characterization and Control of Powder Properties for Additive Manufacturing, JOM. 67 (2015) 549–554.
[131] L.C. Ardila, F. Garciandia, J.B. González-Díaz, P. Álvarez, A. Echeverria, M.M. Petite, R. Deffley, J. Ochoa, Effect of IN718 recycled powder reuse on properties of parts manufactured by means of Selective Laser Melting, Phys. Procedia. 56 (2014) 99–107.
[132] P. Quinn, S. O'Halloran, J. Lawlor, R. Raghavendra, The effect of metal EOS 316L stainless

steel additive manufacturing powder recycling on part characteristics and powder reusability, Adv. Mater. Process. Technol. 5 (2019) 348–359.
[133] B. Liu, R. Wildman, C. Tuck, I. Ashcroft, R. Hague, Investigation the effect of particle size distribution on processing parameters optimisation in selective laser melting process, Int. Solid Free. Fabr. Symp. an Addit. Manuf. Conf. (2011) 227–238.
[134] G.K.H. Chua, C.Y.Y. Choong, C.H. Wong, Investigation of the effects on the print location during selective laser melting process, in: Proc. 3rd Int. Conf. Prog. Addit. Manufacuring (Pro-AM 2018), 2018: pp. 613–618.
[135] ASTM International, E606/E606M-12 Standard Test Method for Strain-Controlled Fatigue Testing, West Conshohocken, PA; ASTM Int. (2012).
[136] P.D. Nezhadfar, R. Shrestha, N. Phan, N. Shamsaei, Fatigue behavior of additively manufactured 17-4 PH stainless steel: Synergistic effects of surface roughness and heat treatment, Int. J. Fatigue. 124 (2019) 188–204.
[137] ASTM International, E2651-19 Standard Guide for Powder Particle Size Analysis, West Conshohocken, PA; ASTM Int. (2019).
[138] X. Fu, D. Huck, L. Makein, B. Armstrong, U. Willen, T. Freeman, Effect of particle shape and size on flow properties of lactose powders, Particuology. 10 (2012) 203–208.
[139] R. Freeman, Measuring the flow properties of consolidated, conditioned and aerated powders - A comparative study using a powder rheometer and a rotational shear cell, Powder Technol. 174 (2007) 25–33.
[140] J.W. Pegues, N. Shamsaei, M.D. Roach, R.S. Williamson, Fatigue life estimation of additive manufactured parts in the as-built surface condition, Mater. Des. Process. Commun. 1 (2019) e36.
[141] C. Meier, R. Weissbach, J. Weinberg, W.A. Wall, A.J. Hart, Modeling and Characterization of Cohesion in Fine Metal Powders with a Focus on Additive Manufacturing Process Simulations, ArXiv Prepr. ArXiv1804.06816. (2018).
[142] I.E. Anderson, E.M.H. White, R. Dehoff, Feedstock powder processing research needs for additive manufacturing development, Curr. Opin. Solid State Mater. Sci. 22 (2018) 8–15.
[143] C. Meier, R.R.R. Weissbach, J. Weinberg, W.A.W.A.W.A. Wall, A.J.J. Hart, Critical Influences of Particle Size and Adhesion on the Powder Layer Uniformity in Metal Additive Manufacturing, J. Mater. Process. Technol. 266 (2019) 484–501.
[144] J. Muñiz-Lerma, A. Nommeots-Nomm, K. Waters, M. Brochu, A Comprehensive Approach to Powder Feedstock Characterization for Powder Bed Fusion Additive Manufacturing: A Case Study on AlSi7Mg, Materials (Basel). 11 (2018) 2386.
[145] A. Simchi, The role of particle size on the laser sintering of iron powder, Metall. Mater. Trans. B. 35 (2004) 937–948.
[146] P.R. Gradl, T.W. Teasley, C.S. Protz, C. Katsarelis, P. Chen, Process Development and Hot-fire Testing of Additively Manufactured NASA HR-1 for Liquid Rocket Engine Applications, in: AIAA Propuls. Energy 2021 Forum, American Institute of Aeronautics and Astronautics, Reston, Virginia, 2021: pp. 1–23.
[147] P.S. Chen, C.C. Katsarelis, W.M. Medders, P.R. Gradl, Segregation Evolution and Diffusion of Titanium in Directed Energy Deposited, (2021) NASA/TM–20210013649.
[148] C. Katsarelis, P. Chen, P. Gradl, C. Protz, Z. Jones, D. Ellis, L. Evans, Additive Manufacturing of NASA HR-1 Material for Liquid Rocket Engine Component Applications, JANNAF Dec. (2019).
[149] P. Chen, M. Mitchell, Alloy NASA-HR-1, Aerosp. Struct. Met. Handb. (2005).

[150] A. Birken, D. Noel, Metallurgical and Thermal Processing Investigation of Additively Manufactured Superalloys JBK-75 and, (2021).
[151] A. Singh, S. Kapil, M. Das, A comprehensive review of the methods and mechanisms for powder feedstock handling in directed energy deposition, Addit. Manuf. 35 (2020) 101388.
[152] ASTM International, F3187-16 Standard Guide for Directed Energy Deposition of Metals, West Conshohocken, PA; ASTM Int. (2016).
[153] S. Li, B. Chen, C. Tan, X. Song, Study on Recyclability of 316L Stainless Steel Powder by Using Laser Directed Energy Deposition, J. Mater. Eng. Perform. 31 (2022) 400–409.
[154] M. Renderos, F. Girot, A. Lamikiz, A. Torregaray, N. Saintier, Ni based powder reconditioning and reuse for LMD process, Phys. Procedia. 83 (2016) 769–777.
[155] S.A. Shalnova, Y.O. Kuzminova, S.A. Evlashin, O.G. Klimova-Korsmik, A.M. Vildanov, A.A. Shibalova, G.A. Turichin, Effect of recycled powder content on the structure and mechanical properties of Ti-6Al-4V alloy produced by direct energy deposition, J. Alloys Compd. 893 (2022) 162264.
[156] C.A. Schneider, W.S. Rasband, K.W. Eliceiri, NIH Image to ImageJ: 25 years of image analysis, Nat. Methods. 9 (2012) 671–675.
[157] ASTM International, B213 Standard Test Methods for Flow Rate of Metal Powders Using the Hall Flowmeter Funnel, West Conshohocken, PA; ASTM Int. (2016).
[158] ASTM International, ASTM E2594 Standard Test Method for Analysis of Nickel Alloys by Inductively Coupled Plasma Atomic Emission Spectrometry (Performance-Based Method), West Conshohocken, PA; ASTM Int. (2009) 1–13.
[159] ASTM International, B964 Standard Test Methods for Flow Rate of Metal Powders Using the Carney Funnel, West Conshohocken, PA; ASTM Int. (2016).
[160] N. Hadjipantelis, B. Weber, C. Buchanan, L. Gardner, Description of anisotropic material response of wire and arc additively manufactured thin-walled stainless steel elements, Thin-Walled Struct. 171 (2022) 108634.
[161] S. Lee, B. Rasoolian, D.F. Silva, J.W. Pegues, N. Shamsaei, Surface roughness parameter and modeling for fatigue behavior of additive manufactured parts: A non-destructive data-driven approach, Addit. Manuf. 46 (2021) 102094.
[162] A. Mostafaei, C. Zhao, Y. He, S. Reza Ghiaasiaan, B. Shi, S. Shao, N. Shamsaei, Z. Wu, N. Kouraytem, T. Sun, J. Pauza, J. V Gordon, B. Webler, N.D. Parab, M. Asherloo, Q. Guo, L. Chen, A.D. Rollett, Defects and anomalies in powder bed fusion metal additive manufacturing, Curr. Opin. Solid State Mater. Sci. 26 (2022) 100974.
[163] D. Arola, M. Ramulu, An Examination of the Effects from Surface Texture on the Strength of Fiber Reinforced Plastics, J. Compos. Mater. 33 (1999) 102–123.
[164] J. Jakumeit, G. Zheng, R. Laqua, S.J. Clark, J. Zielinski, J.H. Schleifenbaum, P.D. Lee, Modelling the complex evaporated gas flow and its impact on particle spattering during laser powder bed fusion, Addit. Manuf. 47 (2021) 102332.
[165] J.E. Shigley, Mechanical engineering design, McGraw-Hill Companies, 1972.
[166] S. Lee, N. Ahmad, K. Corriveau, C. Himel, D.F. Silva, N. Shamsaei, Bending properties of additively manufactured commercially pure titanium (CPTi) limited contact dynamic compression plate (LC-DCP) constructs: Effect of surface treatment, J. Mech. Behav. Biomed. Mater. 126 (2022) 105042.
[167] B. Blakey-Milner, P. Gradl, G. Snedden, M. Brooks, J. Pitot, E. Lopez, M. Leary, F. Berto, A. du Plessis, Metal additive manufacturing in aerospace: A review, Mater. Des. 209 (2021) 110008.

[168] J. Zhang, M. Habibnejad-korayem, Z. Liu, T. Lyu, Q. Sun, Y. Zou, A Computer Vision Approach to Evaluate Powder Flowability for Metal Additive Manufacturing, Integr. Mater. Manuf. Innov. 10 (2021) 429–443.
[169] E.A. Holm, R. Cohn, N. Gao, A.R. Kitahara, T.P. Matson, B. Lei, S.R. Yarasi, Overview: Computer Vision and Machine Learning for Microstructural Characterization and Analysis, Metall. Mater. Trans. A Phys. Metall. Mater. Sci. 51 (2020) 5985–5999.
[170] L. Scime, J. Beuth, Anomaly detection and classification in a laser powder bed additive manufacturing process using a trained computer vision algorithm, Addit. Manuf. 19 (2018) 114–126.
[171] L. Scime, J. Beuth, A multi-scale convolutional neural network for autonomous anomaly detection and classification in a laser powder bed fusion additive manufacturing process, Addit. Manuf. 24 (2018) 273–286.
[172] Z. Liang, Z. Nie, A. An, J. Gong, X. Wang, A particle shape extraction and evaluation method using a deep convolutional neural network and digital image processing, Powder Technol. 353 (2019) 156–170.
[173] B.L. DeCost, E.A. Holm, Characterizing powder materials using keypoint-based computer vision methods, Comput. Mater. Sci. 126 (2017) 438–445.
[174] B.L. DeCost, H. Jain, A.D. Rollett, E.A. Holm, Computer Vision and Machine Learning for Autonomous Characterization of AM Powder Feedstocks, Jom. 69 (2017) 456–465.
[175] X. Zhou, N. Dai, X. Cheng, A. Thompson, R. Leach, Intelligent classification for three-dimensional metal powder particles, Powder Technol. 397 (2022) 117018.
[176] Freeman Technology, Applications of the FT4 Powder Rheometer® in Additive Manufacturing, (2017) 3–6.
[177] G. Shanbhag, M. Vlasea, Powder Reuse Cycles in Electron Beam Powder Bed Fusion—Variation of Powder Characteristics, Materials (Basel). 14 (2021) 4602.
[178] M.D. Mohanty, M.N. Mohanty, Chapter 5 - Verbal sentiment analysis and detection using recurrent neural network, in: S. De, S. Dey, S. Bhattacharyya, S.B.T.-A.D.M.T. and M. for S.C. Bhatia (Eds.), Hybrid Comput. Intell. Pattern Anal., Academic Press, 2022: pp. 85–106.
[179] T. Menzies, E. Kocagüneli, L. Minku, F. Peters, B. Turhan, Chapter 24 - Using Goals in Model-Based Reasoning, in: T. Menzies, E. Kocagüneli, L. Minku, F. Peters, B.B.T.-S.D. and M. in S.E. Turhan (Eds.), Morgan Kaufmann, Boston, 2015: pp. 321–353.
[180] S. Abirami, P. Chitra, Chapter Fourteen - Energy-efficient edge based real-time healthcare support system, in: P. Raj, P.B.T.-A. in C. Evangeline (Eds.), Digit. Twin Paradig. Smarter Syst. Environ. Ind. Use Cases, Elsevier, 2020: pp. 339–368.
[181] A. Meyer-Baese, V.J. Schmid, Pattern recognition and signal analysis in medical imaging, Elsevier, 2014.
[182] D. Thomas, S. Gilbert, Costs and Cost Effectiveness of Additive Manufacturing - A Literature Review and Discussion, (2014) 1–77.
[183] D.L. Bourell, Perspectives on Additive Manufacturing, Annu. Rev. Mater. Res. 46 (2016) 1–18.
[184] P. Fathi-Hafshejani, A. Soltani-Tehrani, N. Shamsaei, M. Mahjouri-Samani, Laser Incidence Angle Influence on Energy Density Variations, Surface Roughness, and Porosity of Additively Manufactured Parts, Addit. Manuf. 50 (2021) 102572.
[185] N. Biswas, J.L. Ding, V.K. Balla, D.P. Field, A. Bandyopadhyay, Deformation and fracture behavior of laser processed dense and porous Ti6Al4V alloy under static and dynamic

loading, Mater. Sci. Eng. A. 549 (2012) 213–221.
[186] T.H. Becker, T.J. Marrow, R.B. Tait, Damage, crack growth and fracture characteristics of nuclear grade graphite using the Double Torsion technique, J. Nucl. Mater. 414 (2011) 32–43.
[187] T.H. Becker, M. Mostafavi, R.B. Tait, T.J. Marrow, An approach to calculate the J-integral by digital image correlation displacement field measurement, Fatigue Fract. Eng. Mater. Struct. 35 (2012) 971–984.
[188] T. V. Hareesh, F.P. Chiang, Integrated experimental-finite element approach for studying elasto-plastic crack-tip fields, Eng. Fract. Mech. 31 (1988) 451–461.
[189] R. Moutou Pitti, C. Badulescu, M. Grédiac, Characterization of a cracked specimen with full-field measurements: Direct determination of the crack tip and energy release rate calculation, Int. J. Fract. 187 (2014) 109–121.
[190] J.P. Isaac, S. Dondeti, H. V. Tippur, Crack initiation and growth in additively printed ABS: Effect of print architecture studied using DIC, Addit. Manuf. 36 (2020) 101536.
[191] A.T. Owens, H. V. Tippur, Measurement of mixed-mode fracture characteristics of an epoxy-based adhesive using a hybrid digital image correlation (DIC) and finite elements (FE) approach, Opt. Lasers Eng. 140 (2021) 106544.
[192] B. Pan, K. Qian, H. Xie, A. Asundi, Two-dimensional digital image correlation for in-plane displacement and strain measurement: A review, Meas. Sci. Technol. 20 (2009).
[193] M.S. Kirugulige, H. V. Tippur, Measurement of fracture parameters for a mixed-mode crack driven by stress waves using image correlation technique and high-speed digital photography, Strain. 45 (2009) 108–122.
[194] M.S. Kirugulige, H. V. Tippur, T.S. Denney, Measurement of transient deformations using digital image correlation method and high-speed photography: Application to dynamic fracture, Appl. Opt. 46 (2007) 5083–5096.
[195] D. Lee, H. Tippur, M. Kirugulige, P. Bogert, Experimental study of dynamic crack growth in unidirectional graphite/epoxy composites using digital image correlation method and high-speed photography, J. Compos. Mater. 43 (2009) 2081–2108.
[196] G.P. Cherepanov, Crack propagation in continuous media. PMM vol. 31, no. 3, 1967, pp. 476-488, J. Appl. Math. Mech. 31 (1967) 503–512.
[197] J.R. Rice, A path independent integral and the approximate analysis of strain concentration by notches and cracks, J. Appl. Mech. Trans. ASME. 35 (1964) 379–388.
[198] R.W. Bedsole, P.B. Bogert, H. V. Tippur, An experimental investigation of interlaminar and intralaminar dynamic fracture of CFRPs: Effect of matrix modification using carbon nanotubes, Compos. Struct. 132 (2015) 1043–1055.
[199] J. Yin, D. Wang, L. Yang, H. Wei, P. Dong, L. Ke, G. Wang, H. Zhu, X. Zeng, Correlation between forming quality and spatter dynamics in laser powder bed fusion, Addit. Manuf. 31 (2020) 100958.